Exploring solid-solid interfaces in Li6PS5Cl-based cathode composites for all solid state batteries

Elisa Quemin

Sorbonne Université

Ecole doctorale - ED 397 - Physique et Chimie des Matériaux

Collège de France

Laboratoire - Chimie du Solide et Energie

Exploring solid-solid interfaces in Li_6PS_5Cl-based composites for all-solid-state batteries

Elisa Quemin

Doctoral thesis in Materials Science / Chemistry

Supervised by Jean-Marie Tarascon and Romain Dugas

President of the jury: Sylvain Franger

Presented and defended in public on November 27th 2023 in front of the jury:

Jurgen Janek	Director, ZfM, JLU, Giessen, Germany	Referee
Laurence Croguennec	Director, ICMCB, Bordeaux, France	Referee
Sylvain Franger	Professor, ERIEE-ICMMO, Orsay, France	Examiner
Olivier Guillon	Director, IEK, Jülich, Germany	Examiner
Jean-Marie Tarascon	Director, Collège de France, France	Director
Romain Dugas	CNRS engineer, Collège de France, France	Co-supervisor

Sorbonne Université

Ecole doctorale - ED 397 - Physique et Chimie des Matériaux

Collège de France

Laboratoire - Chimie du Solide et Energie

Les interfaces tout solide dans les composites à base de Li_6PS_5Cl

Elisa Quemin

Thèse de doctorat en chimie des materiaux

Dirigée par Jean-Marie Tarascon et Romain Dugas

Président du jury : Sylvain Franger

Présentée et soutenue publiquement le 27 Novembre 2023, devant un jury composé de:

Jurgen Janek	Directeur, ZfM, JLU, Giessen, Germany	Rapporteur
Laurence Croguennec	Directrice, ICMCB, Bordeaux, France	Rapportrice
Sylvain Franger	Professeur, ERIEE-ICMMO, Orsay, France	Examinateur
Olivier Guillon	Directeur, IEK, Jülich, Germany	Examinateur
Jean-Marie Tarascon	Directeur, Collège de France, France	Directeur
Romain Dugas	Ingénieur CNRS, Collège de France, France	Co-superviseur

Acknowledgements

First and foremost, I want to convey my deep appreciation to Jean-Marie Tarascon for dedicating significant time and effort to assist me in constructing my articles and presentations. His guidance has been a crucial factor throughout these three years. I also want to express my gratitude for creating a remarkable laboratory and for consistently being accessible and supportive of my thesis work while allowing me a significant degree of autonomy.

My gratitude also goes to Romain Dugas for his great help. His scientific knowledge and the discussions we had were extremely helpful for this work. I also highly benefited from the three-electrode cell that he designed.

I wish to express my appreciation for Jürgen Janek and Laurence Croguennec for willing to undertake the task of refereeing this thesis, and to Sylvain Franger and Olivier Guillon for agreeing to be part of the jury. I am grateful for the time spent on reviewing my PhD work.

Many thanks to the collaborators who have contributed significantly to my PhD work. Special mentions go to Anshuman Chaupatnaik for his work on $Li_4Ti_5O_{12}$ synthesis, Ronan Chometon and Juan Forero-Saboya for their contributions to SEM, Gwenaelle Rousse for her expertise in crystallography and XRD interpretation, and Benjamin Hennequart for his valuable input on Halide solid electrolyte.

My warmest thanks goes to my wonderful co-workers Ronan Chometon and Benjamin Hennequart for the friendly and supportive environment I benefited from working alongside you. It has been a true pleasure to work in the solid-state team with you. I am also grateful to many of my past and present lab colleagues for creating a joyful environment despite the ups and downs of the PhD. Special mentions go to Ivette, Ronan, Benjamin, Clémence, Aleksandra, Juan, Zhenying, Alexia, Laura and others for the memorable times we spent together inside and outside the lab. I wish you all the best.

Finally, my deepest appreciation goes to my family, for their unwavering support throughout this journey.

Table of Contents

Chapter 3: In situ electronic conductivity of Li_6PS_5Cl based composites

Chapter 4: Exploring high potential degradation of Li_6PS_5Cl based composites

Chapter 1

Background and motivation

Summary

1.1 Broader context and thesis outline

Broader context

The development of the steam engine in 1780 marked the beginning of the industrial revolution, leading to an era of significant anthropogenic influence on Earth's geology and ecosystems, known as the Anthropocene era[1]. This period is characterized by the unregulated consumption of finite energy sources such as coal and petroleum, resulting in greenhouse gas emissions and climate change. To limit the environmental and health impacts of these products, it is necessary to reduce energy consumption and to transition to renewable energy sources, such as wind, geothermal, and solar power. Energy-storage technologies are essential in this transition, as they provide flexibility to fluctuating renewable energies.

Li-ion batteries have undergone significant advancements and are now the dominant energy storage system for portable devices, providing high energy density and reliability[2,3]. Batteries also play a crucial role in the development of electric vehicles, which are expected to exponentially increase in demand in the coming years due to EU policies (no more gasoline-fuelled car sold in EU after 2035)[4]. To meet the demand for higher safety and energy density in EV batteries, research is focusing on "beyond Li-ion technology", particularly All-Solid-State Batteries (ASSB), which are proposed as a superior alternative to Li-ion batteries[5–7]. This thesis aims to contribute to the development of ASSB, as elaborated in the subsequent section.

Thesis outline

The aim of this thesis is to contribute to ASSB development, and more specifically to explore the interfacial detrimental phenomena occurring in cathode composite, based on Li_6PS_5Cl solid electrolyte (SE). Indeed, mastering solid-solid interfaces is at the core of ASSB optimization.

This manuscript is structured in the following chapters.

Chapter 1: Background and motivation

Chapter 1 gives a brief overview of the lithium-ion battery technology history. It is followed by the core of this thesis subject, namely the ASSB. We explain why ASSB are seen as the next generation of battery, especially to power the EV. Then, we will go deeper by studying the cathode composites interfacial challenges. Finally, an outline of the best ASSB performances released in recent years is given.

Chapter 2: Electrochemical/chemical stability of Li_6PS_5Cl based cathode composites

Chapter 2 serves as a base to understand what drives the performances of a cathode composite based on Li_6PS_5Cl (Argyrodite) solid electrolyte. This solid electrolyte small stability window hinders the stability and kinetic performances. It is therefore crucial to understand its mechanistic in contact or not with other materials. The influence of electronically conductive additive is discussed, so as the active material nature. We decoupled two interfacial reactivities affecting battery performances and tackled their properties and parameters of importance. This study uses impedance spectroscopy as tool to decorrelate interfaces.

Chapter 3: In situ electronic conductivity of Li_6PS_5Cl based composites

The electronic conductive additive is proven to enhance degradation in Chapter 2. Thus, Chapter 3 explores the possibility to suppress it. Focusing on the electronic conductivity of carbon-free cathode composites during cycling, we looked at the effect of particle size,

volumetric changes of active material and active material nature on composites electronic conductivity. To proceed, we use a homemade unique device to track *in situ* the electronic conductivity changes of cathode composites.

Chapter 4: Exploring high potential degradation of Li_6PS_5Cl based composites

To suppress interfacial reactivities and enhance the stability of Li_6PS_5Cl composites, we explore the impact of plural parameters, namely the assembly pressure, the cathode loading, the impact of carbonate coating on SE and active material (AM), and formation cycle protocols. In the end, we combined the best parameters and propose an optimized composites/cycling protocol.

1.2 From liquid electrolyte-based Li-ion to all-solid-state battery

1.2.1 Operating principles of liquid electrolyte-based Li-ion battery

Figure 1.1 illustrates a standard schematic of a Li-ion battery. The battery comprises a negative electrode, which is typically made of graphite, and a positive electrode, which is usually composed of a layered oxide material or $LiFePO_4$. These two electrodes are separated by a porous separator, which is filled with an organic electrolyte to prevent short circuit and enable Li^+ ions conduction. The electrolyte contains $LiPF_6$ salt dissolved in a mixture of alkyl carbonate solvents, such as ethylene carbonate (EC) and dimethyl carbonate (DMC). Commercial electrolytes may also contain other additives to suit specific operating conditions. The electrodes are fabricated using a slurry process on a metal foil, which involves active material particles (typically of micrometre-scale), an electrically conductive additive (such as carbon-based ones: Super P, C65, or VGCF), and a polymeric binder. All electrodes alike the separator are porous, and filled by the electrolyte to ensure ionic motion near active surfaces.

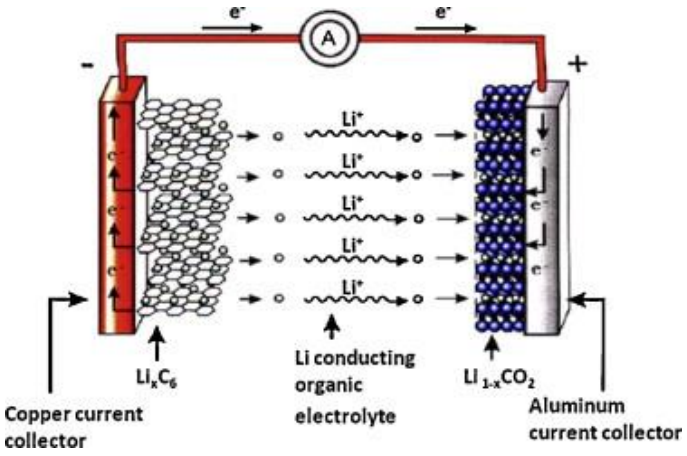

Figure 1.1: Scheme of a common lithium ion battery. Reproduced from reference. [7]

Several parameters are required for optimal performances of rechargeable batteries. These parameters encompass high energy density, high specific energy, low cost, extended cycle life, high power density, high safety, and elevated temperature tolerance. Among these

parameters, energy density and specific energy are of paramount importance for electric vehicle (EV) development. These parameters are typically calculated at a particular current (i.e., a specific C-rate) and are the product of the cell potential by the capacity. It can be expressed in per unit of weight (Wh/kg) (following equation below), or per unit of volume (Wh/L) :

$$E\ (Wh.kg^{-1}) = Q(A.h.kg^{-1}).U(V)$$

Specific Energy (or massic energy, in Wh/kg) relates to the amount of energy that can be stored per mass. As example, lead-acid battery can store 30-70 Wh/kg, while Li-ion battery reach 250-370 Wh/kg.

Energy density (or volumetric energy, in Wh/L) relates to the amount of energy that can be stored per volume. It is an important measure for application needing small volume storage, such as smartphones or EV. As example, lead-acid battery can store around 80 Wh/L, while a Li-ion battery pack reached 600 Wh/L.

The energy density and specific energy of a cell mainly depend on the specific capacity (mA.h/g) and potential (V) of the two electrodes. Thus, tuning the properties of the active material unlocked the performances of Li-ion batteries[8]. To tune those properties, one needs to understand the specific capacity and the cell voltage.

The **specific capacity** of an active material is defined by the theoretical amount of charge species, which can be insert/disinsert in the structure and is calculating with the following equation:

$$Q = \frac{n(Li^{+})F}{3600 * M}$$

n is the number of electron involved, F is the faraday constant (96485 C/mol), M is the molar mass (g/mol). For instance, $LiNi_{0.6}Mn_{0.2}Co_{0.2}O_2$ (NMC 622) theoretical capacity is around 275 mA.h/g, while the one of $LiFePO_4$ (LFP) is around 170 mA.h/g.

The total **voltage of a cell** (U) can be determined by the difference between the potentials of the two electrodes, which are determined by the active materials used and the chemical potential of lithium associated with them. This establishes the open-circuit voltage

(OCV) of the battery before use. During cycling, the cell voltage changes due to the thermodynamics of the electrochemical reaction. The Nernst equation provides a way to relate this voltage to the activity of the reactants in the system, particularly for a single reaction.

$$xO_x + ne^- \leftrightarrow y\,Red$$

$$E = E^0 - \frac{RT}{nF}\ln\left(\frac{a_{Red}^y}{a_{Ox}^x}\right)$$

Owing to the high theoretical capacity of lithium (3860 mA.h/g), its low potential (-3.04 V vs. SHE) and its light molar weight (6.94 g/mol), lithium-insertion compounds were early on explored in primary and secondary batteries. The road to material development for Li-ion battery is a rich history dating back to the 1970's. In 1975, chalcogenide TiS_2 was first reported by Whittingham as an interesting lithium intercalation material for Li metal batteries, following the reactions described below[9–11].

$$(at\ cathode)\ TiS_2 + Li^+ + e^- \leftrightarrows LiTiS_2$$

$$(at\ anode)\ Li \leftrightarrows Li^+ + e^-$$

The Li metal/TiS_2 and Li metal/MoS_2 systems were initially considered as promising and commercialization with Moli Energy was launched, but high safety risks were revealed. Such failure originates from the lithium dendrite growth issues, leading to internal short-circuits and fire accidents[12]. To overcome this issue, the "rocking-chair battery" concept was proposed in 1980[13]. This idea supposes the replacement of Li metal by an insertion material at the negative electrode, especially LiC_6 graphite. Graphite is a competitive anode material, due to its high surface area and theoretical capacity of 372 mA.h/g[14]. The cathode is replaced by a lithiated oxide intercalation material. This choice is driven by the need for a new Li source in the battery, as Li anode is removed. Additionally, the increased in cell potential of oxides as compared to chalcogenide, and the higher electronegativity of Oxygen as compared with Sulphur, are beneficial for cell performances. This new technology led to the commercialization in 1991 of a Sony cell, using graphite as anode and $LiCoO_2$ as cathode, an oxide layered compound developed by John Goodenough[12,15,16]. Despite the good reversibility

of the $LiCoO_2$ reactions depicted below, a limited capacity is obtained, and cobalt mining poses serious ethical issues[17].

$$(at\ cathode)\ LiCoO_2 \leftrightarrows xLi^+ + xe^- + Li_{1-x}CoO_2$$

$$(at\ anode)\ C_n + xLi^+ + xe^- \leftrightarrows C_nLi_x$$

Thus, other compounds were discovered, such as the "spinel" $LiMn_2O_4$ and the "polyanionic" $LiFePO_4$[18–20]. Moreover, the layered oxide materials family largely expanded, with the exploration of transition metals that are cheaper and more abundant than cobalt[21]. As such, in 2000's the NMC and NCA family ($Li_xNi_{1-y}Mn_yCo_yO_2$ and $Li_xNi_wCo_yAl_zO_2$) started to be explored[22–24]. In those compounds, the cobalt is partially substituted by other transition metals, favouring greater stability and energy density. For instance, transitioning from $LiNi_{0.33}Mn_{0.33}Co_{0.33}O_2$ (NMC 111) to $LiNi_{0.6}Mn_{0.2}Co_{0.2}O_2$ (NMC 622) enabled a capacity enhancement from 150 mA.h/g to 200 mA.h/g[24]. Today, NMC/NCA active materials are widely commercialized for industrial application.

To even push further the energy density of the batteries, research is heading towards new generations of storage systems, especially All-Solid-State Batteries (ASSB).

1.2.2 Expected benefits of All-Solid-State Batteries

After a decade of oblivion, the discovery of LGPS ($Li_{10}GeP_2S_{12}$), a highly conductive solid-state electrolyte with ionic conductivity comparable to that of liquid electrolytes (10^{-2} S/cm), sparked renewed interest in the development of all-solid-state batteries in 2011[25]. The ideal ASSB cell design includes a negative lithium metal electrode, a solid electrolyte separator, and a positive lithium intercalation electrode, as shown in **Figure 1.2**[26].

These batteries are viewed as the next major generation of energy storage systems for applications such as electric vehicles, offering higher energy density, specific energy, and individual safety. Indeed, ASSB use solid ionic conductors, either oxide, halide or sulphide-based, rather than the organic liquid electrolytes used in conventional Li-ion batteries. As a result, ASSB are expected to be safer, with no risk of flammable electrolyte leakage, and to

have a higher cycling kinetics, as the Li^+ transference number in solid electrolytes is unity, eliminating concentration polarization observed in liquid systems[27,28].

Moreover, great hopes were placed on the possibility to use a lithium metal anode, thanks to greater mechanical strength of SE as compared to liquids. However, in recent years numerous studies have demonstrated that SE cannot prevent dendrite growth[29–31]. Thus, despite the promising performances of ASSB, remaining issues need to be tackled by the industrial and academic community, as explained in next section.

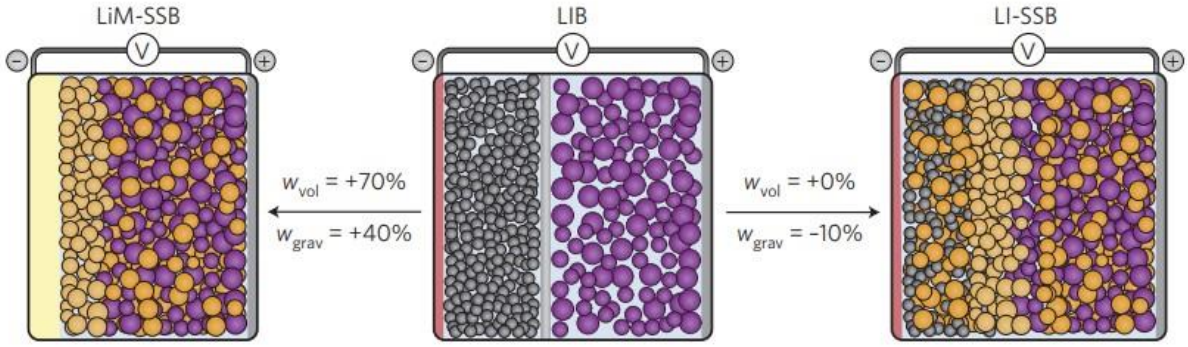

Figure 1.2: Typical battery architectures for the conventional lithium-ion and solid-state batteries. The volumetric and gravimetric energy densities are represented by w_{vol} and w_{grav}, respectively. Reproduced from reference[26].

1.2.3 Context and challenges regarding ASSB development

Despite the promising potential of all-solid-state batteries, their performances remain poor due to various micro to macro level issues. On the road to full cell battery packs, numerous problematics remain.

Firstly, interfacial instability issues at both cathode and anode sides, stemming from the small SE stability window, remain significant obstacles[32]. Poor stability is often reported, as compared with commercial liquid Li-ion cells. Especially, developing a stable lithium metal/solid electrolyte interface would unlock the ASSB performances.

Secondly, the cathode composite pressure needs to be reduced to atmospheric or low pressure to allow for integration of the lithium metal anode and to achieve a competitive volumetric energy. The issue of maintaining intimate contact at low external pressure, while

AM particles undergo internal volume changes upon cycling, requires efficient processing and wise choice of materials[33,34].

Thirdly, a higher loading and higher AM wt. % (> 80 %) need to be reached in the cathode, without compromising the performances[35]. The current literature proposes good performances with very low cathode composite loading (< 5 mg/cm²) and 70% weight percentage of AM. A factor of 10 increase in loading is needed to achieve acceptable volumetric and mass energy density[30,36].

Lastly, decreasing and mastering solid electrolyte layer thickness is crucial for cost and energy density. Indeed, one kilogram of $Li_7La_3Zr_2O_{12}$ (LLZO), LGPS and Li_6PS_5Cl costs respectively \$2000, \$69,500 and \$36,000[35,37,38]. In fact, as reported in **Figure 1.3**, the typically used solid electrolyte layer of 50 µm can bring 75% of dead weight to the battery. Note that a commercial Li-ion battery tend to have a separator thickness between 20 – 25 µm[39]. The high cost of SE materials underscores the importance of thin, defect-free solid electrolyte processing for large-scale applications, which is challenging due to the rigid and brittle nature of most SE[40].

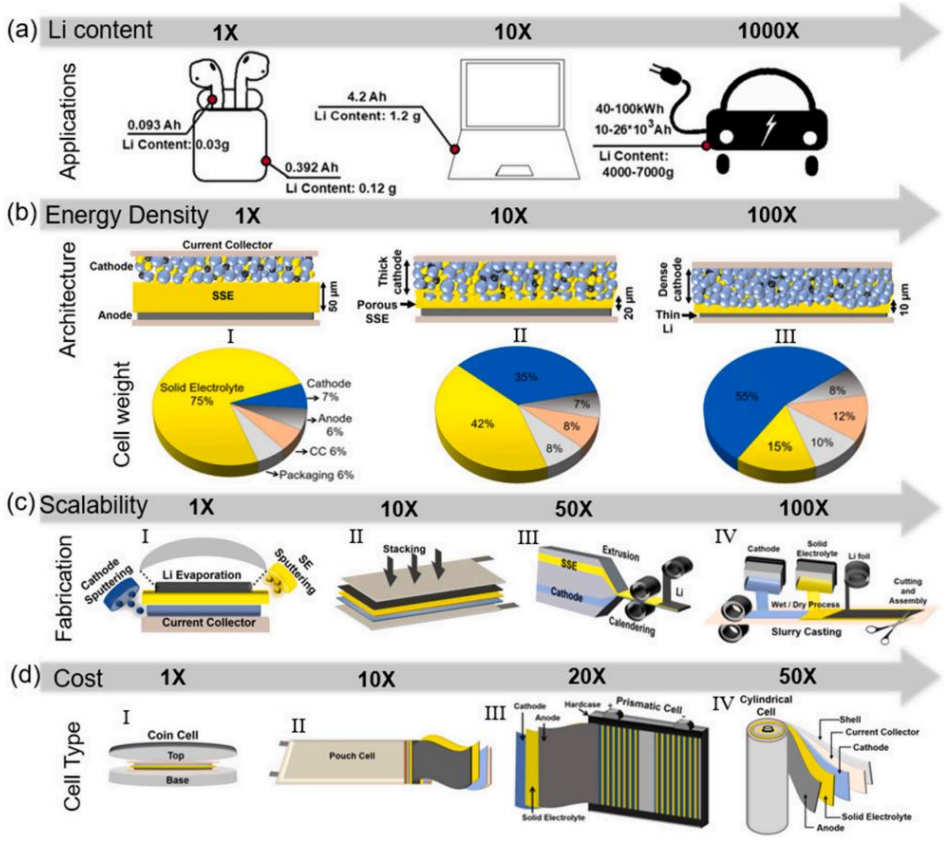

Figure 1.3: Schematic of **(a)** battery-driven applications, namely ear pods, computer and electric vehicle **(b)** battery architecture from low to high energy density, corresponding weights of battery components **(c)** manufacturing processes of ASSB with respect to scalability and **(d)** cell type with respect to production cost. Reproduced from reference[35].

1.3 Bottlenecks regarding cathode composites and current state of the art

One of the main obstacles lies in attaining dense and highly energetic composites, which necessitates efficient formulation and processing techniques. Distinct methods and strategies were employed to reach this objective, what this section is all about.

1.3.1 Processing and formulation of solid-state composites

A solid-state composite is typically composed of a lithium-ion conducting phase (SE), and an active electronically conductive phase (AM and possibly carbon additives). For effective performances, a composite cathode design should minimize voids, maximize the AM/SE exchange surface, and include the minimum amount of SE necessary to ensure sufficient Li diffusion from the bulk SE to the AM/SE interfaces. Theoretically, this can be achieved by using infinitely small interconnected ionic/electronic conductive materials, to create an infinite exchange surface. Obviously, reality deviates from this model as the composites are composed of particles with nm to µm scale sizes (AM: 100 nm to 20 µm, SE: 100 nm to 100 µm), and their architecture being akin to an isotropic system (see **Figure 1.4**). This is translated in the formation of isolated or disconnected regions of lithium-ion/electron conducting phase, which lead to poor ionic/electronic composites conductivity, reduced battery efficiency and forces the use of low composites loading[41,42]. One of the key metrics to assess the quality of a composite is the porosity[33,43]. The level of porosity varies depending on the type of SE and their processing, with oxide SE having the lowest porosity due to high-temperature sintering, typically reaching less than 5 %[44]. However, this manuscript will focus on sulphide-based SE, generally presenting between 20 and 30 % porosity. Altogether, these above limitations need to be addressed. To do so, previous studies have focused on various parameters, including

assembly pressure, the AM/SE ratio, AM and SE particle sizes, and mixing technique efficiency, which will be discussed here.

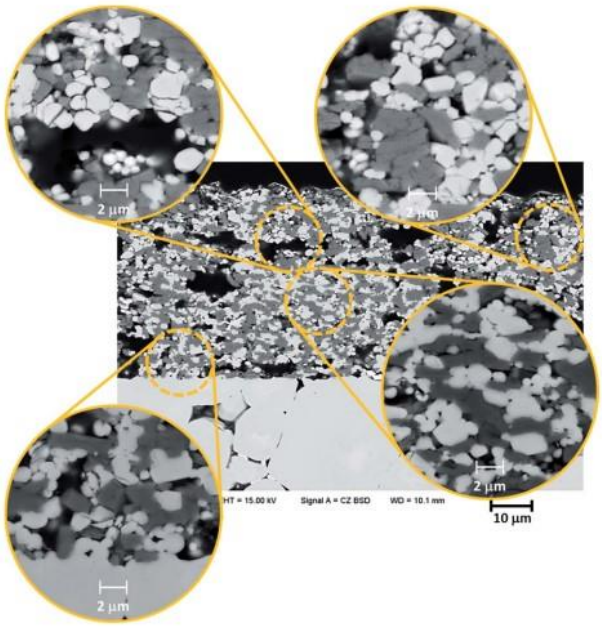

Figure 1.4: SEM (Scanning Electron Microscopy) cross section images of a ASSB that underwent 100 galvanostatic charge–discharge cycles at 50 °C, using Tantalum-doped $Li_7La_3Zr_2O_{12}$ as SE, LCO as AM and indium foil as anode. Reproduced from reference [45].

Of utmost importance are the **mixing technique and protocol** used. Indeed, the production of ASSB composites encompasses multiple processes that offer varying degrees of homogeneity and repeatability. This variability in processes finds analogy in the domains of asphalt and concrete design, wherein numerous protocols where investigated. Their efficiency necessitates the consideration of several factors, including the distribution of voids and the quantity and spatial arrangement of coarse aggregate particles (coarse aggregates are a construction component made of rock quarried from ground deposits)[46–48]. Our research aligns with these concerns and can draw insights from these researches, while distinguishing between dry and wet processes.

Dry processing commonly involves hand grinding of the components, using an agate mortar and a pestle, or ball-milling techniques, with the latter being preferred for higher homogeneity. Both approaches offer the advantages of rapid implementation and ease of

use[49,50]. In this perspective, current research is exploring two paths, using innovative methods such as mechano-fusion, as well as the optimization of various ball-milling parameters[51,52]. Considering ball-milling parameters, it typically include the sequence of material addition, rotation speed, composite mass, number of balls, jar volume, and duration of rotation. Given the complexity of these factors, it is not surprising that ball-milling techniques often lack repeatability.

In order to address these limitations, researchers have turned their attention to **wet processes**, which typically offer improved homogeneity and repeatability. These wet processes involve the use of slurry-based techniques and ball milling with the aid of a solvent, with the latter still submitted to the aforementioned considerations. Slurry based techniques are industrially adaptable for ASSB, and their processing is comprised of conventional Li-ion batteries coating strategies: wet/dry mixing of composites, tape formation, stacking and lamination[53,54]. In this perspective, current research considers the premixing of some components to achieve higher electronic/ionic conductivity, the reactivities of the distinct battery compounds with the solvents and proper ink formulation[55,56]. Thus, transitioning to a slurry-based technique necessitates a revaluation of the composite formulation as compared to dry processes based ASSB composites, where all the difficulty lies.

Turning to **battery assembly pressure**, it is of utmost importance as it can affect the relative density of the composite and the electronic/ionic percolation, by enhancing interparticle contact[57]. This is exemplified by switching formation pressure from 55 MPa to 370 MPa, the relative density of Li_6PS_5Cl pellets increases from 68 to 77 %, as shown in **Figure 1.5**[58]. It results in a threefold increase in ionic conductivity, as seen in **Figure 1.6**, when going to 370 MPa.

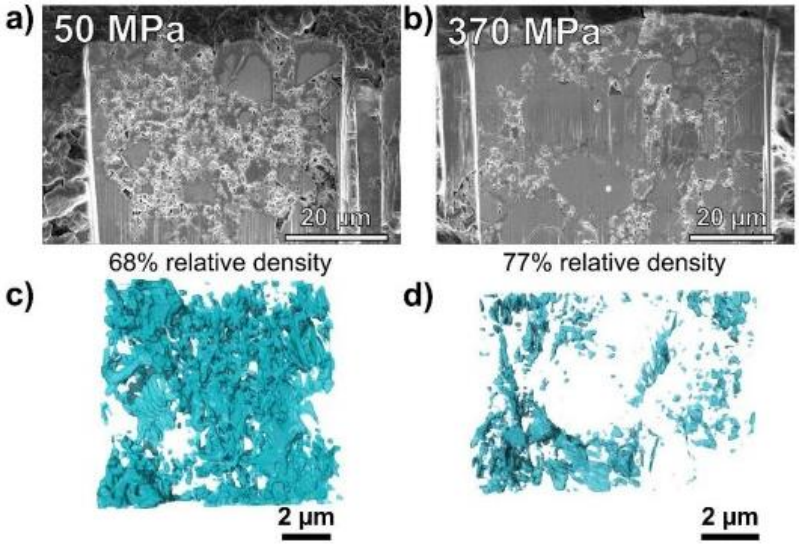

Figure 1.5: SEM images of FIB (Focused Ion Beam) cross-sections of Li_6PS_5Cl electrolyte pellets made with a fabrication pressure of **(a)** 50 MPa and **(b)** 370 MPa, with their corresponding relative density estimated by physical measurements. The resulting FIB reconstructions show the porosity in blue for the **(c)** 50 MPa pellet and **(d)** 370 MPa pellet. Reproduced from reference[58].

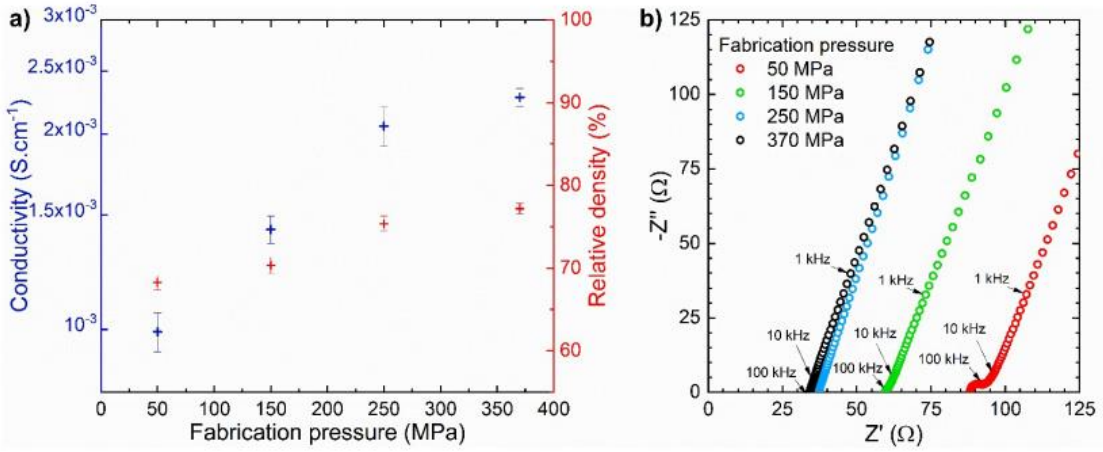

Figure 1.6: **(a)** Conductivity and relative density of Li_6PS_5Cl electrolyte as a function of the fabrication pressure, and **(b)** Nyquist diagrams of the electrochemical impedance spectra at the same fabrication pressures. All measurements were performed with a stack pressure of 25 MPa. Error bars represent the standard deviation on four samples. Reproduced from reference[58].

Additionnaly to these processing aspects, **composites formulation** is critical as it significantly impact battery performances[41,43,59,60]. In composites typically comprising active

material, solid electrolyte and a carbon additive, an ideal particle size ratio is typically achieved when the SE size is 2-3 times smaller than the AM particle size, as illustrated in **Figure 1.7**[59]. Alongside the particle size optimization, the AM/SE mass ratio should also be optimized, as highlighted through experimental and computational studies, with a high fraction of AM desired (> 80 wt. %) to reach high energy density[59,61,62]. However, it is important to acknowledge certain limitations, such as the adverse effects of solid-state diffusion, particularly when the particle size of the AM exceeds a certain threshold, as illustrated in **Figure 1.8**.

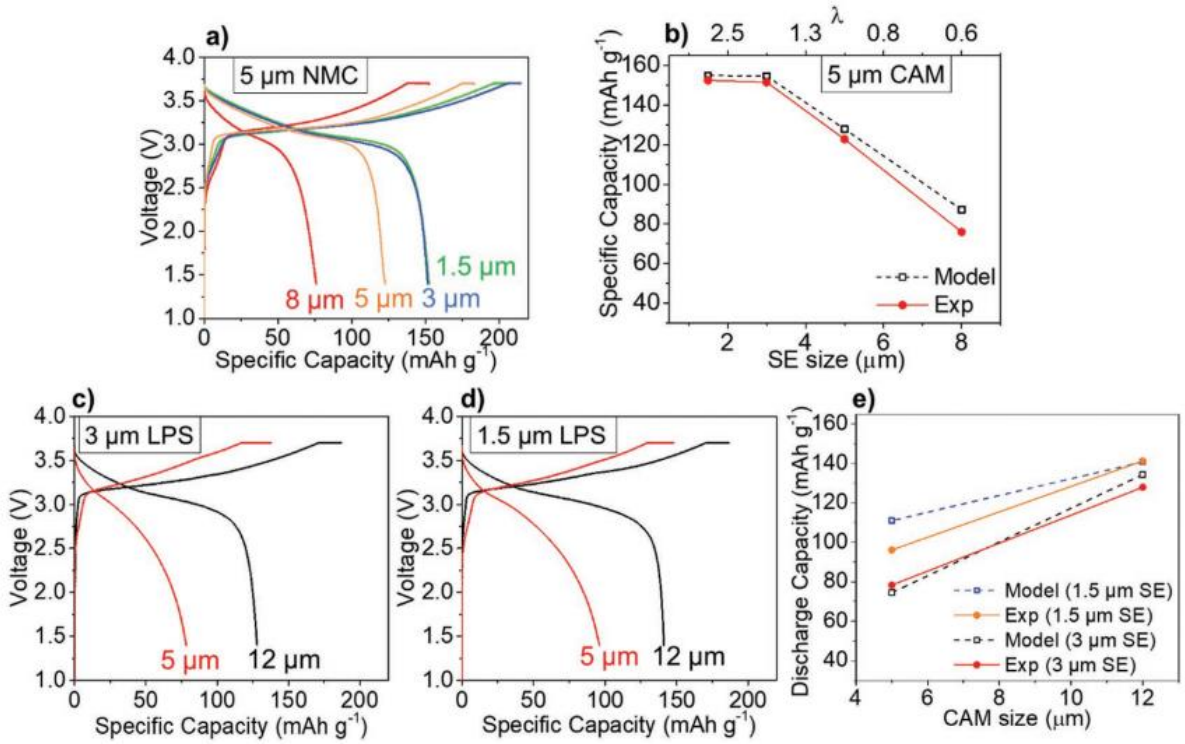

Figure 1.7: **(a)** First-cycle using different-sized LPS particles with fixed NMC size (5 µm) and 60 wt. % NMC. **(b)** Comparison of experimental capacities with model-predicted capacities. **(c),(d)** First-cycle voltage curves using different-sized NMC particles (5 and 12 µm) with fixed LPS size (3 µm for (c) and 1.5 µm for (d)) and 80 wt. % NMC. **(e)** Comparison of experimental capacities in (c) and (d) with model-predicted capacities. Reproduced from reference[59].

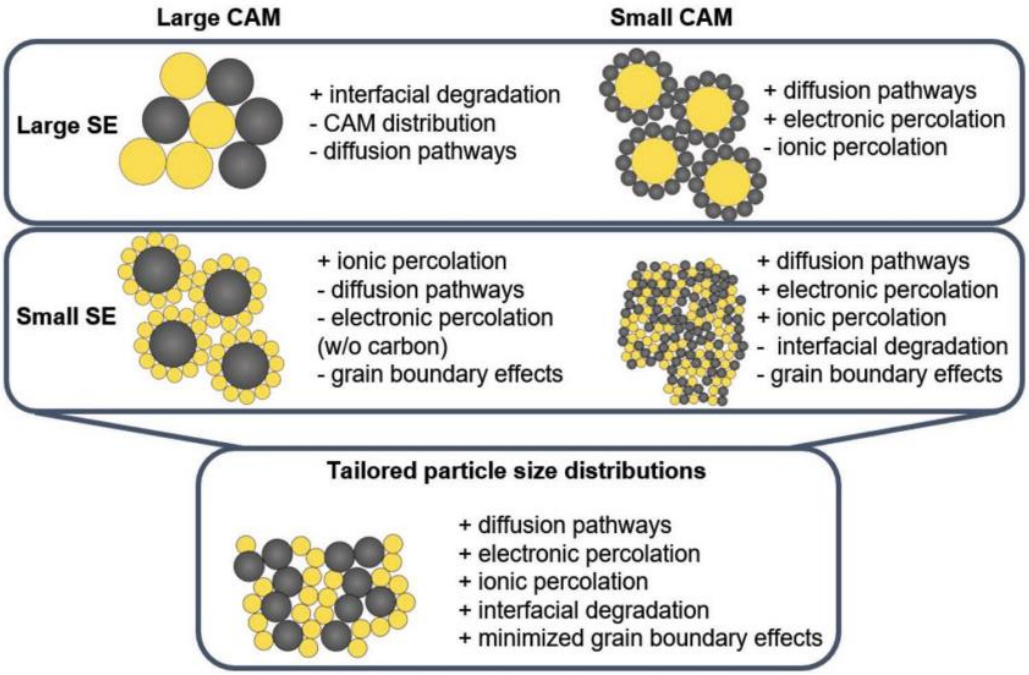

Figure 1.8: Influence of cathode active material and SE particle size on the different aspects of requirements for ASSB cathodes. Reproduced from reference[43].

Overall, to optimize the performance of ASSB composites, it is necessary to conduct a comprehensive experimental plan, which is time-consuming and limited to a single combination of AM and SE materials and particle size distributions. Thus, computational holistic studies are valuable for addressing these challenges. Despite the difficulty, combining experimental and theoretical studies can provide a solid foundation for understanding the effects of various design factors such as material quantity, particle size, pressure, and mixing process on the performance of ASSB composites. Thus, by carefully selecting the optimal values for each of these factors, it is possible to access the full potential of composites. It is noteworthy to emphasize that the mixing process efficiency holds significant importance although the literature on this subject is limited, particularly in terms of comparative analyses and repeatability assessments, with such investigations predominantly confined to industrial secret research.

Additionally to this complex spectrum of parameters, one should also add the different chemical/electrochemical degradation processes, occurring at all composites interfaces

during cycling. It will depend on the carbon and AM exchange surfaces, the nature of the compounds, and the cycling parameters. Such phenomena need to be taken into account in the optimization process, as we will see in the following sections.

1.3.2 Interfacial chemical/electrochemical reactivities in ASSB composites

Various parameters such as the chemical and electrochemical nature of the reaction, the conductive properties of the new phases formed, the potential, growth rate, and the location of the reaction can influence battery performances. Three types of degradation should be considered for ASSB composites, namely environmental reactivity, intrinsic electrochemical decomposition of the solid electrolyte, and reactivity towards the active materials. The type of SE used determines the distinct interfacial degradations observed, and different scenarios occur among the three main ionic conductor families (oxide, sulphide, and halide).

Environmental reactivity is a major concern for large-scale battery fabrication. Comparing the three SE types, oxide-based SE demonstrate the highest environmental stability[63]. Both halide and sulphide SE are reacting with humidity, with halide presenting a lower health hazard risk, as compared to sulphides that are well-known for releasing H_2S and lithium hydroxide (LiOH) when exposed to air and humid environment[64,65]. Despite this well-known process, two other degradation pathways have been identified, namely the intrinsic stability of the SE and the reactivity with layered oxide AM.

In relation to the **intrinsic stability** of a solid electrolyte, it corresponds to the range of potential values in which the SE remains stable. This stability is evaluated using both experimental techniques, especially cyclic voltammetry (CV), and computational methods such as Density Functional Theory (DFT)[66,67]. These two approaches rely on distinct foundations. Specifically, the DFT computational method employs thermodynamic considerations to determine the stability window, but it often conflicts with experimental data due to the significant influence of kinetics on battery performance. On the contrary, cyclic voltammetry provides a practical assessment of the stability window and combines thermodynamic and kinetic considerations. This technique utilizes various parameters, including sweep voltage and electronic exchange surface, which must be carefully selected to reveal the stability window. Considering these statements, CV is typically favoured for

comparing the stability window of different SE. Thus, **Figure 1.9** illustrates the stability window through CV experiments, for representative halide, argyrodite, and oxide SE. Oxide SE like $Li_7La_3Zr_2O_{12}$ (LLZO) present a large stability window and are consequently ideal for lithium metal integration, as illustrated in **Figure 1.9.a**[68]. Turning to Halide, their composites often demonstrate favourable cycling stability, but a common halide such as Li_3InCl_6 typically experience decomposition starting from ~ 3.3 V vs. Li-In/In (where 0 V versus Li-In/In is equivalent to 0.62 V versus Li^+/Li), as seen in **Figure 1.9.c**[69]. This intriguing observation arises from two considerations. Firstly, Li_3InCl_6 can not only oxidize, but can also be reduced. Secondly, the resulting decomposition products are likely to be less resistive and/or passivating faster than those observed for sulphide-based SE. This high cycling stability of Li_3InCl_6-based composites contrasts with the well-known stability issues associated with sulphide-based composites. For instance, sulphides such as Li_3PS_4, Li_6PS_5Cl (**Figure 1.9.b**), or $Li_{10}GeP_2S_{12}$ are known to undergo electrochemical oxidation starting from approximately 2.7 V versus Li-In/In[60,70–74]. It leads to the formation of highly insulative products (such as LiCl and P_2S_5), and especially elementary sulphur[68,74]. The reaction mechanism proposed for Li_6PS_5Cl oxidation is the following[74]:

$$Li_6PS_5Cl \Rightarrow LiCl + \frac{1}{2}P_2S_5 + \frac{5}{2}S + 5Li^+ + 5e^-$$

This reactivity is characterized by the additional slope observed in first charge of Li_6PS_5Cl-based batteries (see **Figure 1.10**) and a fast capacity fading[72,74,75]. The degree of such reactivity is primarily reliant on the specific surface area of the electronically conductive additive, such as Vapour Grown Carbon Fibre (VGCF) or carbon nanotubes[74,76]. Note that this decomposition is seen in Lithium-Sulfur ASSB, resulting in capacities above theoretical[77,78].

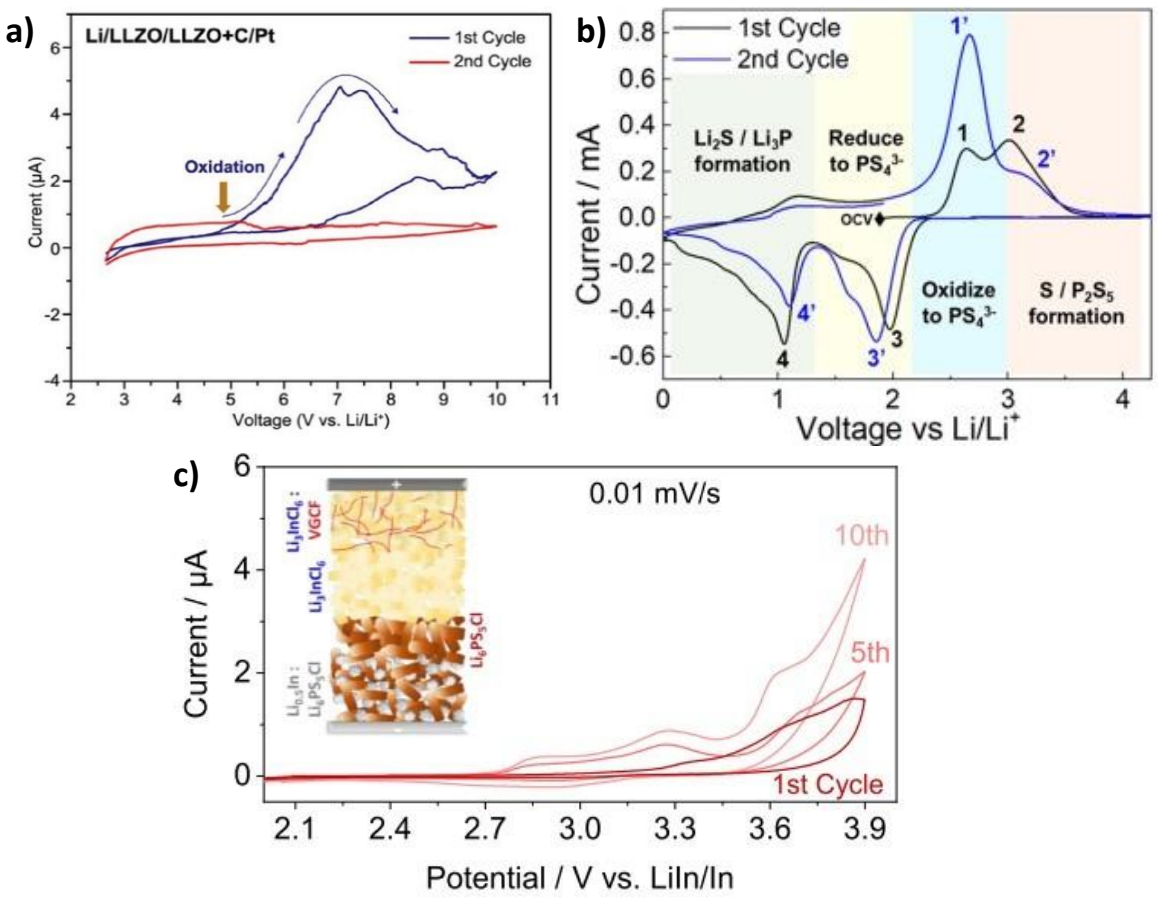

Figure 1.9: **(a)** Cyclic voltammetry of Li/LLZO/LLZO+Carbon/Pt cell within the voltage range of 2.6–10.0 V. Adapted from reference[68]. **(b)** Cyclic voltammograms of Li_6PS_5Cl-Carbon composites for the first two cycles; between 0 and 4.2 V (vs Li/Li^+) at 100 μV s^{-1}. Adapted from reference[74]. **(c)** Cyclic voltammetry measurement at 0.01 mV/s upon 10 cycles between 2 and 3.9 V vs Li-In/In. Li_3InCl_6 + VGCF is used as cathode. Adapted from reference[69].

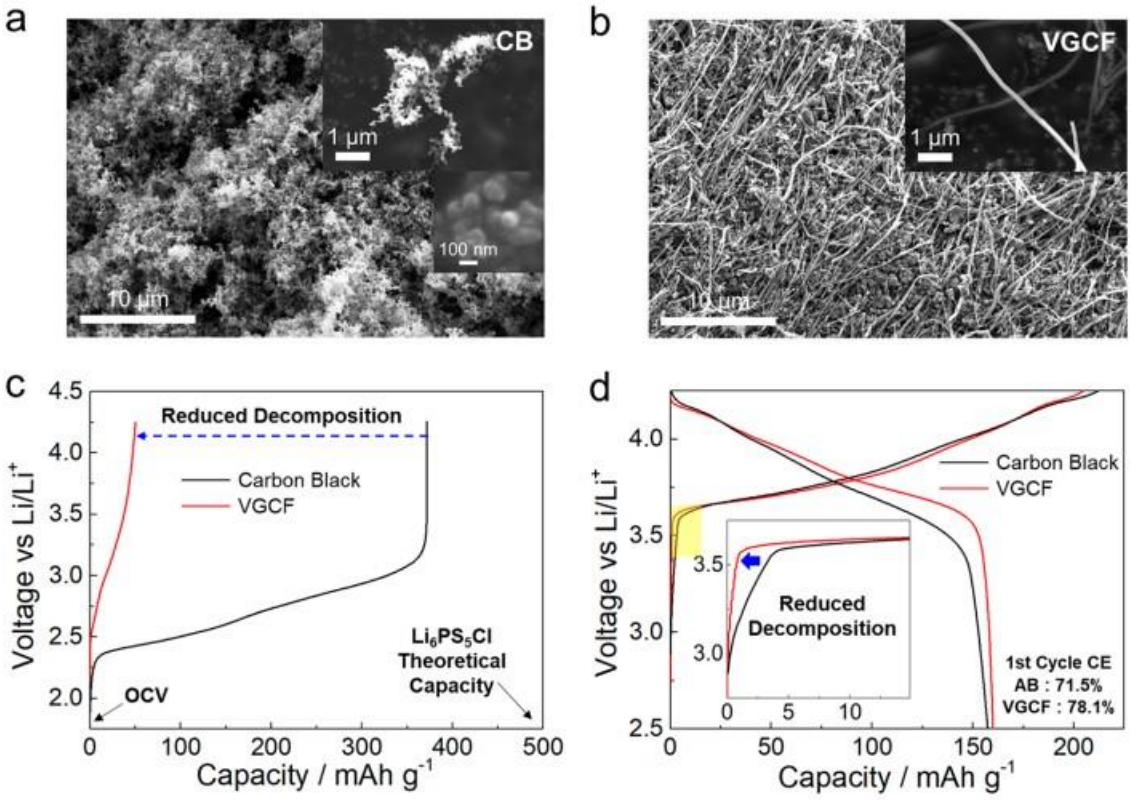

Figure 1.10: SEM images of **(a)** Carbon Black (CB) and **(b)** VGCF. **(c)** Charge voltage profiles of Li–In | Li_6PS_5Cl | Li_6PS_5Cl–C cells using 30 wt. % CB (surface area: ~80 m^2/g) vs VGCF (surface area: ~24 m^2/g)). **(d)** Charge and discharge voltage profiles of Li–In | Li_6PS_5Cl | NCM 811 cells using 1 wt. % of CB vs VGCF. Reproduced from reference[74].

Lastly, **stability of SE versus layered-oxide type AM** is challenging, as it will depend on the AM utilization, the Ni-content of the AM, the amount of structural defects and surface species, among others. While oxide-type SE were previously considered stable in comparison to cathode active materials, recent studies have shown that they induce rapid capacity fading when cycled with NMC 811 or $LiCoO_2$ (LCO)[45,79,80]. This is evidenced by the poor electrochemical stability of Tantalum-doped LLZO (LLZO:Ta)/AM attributed to species interdiffusion and/or electrochemical/chemical reactivity. Similar considerations apply to halide-based composites, previously overlooked as highly stable. Although research on this topic is limited, the behaviour of halide systems appears to be dependent on the metal involved, with different degradation pathways being reported. For instance, $Li_{5/2}Y_{1/2}Zr_{1/2}Cl_6$ high potential cycling led to the formation of YOCl and likely ZrO_2 due to oxygen redox

reactions occurring with NCM85[81]. Conversely, $Li_2Sc_{1/3}In_{1/3}Cl_4$ and Li_3InCl_6 exhibited excellent stability during long-term cycling of ASSB with NCM85, particularly at high voltages (up to 4.8 V)[69,81,82]. Greater consensus is observed for sulphide-based composites, all of which react with layered oxide AM at high potentials, resulting in the formation of a growing layer of phosphate (POx) and sulphate (SOx) species. This appearance has been demonstrated through X-ray Photoelectron Spectroscopy (XPS) and Time-of-Flight Secondary Ion Mass Spectroscopy (ToF-SIMS) experiments, as illustrated in **Figure 1.11**[70,83]. It is commonly attributed to a chemical reaction with oxygen species, which can originate from two sources. Firstly, it may arise from surface species like oxygen, water or carbonates, inevitably coexisting with NMC materials during storage or synthesis. Secondly, the O_2 release at high potential (> 4.2 V vs. Li^+/Li) from the transition metal layered oxide materials may act as oxygen source[84]. This latter possibility is well-known in liquid systems, where the release of O_2 and the structural densification of the AM lead to a disastrous reactivity with the organic electrolyte[85–87]. As key metrics to characterize such phenomenon in ASSB, dioxygen release is monitored during cycling with solid-state OEMS/DEMS (Online/Differential Electrochemical Mass Spectroscopy), with its release approximately starting at 3.6 V vs. Li-In/In until the end of charge[88,89]. Interestingly, the gas release causes a porous interface around the AM particles, as exemplified in **Figure 1.12**. Consequently, this porous interface is likely to affect the AM/SE interfacial contacts, thereby necessitating further research in this area.

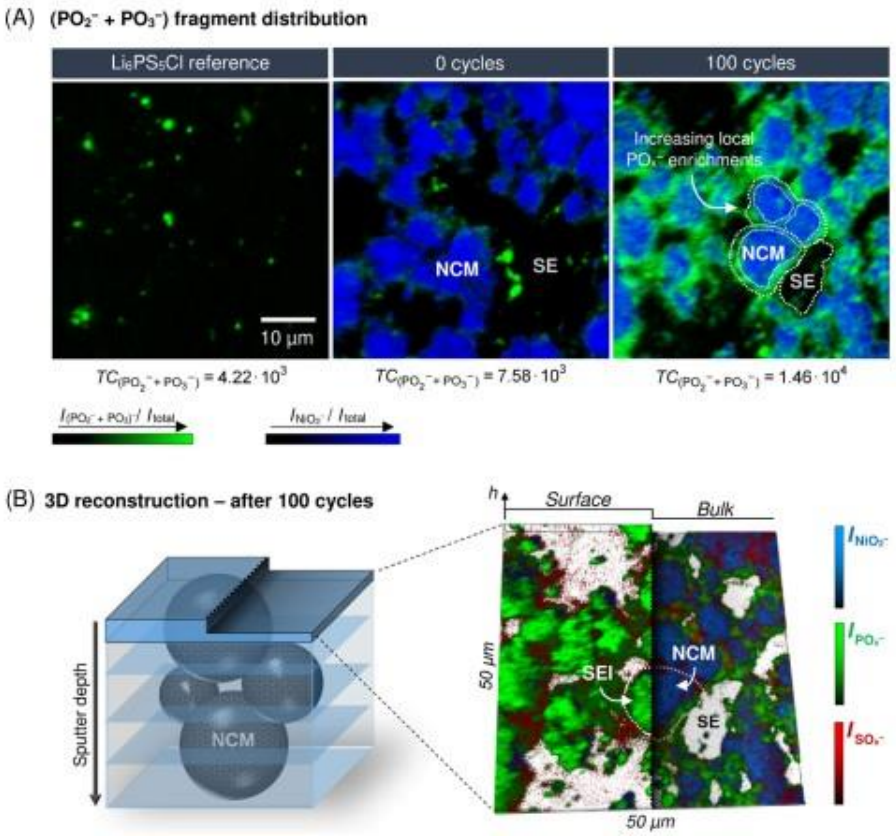

Figure 1.11: **(a)** Local fragment distribution of NiO_2^- (blue) and PO_x^- (green) fragments for the reference SE and the uncycled and cycled composite cathode. The sum of the first four scans of the depth profile is shown. The solid electrolyte shows local PO_x^- fragment enrichments, which can also be identified in the composite cathodes (middle picture, most intensive signals). Signals from PO_x^- fragments at the NMC622/SE interface significantly increase after the battery cycling (total counts (TC) of PO_x^- fragments become double). **(b)** Three-dimensional reconstruction of the depth profile of the cycled composite cathode. Shown are local fragment distributions of NiO_2^- (blue), PO_x^- (green), and SO_x^- (red) on the surface and in the bulk. This shows that a SEI (Solid Electrolyte Interphase) layer is formed directly at the NMC622/SE interface due to battery cycling. Reproduced from reference[90].

Within the **recent advancements** and **unresolved inquiries** in the field, a captivating topic pertains to the greater high potential stability of composites based on nickel-rich NMC materials, as compared to liquid-based Li-ion batteries. The influence of structural densification on this stability remains unclear, raising questions regarding the possibility of an electrochemically active rock salt layer[93]. Furthermore, a novel form of interfacial degradation has recently been identified in Li_6PS_5Cl-based composites, involving the interdiffusion of transition metals. Cryogenic transmission electron microscopy (cryo-TEM) was employed to

visualize this phenomenon for the first time in 2023[91]. Consequently, additional research is needed to fully comprehend the consequences of such phenomena on the durability of ASSB.

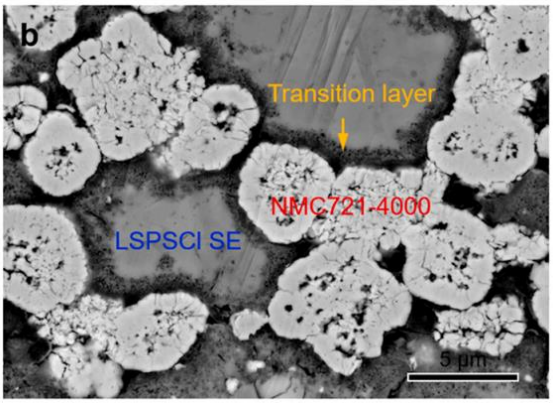

Figure 1.12: SEM characterization of the Li_6PS_5Cl/NMC721 interfaces after 4000 cycles. A low magnification SEM image of the Li_6PS_5Cl /NMC721 interface[92].

Overall, this section has compiled information on various types of instabilities that manifest in different types of solid electrolytes, either of chemical or electrochemical origin. The discussion has then been narrowed down to the specific issues encountered in composites alike Li_6PS_5Cl-based ones. Li_6PS_5Cl presents a narrow stability window and a high reactivity with NMC-like cathode materials at high potentials. Despite these reactivities, sulphide-based SE offer attractive benefits such as high ionic conductivity, ductility, abundancy and ease of fabrication[93]. Hence, they hold potential as ideal materials for high-energy dense cathode composites if their reactivities can be effectively managed. In order to address these complex challenges while preserving the favourable properties of sulphides, protective coatings are commonly used to safeguard the interfaces between the solid electrolyte and anode materials. The subsequent section will delve further on this topic.

1.3.3 On the impact of coating on interfacial issues

Coatings have long be used in Li-ion batteries for mitigating surficial reactions occurring at the AM-electrolyte interface and are equally needed in solid state batteries to minimize local reactivity between oxide-base AM and S-based electrolyte, hence the colossal amount

of ongoing studies. It also serve multiple purposes beyond mitigating reactivity, such as minimizing mechanical degradation, decreasing space charge layer effects, enhancing interparticle contacts, and limiting interdiffusion of species. As coatings are reportedly effective in mitigating almost all of the detrimental effects associated with ASSB composites, optimizing their design is of utmost importance.

Typical coatings usually composed of ternary or binary oxides, should exhibit stability within the operating potential window and act as a lithium-ion conducting barrier and be made of an electronic insulating material. Moreover, coatings must be conformal and thin to enable electron tunnelling and ensure electronic percolation despite their electronically insulating nature. Indeed, full coverage of the particle would hinder AM-AM electronic contact and inhibit the composite's functionality, as depicted in the **Figure 1.13**.

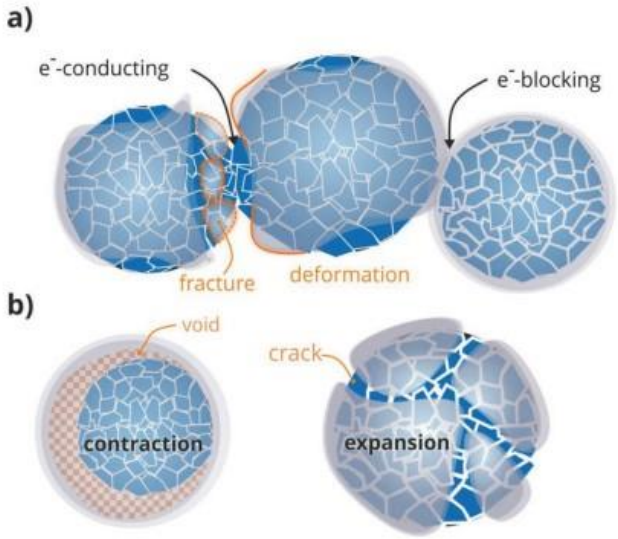

Figure 1.13: Schematic illustrating **(a)** the possible scenarios for achieving electrical contact between coated CAM particles during processing, as well as **(b)** influence of volumetric changes of the electrode materials on the coating. Reproduced from reference[94].

Capacity wise, numerous studies have demonstrated that applying a coating to ASSB can lower interfacial resistances prior to cycling, leading to reduced polarization and increased capacity[88,95]. This effect may arise from three potential mechanisms. First, adding a coating creates two new interfaces, the AM/coating and SE/coating interfaces, instead of the previous

AM/SE interface. The sum of these two interfaces can lead to a lower interfacial resistance. Especially, better contact can be achieved. On this, the impact of coating deposition technique is crucial (Atomic Layer Deposition, Wet chemical approaches, Spray coating, Chemical Vapour Deposition) as it can influence the wettability and uniformity of the coating. The second possibility is the reduction of space-charge layer effects. Specifically, the lithium chemical potentials of AM and SE are believed to provoke the formation of an interfacial barrier, which is a lithium deficient layer[96,97]. However, although computational studies have investigated this effect, experimental proof of detrimental space-charge layers is still lacking. Finally, it should be noted that surface species that are present on the surface of the AM particles because of storage and synthesis processes, can chemically react with the sulphide-based SE. Coating the AM particles can prevent this chemical reaction from occurring, provided that there are no surface species or less reactive ones present at the coating surface.

Stability-wise, coatings have been shown to diminish capacity fading through multiple possible mechanisms. Firstly, they effectively reduce the reactivity between high potential active material and solid electrolyte, as evidenced by various studies which show a decrease in the release of O_2 gas in coated active material[89,95,98,99]. This suggests that coatings may confine or obstruct the release of O_2 gas. Furthermore, coatings can hinder interdiffusion, as exemplified by reduced diffusion of Co in a Li_2SiO_3-coated LCO/Li_2S-P_2S_5 composite, as shown in **Figure 1.14**[100]. Finally, coatings are hypothesized to limit and accommodate pressure changes by serving as an elastic layer surrounding active material particles, thereby enhancing mechanical cohesion[94,101]. Although research on this topic is still in its early stages, recent studies demonstrated this highly interesting impact of coating. To do so, polylithic layered oxide AM are preferentially used, as they are known for mechanically degrading rapidly due to their anisotropy which favours particle fracturing during chemo-mechanical effect of Li insertion/disintertion[102–104]. This is exemplified by the effect of infiltrating $LiAlO_2$ inside polylithic $Li_{1.2}Mn_{0.26}Ni_{0.26}O_2$ which led to improved stability (see **Figure 1.15**).Through nano-indentation, HAADF-STEM (High-Angle Annular Dark-Field Scanning Electron Transmission Microscopy) and theoretical consideration, this coating is clearly proved to act as a mechanical binder[98].

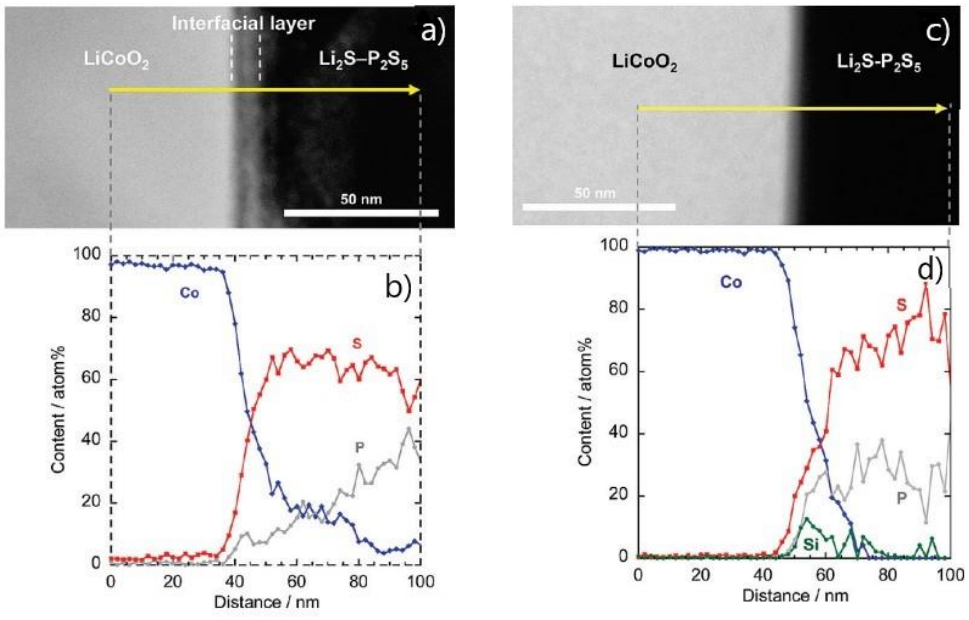

Figure 1.14: **(a)** Cross-sectional HAADF-STEM image of $LiCoO_2$ electrode/Li_2S-P_2S_5 solid electrolyte interface after initial charging and **(b)** cross-sectional EDX line profiles for Co, P, and S elements. The arrow in a presents the positions at which EDX measurements were taken **(c)** Similar procedure with Li_2SiO_3-coated $LiCoO_2$/Li_2S-P_2S_5 interface after initial charging and **(d)** cross-sectional EDX line profiles for Co, P, S, and Si elements. Adapted from reference[100].

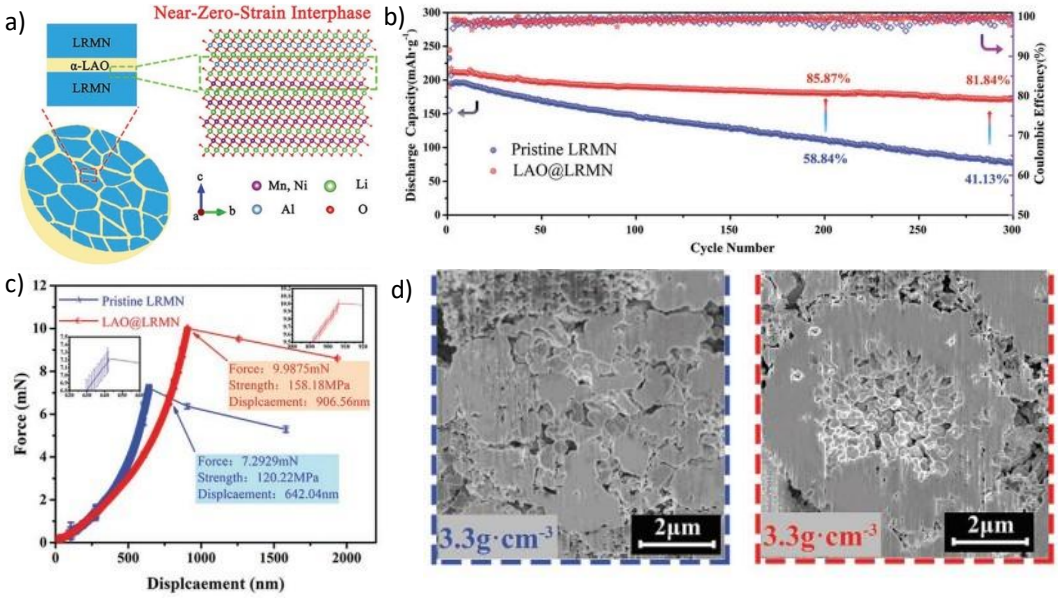

Figure 1.15: **(a)** Schematic diagram showing the reactive infiltration of $LiAlO_2$ (LAO) in the grain boundaries of LRMN ($Li_{1.2}Mn_{0.54}Ni_{0.26}O_2$) secondary particles to form a stable and interlocked coherent interface **(b)** cycling performance of the samples at 1 C **(c)** Experimental crushing test results for Pristine LRMN and LAO@LRMN

particles (Loading speed: 20 mN min^{-1}, the standard deviations of the applied crushing forces are less than 5%) **(d)** Cross-sectional SEM micrographs of Pristine-LRMN (blue dots) and LAO@LRMN (red dots) with calendering density of 3.3 g cm^{-3}. Adapted from reference[98].

Among the recent studies, the **SE coating** is starting to be investigated. This is evidenced through the introduction of a new coating methodology in the year 2023, capitalizing on the reactivity of lithium surface species with CO_2 gas, creating a Li_2CO_3 layer around SE particles[105]. This approach improved the atmospheric stability of Li_6PS_5Cl and exhibited favourable stability performance of composites, as demonstrated in the accompanying **Figure 1.16**. Likewise, Al_2O_3 deposited on Li_6PS_5Cl by atomic layer deposition (ALD) technique showed comparable results. Specifically, ALD alumina coating was found to improve the stability of argyrodite under both humid and oxidizing conditions, and effectively stabilized the SE against reactivity with Li metal[106].

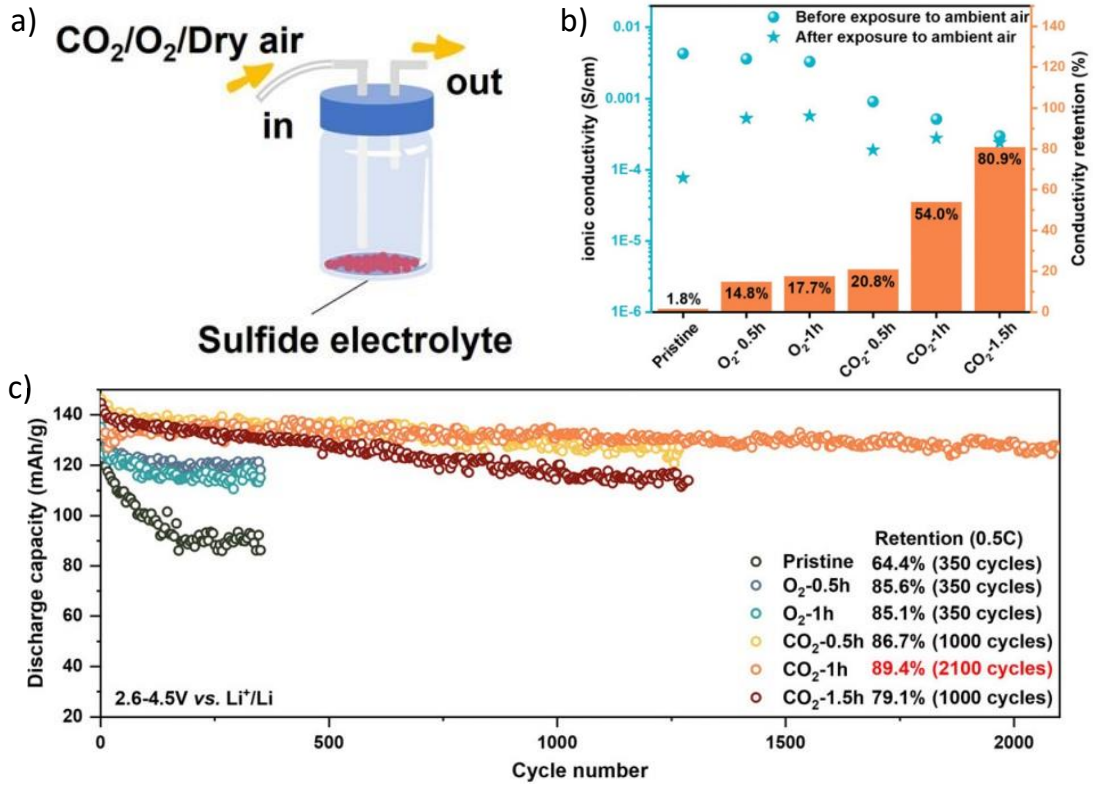

Figure 1.16: **(a)** Schematic illustration of the solid–gas reaction. **(b)** The ionic conductivity of gas-treated Li_6PS_5Cl samples before and after exposure to ambient air with a relative humidity of 17% for 1 hour and its conductivity retention. **(c)** Long-term cycling performance at 0.5C. Adapted from reference[105].

Overall, significant progress has been achieved through the incorporation of coatings; however, several aspects warrant careful consideration. Firstly, the lack of consistency in coating methodologies and performances across different studies, even when utilizing coatings of the same nature. This discrepancy can be attributed to challenges associated with achieving precise uniformity and thickness of the coatings, as their synthesis involves numerous parameters regardless of the methodology employed. Furthermore, it should be noted that the quality of the active material's surface prior to coating plays a crucial role in the coating quality, despite being insufficiently explored in the literature. Secondly, there remains uncertainty regarding the differentiation between incidental doping and coating effects, as the high-temperature processing steps commonly involved in coating techniques can inadvertently introduce dopants to the surface of the active material. Especially, the introduction of dopants into the active material has demonstrated effectiveness in mitigating the occurrence of high potential O_2 gas release and modifying the chemo-mechanical properties of the material, particularly in studies conducted in liquid environments[107–110]. Thus, further studies are needed to fully comprehend the impact of coating and/or doping.

1.3.4 Current state of the art performances

In the latest years, remarkable performances were released from articles using innovative methodologies of cell design, new ionic conductor materials, the implementation of high energy anodes (lithium metal or silicon) and efficiently structured cathode composites.

One of the first disruptive solid-state papers was presented by Lee et al. in 2020, proposing an advanced design for both cathode and anode part. The optimized cathode composite contains small Li_6PS_5Cl particles (< 1 µm), a Li_2O-ZrO_2 coated NMC and VGCF carbon additive[31]. The important breakthrough arise from the usage of an “anode less” system, were no excess lithium is used. The implementation of an Ag-C anode enables to override the persistent issue of lithium dendrite formation. This anode proved itself to enable homogeneous and efficient lithium lithiation/delithiation through silver particles alloying. This design enabled the formation of a prototype pouch cell (0.6 A.h) and long cycle life (> 1000 cycles). Noteworthy, it is the first time such performances were obtained at low pressure (20 bar). However, 60°C operating temperature is used to increase capacity and prevent dendrite

formation. Nonetheless, this study is one of the first to demonstrate a long-term stability and high energetic battery design, paving the way for new high performances studies (see **Figure 1.17**).

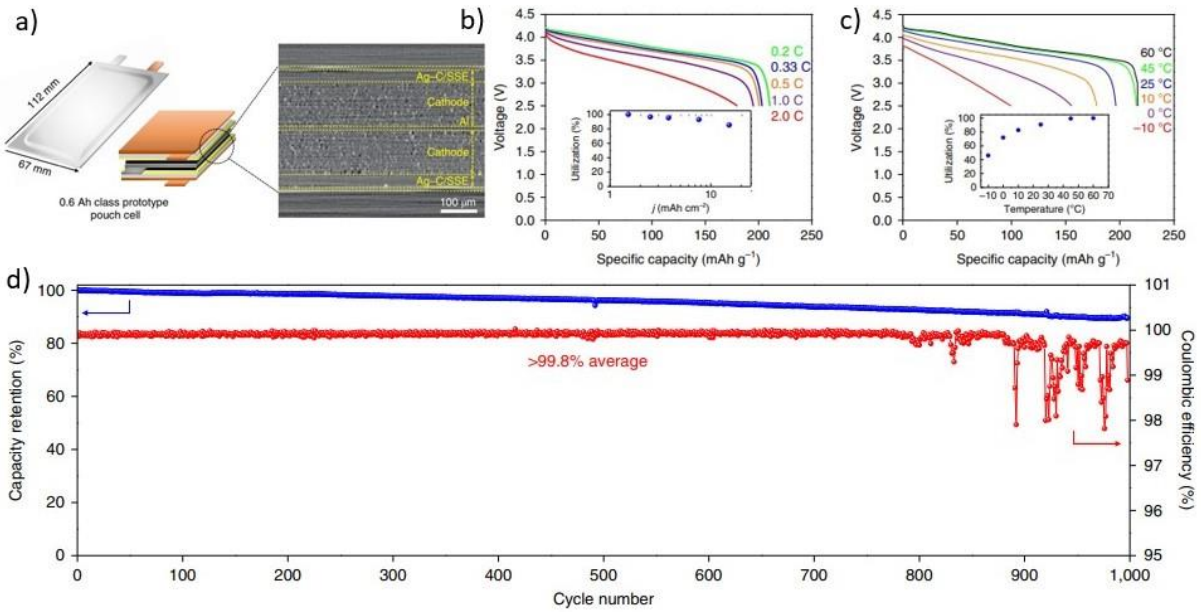

Figure 1.17: **(a)** Characterization of a 0.6 Ah class prototype pouch cell and illustration of a bi-cell structure **(b,c)** Discharge capacities were monitored under 0.1 C/0.1 C charge/discharge conditions as the discharging temperature was varied from 60 to −10 °C. The charging temperature was fixed at 60 °C. **(d)** Cycling performance and Coulombic efficiency of the Ag–C|SSE|NMC prototype pouch cell (0.6 Ah) are plotted against the cycle numbers. A constant current mode with the charge/discharge rate of 0.5 C/0.5 C was applied (voltage window, 2.5–4.25 V versus Li^+/Li at 60 °C). The areal capacity loading of the NMC cathode was 6.8 mAh cm^{-2} (1.0 C = 6.8 mA cm^{-2}). Reproduced from reference[31].

In 2021, another breakthrough is reached on the anode side by Tan et al., with the successful implementation of the highly energetic silicone material (> 3500 mA.h/g), so far prevented by its volumetric change upon cycling (> 300 % expansion during lithiation)[111]. Such strategy also overcomes the hurdle of lithium metal integration. By using high pressure (1 t/cm²) during a formation cycle and a small loading of silicon (1.67 mg/cm²), 80% capacity retention after 500 cycles at 1C is reached. Noteworthy is the high silicon content of the anode (99.9 %) compared to traditional silicon anode. However, no low C-rate performances are shown, possibly hiding a long-term instability, well known for Li_6PS_5Cl SE using carbon additive.

Nonetheless, it is the first time silicon anode is successfully integrated in ASSB, opening the path for future optimization (see **Figure 1.18**).

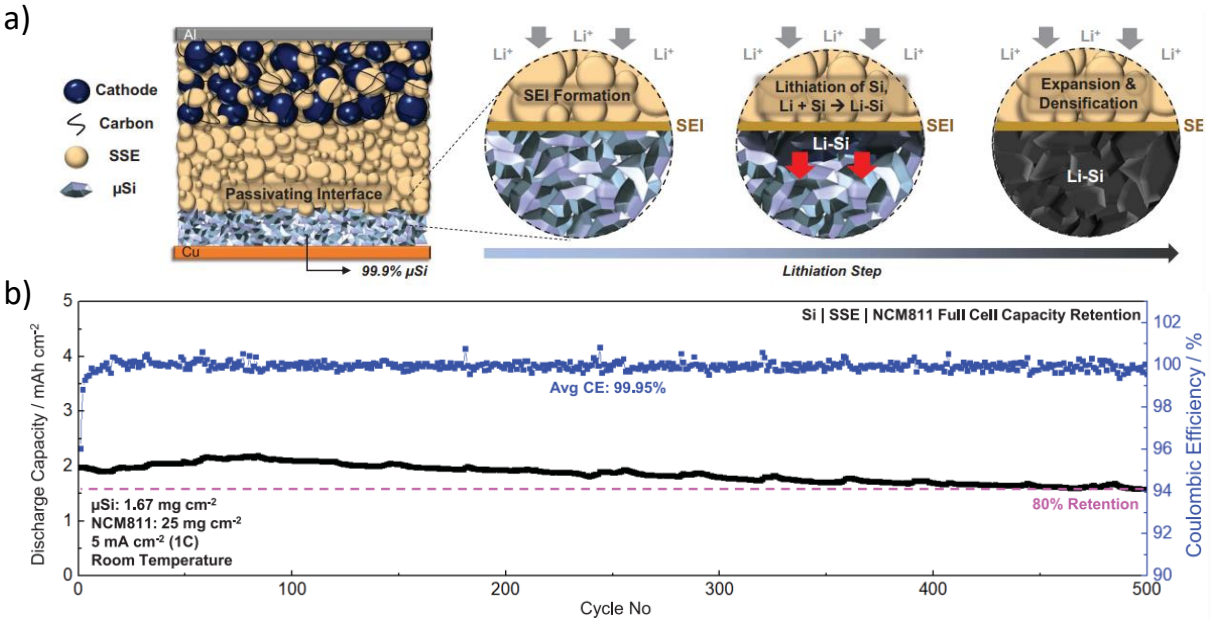

Figure 1.18: **(a)** Schematic of 99.9 wt. % micro Si electrode in an ASSB full cell. During lithiation, a passivating SEI is formed between the micro Si and the SE, followed by lithiation of micro Si particles near the interface. The highly reactive Li-Si then reacts with Si particles within its vicinity. The reaction propagates throughout the electrode, forming a densified Li-Si layer. **(b)** Cycle life at room temperature. All cells were tested under similar charge and discharge conditions between 2.0 and 4.3 V. The first cycle voltage profile of each respective cell is plotted in black. Reproduced from reference[111].

Focusing on the cathode composite side, remarkable performances were initiated by Kim et al. in 2023, using Ni-rich single crystal NMC 811 and a halide solid electrolyte (Li_3YCl_6, LYC), enabling 170 mA.h/g at C/5 and an 80 % capacity retention after 1000 cycles at C/2[112]. Such performances rely on a stable halide solid electrolyte, presenting high ionic conductivity, coupled with a high capacity active material. The relatively small SC-NMC811 particle size (2 µm), successfully match with 2 µm LYC particles, created a high electronic and ionic percolation made possible by tailored particle sizes. Noteworthy, no coating is used for the active material, pointing out at the oxidative stability of LYC and at the importance of solid

electrolyte nature on the composite optimization and design (see **Figure 1.19**). However, the usage of Yttrium in this SE raises the question of industrial cost and resources available for commercialization.

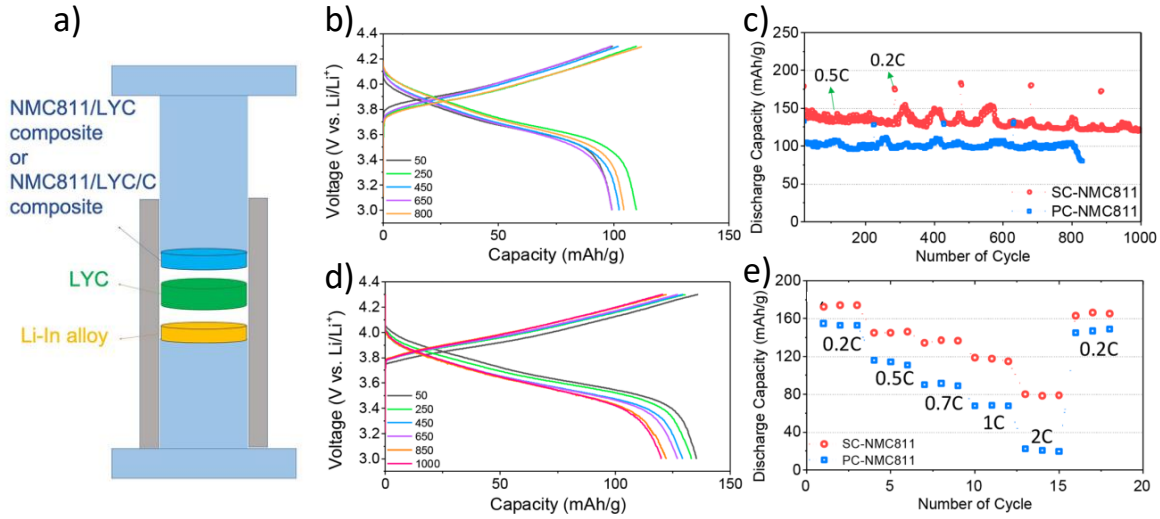

Figure 1.19: **(a)** Schematics of ASSB cell configuration. Charge/discharge voltage profiles of **(b)** Polycristalline-NMC811 (PC-NMC 811) and **(c)** Single crystal-NMC811 (SC-NMC811) ASSB cells. **(d)** Capacity retention plots for the cells cycled at 0.5 C for 200 cycles followed by 3 cycles at 0.2 C. The same sequence repeats throughout the test. Note that the performance fluctuation is due to changes in laboratory ambient temperature during the test. **(e)** Rate capability comparison of PC-NMC811 and SC-NMC811 ASSB cells. Reproduced from reference[112].

Of interest regarding SE development, are the performances revealed by Peng et al. using chlorine-rich lithium argyrodite ($Li_{5.5}PS_{4.5}Cl_{1.5}$) and a typical NMC622/Li-In alloy system[113]. Remarkable stability and capacity is presented over a wide range of C-rates and temperature (see **Figure 1.20**). Of interest are the low cost and high conductivity (9.03 mS/cm) of this SE, which can be easily synthesized by a simple solid-state synthesis route. Also, the lack of carbon additive, known to be detrimental with Argyrodite, suggests that a high C-rate in non-carbon containing system is possible. However, the extremely low loading of the cathode composite (2.5 mg/cm²) questions the impact of a higher loading on the high rate performances.

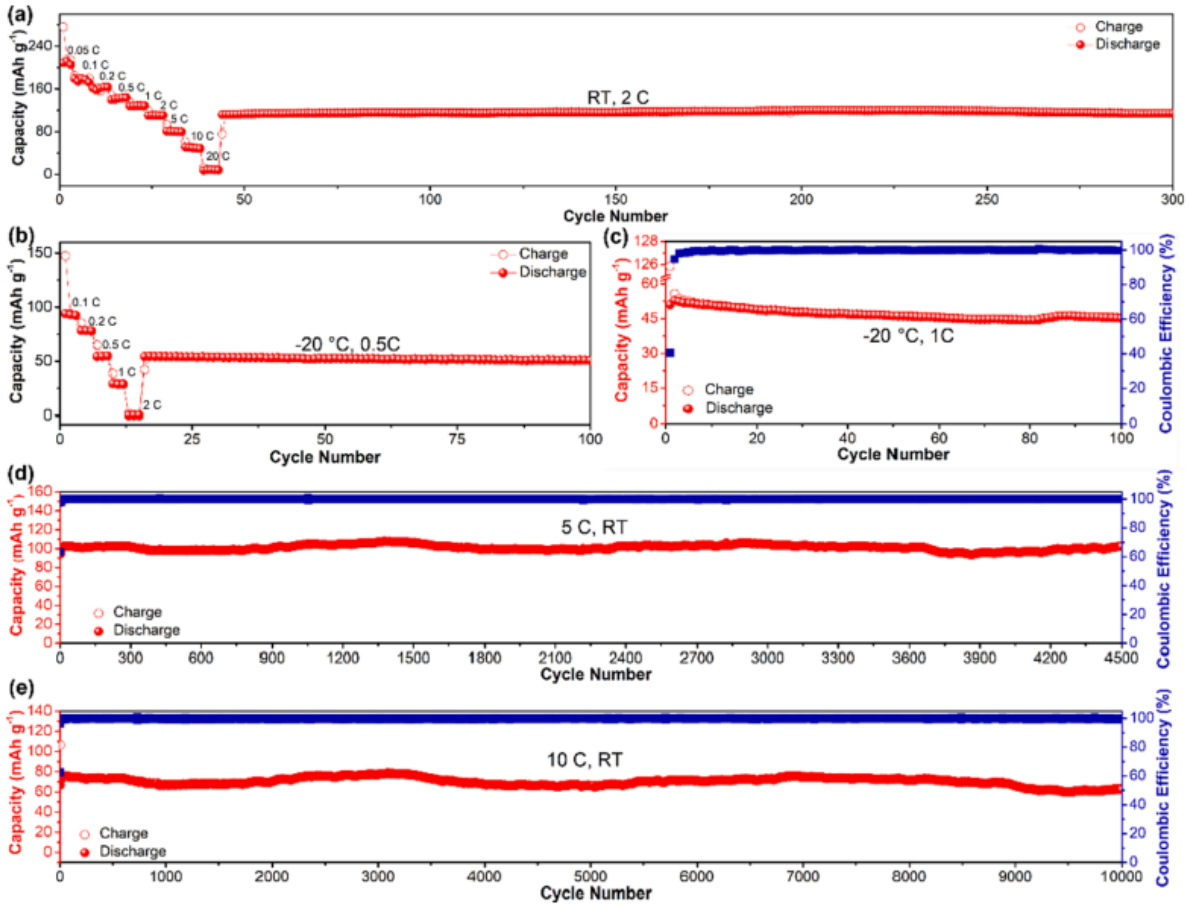

Figure 1.20: Rate capability and cyclability evaluation of the $LiNi_{0.6}Mn_{0.2}Co_{0.2}O_2$/ $Li_{5.5}PS_{4.5}Cl_{1.5}$/ In-Li SSBs. The rate capability of the fabricated ASSB working at **(a)** RT and **(b)** – 20°C. Cycling performance of $LiNi_{0.6}Mn_{0.2}Co_{0.2}O_2$/$Li_{5.5}PS_{4.5}Cl_{1.5}$/In-Li ASSB working under different temperatures and charge/discharge rates: **(c)** cycled at 1C under – 20 °C. Solid-state batteries cycled under room temperature at **(d)** 5C and **(e)** 10C. The loading amount of cathode used for assembling solid-state batteries in this section was 2.5 mg composite cathode/cm. Reproduced from reference[113].

One of the most striking performances obtained in the latest years (2022) are demonstrated in Zhou et al. study, with remarkable capacity retention (> 3000 cycles for 80 % capacity retention) and C-rate capability[82]. This breakthrough originates from the development of a new solid ionic conductor family ($Li_2In_xSc_{0.666-x}Cl_4$ ($0 \leq x \leq 0.666$)) coupled with Ni-rich NMC 851005 cycled at high cut-off potential (4.8 V vs. Li^+/Li). The high ionic conductivity (up to 2 mS/cm) and the large potential window of those SEs enabled the usage of high loading and high oxidative potential for cycling (see **Figure 1.21**). As critic, a long-cycling at C/5 could enable an appreciation of the cycling stability of such highly performing system. In addition, the use of Scandium and Indium elements raise the question of resources

and costs. However, these figures of merits are exciting regarding both the high C-rate performances and the high percentage of AM of > 85 wt. % used inside the cathode.

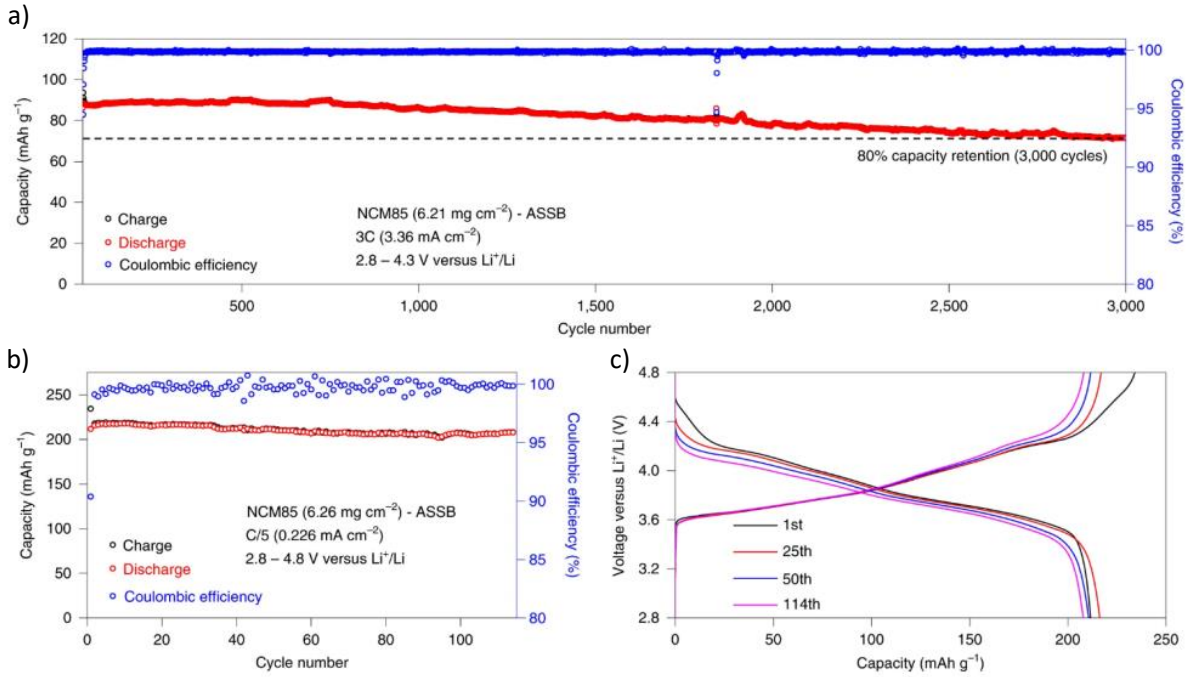

Figure 1.21: Long-term cycling of the NCM85 ASSB (performed after rate cycling) at a 3C rate **(a)** and ultra-high voltage NCM85 ASSB cycled between 2.8 and 4.8 V versus Li^+/Li **(b)** and the corresponding charge–discharge voltage profile **(c)**. Reproduced from reference[82].

In 2021, good performances and high rate capability were obtained by Yoonjae et al., using LYC halide SE coupled with highly energetic NCA ($LiNi_{0.88}Co_{0.11}Al_{0.01}O_2$)[114]. Using Li-In anode, this system presents a 96.8% capacity retention after 200 cycles at C/2 with more than 180 mA.h/g, and remarkable 130 mA.h/g of capacity at 4C (30 °C temperature) (see **Figure 1.22**). Such performances were made possible by the usage of a stable and ionically conductive LYC, and by the efficient design of the cathode. Of interest is the AM/SE ratio, which is proven detrimental when 70/30 wt.% is used, while 60/40 wt.% usage enabled incredible performances, perfect percolation and prevention of mechanical cracking. Although such high quantity of SE in cathode composite is detrimental for battery cost and energy density, this paper highlights the huge impact of AM/SE particle size matching and ratio for designing efficient ASSB.

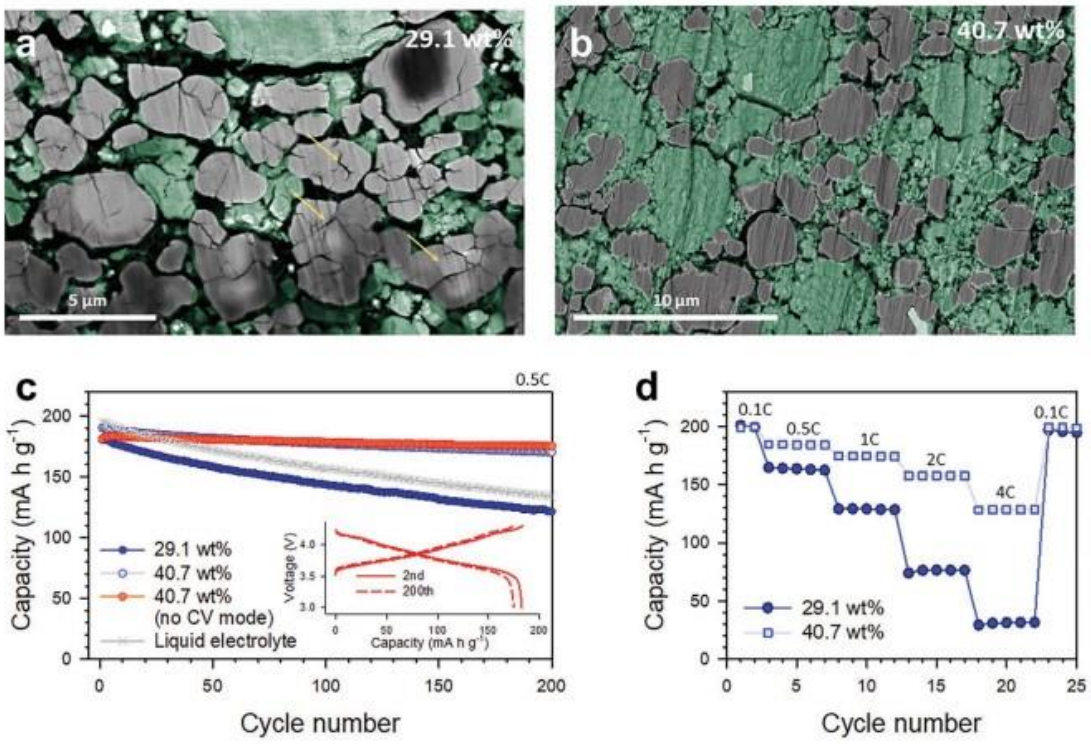

Figure 1.22: Results of S/LYC electrodes with an excessive amount of LYC (40.7 wt. %) for all-solid-state half cells tested at 30 °C. Cross-sectional SEM-BSE images of S/LYC electrodes with **(a)** 29.1 wt. % and **(b)** 40.7 wt. % LYC after first discharge to 3.0 V (vs Li/Li^+). Note the cracks formed inside the single NCA, indicated by the arrows in (a). **(c)** Cycling performances at 0.5C for the S/LYC electrodes with varied amounts of LYC. The cells were charged with or without CC–CV (constant current–constant voltage) mode. In the inset, the charge–discharge voltage profiles at the 2nd and 200th cycles for S/LYC with 40.7 wt. % LYC are shown. A result for S-NCA electrodes in liquid electrolyte cells is also compared. **(d)** Rate capabilities. Reproduced from reference[114].

1.4 Conclusion of the chapter

We have provided an overview of the development of Li-ion batteries, which has been driven by innovative research on electrode materials since the 1970s. However, the demand for batteries for electric vehicles requires higher energy and safety standards. Thus, we focused on advanced solid-state batteries, which have gained increasing interest as a next-generation battery and are nearing commercialization. Out of all SE material for ASSB, Li_6PS_5Cl exhibits excellent properties such as ionic conductivity, ductility, and easy processability. Nevertheless, several scientific challenges must be addressed. Especially, we explored the

current state of knowledge regarding the impact of composite's composition and processing and the impact of the distinct reactivities occurring in the ASSB composites interfaces. Both considerations hinder the ASSB performances. To overcome these challenges, an efficient and comprehensive optimization plan for composite formulation and the careful selection of appropriate coatings are being explored. Despite the continuous advancements in ASSB performances, research still lags behind the expected level required for commercialization. This assessment is attributed to the formidable task of addressing specific issues related to solid-solid interfaces, including contact and mechanical evolutions, while simultaneously dealing with the low stability observed in current SE materials, versus lithium metal and in the cathode composites.

Chapter 2

Electrochemical/chemical stability of Li_6PS_5Cl based cathode composites

Summary

This chapter includes the following publication:
Quemin, E.; Dugas, R.; Koç, T.; Hennequart, B.; Chometon, R.; Tarascon, J.-M. Decoupling Parasitic Reactions at the Positive Electrode Interfaces in Argyrodite-Based Systems. *ACS Appl. Mater. Interfaces* **2022**, *14* (43), 49284–49294. https://doi.org/10.1021/acsami.2c13150.

2.1 Introduction

As discussed in the preceding chapter, All-Solid-State Batteries have emerged as a prospective battery technology to meet the demands of the expanding electric vehicle market. Among the various systems being investigated, sulphide-based ASSBs exhibit favourable characteristics such as ease of processing and promising performances. However, these systems encounter a significant drawback, namely long-term capacity degradation caused by increased decomposition reactions. Although previous literature has addressed these instabilities to some extent, a comprehensive analysis encompassing all aspects of these issues in our system is essential.

Thus, the current chapter presents an exhaustive investigation into the reactivities of Li_6PS_5Cl-based systems, using NMC 622 as reference material and considering diverse operational conditions, including changes of active material, voltage window and carbon additive amounts. Firstly, the study focuses on SE decomposition, by evaluating the influence of the type and quantity of carbon additives on the initial cycle and cell capacity retention Secondly, the reactivity at the interface between NMC and solid electrolyte is examined, with a detailed study of the effects of potential window and active material characteristics. Finally, the study delves into the effects of both active material and electronic conductive additive by employing the Potentiostatic Electrochemical Impedance Spectroscopy (PEIS) method to effectively analyse and differentiate the two interfaces and reactivities under investigation.

2.2 Intrinsic decomposition of Li_6PS_5Cl

2.2.1 Influence on first cycle performances

To investigate the intrinsic reactivity of Li_6PS_5Cl, we assessed its stability window and scrutinized the impact of a carbon additive on the initial cycle performance. In order to accomplish this, we employed a commercial Argyrodite solid electrolyte provided by NEI company, which exhibits a wide particle size range spanning from 100 nm to 30 µm, as depicted in **Figure 2.1.a**. To start with, Li_6PS_5Cl particles are mixed with 5 wt. % VGCF (Vapour Grown Carbon Fibre) and tested in a two-electrode configuration, versus Li-In/Li_6PS_5Cl anode composite. The cell assembly procedure and composite preparation are outlined in the **Appendix 2.1.**

Cyclic-voltammograms were recorded for this system using a scan rate of 0.05 mV/s, covering a voltage range up to 3.9 V vs. Li-In/In at different temperatures: 25°C, 55°C, and 75°C. The results presented in **Figure 2.1.b** demonstrate that higher temperatures are associated with an increase in current amplitude, indicating a degradation process of the solid electrolyte governed by kinetic factors. Notably, the decomposition of Li_6PS_5Cl exclusively occurs through oxidation within the potential window of 2.1-3.9 V vs. Li-In/In. To further investigate this phenomenon, X-ray diffraction (XRD) analysis was conducted on the VGCF/SE composite after oxidation at 55°C for a duration of one month, revealing the disappearance of Li_6PS_5Cl peaks and the formation of an amorphous component (for more details, refer to the **Appendix 2.2**). These findings align with the decomposition mechanism reported in the literature for Li_6PS_5Cl, where the oxidation of Argyrodite within the same potential range results in the generation of highly insulating products such as S and P_2S_5[73,74].

In a typical composite comprising NMC 622, the intrinsic decomposition of the solid electrolyte described above, is reflected by a characteristic first cycle early delithiation slope. This behaviour is demonstrated by examining the first cycle performance of our Li_6PS_5Cl/NMC 622 composites (70/30 wt. %), with the inclusion of 1 or 5 wt. % of VGCF or without any additive (refer to **Figure 2.1.c**)[70,72]. As anticipated, an increasing additional slope is observed within the voltage range of 2.1 to 3.1 V vs. Li-In/In, with higher amount of VGCF.

At this point, it is imperative to explore the influence of the newly formed degradation products on the performances of the first cycle. To address this, we proceed to vary the amount of carbon additive in composites, between 0 to 10 wt. % and study its impact on the initial cycle. As demonstrated in **Figure 2.2.a**, the composites with VGCF exhibit lower active material utilization, and a higher level of polarization arising from an enhanced resistance with increased VGCF content, at C/10 (1C is calculated with the theoretical capacity value of the AM in the whole manuscript). Such effect is highlighted by the impedance spectra evolution, taken at end of first charge in three-electrode setup, which presents a growing resistance with increasing amount of VGCF (see **Figure 2.2.b**). Note that the three-electrode assembly used here is built via a multistep process described in **Appendix 2.3**, using $Li_{0.5}In$ + Li_6PS_5Cl (60/40 wt. %) composite as reference electrode.

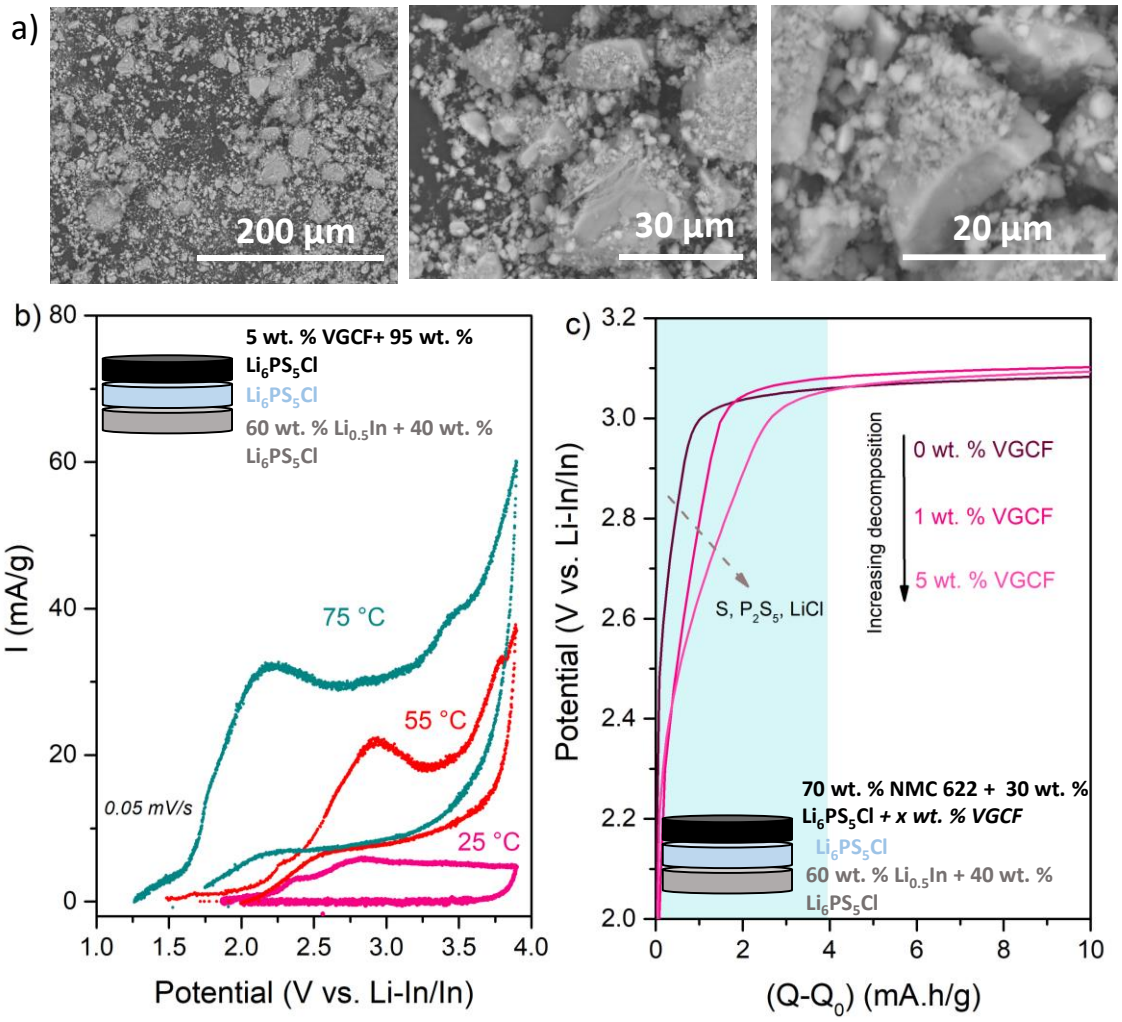

Figure 2.1: **(a)** SEM pictures of Li_6PS_5Cl **(b)** Cyclic voltammetry of VGCF + Li_6PS_5Cl (5/95 wt. %) at different temperatures. Cyclic voltammograms at 0.05 mV/s and at three different temperatures (25°C, 50°C and 75°C).

(c) Early delithiation of first cycle of NMC 622 + Li_6PS_5Cl (70/30 wt. % ratio) with additional VGCF put in 1 or 5 wt. %. Cells are cycled at C/10 and a loading of 16 mg/cm² of composite is used.

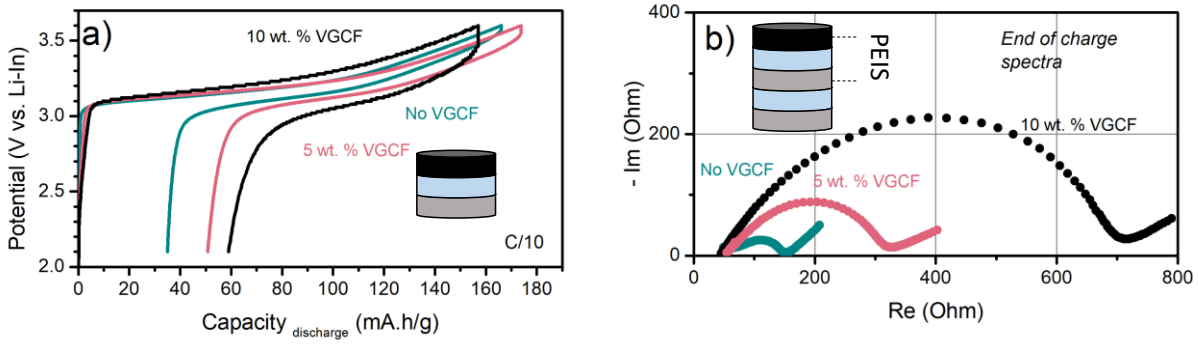

Figure 2.2: **(a)** First cycle at C/10 using NMC 622 + Li_6PS_5Cl (70/30 wt. % ratio) as cathode composites with 5 wt. % or 10 wt. % additional VGCF, or without VGCF. A loading of 16 mg/cm² of composite is used. **(b)** Composites of same formulation are implemented in three electrode setup, to take PEIS measurements at the end of the first charge (3.6 V vs. Li-In/In) at C/10, 10 hours of relaxation is made prior the measurements.

In order to gain a deeper understanding of the system's behaviour, we employed the concept of first cycle irreversible capacity as a valuable tool. The irreversible capacity observed during the initial cycle is commonly attributed to either slow kinetics or irreversible phenomena[115]. To distinguish between these possibilities, the cells potential was kept at the end of discharge, and the amount of capacity recovered was used as an indicator of the kinetic limitations within the cells. Concurrently, the resulting final irreversible capacity provided valuable insights into the occurrence of side reactions, as depicted in **Figure 2.3.a**. We will further refer to the "apparent irreversible capacity" and the "true irreversible capacity" for the irreversible capacity prior and after potential imposition, respectively. It is important to note that the extent of kinetic limitations and reactivity is highly influenced by the nature of the solid electrolyte, as demonstrated in the **Appendix 2.4** through a comparison of the first cycle of solvent and/or solid-state synthesized Li_6PS_5Cl, Li_3InCl_6, and Li_3PS_4. Furthermore, it is noteworthy that this methodology has been successfully employed in the investigation of lithium-ion cells[115,116]. However, when comparing liquid and solid-state cells, we observed a lower true irreversible capacity in the liquid system, as exemplified by our NMC 622 in **Figure 2.3.b**, suggesting an enhanced reactivity in the solid-state.

We implemented this methodology on coated NMC 622 system with various carbon additives nature and content, offering different morphologies and specific surfaces: C 65 (62 m^2/g), VGCF (24 m^2/g) and Super P (80 m^2/g). We discharged Carbon-free (C-free) and Carbon-containing (C-containing) cells on their first cycle to 2.1 V vs. Li-In/In in a galvanostatic mode at C/10, prior switching to a constant potential mode for 30 hours when the discharge cut-off potential was reached. As seen in **Figure 2.3**, we could retrieve most of this irreversible capacity for the C-containing cells under this procedure, indicating that the apparent irreversible capacity is mainly arising from kinetic limitations. Furthermore, both apparent and true irreversible capacities are increasing with the electronic surface, pointing at both an enhanced side reaction with Li_6PS_5Cl and worse kinetic of the first cycle linked to the new highly insulative phases formed. Comparing the three carbon additives, VGCF shows a lower reactivity with 10 mA.h/g of true irreversibility, while C65 and Super P-containing systems respectively present 13 and 17 mA.h/g for 5 wt. % additive addition. This small difference is most likely due to the VGCF lower BET (Brunauer-Emmet-Teller) specific surface (24 m^2/g)[72,117]. Moreover, the optimized nature of the long fibers has been proven to allow efficient electronic percolation in solid-state systems[118]. If the reader is interested, we also made high temperature experiment on a variety of systems using distinct AM, as depicted in **Appendix 2.5**, and we found an enhanced final irreversibility alongside a lower apparent irreversibility when using 55 °C, matching a reactivity governed by kinetics. Surprisingly, a discrepancy in the apparent irreversibility trend is found for 10 wt. % VGCF in **Figure 2.3.c**, exhibiting poor kinetics with an apparent capacity loss of 37-45 mA.h/g. Such behaviour questions the impact of morphology on the kinetics, additionally to the side reactions effect. Indeed, a legitimate question arise from whether the slow kinetics observed are only linked to the newly formed interfaces, or also to a carbon additives physical presence effect.

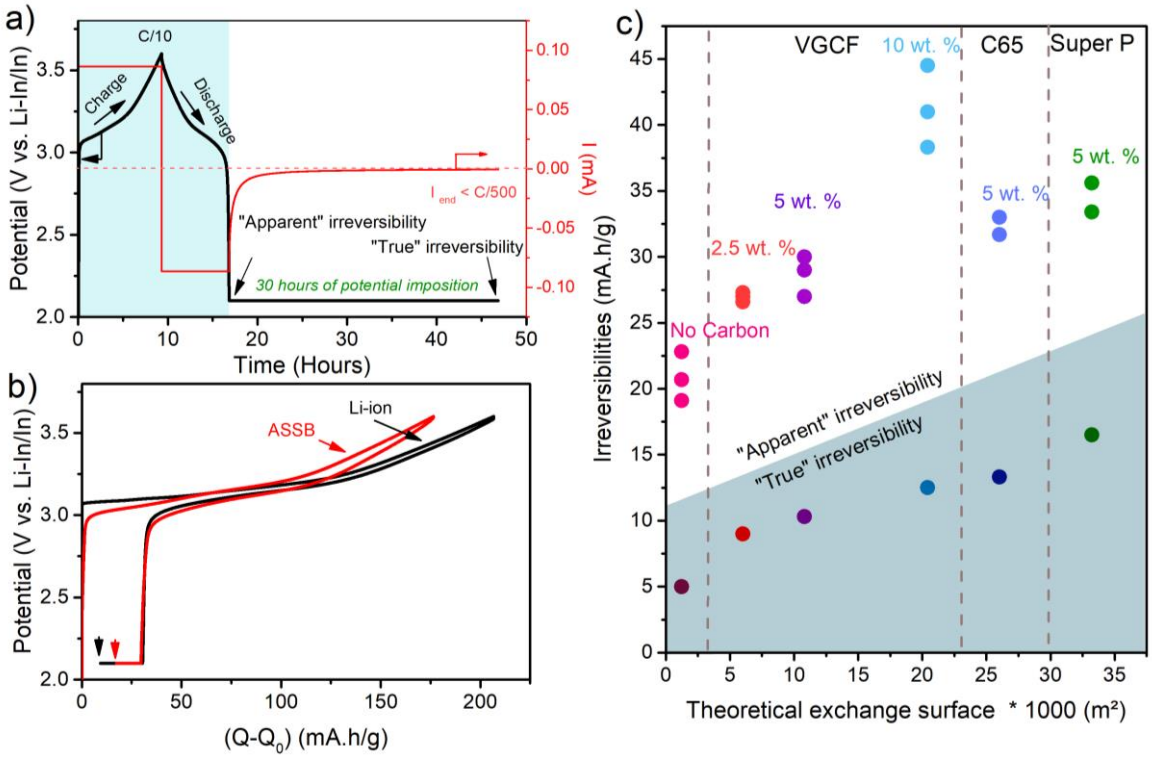

Figure 2.3: (a) Scheme of the first cycle irreversibility measurement. The "true" irreversibility is obtained after one cycle, by clamping the potential at 2.1 V vs. Li-In/In at the end of discharge for 30 hours, ensuring an ending current below C/500. Galvanostatic cycling is made between [3.6 V-2.1 V vs. Li-In/In] at C/10. **(b)** Apparent and true irreversibility of NMC 622 liquid and solid-state based cells, with 5 wt. % VGCF **(c)** Apparent and true irreversibility of cells using 70/30 wt. % NMC 622-Zr coated/Li_6PS_5Cl with pristine or 2.5 wt. %, 5 wt.% and 10 wt. % VGCF, 5 wt.% C65 and 5 wt.% Super P. The theoretical exchange surface is computed by taking the mass of carbon additive and their expected BET surfaces given by the manufacturers (VGCF: 24 m^2/g, Super P: 80 m^2/g and C65: 62 m^2/g). We also add the surface of our NMC, which is computed by making the hypothesis of spherical particles.

2.2.2 Sluggish kinetics of carbon-containing systems

As evidenced through last section, a question remains regarding the kinetic limitations of the 10 wt. % VGCF composite. To explore this surprising result, we investigated the impact of carbon additive presence on the ionic and electronic resistance of ASSB composites, prior any cycling. Firstly, the composites ionic conductivity is assessed via Potentiostatic Electrochemical Impedance Spectroscopy in a three-electrode cell setup developed in house[119], so as to decouple WE impedance evolution from the CE one. Detailed explanation

on three-electrode assembly can be find in **Appendix 2.3**. A scheme of the cell is shown in **Figure 2.4**. We used $Li_{0.5}In$/In + Li_6PS_5Cl (60/40 wt. %) as both reference and counter electrode composites, 1 t/cm² pressure is applied upon cycling and the system is designed to be airtight. Two solid electrolyte layers of 30 mg (adding approximately 0.2 mm to the stack thickness each) are added on both sides of the reference layer, creating a five-layer configuration for PEIS measurements. Secondly, electronic resistance values are obtained by DC conductivity measurement of an 80 mg composite, pelletized at 1 t/cm² in a two electrode cell setup. To do so, 10 mV polarization is imposed until a steady-state current is reached, and the electronic resistance is computed by Ohm's law. A scheme of the experiment is shown in **Figure 2.5.a**.

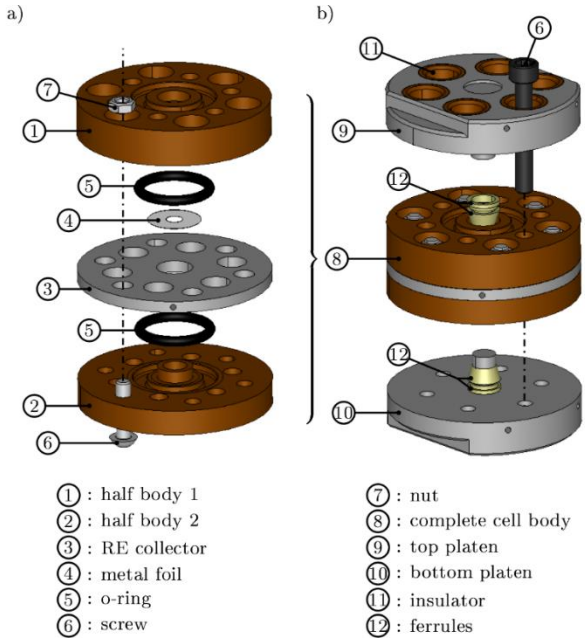

Figure 2.4: Schematic of the three-electrode setup used to take PEIS measurements.

For interpreting such impedance spectra, an equivalent model is necessary as solid-state composite systems present complex spectra. Transmission Line Models (TLM) is used as a model of choice in the literature since it present a direct transcription of the physics behind such mixed ionic/electronic systems[120–125]. The system is assumed to be 1D, and we consider uniform values of the parameters, to highly simplify the fitting process by using the mathematical equations proposed by Ioroi et al.[126]. This model features two railways representing ionic and electronic conduction paths along the mixed conductive system. Between them lies the interfacial phenomena arising from AM/SE. Considering the non-

faradaic case of an uncycled electrode (no charge transfer or solid-state diffusion), we place a Constant Phase Element (Q) to account for the blocking electrodes. Note that, Constant Phase Elements (CPE) are used to represent capacitive behaviour in battery systems, as real devices capacitive response displays a distribution of relaxation times[127,128].

Figure 2.5.b, presents the distinct ionic and electronic resistance evolution, with our C-free reference system (70/30 wt. % NMC 622/SE) showing R_{elec} and R_{ion} values of 60 and 120 Ohms, respectively, using a loading of 16 mg/cm² and an electrode thickness of approximately 70 µm. Switching to carbon containing cells, the electronic resistance is dropping below 1 Ohm by adding only 2 wt. % of VGCF. Thus, electronic resistance is supposed negligible in the TLM model when more than 2 wt. % carbon is added, in accordance with the DC conductivity measurements. More surprising results are seen for the ionic conductivity. Indeed, increasing carbon amount goes along with an unexpected rise of the ionic resistance, counterbalancing the positive effect of the electronic conductivity decrease. Hence, the carbon addition is not only promoting side reactions, but is also detrimental for the ionic motion when a large amount is used. This is evidenced by the limited kinetics observed in 5 wt. % VGCF containing systems (see the C-rate tests presented in **Appendix 2.6**). A plausible hypothesis lies in the increasing tortuosity of Li^+ pathway when carbon is added. Another one is the chemical reactivity of Li_6PS_5Cl with surface species existing on carbon additive surfaces. Overall, as carbon is essential for improving the overall electronic conductivity of ASSB composites, our results suggest that keeping the amount of additive between 1 to 2 wt. % is sufficient to provide a proper electronic motion while maintaining a low increase of ionic resistivity.

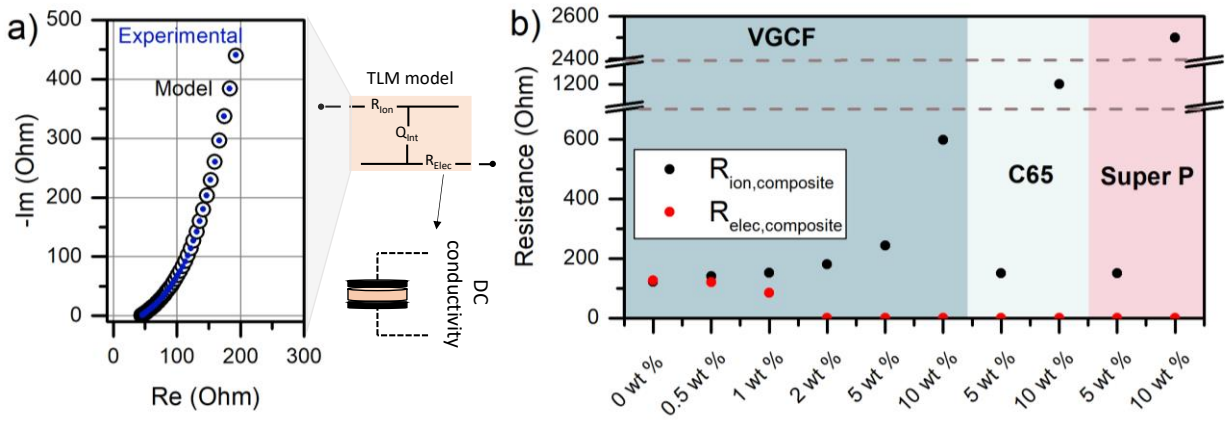

Figure 2.5: **(a)** Scheme of the experiment used for both DC conductivity measurements in pellet system and ionic conductivity measurement in 3-electrode system. **(b)** Resulting electronic and ionic resistance of the composites using different addition of carbon additives. Pristine state is made with 70/30 wt. % ratio of NMC 622/Li_6PS_5Cl. Same amount of composites (80 mg) is used for all experiments.

2.2.3 Effect on stability upon cycling

Turning to carbon additive impact on cell lifetime, C-free composites are compared with 5 wt. % VGCF containing ones. Here in, a large amount of carbon additive is chosen to neglect the active material electronically conductive surface, which therefore becomes 10 times lower than the VGCF one in C-containing cells, in the aim of solely focusing on VGCF/SE interfaces.

We decided to monitor the resistance evolution of C-free and C-containing cells, following the procedure described in **Figure 2.6.a**. The cells are maintained at a defined cut-off potential (3.6 V vs. Li-In/In here) and a relaxation of 10 hours is done after each 10 hours of imposition. This relaxation is followed by a 10 mV potential imposition step for 20 min, and the steady-state current obtained after 1000 seconds is used to compute the resistance R_{1000s} of the cell, by simple ohmic law. This procedure is repeated 15 times. As a result, the C-containing system is showing a linear increase with time, while the C-free one rapidly reach a constant resistance after 20 hours, mirroring a passivating interface formation (see **Figure 2.6.b**). On the contrary, the C-containing cells reflect a continuous insulative phase formation building up at VGCF/SE interfaces, which does not passivate in 150 hours. Such evolutions are mirrored by the capacity retention at C/10 of C-free and C-containing cells, which are shown

in **Figure 2.6.c**. Especially, the C-containing system shows a clear decay by losing approximately 10 % of capacity in 25 cycles, contrasting with the stability of the C-free system.

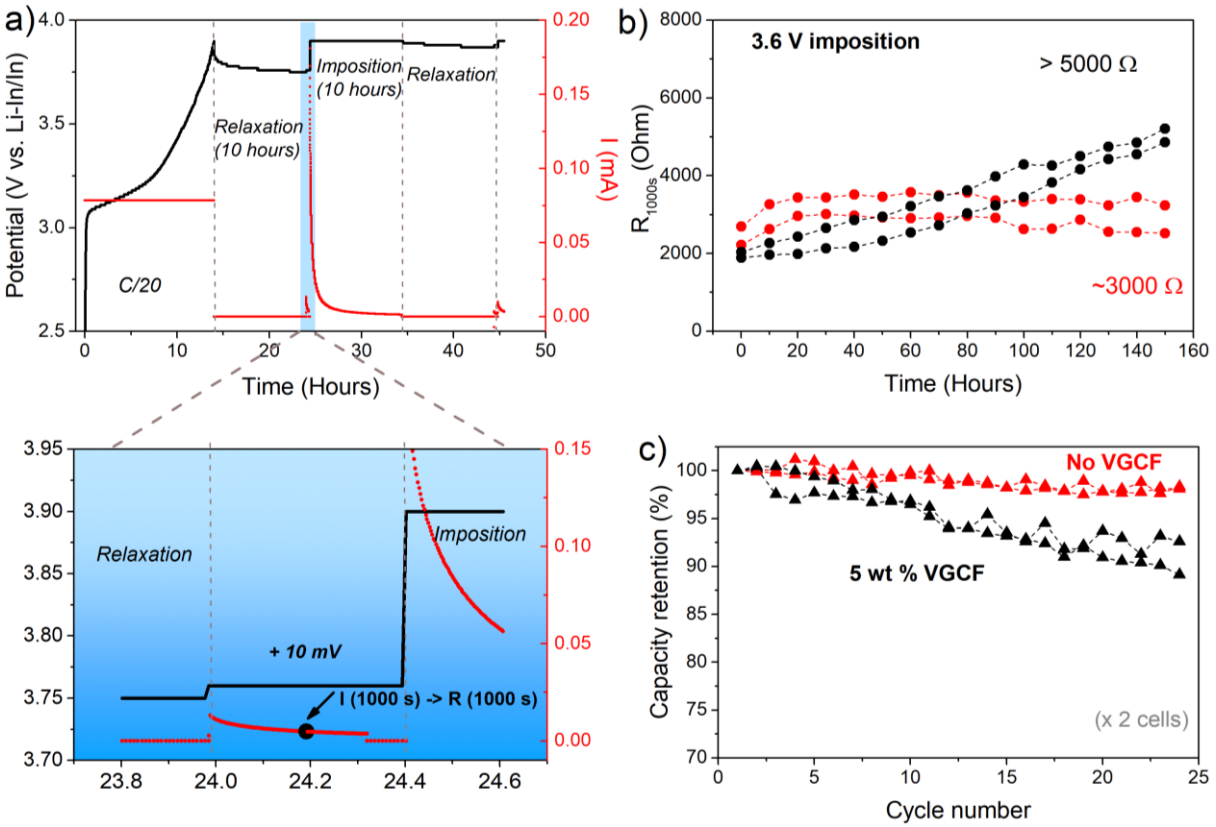

Figure 2.6: (a) scheme of the protocol. A monitoring of resistance is done during a constant potential imposition (at 3.6 or 3.9 V vs. Li-In/In). A first charge at C/10 is directly followed by a potential imposition. Every 10 hours of constant voltage, 10 hours of relaxation is done, followed by a 10 mV step for 20 minutes. **(b)** Resistance evolution during potential imposition at 3.6 V vs Li-In/In. Two cells per system are shown. **(c)** Capacity retention evolution in C-containing and C-free systems, cycling at C/10 until 3.6 V vs. Li-In/In. Two cells per system are shown.

2.3 High potential reactivity of Li_6PS_5Cl with NMC active materials

2.3.1 Impact of cut-off potential

Transition layered metal oxide AM (TLMO) are suspected to also lead to irreversible phase formation when put in contact with Li_6PS_5Cl. To interrogate this aspect we studied the

reactivity of Li_6PS_5Cl in a variety of carbon-free composites and performed electrochemical tests according to the protocol shown in **Figure 2.7.a**. The cells are cycled in conventional potential window for two cycles at C/10. On third charge, the cell potential is set at a define potential (3 V, 3.4 V, 3.6 V or 3.9 V vs. Li-In/In) for 60 hours and the resulting effect on the following cycles is studied.

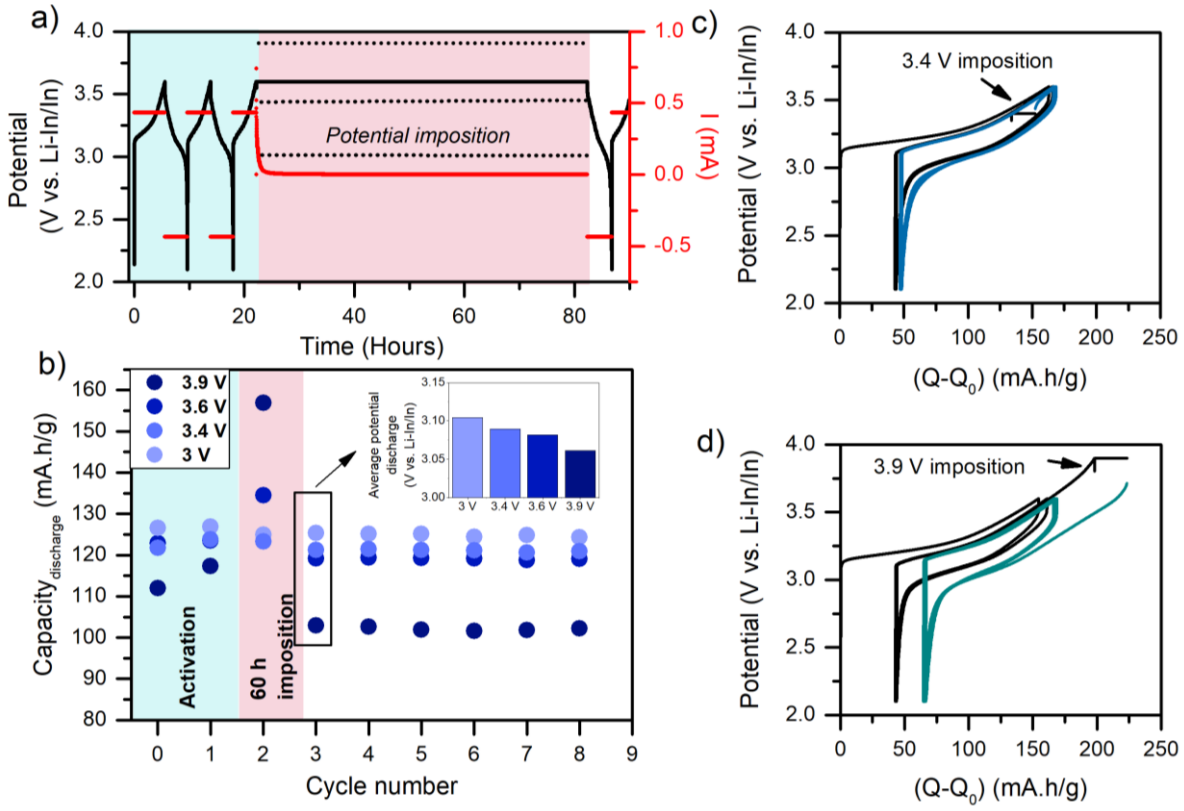

Figure 2.7: Potential imposition effect on NMC 622 + Li_6PS_5Cl (70/30 wt. %) system **(a)** Scheme of the procedure **(b)** Galvanostatic charge-discharge at C/10 in NMC 622/Li_6PS_5Cl/Li-In-Li_6PS_5Cl system with a 60 hours potential imposition on the third charge at different potential (3 V, 3.4 V, 3.6 V and 3.9 V vs. Li-In/In). Additionally, the average discharge potential of the 4th cycle is shown.

Using NMC 622 as AM, **Figure 2.7.b-d** shows that the higher the imposition potential, the higher the loss of capacity and the polarization of the following cycle. This degradation is the worst for 3.9 V vs. Li-In/In imposition with more than 12 mA.h/g lost on the 4th discharge. In contrast, we found that a 3 V vs. Li-In/In imposition does not affect the cycling, while 3.4 V and 3.6 V vs. Li-In/In demonstrate a negligible impact with less than 5 mA.h/g losses. This is not new, as it has been proven that going above 3.6 V vs. Li-In/In induces high surficial

reactivity in liquid cells, particularly in the case of Ni-rich NMC. This phenomenon arises from the oxygen release, the H2-H3 phase transition, and the highly reactive Ni^{4+} appearing during charged state of NMC[85,129].

Moreover, using similar methodology, we show the dependency of this effect with the nature of the layered oxide used in our composite (**Figure 2.8.a**). The worst behavior of NMC 811 (6 % capacity loss) as opposed to 4 and 2.5 % for NMC 111 and $LiNi_{0.9}Co_{0.1}O_2$ (NC9010) respectively, suggests different degradation rates. This effect is suspected to arise from the nickel content, as the stability of cathodes in liquid electrolytes was shown to decrease with increased Ni content[85,86,129]. However, as Ni content also affects the electronic conductivity of NMC, it raises a legitimate question regarding the impact that it could have on the observed degradation mechanism, especially considering the decomposition of our SE explained in the previous section[130]. Thus, we assessed the electronic conductivity of both the active materials mixed with 1 wt. % PTFE or with 30 wt. % Li_6PS_5Cl, which are displayed in **Figure 2.8.b**. Although the electronic conductivity of NC90 material, either mixed with Argyrodite or not, is greater than other NMC, it demonstrates slightly lower capacity loss on **Figure 2.8.a**. This suggests that the degradation mechanism in presence of SE and transition layered oxide materials is not solely governed by the electronic conductivity. Note that, we are comparing similar average particle size systems (~ 4 µm) as seen on **Figure 2.8.c-e**, but distinct morphologies and possibly distinct particle size dispersions are observed in between those three active material particles. Thus, a legitimate question regards the effect of such parameters on the electronic percolation inside composites. Nevertheless, similar trend were demonstrated between 1 wt. % PTFE and 30 wt. % Li_6PS_5Cl containing systems. Therefore, we can attribute the composites electronic conductivity changes as mostly pertaining to the nickel content present in the active material.

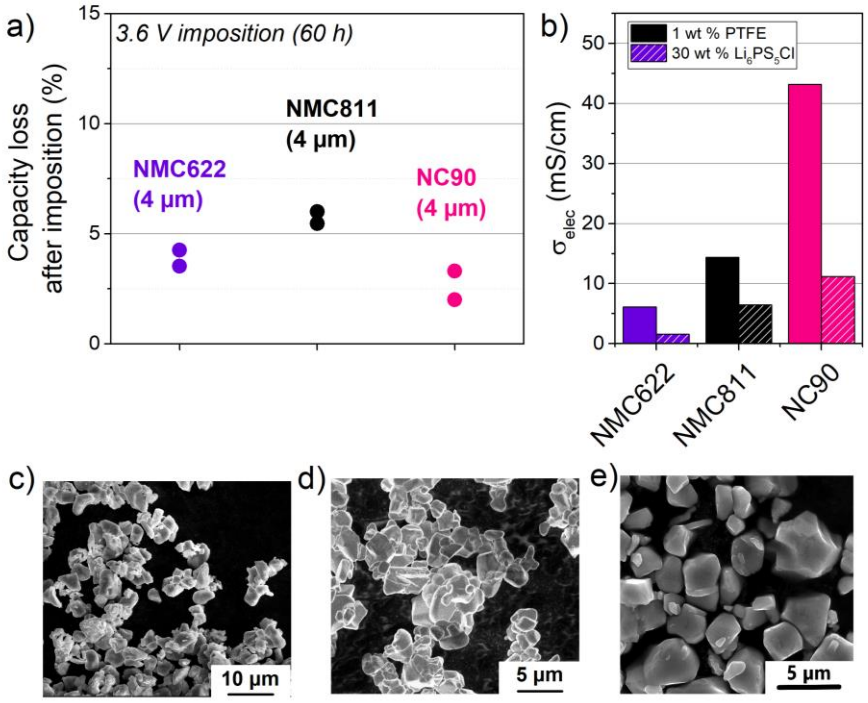

Figure 2.8: Potential imposition effect on various transition metal oxide **(a)** Similar procedure as in **Figure 2.7** is used, with a 3.6 V imposition. Capacity loss (%) on the 4th cycle after 60 hours imposition is shown for different active material. Two cells are plotted. **(b)** Electronic conductivity of systems with AM +1 wt. % PTFE and AM + Li_6PS_5Cl (70/30 wt. %) (30-50 mg of composite is used for those last systems). SEM micrographs of **(c)** NMC 622 **(d)** NMC 811 and **(e)** NC 9010.

2.3.2 Effect on stability upon cycling

To tackle the impact of the AM/SE detrimental phenomena upon cycling, the cells were cycled using a cut-off potential of 3.9 V vs. Li-In/In to further enhance instabilities issues previously spotted.

Figure 2.9 show capacity retentions and resistance evolutions at C/10 for C-free and C-containing cells cycled up to 3.9 V. Both show a ~ 20 % capacity loss after 20/25 cycles, and possibly a slight beneficial effect of carbon. By employing a similar methodology as depicted in **Figure 2.6** (voltage clamping), both cell types exhibit a substantial and rapid increase in cell resistance within the initial 25 hours of cycling, reaching nearly 13 000 Ohm after 80 hours. This phenomenon suggests the occurrence of an AM/SE interfacial passivation, as observed in **Figure 2.9**. Collectively, these findings imply a significant deleterious reactivity, surpassing the

SE decomposition effect by far. Comparison with **Figure 2.6** reveals distinct behaviours associated with the two different cut-off potentials. This observation indicates the presence of two degradation mechanisms governing the fade in cell capacity, along with distinct effects of carbon additives.

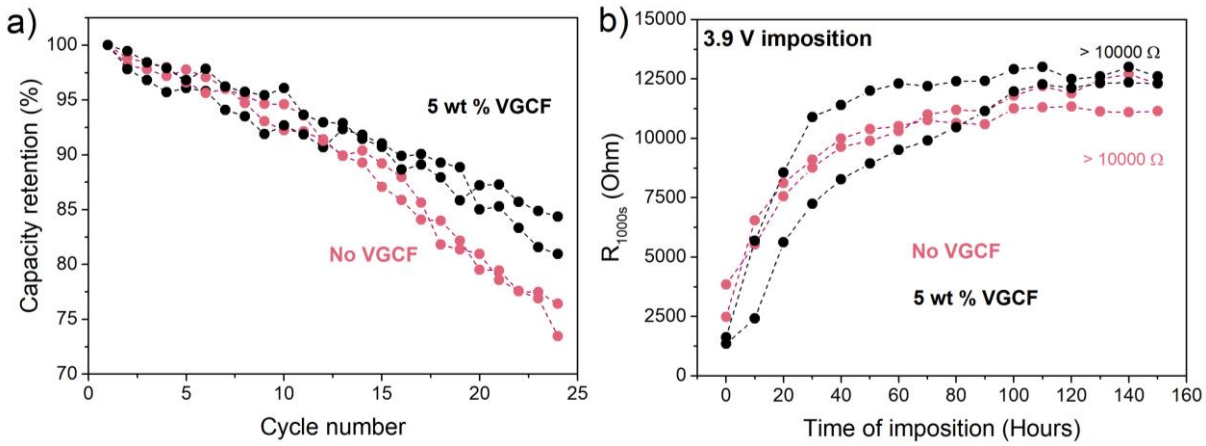

Figure 2.9: **(a)** Capacity retention of galvanostatic cycling at C/10 with 3.9 V vs. Li-In/In. Two cathode composites are used: NMC622 + Li_6PS_5Cl (70/30 wt. %) and NMC622 + VGCF + Li_6PS_5Cl (66.5/5/28.5 wt. %). **(b)** Resistance evolution during potential imposition at 3.6 V vs Li-In/In. Two cells per system are shown.

2.4 Decorrelating the two interfacial reactivities using PEIS

To decouple the distinct effects of VGCF as function of cut-off potential, and of both interfacial reactivities (AM/SE and VGCF/SE), we model resistance evolutions through impedance spectroscopy measurements.

2.4.1 Equivalent model development

Potentiostatic Electrochemical Impedance Spectroscopy is a technique of choice to assess degradation phenomena occurring in a battery. Especially, it can efficiently decorrelate phenomena affecting distinct interfaces or/and having different kinetics, provided that they have distinct characteristic frequencies. **Figure 2.10.a-d** presents the PEIS spectra evolution at end of charge of NMC 622 composite cathodes for 10 cycles, cycled until both 3.6 V and 3.9 V and with or without 5 wt. % VGCF. PEIS is done at equilibrium, after a 10 hours relaxation, in the frequency range of 500 kHz to 3 mHz, and we have used a 20 mV perturbation to ensure

a limited noise and the stability of the system along the measurement. Data were reproduced at least once for every system. Moreover, we proceeded to fit the data through a homemade Matlab program, and the fitting results are presented in open black circles alongside the experimental data on **Figure 2.10.a-d**. Both data set greatly match with each other.

To build the equivalent model used, we complexify the transmission line circuit previously employed in **section 2.2.2**, to account for the phenomena occurring during cycling, such as charge transfer. The resulting detailed equivalent model used in this study is depicted in **Figure 2.10.e.** Different circuit elements are added between the two rails to represent the charge transfer (R_{CT}, Q_{CT}) and the solid-state diffusion of the AM presenting a Warburg-like impedance (W). Additionally, a R//Q (R_{Int} // Q_{Int}) is implemented to account for a low frequency additional feature. However, considering the uncertainty of its origin, we did not further investigate its values. We would like to emphasize that its addition does not alter the estimated values of interest, (R_{Ion}, R_{Elec} and R_{CT}) as those phenomena are decorrelate from higher frequencies (see **Appendix 2.7** for further explanation). As a necessary first step, we will transform this model into the one depicted in **Figure 2.10.f**, due to the mirror effect of $R_{Ion, composite}$ and $R_{Elec, composite}$, making them impossible to decorrelate. We will therefore refer to a global conduction resistance ($R_{Global, conduction} = f(R_{Ion, composite}, R_{Elec, composite})$) merging ionic and electronic evolution in a non-linear equation. For a complete explanation on our impedance modelling and on the impact of each parameter, see **Appendix 2.7**.

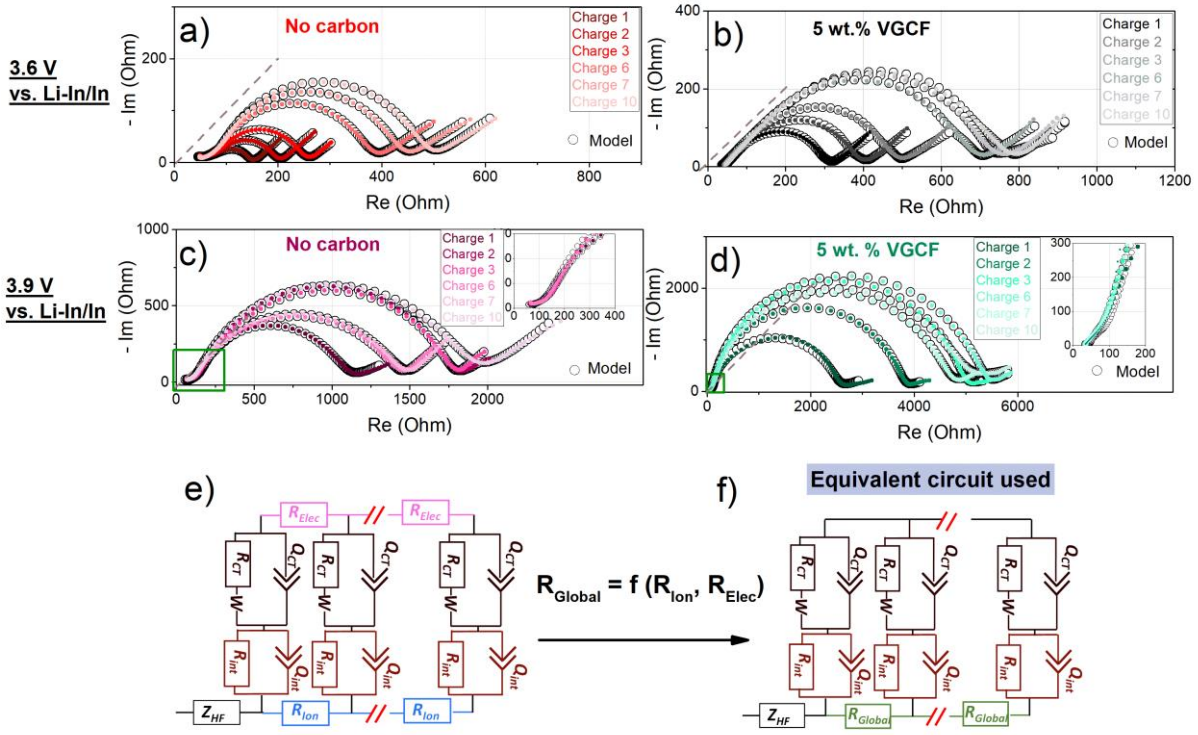

Figure 2.10: Effect of VGCF and cut-off potential via impedance spectroscopy. **(a), (b)** Spectra of cells cycling with 3.6 V vs. Li-In/In cut-off potential in C-free and C-containing systems **(c), (d)** Spectra of cells cycling with 3.9 V vs. Li-In/In cut-off potential in C-free and C-containing systems. PEIS spectra are taken at the end of charge of cycle n°1, 2, 3, 6, 7 and 10. 20 mV of amplitude is applied after 10 hours of relaxation, [500 kHz - 3 mHz]. The fitted spectra obtained by a personal Matlab optimization program are plotted along with each experimental data in open black circle. **(e)** Original TLM model representing all phenomena occurring inside our composites **(f)** TLM practically used for fitting with $R_{Global, conduction} = f(R_{Elec, composite}, R_{Ion, composite})$.

2.4.2 Experimental data results

Figure 2.11 presents the capacity evolution at C/30 and the $R_{Global, conduction}$ and R_{CT} values, both extracted from the four cells used in **Figure 2.10**. Despite a lower C-rate and an enhanced capacity fading, the three-electrode cell follows the same trends as the one of two-electrode cells (see **Figure 2.8.a** and **Figure 2.5.c**). Turning to the evolution of $R_{Global, conduction}$ and R_{CT}, it presents different behaviour in respect to cut-off potential and carbon additive presence. At 3.6 V vs. Li-In/In cut-off, the C-free cell metrics remain quite stable, in line with its stable capacity, while the $R_{Global, conduction}$ continuously increases in C-containing cells (growing from 200 to nearly 2000 Ohm) (**Figure 2.11.a**). Note that the two cells show equally a small increase of R_{CT}. Interestingly, cells reaching 3.9 V vs. Li-In/In experience an important

rise of their charge transfer resistance (with VGCF: 2200 to 4500 Ohm and without VGCF: 1000 to 1600 Ohm), while their global conduction resistance remains quite stable around 150 Ohm (**Figure 2.11.b**).

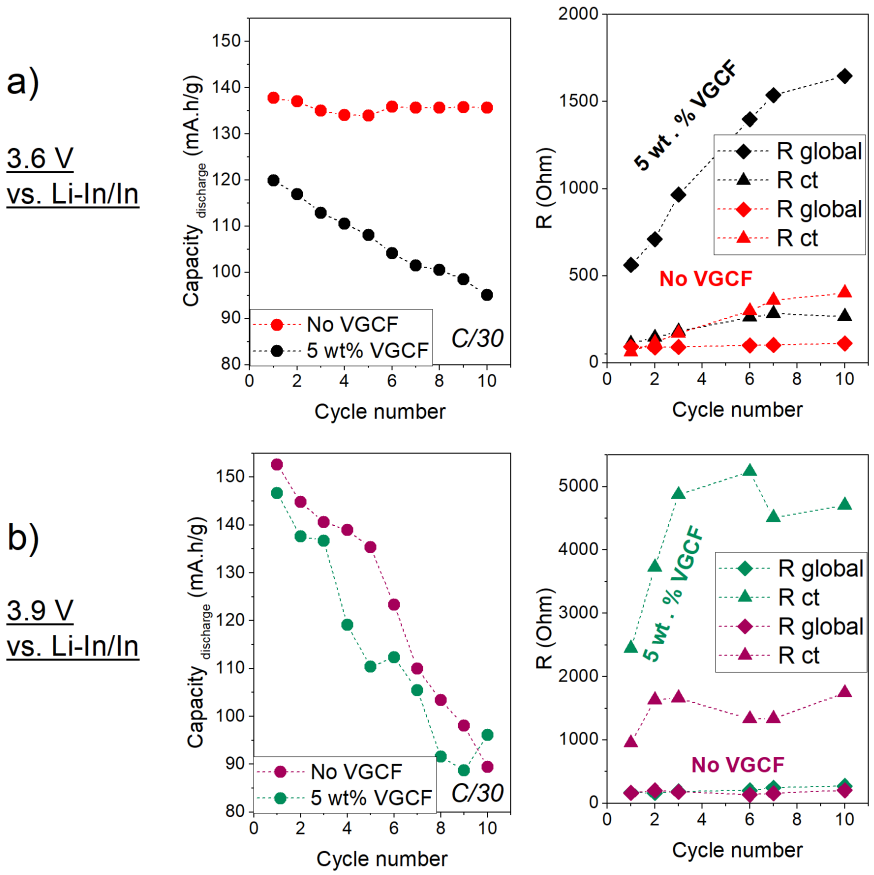

Figure 2.11: Result of PEIS fitting. Results are presented for cells cycling (already shown in **Figure 2.10**) with cut-off potentials reaching 3.6 V vs. Li-In/In **(a)** and 3.9 V vs. Li-In/In **(b)** Galvanostatic cycling at C/30 of the three-electrode cells are shown, next to R_{Global} and R_{CT} evolution during the first 10 cycles, computed by PEIS fitting of the spectra. R_{Global} account for the global conduction resistance.

To extract $R_{Ion,\ composite}$ and $R_{Elec,\ composite}$ values from $R_{Global,\ conduction}$ evolution, we proceeded to compute their values prior cycling and after cycle 10, with the last one made on the same cells previously used in **Figure 2.10** and **2.11**.The evolution of both parameters is presented in **Figure 2.12**.

For this, two methodologies were applied to extract $R_{Ion,\ composite}$ and $R_{Elec,\ composite}$. Firstly, for **cycle 0** (pristine pellet) $R_{Elec,\ composite,\ cycle\ 0}$, is obtained from pellets DC conductivity

measurements, collected using 80 mg of composites and placing the pellets in between two carbon current collectors in two-electrode cells. Turning to $R_{Ion,\ composite,\ cycle\ 0}$, its values were obtained from PEIS measurements in three-electrode cells, using exactly the same methodology as in **Figure 2.4**. This procedure is schematically explained in **Figure 2.12.a**. For cycle 10, it is not possible to collect pellet from the cycled cell without breaking it. Thus, we developed another strategy to decorrelate $R_{Elec,\ composite,\ cycle\ 10}$ and $R_{Ion,\ composite,\ cycle\ 10}$. The cells undergoes different temperatures and spectra are collected between 0 °C and 30 °C. We assume that $R_{Elec,\ composite}$ is not dependent on temperature, and that $R_{Ion,\ composite}$ follows an Arrhenius law. It enables us to get a system of non-linear equations in function of temperature to optimize, as explained in **Figure 2.12.b** (for complete explanation on the method, see **Appendix 2.8**).

The resulting evolution of both parameters before cycling and after 10 cycles is depicted in **Figure 2.12.c**. This method reveals $R_{Ion,\ composite}$ to be the major contributor to the C-containing system's impedance rise in low potential window, growing from 200 to 2000 Ohm. In C-free system, $R_{Elec,\ composite}$ slightly rises with a minor increase of about 20-40 Ohm, while it remains below 1 Ohm in C-containing cells, which is not a surprise considering the large amount of VGCF used (5 wt. %). In the high potential window, minor changes of $R_{Ion,\ composite}$ and $R_{Elec,\ composite}$ are obtained. This is expected, considering that R_{CT} is the only parameter evolving in **Figure 2.11.b**. Those results reassert the distinct behaviours previously observed regarding the mixed effect of carbon additive and cut-off potential on Li_6PS_5Cl-based systems. On one hand the increasing charge transfer resistance when cycling up to 3.9 V, suggests a detrimental phenomenon originating from the active material interfaces with Li_6PS_5Cl or from the material degradation itself. On the other way, the increase of $R_{Ion,\ composite}$ in cells comprising VGCF and cycled up to 3.6 V, results from the VGCF/SE reactivity arising from SE decomposition.

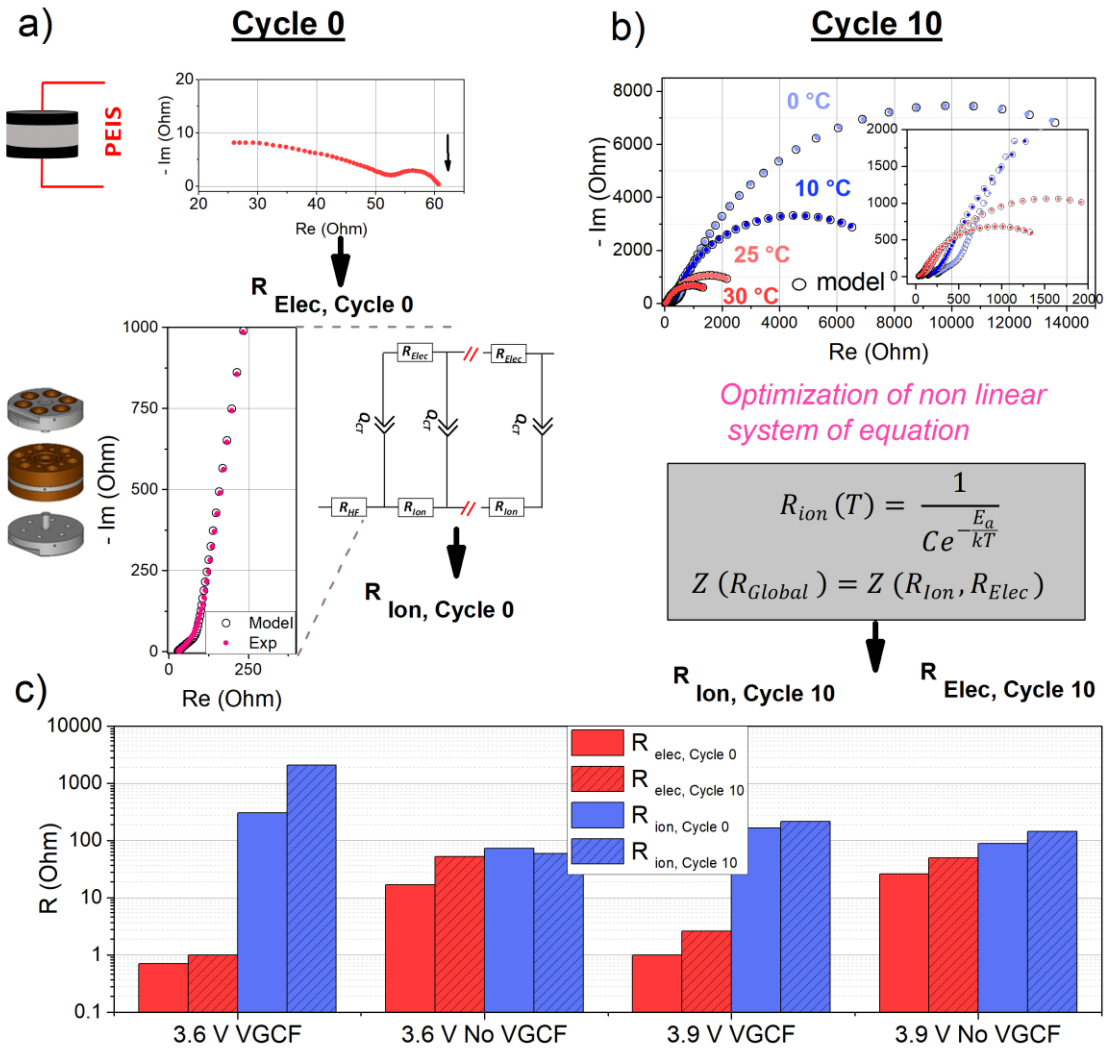

Figure 2.12: Decorrelation of $R_{Ion,\ composite}$ and $R_{Elec,\ composite}$ from $R_{Global,\ conduction}$ **(a)** Scheme of the fitting procedure to extract $R_{Elec,\ composite,\ cycle\ 0}$ and $R_{Ion,\ composite,\ cycle\ 0}$. **(b)** Scheme of the fitting procedure to extract $R_{Elec,\ composite,\ cycle\ 10}$ and $R_{Ion,\ composite,\ cycle\ 10}$ **(c)** Results of the fitting procedures comparing cycle 0 and 10 in log scale, on the cells presented in **Figure 2.10.** R_{Global} account for the global conduction resistance.

2.5 Conclusion

Altogether, the results presented in this section demonstrate a degradation mechanism of Li_6PS_5Cl in ASSB that is ruled by two interfaces, namely Li_6PS_5Cl/VGCF and Li_6PS_5Cl/AM (see **Figure 2.13**). Note that the first one, the intrinsic decomposition of Li_6PS_5Cl when put in contact with an electronic conductor, should also occurs versus the active material. However, we showed that such effect is minimized when using the C-free cells, as

mirrored by their high stability and small resistance increase (see **Figure 2.5**). When **cycled below 3.6 V vs. Li-In/In**, the main source of capacity fading originates from the SE/VGCF interfaces and yield to 10 % fading in 25 cycles when 5 wt. % VGCF is added. Moreover, the addition of VGCF is proven detrimental for the ionic conduction of the cathode prior cycling, when more than 2 wt. % is added. Such statements push the belief that small amount of carbon additive should be used for both high kinetics and stability. Going to **higher potential window** (3.9 V vs. Li-In/In cut-off potential), distinct behaviour are observed as the main degradation source shifts toward the SE/AM interfaces. This high potential reactivity yields to a building up strongly resistive interface around AM particles, resulting in 20-25 % capacity loss in 25 cycles. Surprisingly, no additional effect of VGCF is found is this potential window and this phenomenon will be further investigated in **Chapter IV**.

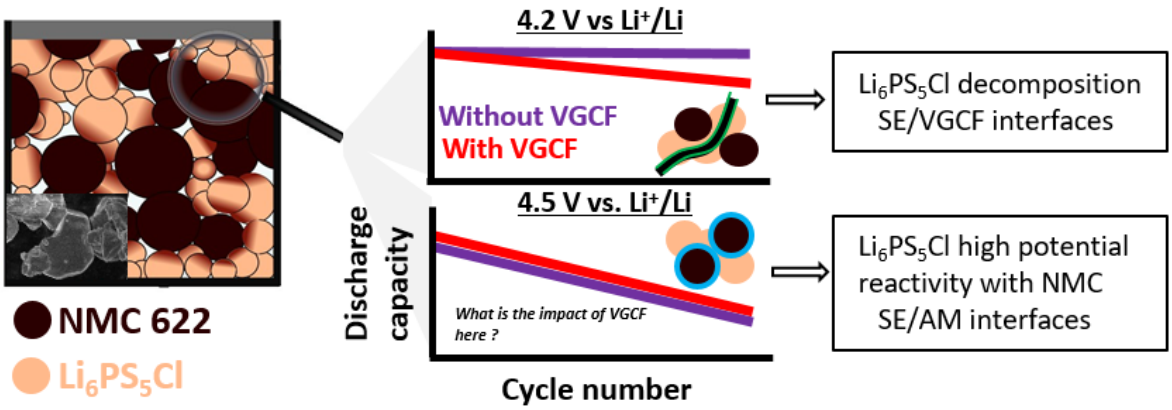

Figure 2.13: Global schematic of the distinct behaviour of NMC 622/Li_6PS_5Cl cathode composite as function of both VGCF presence and cut-off potential.

Toward the goal of higher stability and capacity, the next chapters will investigate how we can alleviate those instabilities, by focusing on two possibilities. Firstly, we will investigate the kinetics of C-free cells by focusing on the electronic conductivity evolution of composites, linked with particle size effect, percolation and phase transitions. Secondly, **Chapter IV** will investigate the impact on distinct parameters to try to negate both AM/SE high potential and VGCF/SE reactivity.

Chapter 3

In situ electronic conductivity of Li_6PS_5Cl based composites

Summary

This chapter includes the following publication:
Quemin, E.; Dugas, R.; Chaupatnaik, A.; Rousse, G.; Chometon, R.; Hennequart, B.; Tarascon, J. An Advanced Cell for Measuring In Situ Electronic Conductivity Evolutions in All-Solid-State Battery Composites. *Adv. Energy Mater.* **2023**, 2301105. https://doi.org/10.1002/aenm.202301105.

3.1 Introduction

As discussed in the preceding chapters, important polarization and transport resistances undermine sulphide-based ASSB performances, due to the distinct reactivities occurring at composites interfaces and unoptimized ionic and electronic percolation. Especially, the addition of carbon additives leads to a fast capacity decay when cells are cycled in the conventional potential window.

In order to investigate these issues and determine kinetic parameters, we propose a unique new device, enabling to track in situ the global variation of a composite electronic conductivity upon cycling. A composite's electronic evolution upon charge and discharge can reflect multi-scale phenomena that enlist inter- and intra-particle contacts, percolation and electronic band structure changes of the active material, among others[131–134]. Thus, we will explore these phenomena in a variety of composites based on lithium transition metal layered oxide materials ($LiCoO_2$, $LiNiO_2$, NMC622, NMC811, NMC111 and $LiNi_{0.9}Co_{0.1}O_2$ (NC9010)) and $Li_4Ti_5O_{12}$ (LTO) active materials. Especially, we investigate the effect of phase transitions, chemo mechanical Li driven process and particle size on the global electronic conductivity first cycle evolutions.

3.2 Validation and presentation of the device

3.2.1 Presentation of the cell

In our attempt to monitor electronic conductivity of ASSB composites upon cycling, we developed a new setup. This setup is based on the three-electrode cell configuration previously employed for performing PEIS measurements in last chapter. It relies on the use of two potentiostat channels connected to this cell, with one used for galvanostatic cycling and the other one for direct current (DC) conductivity measurements. To enable the measurement of direct current conductivity, a 60 µm thick aluminium mesh is positioned at the reference connection level, as illustrated in **Figure 3.1**. Regarding the assembly procedure, we utilize a trilayer configuration, wherein the cathode composite is initially pelletized to fit between the aluminium mesh and the upper piston. Additionally, to prevent any electrical short circuit, a large amount of cathode material (60-80 mg/cm²) is employed, the cell integrates 30 to 40 mg of Li_6PS_5Cl, and a large quantity (> 120 mg/cm²) of counter electrode composite is added as well. Lastly, the entire stack undergoes a compression force of 1 t/cm² during the cycling process, using similar procedure as for the two-electrode assembly.

Turning to the cycling protocol, it encompasses two channels. To ensure a good synchronization between those two, the trigger IN and trigger OUT of the channels are connected to one another. Moreover, to avoid any leakage current, the CE to GROUND connection is used for both channels. One channel enforces galvanostatic cycling, periodically halted at intervals of t1, followed by a relaxation period of t2 to ensure that the system reaches the equilibrium state. The second channel is utilized for measuring the DC electronic conductivity when the system is at equilibrium. A minor additional polarization for a duration of t3 is applied to attain a steady-state condition (refer to **Figure 3.2**) at which R_{Elec} is evaluated. Note that the value of the additional polarization allows a good signal-to-noise ratio and maintains system stability throughout the experimental procedure. Lastly, the data extracted from each channels are combined to form the resulting σ_{Elec} vs. lithiation state of the AM curves, by doing a thickness estimation to transform R_{Elec} in σ_{Elec}. This thickness is estimated via the average value of thickness per mass of composite, as measured on at least two pellet measurements per system. Additionally, 60 µm is subtracted to account for the aluminum mesh, as it is embedded in the cathode composite upon assembly.

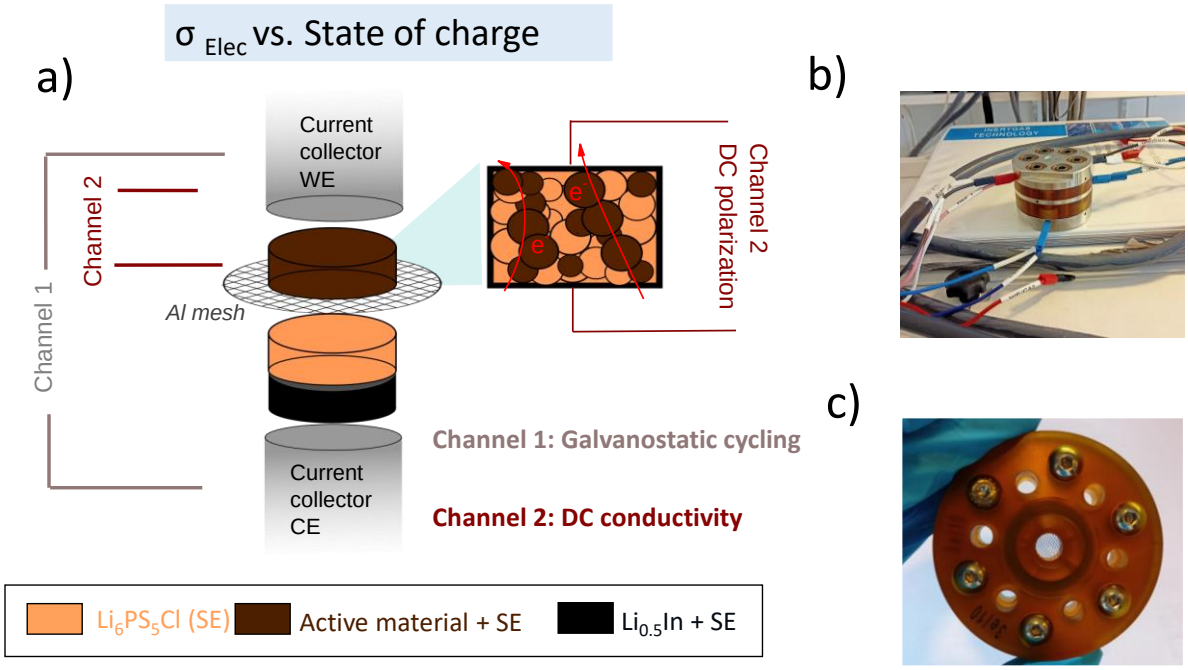

Figure 3.1. (a) Scheme of the in-situ electronic conductivity measurement upon cycling. **(b)** Picture of a cycling cell in CE to GROUND connection. **(c)** Picture of the cell body with the aluminium mesh placed inside.

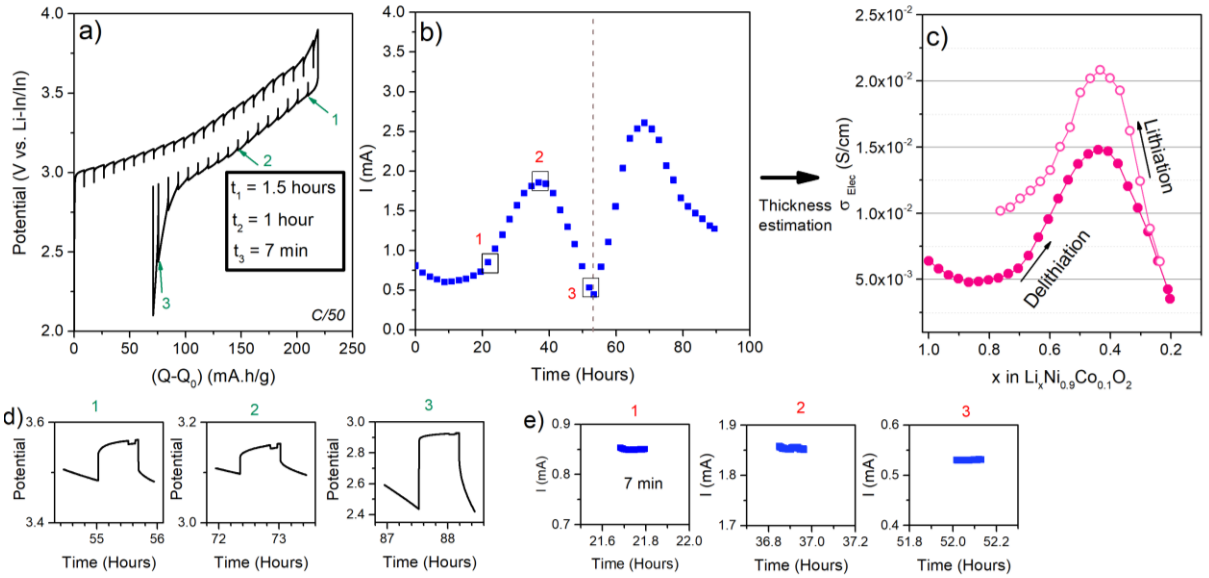

Figure 3.2. Presentation of the data treatment using $LiNi_{0.9}Co_{0.1}O_2$ composites as example **(a)** GITT-like curve obtained from channel 1 **(b)** Current versus time obtained from channel 2 **(c)** Resulting electronic conductivity vs. x curve. **(d), (e)** Insets showing specific DC polarization points in potential and current versus time. All current versus time points present a stable behaviour, with small fluctuation restricted to a range of merely 0.01 mA (which would only result in an insignificant deviation below 0.5% for points 1 to 3).

3.2.2 Accuracy and repeatability of the cell: a $LiCoO_2$ study

To illustrate the significance of this approach, our study focused on investigating the phase transitions occurring in a well-established material, specifically monolithic $LiCoO_2$ powders (provided by UMICORE) composed of primary particles ranging in size from 2-3 µm, which exhibit partial agglomeration into 10 µm particles as observed in scanning electron microscopy images (**Figure 3.3.a-b**). In order to conduct this investigation, $LiCoO_2$ was combined with Li_6PS_5Cl for both galvanostatic intermittent titration technique (GITT) and in situ direct current conductivity measurements, as shown in **Figure 3.3.c-f**, respectively performed in two-electrode and in situ conductivity cell setups. For the in situ conductivity measurements, galvanostatic cycling at a rate of C/50 was periodically interrupted every 1 hour and 30 minutes on channel 1, followed by a relaxation period of 1 hour. Subsequently, channel 2 was activated, imposing a potential step of 10 mV between the aluminum mesh and the upper piston for a duration of 7 minutes. This experimental procedure was repeated on three cells, demonstrating exceptional repeatability of the electronic conductivity evolution.

During the early stages of delithiation, when approximately 0.04 Li is removed from $LiCoO_2$, a remarkable increase in electronic conductivity is observed. This behaviour is attributed to a first-order Mott transition, which has been experimentally and theoretically validated[135,136]. The significant five orders of magnitude increase in conductivity is effectively captured by our in situ tool (**Figure 3.3.e**) and exhibits a similar magnitude as ex situ measurements conducted on delithiated LCO obtained from liquid cells. More precisely, we delithiated LCO powders in Swagelok cells, using the experimental procedure described in **Appendix 3.1**. The delithiated powders are further washed and dried, prior being mixed with Li_6PS_5Cl to take DC conductivity measurements in two-electrode cells. Following this metal-insulator transition, and in accordance with existing literature, a biphasic system ($0.75 < x < 0.96$) emerges, consisting of two end members, $Li_{0.75}CoO_2$ and $Li_{0.96}CoO_2$, exhibiting an O3 structure with distinct lattice parameters[137]. This gives rise to a characteristic bell-shaped variation in diffusion coefficients, as manifested by the evolution of the apparent diffusion coefficient, D_{App} (**Figure 3.3.c**). Such behaviour is commonly observed in biphasic insertion materials, such as $LiFePO_4$, for instance[138,139]. Subsequently, a solid solution behaviour is observed until $x = 0.4$, without any notable features in terms of electronic conductivity or apparent diffusion coefficient. Overall, the observed evolution aligns perfectly with the

reported phase transitions in LCO. More importantly, we have established the excellent repeatability and accuracy of our device (**Figure 3.3.d-f**).

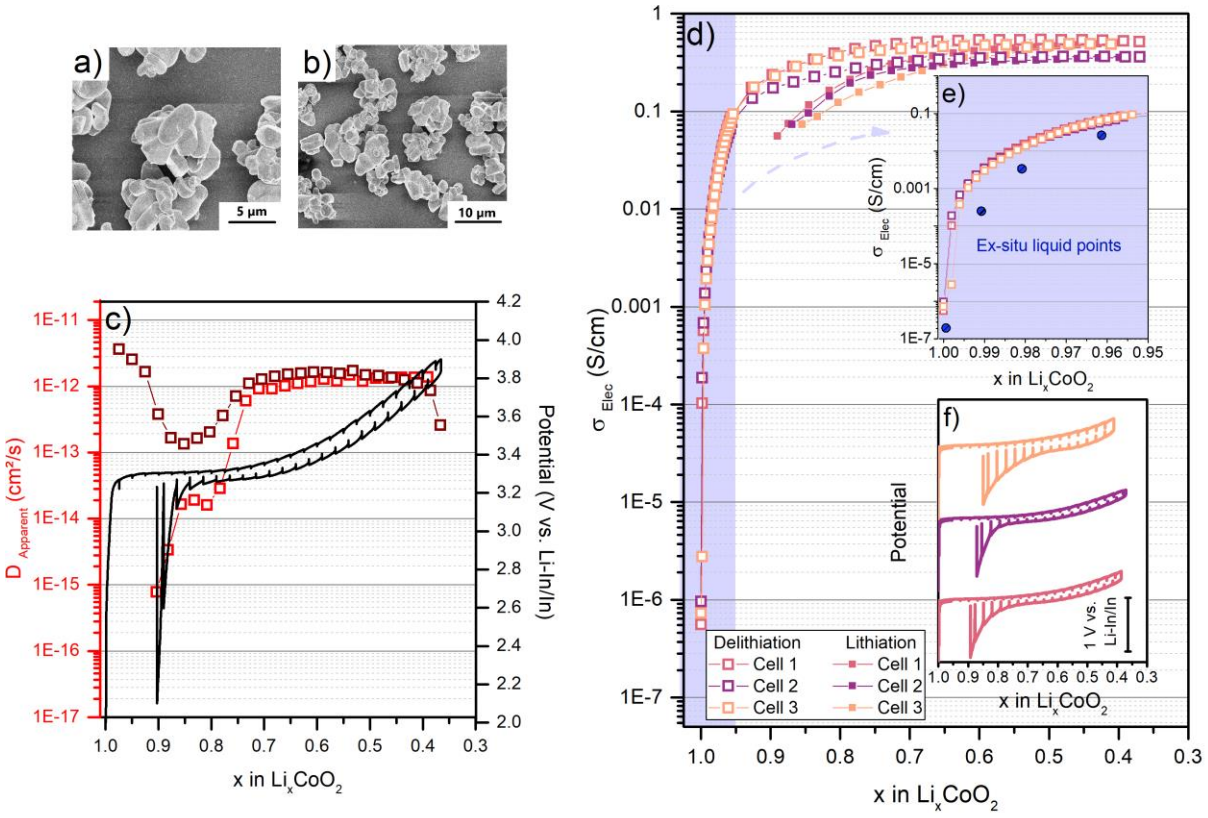

Figure 3.3 (a) (b) SEM images of LCO particles. **(c)** The apparent diffusion coefficient (D_{App}) and corresponding GITT curves of an LCO cell cycled in two-electrode setup (16-18 mg/cm²). **(d)** Evolution of electronic conductivity during first cycle of three cells. **(e)** Inset of electronic conductivity of LCO during early delithiation, with ex situ liquid points added as blue dots. **(f)** Galvanostatic cycling at C/50 of the cells used for monitoring electronic conductivity.

3.3 Chemo mechanical effect in TLMO-based composites

3.3.1 Active material vs. composites electronic conductivity

Following the successful demonstration of our proof of concept, our research subsequently shifted towards investigating more interesting active materials for solid-state research, specifically NMC 111, NMC 622, NMC 811, $LiNi_{0.9}Co_{0.1}O_2$, and $LiNiO_2$ (see **Appendix 3.2** for further details). To initiate this exploration, we interrogate the issue of electronic

percolation in ASSB composites. In order to accomplish this, we use Li_6PS_5Cl powder from NEI, possessing electronic conductivity in the range of approximately 10^{-9} to 10^{-10} S/cm[140,141] and exhibiting a significant dispersion in particle size (ranging from 1 to 50 µm, as illustrated in **Figure 3.4.a**). Li_6PS_5Cl is further mixed with the five targeted transition metal layered oxides, each possessing distinct particle sizes and morphologies (as observed in SEM micrographs depicted in **Figure 3.4.b-f**), in a weight ratio of 30/70 wt.%. The electrochemical performance of all the investigated composites, cycled for 15 cycles at a rate of C/10, is presented in **Figure 3.4.g**. It is noteworthy that all the composites exhibit a consistently low and stable capacity ranging from 90 to 150 mA.h/g, depending on the composition of the sample. In contrast, all of these layered oxides demonstrate capacities exceeding 150 mA.h/g in liquid cells. This disparity can be attributed to the comparatively sluggish kinetics observed in the solid-state due to unoptimized percolation.

In order to investigate this hypothesis, a comparison was made between the electronic conductivities of composites consisting of Li_6PS_5Cl/TLMO (70/30 wt. %) and films composed of PTFE/TLMO (2/98 wt. %), prior any cycling. Triple measurements per point of DC conductivity measurements in two-electrode cells were taken. Then, the electronic conductivity values for both series, along with their corresponding standard deviations, are presented in **Figure 3.4.h**. The plain and striped coloured rectangles in the figure represent the argyrodite-based composites and PTFE films, respectively. Overall, the inclusion of Li_6PS_5Cl in the mixing process resulted in a significant reduction in conductivity, ranging from 5 to 100 times lower compared to PTFE/TLMO films. It should be noted that the conductivity values of the PTFE-based NMC films exhibit an expected increase with higher nickel content, as previously reported[142]. However, this trend is not observed in the Li_6PS_5Cl-based composites, where the argyrodite-based NMC 811 and NMC 622 composites only exhibit conductivities of 0.3 mS/cm and 0.8 mS/cm, respectively, in contrast to the values of 10 mS/cm and 5 mS/cm observed for the PTFE-based NMC 811 and NMC 622 films. These differences are likely attributable to particle size mismatch (as depicted in **Figure 3.4.a-f**), variations in packing density, surface properties, and porosities of the materials, all of which contribute to the overall electronic conductivity of the ASSB composites. These results point at the necessity to add carbon additive and to carefully optimize both particles sizes and AM/SE ratio, to reach the full performances of these AM.

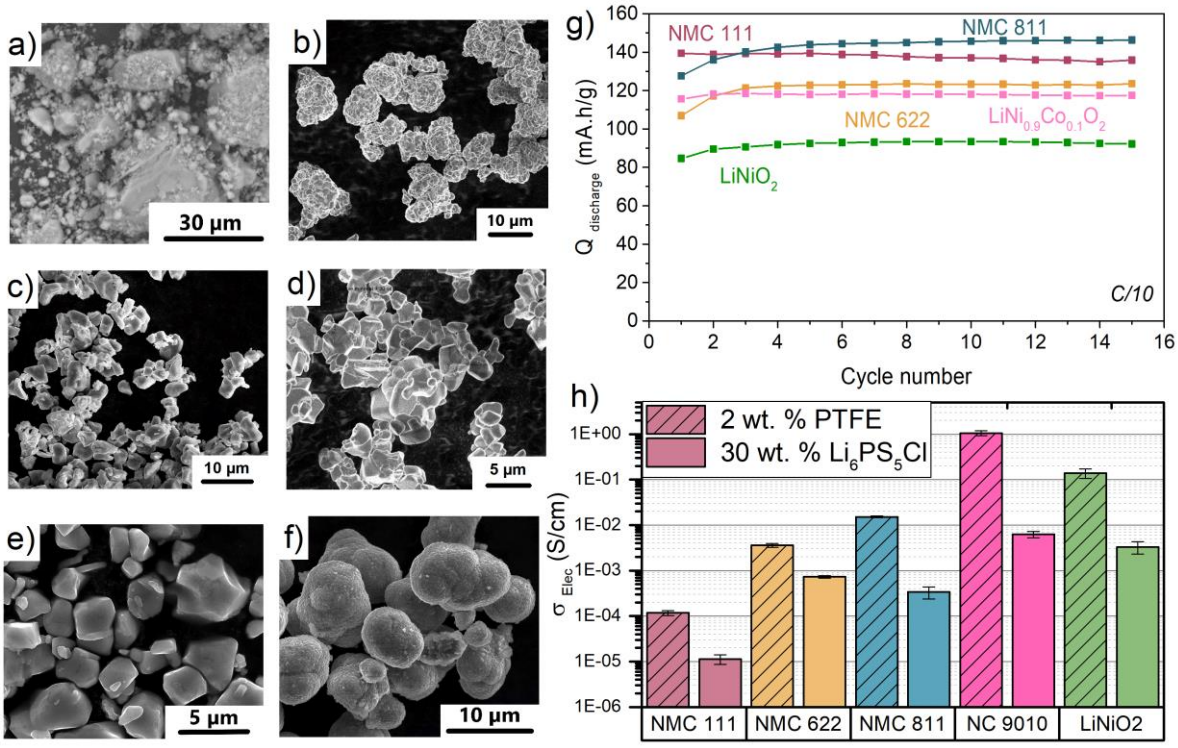

Figure 3.4: SEM micrographs of **(a)** Li_6PS_5Cl, and **(b)** NMC111, **(c)** NMC622, **(d)** NMC811, **(e)** NC9010 and **(f)** $LiNiO_2$.**(g)** Cycling performances of NMC111, NMC622 and NMC811, NC9010 and $LiNiO_2$ at C/10, in the [2.1 V- 4.5 V vs. Li^+/Li] potential window, and using a 70/30 wt. % active material/Li_6PS_5Cl ratio (first 15 first cycles are presented). **(h)** Electronic conductivity measurements of active material + 2 wt. % PTFE films at 1 t/cm² in 2-electrode setup and electronic conductivity measurements of active material + 30 wt. % Li_6PS_5Cl at 1 t/cm² prior cycling, in 2-electrode setup. Three cells are done for each measurements. The average and the standard deviation are represented.

3.3.2 First cycle evolution of five TLMO composites

To go even deeper, we monitored the first cycle electronic conductivity evolution in our five TLMO-based composites, by using our in situ setup. The electronic conductivity profiles are presented in **Figure 3.5**, while exemplary corresponding potential versus capacity curves can be found in **Appendix 3.3**. It should be emphasized that the initial electronic conductivity values depicted in **Figure 3.5** align closely with our prior findings (**Figure 3.4.h**).

For the majority of TLMO compounds, namely NMC 622, NMC 811, NC 9010, and $LiNiO_2$, the electronic conductivity exhibits slight variations in the early stage of lithium removal, prior to displaying a distinct bell-shaped evolution upon further delithiation.

Interestingly, this behaviour is absent in the NMC 111 composite, which instead demonstrates a significant increase in conductivity when x < 0.5, surpassing the electronic conductivity values of NMC 622 and NMC 811 at the end of the charge cycle (**Figure 3.5.f**). The observed rise in electronic conductivity (σ_{Elec}) of NMC particles can be attributed to the presence of Ni^{3+}/Ni^{4+} valence states, as previously reported through experimental and computational studies[130,132,142,143]. However, the subsequent decrease in conductivity at higher levels of lithium removal for high Ni-content TLMO composites represents a novel observation in our knowledge. Especially, it can even lead to values of σ_{Elec} lower than the initial measurement at Li content x = 1, such as for NMC 811.

To understand this intriguing phenomenon, we investigated the influence of AM morphology and phase transitions. Firstly, the polylithic nature of NMC 111 cannot explain this effect, as this decline in conductivity is also occurring in polylithic NMC 622, using particles of similar sizes (see **Appendix 3.4**). Secondly, to explore the potential influence of structural phase transitions, the present study employed Galvanostatic Intermittent Titration Technique measurements on NMC 111 and NMC 811 samples (refer to **Appendix 3.5**). The GITT profile of NMC 811 at a high state of charge exhibited a notable reduction in the diffusion coefficient, indicating the occurrence of the H2-H3 transformation as reported in existing literature[144–146]. This transformation is known to be accompanied by a decrease in the *c* lattice parameter[137,147,148]. In contrast, the observed phenomenon was less pronounced in NMC 111, suggesting that the decline in electronic evolution for phases with high nickel content at high state of charge may be attributed to this phenomenon. Indeed, the chemo-mechanical Li driven effect, which origin lies in the *c* lattice parameter collapse, is largely increased with higher Ni content. To test the hypothesis of a chemo-mechanical origin, the electronic conductivity of NMC 811 was examined using in situ and ex situ measurements in liquid cells (see **Figure 3.6**). Detailed explanation on the procedures are described in **Appendix 3.6**. Neither approach indicated a decrease in electronic conductivity during the delithiation process. On the contrary, they demonstrate a continuous increase of electronic conductivity, thereby confirming that the loss of electronic contact is associated with a mechanical effect occurring in solid-state, which competes with the influence of Ni^{3+}/Ni^{4+} valence states. Thus, this behaviour arises from substantial inter particle contact loss when NMC undergoes volumetric shrinkage. This is significantly amplified in the solid-state configuration due to the

high porosity of the composites and the limited ductility of the Li_6PS_5Cl solid electrolyte. This behaviour persists and is reversible throughout subsequent cycles, as demonstrated in cells based on NC 9010 and NMC 622 (see **Figure 3.7**). Overall, considering the critical importance of mechanical integrity in all-solid-state batteries, the ability to qualitatively monitor contact loss provides a valuable advantage for future optimization.

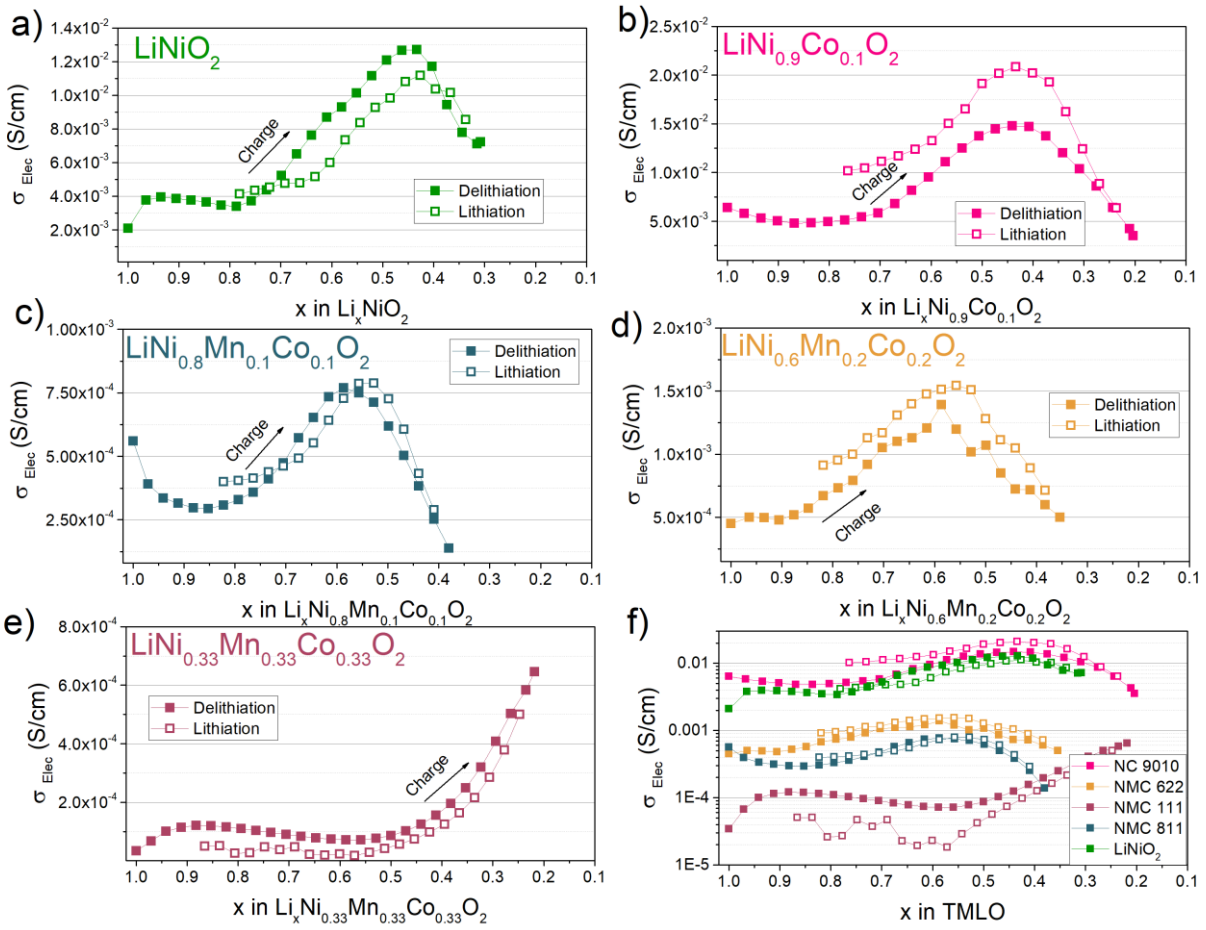

Figure 3.5: Electronic conductivity measurements during first cycle of **(a)** $LiNiO_2$ **(b)** NC 9010 **(c)** NMC 811 **(d)** NMC 622 and **(e)** NMC 111, when mixed with 30 wt. % Li_6PS_5Cl. Galvanostatic cycling is made at C/50 (loading of ~70 mg/cm²), every 1.5 h a point of conductivity is taken after 1 h relaxation. [2.1-4.5 V vs. Li^+/Li] potential window is used. **(f)** Overall dataset represented in logarithm scale.

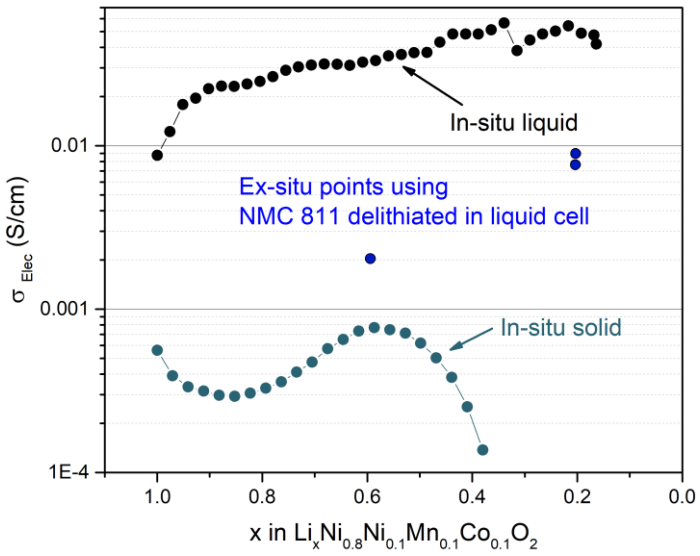

Figure 3.6: Comparison between the *in situ* and *ex situ* electronic monitoring in liquid or solid-state cells. For liquid *in situ* monitoring (black curve), It uses the three-electrode cell from EL CELL company, using a similar setup as in our advanced solid-state cell. NMC 811 with 1 wt. % PTFE film is used as cathode, and LP30 as electrolyte. For the *in situ* solid-state monitoring (dark green curve), we used our usual setup in the advanced cell, with NMC 811 mixed with 30 wt. % Li_6PS_5Cl as cathode composite. For the *ex situ* measurements (blue points), 80-100 mg of NMC 811 is delithiated in Swagelok liquid cells, further washed with DMC and dried. The resulting powder is mixed with 30 wt. % Li_6PS_5Cl and pelletized, to be embedded in a routine cell for DC conductivity points.

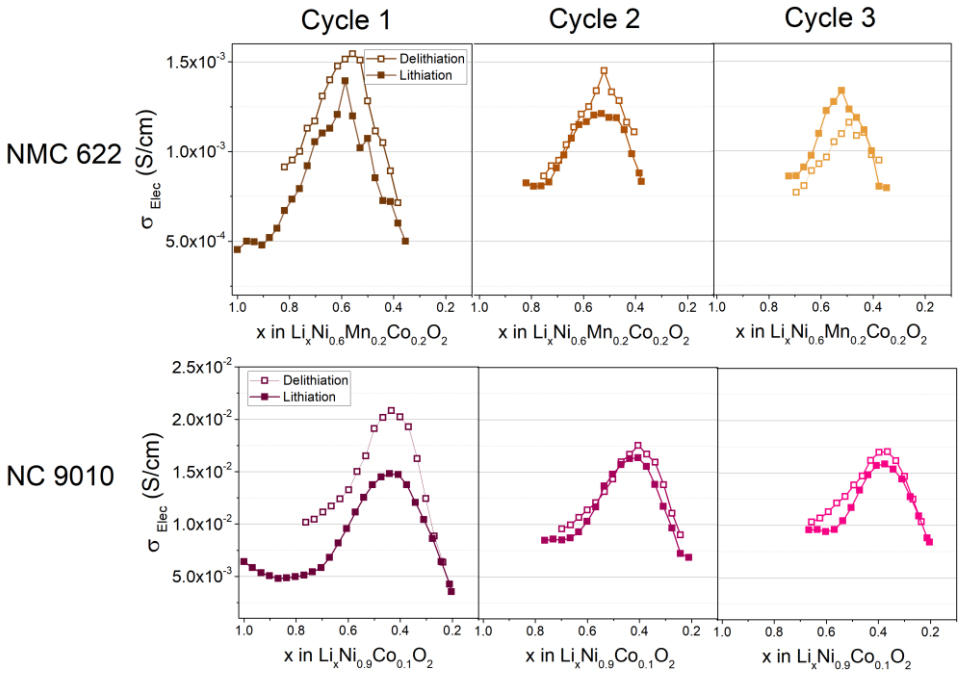

Figure 3.7: First three cycles with electronic conductivity evolution of a) NMC 622 and b) NC 9010.

3.4 Particle size impact on $Li_4Ti_5O_{12}$ composites electronic conductivity

To delve further into the morphology and particle size impact on first cycle electronic conductivity, solid-state and solution-combustion lithium titanium oxide powders were synthesized using established experimental procedures available in the literature. This material was chosen for its original electronic property of a metal-insulator transition in early lithiation, and for its zero-strain ability, enabling us to suppress the chemo-mechanical effect studied in previous section.

3.4.1 AM synthesis and characterization

For the in-house LTO **solid-state synthesis**, TiO_2 (Sigma, purity ≥ 99%) and Li_2CO_3 (5% excess, refer to **Figure 3.8** for optimization of precursor amount) (Sigma, purity ≥ 99%) were combined in stoichiometric quantities. The mixture was manually ground for 10 minutes using an agate mortar, followed by pelletization. Subsequently, the pellets were subjected to a heat treatment at a temperature of 900 °C for a duration of 2 hours with a heating rate of 5°C/min. In some instances, an additional round of manual grinding and heat treatment under similar conditions was performed to minimize the presence of any impurities.

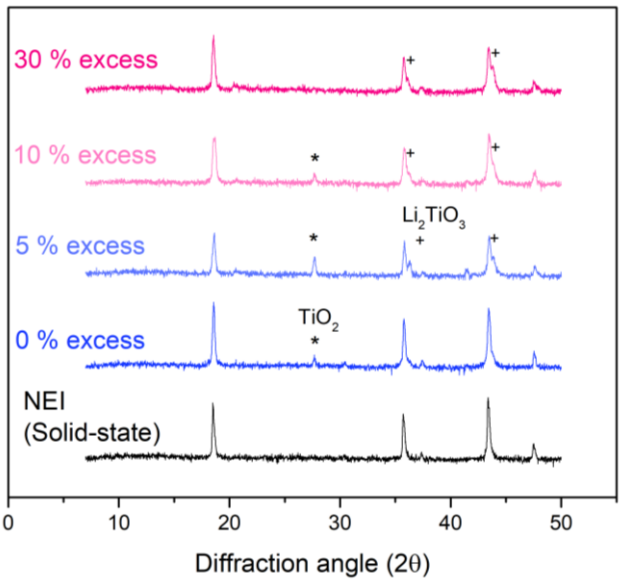

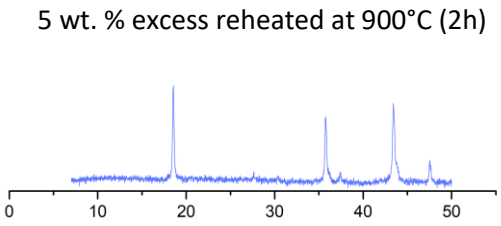

Figure 3.8: XRD diffractograms of LTO made by solid-state synthesis. **(a)** Different excess ratio of Li_2CO_3 are tried to diminish impurities, the hand-grinded and further pelletized pellets are put for 2h at 900°C (5°C/min) **(b)** XRD diffractogram of the 5 % excess sample, re hand-grinded and pelletized for a second heat treatment for 2h at 900°C (5°C/min).

The LTO **solution-combustion** homemade samples were synthesized using a previously reported self-combustion method[149]. Anhydrous lithium nitrate (10 % excess, refer to **Figure 3.9** for precursor optimization) (Alfa, purity 99 %) and titanyl nitrate ($TiO(NO_3)_2$) were employed as oxidizers (O), while glycine (NH_2CH_2COOH) served as the fuel (F) in a 1:1 O/F ratio. For each synthesis, the $TiO(NO_3)_2$ oxidizer was freshly prepared by combining 3 ml of titanium isopropoxide ($C_{12}H_{28}O_4Ti$, Alfa, purity 97 %+) with 9 ml of isopropyl alcohol under ice-cold conditions. Subsequently, 3 ml of a mixture containing 1:1 v/v HNO_3 diluted with deionized water was added while stirring. The resulting combustion ash was divided into four batches, three of which underwent different heat treatment durations (t0 = 0 h, t1 = 15 hours, t2 = 48 hours, t3 = 95 hours) at a temperature of 900 °C with a heating rate of 5 °C/min to achieve distinct particle sizes. X-ray diffraction patterns of the four samples are illustrated in **Figure 3.10.a-b**, and Rietveld refinements can be found in the **Appendix 3.7**. Regardless of the thermal treatment, all samples exhibited a single phase, except for the 0 hour LTO sample which contained a small quantity of rutile TiO_2 (2.5 (2) wt. %) (refer to the **Appendix 3.7** for details).

The four samples examined in this study exhibit an identical cubic lattice parameter, indicating their identical chemical composition. The peak profiles of these samples exhibit broadening, which can be attributed to microstructural effects and microstrain, as determined through Rietveld refinements. Williamson-Hall plots, presented in the **Appendix 3.8**, provide a clear representation of the evolution of sizes (intercept) and microstrain (slope). The analysis revealed a calculated crystallite size of approximately 96 (6) nm, along with some microstrain ($\varepsilon = 0.7784\ (6) \times 10^{-4}$), for the non-annealed LTO sample (0 hours at 900°C). On the other hand, the samples annealed for longer durations at 900°C showed crystallite sizes ranging from 145 (13) to 183 (12) nm, with no broadening due to microstrain. Scanning electron microscopy images of the four LTO samples (**Figure 3.10.c-n**) exhibit various morphologies. The non-annealed LTO sample (0 hours at 900°C) consists of primary particles with a size of

approximately 300 nm (**Figure 3.10.c, g, h**). With increasing annealing time at 900°C, a coarsening of the primary grains is observed, with the largest grains exceeding 3 µm for the sample annealed for 95 hours (**Figure 3.10.f, m, n**). To further analyse the secondary particle size, an Accusizer employing single-particle optical sizing was utilized, revealing that large agglomerates (see **Appendix 3.9** for further details) define a majority of the powder volume. Interestingly, longer heating times result in sintering of the larger agglomerates, leading to a shift in particle size from the range of 100-500 µm to the range of 10-70 µm.

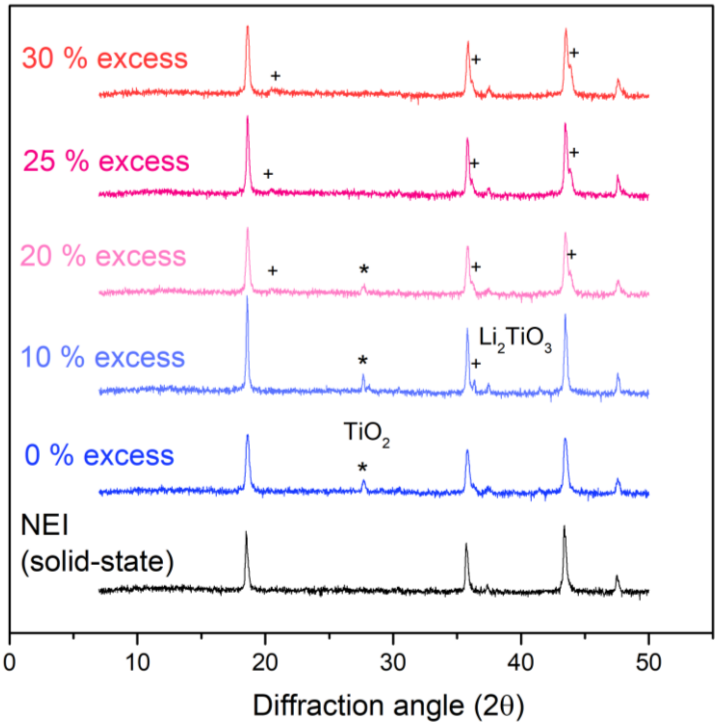

Figure 3.9: XRD diffractograms of LTO made by solution-combustion synthesis. Different excess ratio of Lithium additive are tried to diminish impurities.

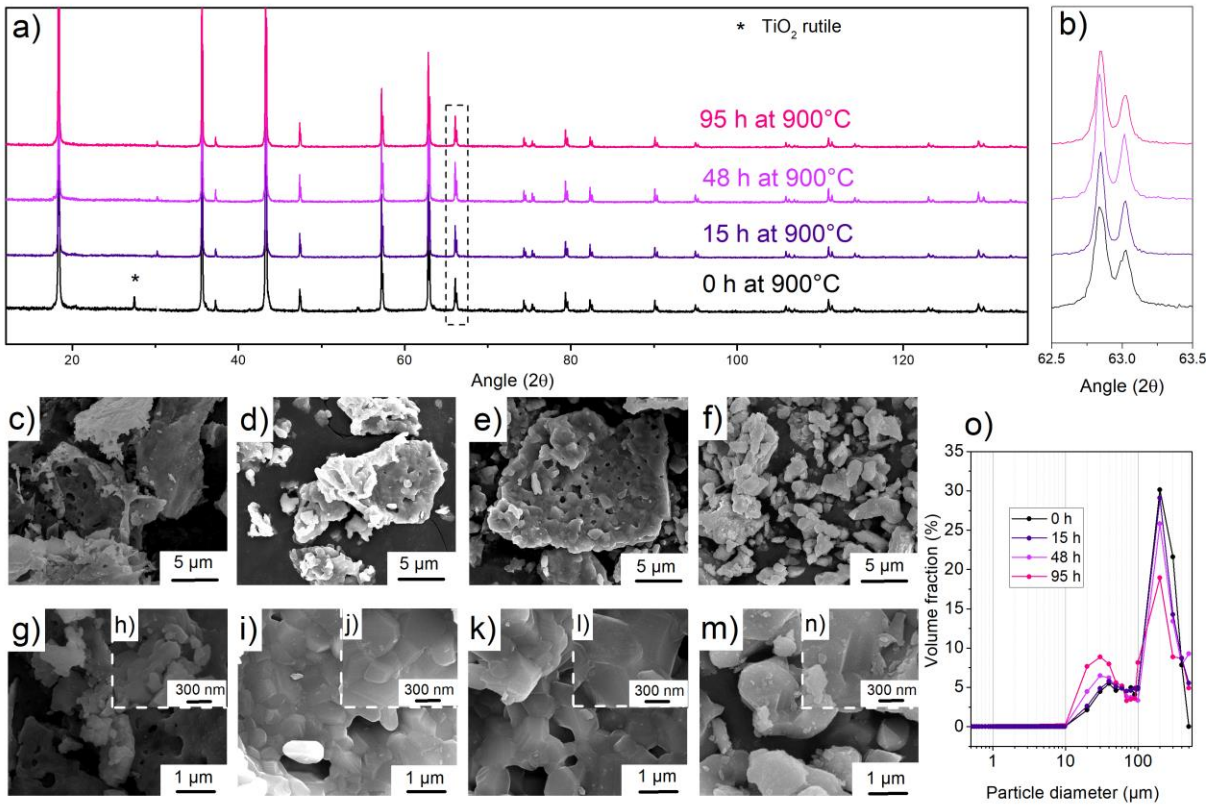

Figure 3.10: **a)** XRD powder patterns (λ_{Cu}) of the four active materials **(b)** Zoom of the XRD patterns around the (440) peak. (**c)-(n)** SEM images of the 0 h, 15 h, 48 h and 95 h solution-combustion LTO materials, depicted from left to right, at 10000, 40000 and 160000 magnification. **(o)** Average among three measurements of particles dispersion between 500 nm and 500 µm, represented in volume fraction (%).The volume fraction is obtained assuming spherical particles.

3.4.2 First cycle electronic conductivity evolution

Initially, we conducted a comparison between LTO powders obtained from NEI and synthesized in-house via solid-state synthesis. The NEI LTO powder consisted of 20 µm spherical agglomerates composed of primary particles smaller than 100 nm, whereas the in-house synthesized LTO powder comprised platelet particles measuring 2-4 µm in size. Both powders exhibited a relatively low capacity during the first cycle when utilized in solid-state batteries, despite optimizing the active material-to-solid electrolyte ratio (refer to the **Appendix 3.10** for details). The electronic behaviour of these powders (illustrated in **Figure 3.11**) revealed a rapid metal-insulator transition during the initial lithiation stage (a four/five-

order magnitude increase for 0.25 Li inserted in NEI LTO). This transition was followed by a gradual increase in conductivity with further lithium insertion. Although the NEI LTO product displayed lower utilization of the active material, it ultimately exhibited the highest conductivity at the end of the lithiation process. This finding raises questions regarding the influence of particle sizes and morphology on electronic transport.

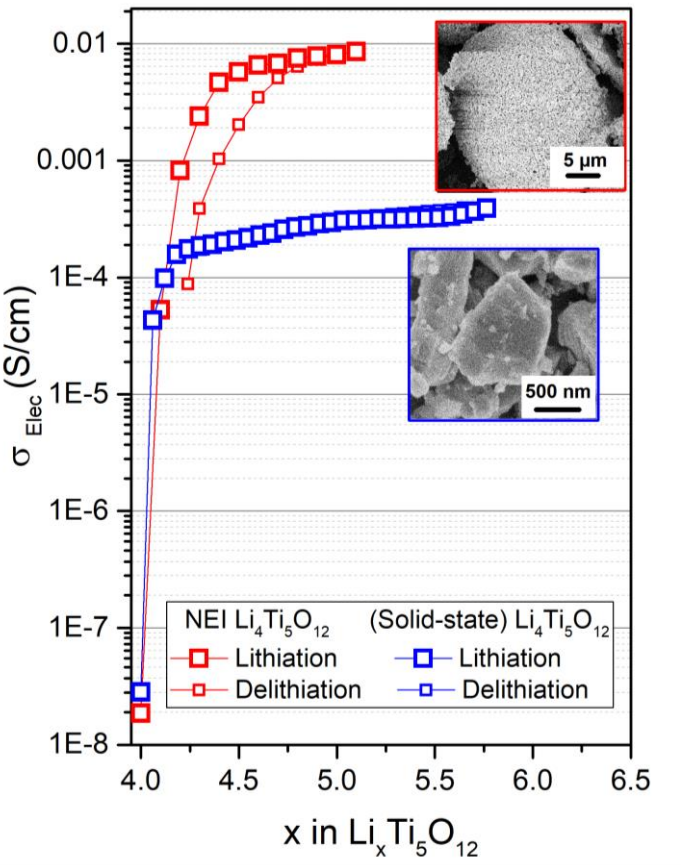

Figure 3.11: Electronic conductivity evolution during first cycle of NEI (60/40 wt.%) and solid-state homemade LTO (70/30 wt.%). Their morphology is depicted with SEM pictures.

To investigate this phenomenon further, we utilized the four LTO samples synthesized through solution-combustion, which exhibit distinct primary and secondary particle sizes as discussed in the previous section. Solid-state batteries were built using these different LTO samples, mixed with 50 wt. % Li_6PS_5Cl as the positive electrode composite. These batteries were initially subjected to cycling tests in standard cells at a rate of C/10 (1C corresponds to 3 moles of Li per mole of active material in 1 hour). The first cycle results revealed reversible capacities that decreased as the duration of the annealing step increased

(refer to the **Appendix 3.11** for detailed). Furthermore, additional charge-discharge tests were conducted on the aforementioned composites at various C-rates, ranging from C/10 to 2C. Notably, the LTO sample synthesized with a 0-hour annealing time demonstrated the highest power rate performance among the tested composites (see **Figure 3.12**).

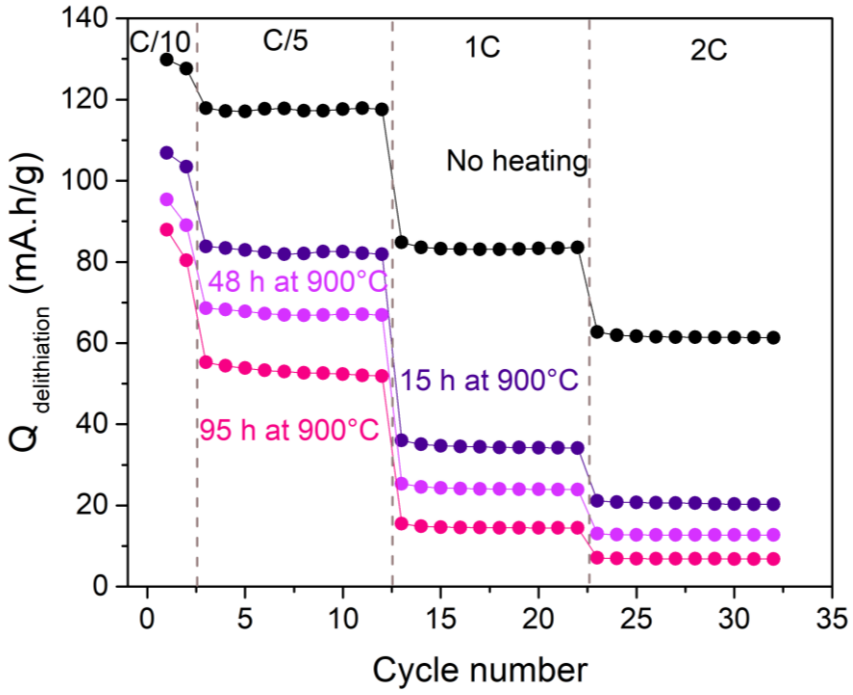

Figure 3.12: C rate tests with the four solution-combustion LTO (0 h, 15 h, 48 h, 95 h at 900°C) mixed with 50 wt. % argyrodite. Cycling is done from C/10 to 2C in two-electrode setup, using $Li_{0.8}In$ + Li_6PS_5Cl (60/40 wt. %) as counter electrode.

To investigate the superior kinetics observed in the unheated LTO sample, we examined the evolutions of electronic conductivity during the first cycle at a rate of C/30 in our advanced cell and for the four composites (see **Figure 3.13**). The nice repeatability and accuracy of the LTO systems were evaluated and are presented in the **Appendix 3.12**, with 48h LTO serving as an exemplary composite. Notably, all the solution-combustion materials demonstrated a rapid increase in electronic conductivity during the early delithiation stage, with conductivity increasing by 10^4 to 10^5 when 0.3 Li was added. Within the range of x = 4.3 to 5 in $Li_xTi_5O_{12}$, all composites exhibited a consistent trend in electronic conductivity before displaying dispersion beyond x = 5 lithium content. In this lithiated state (x > 5 Li), the composite synthesized with 0 hour annealing exhibited the fastest increase in conductivity, while the composite subjected to 95 hour heating displayed the slowest evolution, reaching a

conductivity ten times lower than the former at the end of lithiation. This "two-slope" conductivity evolution above 4.3 Li was observed consistently during cycling and at higher C-rates, as demonstrated in the **Appendix 3.13**. These findings suggest the presence of two distinct particle populations with differing kinetics.

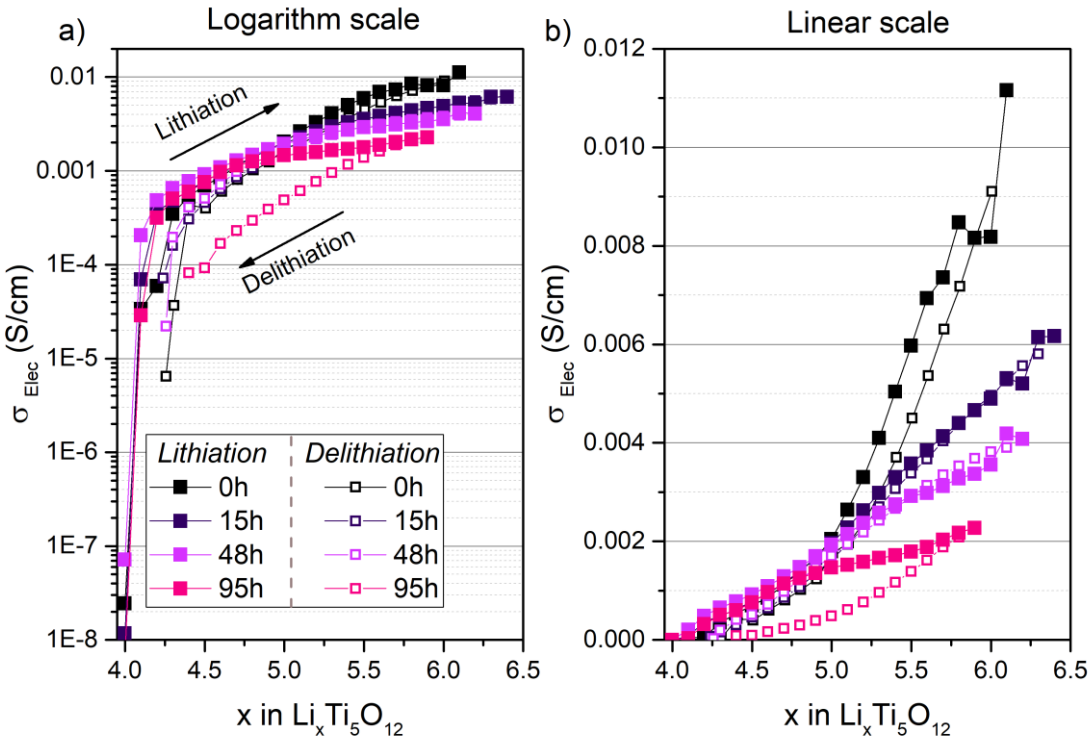

Figure 3.13: **(a)** Electronic evolution of the 0 h, 15 h, 48 h and 95 h solution-combustion LTO mixed with 50 wt. % Li_6PS_5Cl. Galvanostatic cycling is done at C/30, a point of conductivity is made every 1 hour and after 1 hour relaxation, and represented in a logarithm scale. **(b)** Linear scale of the electronic conductivity points between 0-0.012 S/cm.

To explore this hypothesis, the unheated LTO powder was divided into four different size ranges through sieving: > 20 µm, 10 - 20 µm, 5 - 10 µm, and < 5 µm. The electronic conductivities of these size-separated LTO composites were monitored (**Figure 3.14.a-b**). All composites exhibited similar trends in the evolution of σ_{Elec} as observed in **Figure 3.13.a-b**, except for the < 5 µm size batch, which exhibited deviations due to its lower utilization of active material. However, beyond the x = 5, slight variations in trends were observed among the different size batches. Notably, the larger agglomerates facilitated faster

electronic transport at the end of the lithiation process. Further C-rate tests from C/10 to 2C were conducted on these composites, confirming the superior kinetics of the larger agglomerates (**Figure 3.15**). This indicates that the electronic evolution of the composites at the end of lithiation is primarily influenced by the characteristics of the agglomerates rather than the size of the primary particles. Interestingly, an artefact was observed around 4.2 lithium for all the sieved systems. Although direct evidence is not yet available, it may arise from trace amounts of Ti^{3+} impurities, which could form insulative phases (e.g., Ti^{4+}) during the initial lithiation stage.

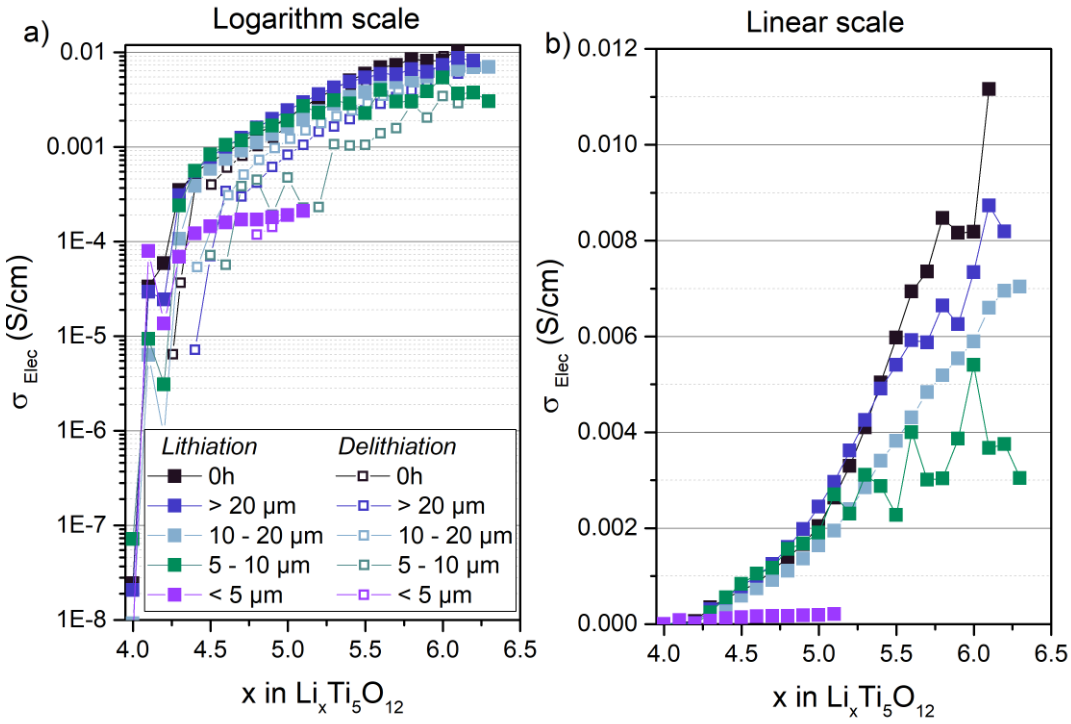

Figure 3.14: **(a)** Electronic evolution of the sieved 0 h solution-combustion LTO mixed with 50 wt. % Li_6PS_5Cl. The pristine composite is presented, as well as the > 20 µm, 10 - 20 µm, 5 - 10 µm and < 5 µm ones. Galvanostatic cycling is done at C/30, a point of conductivity is made every 1 h and after 30 minutes relaxation, and represented in logarithm scale. **(b)** Linear scale of the electronic conductivity points between 0-0.012 S/cm. For ease of interpretation, the delithiation points were removed.

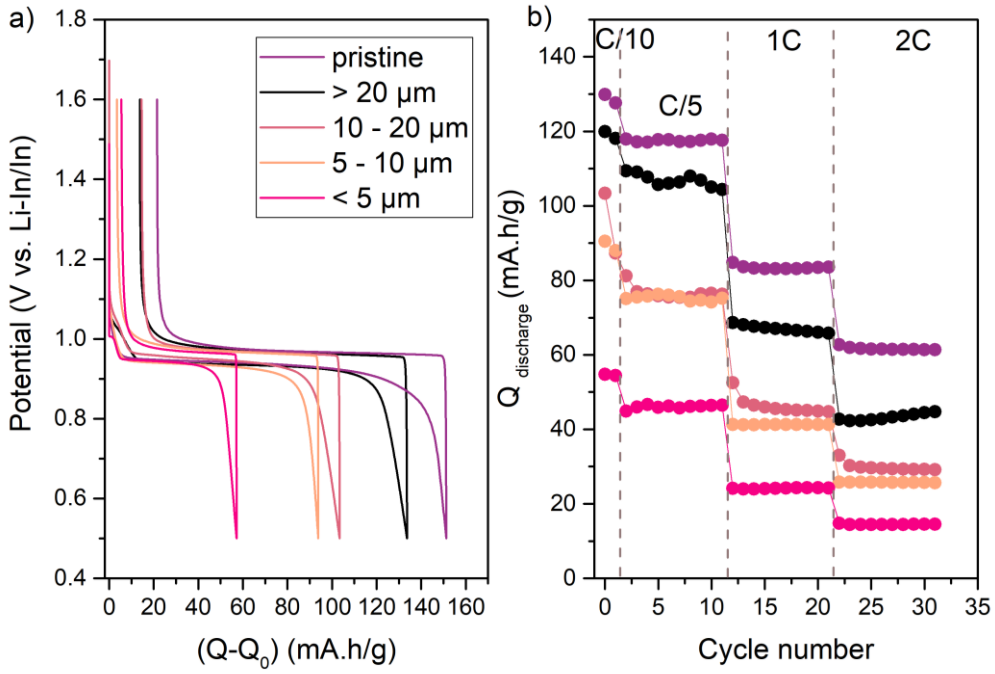

Figure 3.15: (a) First galvanostatic cycle of the sieved LTO (pristine, > 20 µm, 10-20 µm, 5-10 µm and < 5 µm) mixed with 50 wt. % Li_6PS_5Cl. Cycling is done at C/10 in two-electrode setup, using $Li_{0.8}In$ + Li_6PS_5Cl (60/40 wt. %) as counter electrode. **(b)** C rate tests.

Collectively, these findings demonstrate the influence of particle size on the electronic conductivity of LTO-based composites during lithium incorporation, with the larger agglomerates governing the composite's electronic conductivity at high lithium contents. This observation is somewhat counterintuitive, considering that dispersed mixtures generally enable higher active material utilization and faster kinetics due to improved percolation and enhanced surface interactions between ionic and electronic conductors. Surprisingly, composites with agglomerate sizes nearly ten times larger than most NEI Li_6PS_5Cl particles exhibit the highest electronic conductivity, suggesting a different trend in the electrode-electrolyte particle size ratio's effect on performances in LTO composites. These observations can be rationalized by considering the unique nature of the lithium reaction pathway in LTO and the mixing process of solid-state composites.

To begin with, it is important to note that lithium intercalation/deintercalation in LTO occurs via a two-phase reaction between $Li_4Ti_5O_{12}$ (an electronic insulator) and $Li_7Ti_5O_{12}$ (an electronic conductor) during the 1.5 V plateau, as the Ti d-states become partially filled

(e.g., Ti^{3+}) during lithiation[150]. However, the lithiation pathway in LTO has been a subject of controversy, resulting in various models (core-shell, radial, etc.) for phase transformation kinetics, with their validity dependent on the size, morphology, and concentration of Ti^{3+} [151–154]. In situ electron holography studies on liquid cells have described LTO nanoparticles as following a core-shell process within the narrow solid solution range at both ends of the plateau, which aligns with the rapid increase in electronic conductivity observed during early delithiation (as shown in **Figures 3.14 and 3.15**)[155]. Furthermore, using conductive Atomic Force Microscopy, it has been demonstrated that the evolution of electronic conduction pathways in thin film LTO follows a biphasic reaction that does not propagate laterally through grain boundaries or uniformly form across the material. Instead, it proceeds via percolation channels within individual grains[156]. This one-by-one filling of multiple particles emphasizes the significance of good inter-particle contact for the electronic propagation of the LTO phase, which is consistent with the larger agglomerates exhibiting higher efficiency in electronic motion within our systems. In other words, as conductive Li-rich and insulative Li-poor phases coexist, a Li-poor grain is filled when it is in close proximity to a Li-rich phase, following the path of lower resistance. Consequently, the lower tortuosity of the electron pathway in larger agglomerates results in higher electronic conductivity at the end of lithiation. This behaviour can be schematically represented as a function of particle size, as illustrated in **Figure 3.16**.

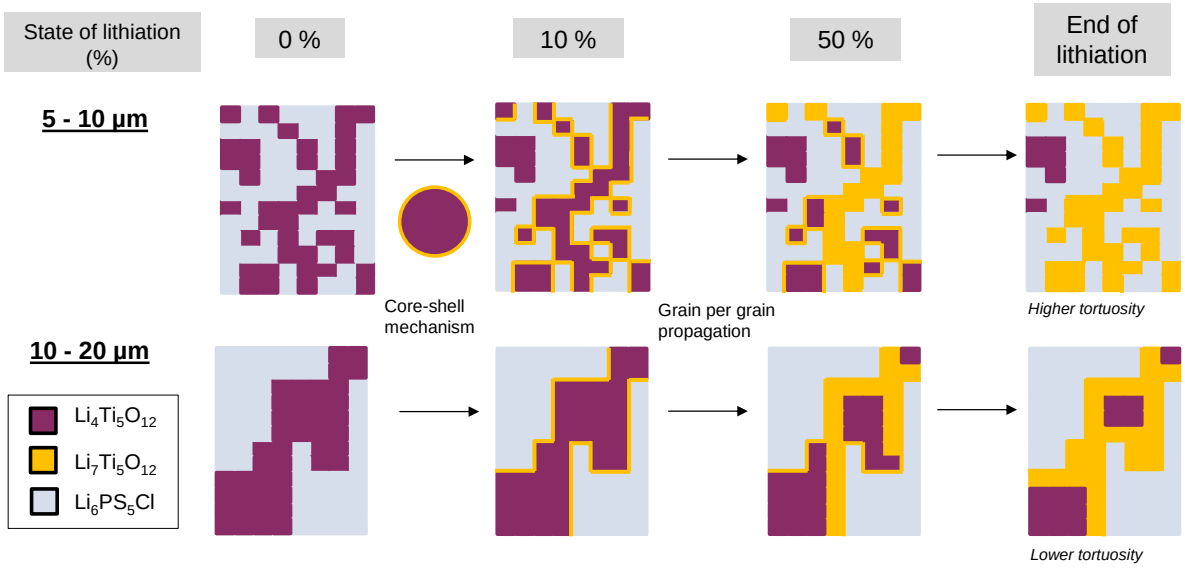

Figure 3.16: Proposed schematic of lithiation pathway in LTO composites

3.5 Conclusion

We have presented a novel homemade electrochemical cell that allows for in situ measurement of electronic conductivity of all-solid-state battery composites. This unique diagnostic tool is achieved by connecting two potentiostat channels to the same cell, providing convenient monitoring of electronic conductivity. The device combines two programs: one for galvanostatic cycling and the other for DC conductivity measurement. It can be easily assembled, maintains airtightness, and the presence of an aluminum mesh does not interfere with the cycling process. Furthermore, its simplicity and accuracy make it suitable for daily usage, providing valuable insights into the apparent electronic transport of composites.

To demonstrate its functionality, we successfully investigated the metal-insulator transition in $LiCoO_2$, which was further validated by ex situ liquid measurements. Additionally, we presented direct evidence of how this new cell can differentiate between the electronic properties of the active material and the overall electronic transport in three-dimensional solid-state mixtures. In essence, this cell paves the way for studying electronic transport in a wide range of cathode-solid electrolyte composites.

Furthermore, we have also chosen to demonstrate the benefit of our new cell to track changes in electronic transport associated with Li-driven chemo-mechanical changes of TLMO-based composites. Specifically, we observed a significant reduction at high SOC in electronic conductivity of composites containing high nickel content, as a result of pronounced volume changes driven by lithium insertion, notably associated with the well-known H2-H3 transition. Additionally, through an examination of the Li insertion process in zero-strain $Li_4Ti_5O_{12}$, we were able to monitor the insulator-metal transition during the initial lithiation of this compound. By using distinct LTO primary/secondary particle sizes, this investigation allowed us to gain insights into how electronic percolation is influenced by particle size and morphology, thereby providing valuable information regarding the intricate lithium reacting pathway.

Overall, numerous parameters influence the electronic conductivity of solid-state composites, including particle size and phase transitions. Especially, the usage of carbon-free high Ni-content NMC based composites is hindered by the high SOC decrease of electronic conductivity, pushing the belief that a minim amount of carbon additive could be highly

beneficial for C rate performances in such systems. The following chapter will explore this possibility, by taking the advantage of carbon additive while simultaneously mitigating the long-term capacity losses associated with carbon addition.

Chapter 4

Exploring high potential degradation of Li_6PS_5Cl based composites

Summary

4.1 Introduction

As we have seen in previous chapters, significant polarization and transport resistances compromise the performance of sulphide-based ASSB performances, due to the distinct reactivities occurring at composites interfaces. Of particular note is the marked drop in capacity observed with the introduction of carbon-based additives during standard cycling. However, considering the problems of Li-driven chemo mechanical loss of contact between particles occurring in high Ni-content NMC, and the lower AM utilization in C-free ASSB composites, the addition of carbon remains necessary provided that carbon-induced reactivities are managed. Thus, this chapter focuses on distinct ways to alleviate the long-term stability issues pertaining to C-containing composite, using 1.5 wt. % VGCF and a NMC 811 (MSE supplies) as standard AM. We also chose to cycle at up to 3.9 V vs. Li-In/In, as we found no additional detrimental effects of VGCF in this potential window (see **Chapter II**) while experiencing a greater capacity gain as compared to a conventional potential window cycling.

Thus, this chapter aims at briefly introducing some optimization work on the Li_6PS_5Cl/NMC811 + 1.5 wt. % VGCF composite, with a special interest on stability. For this, we firstly assessed the repeatability of our cycling on 9 cells originating from two NMC 622-based composites, prior switching to NMC 811. Then, we assessed the cycling behaviour of the NMC 811 composites as function of C-rate, cut-off potential and presence of carbon additive. Afterward, we explored the impact of distinct parameters on stability, namely the assembly pressure, the loading, the impact of SE and AM carbonate coating and formation cycles protocols. Finally, the different approaches are combined and the best composite/cycling protocol obtained is presented.

4.2 Cycling behaviour of high Ni-content NMC composites

4.2.1 Repeatability of cycling and cathode composite processing

Prior conducting any study on improving the stability of ASSB composites, we initiated an assessment of the repeatability of a specific composite consisting of NMC 622 (Umicore) and Li_6PS_5Cl in a weight ratio of 70/30, with the addition of 1.5 wt. % VGCF. Note that a new NMC 622 from Umicore was used as compared to the one from **Chapter II**, due to powder shortage. It displays the same particle size and morphology but a better stability, as demonstrated below.

Figure 4.1 illustrates the initial cycle at a C/10 rate in the [2.1-3.9 V vs. Li-In/In] potential window, for nine cells fabricated from two distinct composites, which were prepared through manual grinding. All cells exhibited excellent repeatability, especially for composite n°2. **Figure 4.2** presents the discharge capacity profiles of the aforementioned cells for a minimum of 80 cycles at a C/2 rate. Overall, the results demonstrate remarkable similarity across all nine cells. Note that the oscillations observed are linked to temperature changes over the days since the experiments were carried-out under non-thermostatic conditions. The average initial cycle capacity at C/10 is 168.1 mA.h/g, with a standard deviation of 2.7 mA.h/g. Subsequently, the second cycle at a C/2 rate yielded a capacity of 135.42 mA.h/g, accompanied by a standard deviation of 3.6 mA.h/g. Additionally, as highlighted in **Figure 4.3**, the capacity decay after 100 cycles was found to be 15.87 % and 15.71 % for composite 1 and 2, associated with a standard deviation of 0.53% and 0.44 %, respectively. Regardless of the slightly more dispersed dataset of composite n°1, our cell preparation process, including the manual grinding step, exhibited good reproducibility in terms of stability, as mirrored by the low standard deviation values. Notably, we can now discern what constitutes a statistically significant variance in the decrease capacity, which in this case is equivalent to around 1 % of the mean value of 15.78 %. Ideally, a larger dataset will enable us to achieve a statistically higher level of confidence in our analyses. However, in view of the practical problems we are facing, we will accept these values and only take into account deviation of more than 1.6 % in the following figures. Note, that we will consider this as the discrepancy associated with the repeatability of the assembly and processing, independently of the active material.

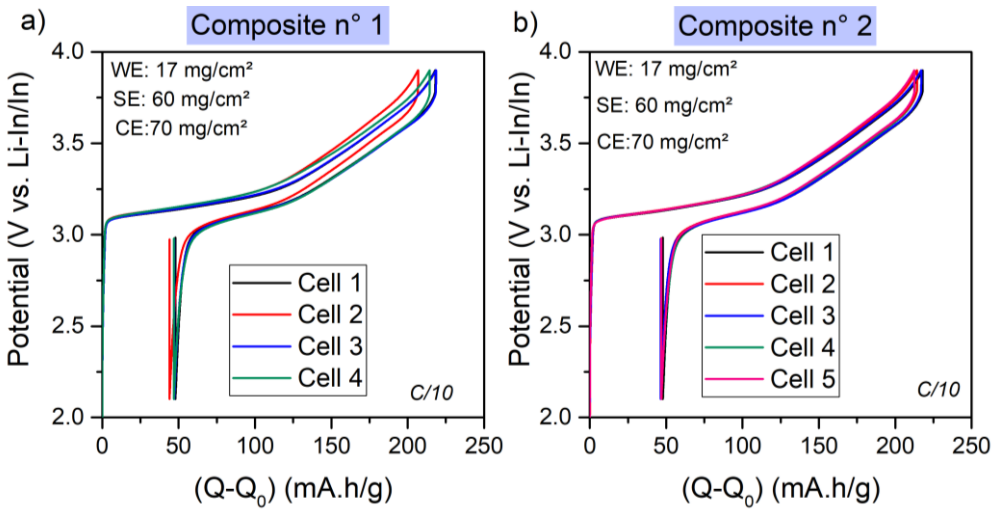

Figure 4.1: **(a)** First cycle of NMC 622 + Li_6PS_5Cl + 1.5 wt. % VGCF first composite prepared by hand grinding, at C/10 and on four different cells. Potential window is 2.1-3.9 V vs. Li-In/In. **(b)** Same experiment with a second composite prepared by hand grinding and on five different cells.

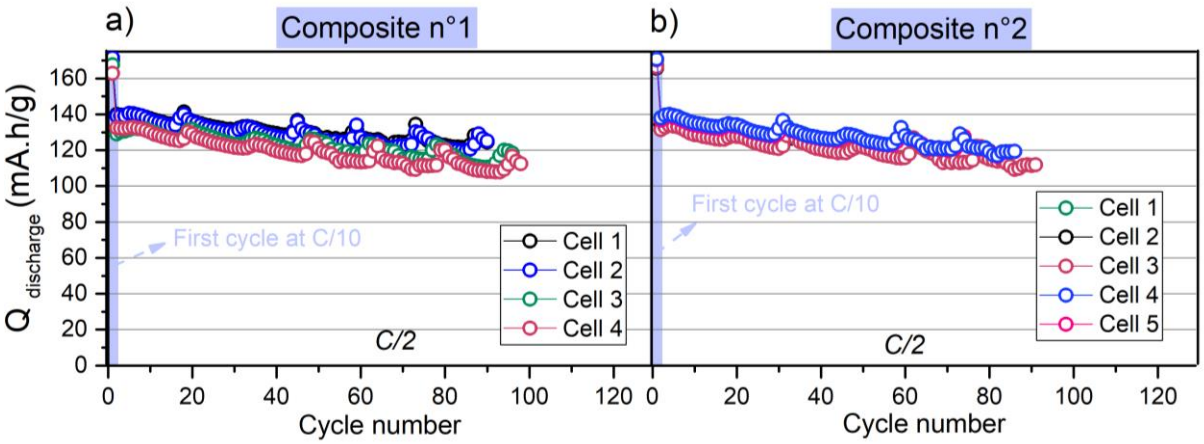

Figure 4.2: **(a)** Cycling performances of NMC 622 + Li_6PS_5Cl + 1.5 wt. % VGCF first composite prepared by hand grinding and on four different cells. The first cycle is made at C/10 while the following ones goes at C/2. Potential window is 2.1-3.9 V vs. Li-In/In. **(b)** Same experiment with a second composite prepared by hand grinding and on five different cells.

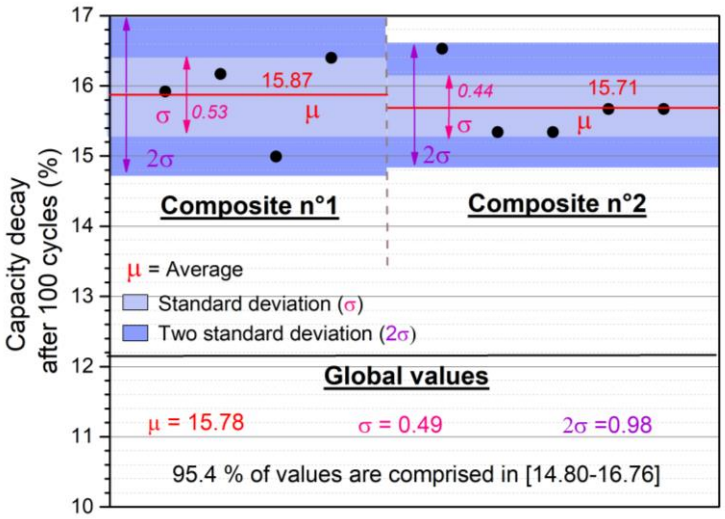

Figure 4.3: Average capacity loss estimated by linear extrapolation after 100 cycles at C/2 for the nine cells belonging to the two composites. one and two standard deviation areas are shown for each composites, and the global values of the nine cells are also written.

4.2.2. Shifting from NMC 622 to NMC 811: what does it imply?

In our quest for highly efficient cathode composites, we have made a transition from the reference NMC 622 monolithic material to a $LiNi_{0.83}Mn_{0.06}Co_{0.11}O_2$ (referred to as NMC 811) AM acquired from MSE Supplies Company. The latter material exhibits a monolithic morphology, with an average particle size of approximately 5 µm (refer to **Figure 4.4.a**). Additionally, it demonstrates a notable increase in first cycle capacity at C/10, reaching approximately 190 mA.h/g, as compared to the 168 mA.h/g capacity of NMC 622, within the potential window of [2.1 – 3.9 V vs. Li-In/In] (refer to **Figure 4.b**). In terms of C-rate capability, the NMC 811 composite containing carbon displays a remarkable capacity up to 170 mA.h/g at C/2 and 150 mA.h/g at 1C, while the C-free cell exhibits capacities of 150 mA.h/g and 125 mA.h/g at C/2 and 1C, respectively (refer to **Figure 4.4.c**). Based on these results, we decided to adopt the NMC 811 (MSE) + Li_6PS_5Cl (70/30 wt. % ratio) composite, with an additional 1.5 wt. % VGCF inclusion, as our new reference cathode composite.

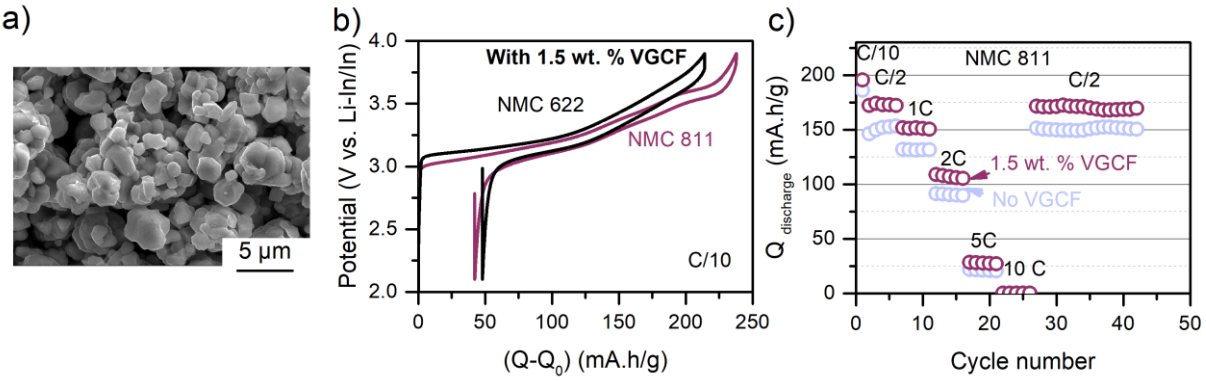

Figure 4.4: **(a)** SEM pictures of NMC 811 (MSE)**. (b)** First cycle at C/10 of both NMC 622 (Umicore) and NMC 811 (MSE) Li_6PS_5Cl composites, with 1.5 wt. % VGCF addition. **(c)** C-rate tests of NMC 811/Li_6PS_5Cl composite with 1.5 wt. % VGCF or without VGCF. The cathode loading is comprised between 16 and 18 mg/cm².

At this point, an investigation of the capacity retention characteristics of the NMC 811 composite becomes imperative, to ascertain whether this new composite exhibits comparable trends to those elucidated in **Chapter II** for NMC 622. Thus, we initiated a comprehensive study on the capacity retention of both NMC 622 and NMC 811 composites, considering varying C-rates (C/2 or C/10), cut-off potentials (3.6 or 3.9 V vs. Li-In/In), and the presence of VGCF (1.5 wt. % VGCF or no VGCF). Each experimental condition was replicated in two cells, leading to the cycling of 32 cells, and the resulting average capacity retention data are summarized in **Table 1**.

Several noteworthy conclusions can be drawn from this study. Firstly, it is evident that lower C-rates correspond to higher degradation. For instance, NMC 811 exhibits a decay of -12.5 % and -38 % in C-containing cells cycled at C/2 and C/10, respectively, and up to 3.9 V vs. Li-In/In (refer to **Figure 4.5.a**). Secondly, the introduction of VGCF has a perceptible negative impact on cells cycled up to 3.6 V vs. Li-In/In (as exemplified in **Figure 4.5.b**), whereas its effect becomes negligible when employing a 3.9 V cut-off (as shown in **Figure 4.5.c**). Lastly, a substantial increase in capacity decay is observed when employing higher cut-off potentials, (as exemplified in **Figure 4.5.d**), with the notable exception of the NMC 811 C-containing cells cycled at C/2. All capacity retention curves are provided in the **Appendix 4.1 and 4.2**. The outcomes of this study does not only confirm the behaviour observed in **Chapter II** with another active material, but also reveal a remarkably similar behaviour when comparing NMC

622 with NMC 811. Furthermore, no additional capacity decay is observed for NMC 811, implying that we can harness the additional capacity offered by NMC 811 while maintaining degradation at levels comparable to our previously utilized reference composite.

Using this new composite, we launched a preliminary investigation into different approaches to mitigate capacity degradation observed when cycling up to 3.9 V vs. Li-In/In in C-containing cells.

		3.6 V vs. Li-In/In		**3.9 V vs. Li-In/In**	
	VGCF amount	0 wt. %	**1.5 wt. %**	0 wt. %	**1.5 wt. %**
C/2	NMC 622	- 4 %	**- 10 %**	- 16.3 %	**-15.8 %**
	NMC 811	- 4 %	**- 12.5 %**	- 13.5 %	**- 12.5 %**
C/10	NMC 622	- 6 %	**- 18 %**	- 34 %	**- 34 %**
	NMC 811	- 6 %	**- 17.5 %**	- 31 %	**- 38 %**

Table 4.1: Resulting capacity decays estimated by linear extrapolation for 100 cycles on NMC 622 and NMC 811 composites, including 1.5 wt. % VGCF or no VGCF. Two cut-off potentials are used: 3.6 and 3.9 V vs. Li-In/In and two C-rate: C/2 and C/10. Each value represent the average of two cells.

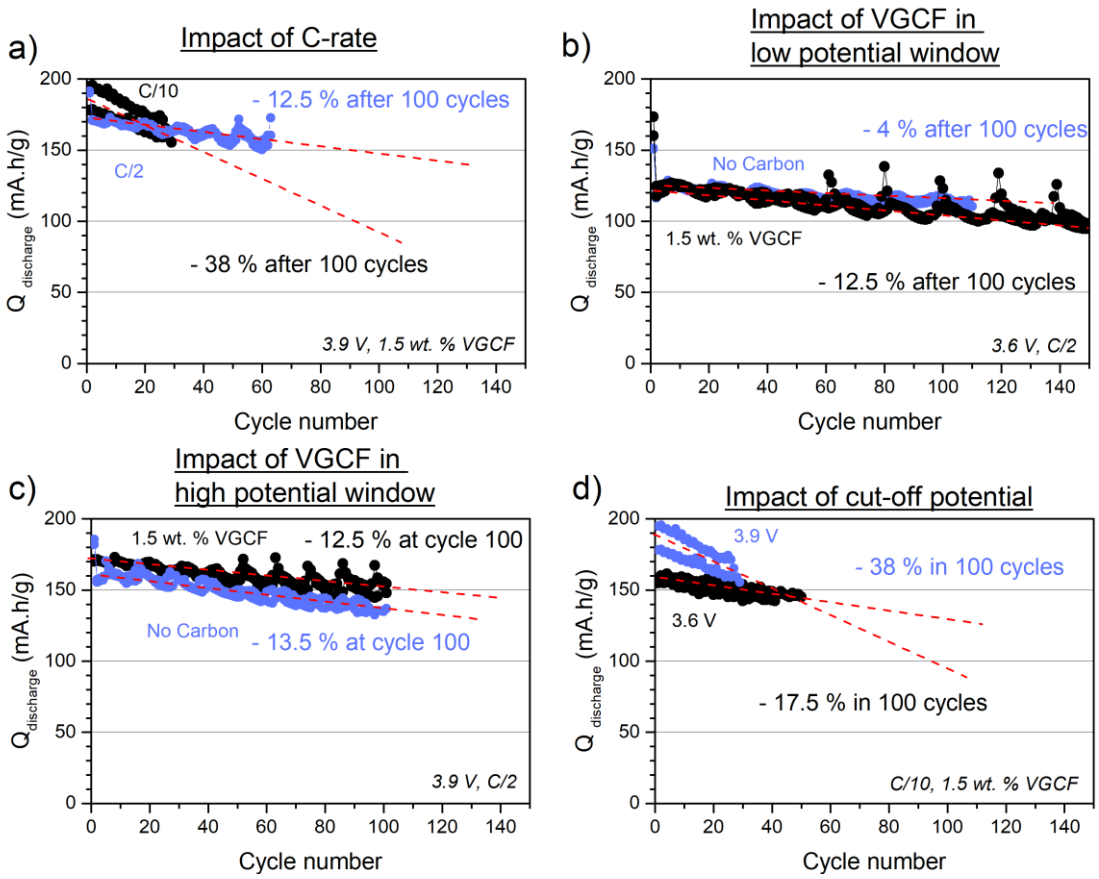

Figure 4.5: Cycling behaviour of NMC 811 + Li_6PS_5Cl composites (70/30 wt. %). 1.5 wt. % additional VGCF can be used. The red dashed lines represent the linear extrapolation of the average of two cells. **(a)** Impact of C-rate, using C-containing cells and cycling up to 3.9 V vs. Li-In/In. C/2 and C/10 are compared, with two cells per systems. **(b)** Impact of VGCF addition, using cells cycling up to 3.6 V vs. Li-In/In and a C-rate of C/2. C-free and C-containing cells are compared, with two cells per systems. **(c)** Impact of VGCF addition, using cells cycling up to 3.9 V vs. Li-In/In and a C-rate of C/2. C-free and C-containing cells are compared, with two cells per systems. **(d)** Impact of cut-off potential, using C-containing cells and a C-rate of C/10. Cells cycled up to 3.6 and 3.9 V vs. Li-In/In are compared, with two cells per system. The capacity retention is extrapolated up to 100 cycles, and we compute the average of the two cells.

4.3 Impact of assembly pressure and loading

4.3.1 Assembly pressure

First of all, assembly pressure has been proposed as an essential parameter for determining the performances of All-Solid-State Batteries, as it directly affects contact phenomena and the chemo-mechanical behaviour of composites[57,58,157,158]. In this study, we

investigate the influence of both low and high assembly pressures and analyse their effects on the initial cycle performance and capacity retention. To achieve this, we changed the assembly pressure to 2, 3, 4, 5 and 6 t/cm² (1 t/cm² = 98 MPa), which is applied for 10 minutes on the whole battery stack, and the resulting first cycle capacity is depicted in **Figure 4.6**. The lowest pressure (2 t/cm²) shows the largest polarization, while higher pressures present similar polarization between each other. If we focus on capacity retention, **Figure 4.7** shows the discharge capacity at a rate of C/2 in relation to the cycle number, along with the capacity retention derived from the moving average capacity curve. In this context, the moving average of discharge capacity serves the purpose of mitigating the fluctuations induced by temperature variations. All original curves can be found in **Appendix 4.3**. As expected, the 2 t/cm² cells present the worse performances, likely linked with large porosity resulting from the low pressure applied. Interestingly, the 3 t/cm² cells present the highest stability, with 9.5 % capacity decay after 120 cycles, while at higher pressures, there is no difference between the capacity retention of the systems assembled at 4 to 6 t/cm². Such results contradict our expectations that higher pressures should lead to enhanced stability and capacity. One possible hypothesis is the impact of pressure on the properties of the SE and AM used. This topic has begun to be explored for SE, but its counterpart for AM is still lacking[159–161]. Especially, an interesting investigation would be to assess the impact of pressure on the AM properties (diffusion, morphology…) and on its mechanical evolution upon cycling. Note that it has already been reported that high stack pressure provokes fractures and disintegration of AM particles[162].

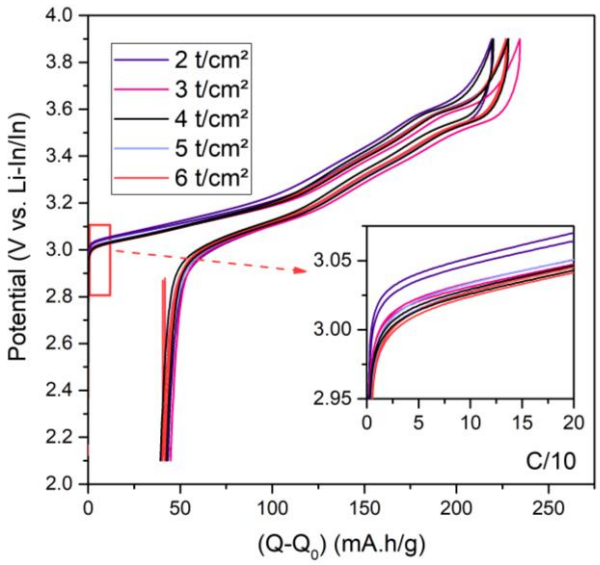

Figure 4.6: First cycle as function of assembly pressure. The assembly pressure is defined between 2 t/cm² and 6 t/cm², and applied for 10 minutes on the battery stack. The first cycle is made at C/10, in the [2.1- 3.9 V vs. Li-In/In] potential window. Inset shows the early delithiation polarization. Two cells per system are presented. All cells were launched on the same week.

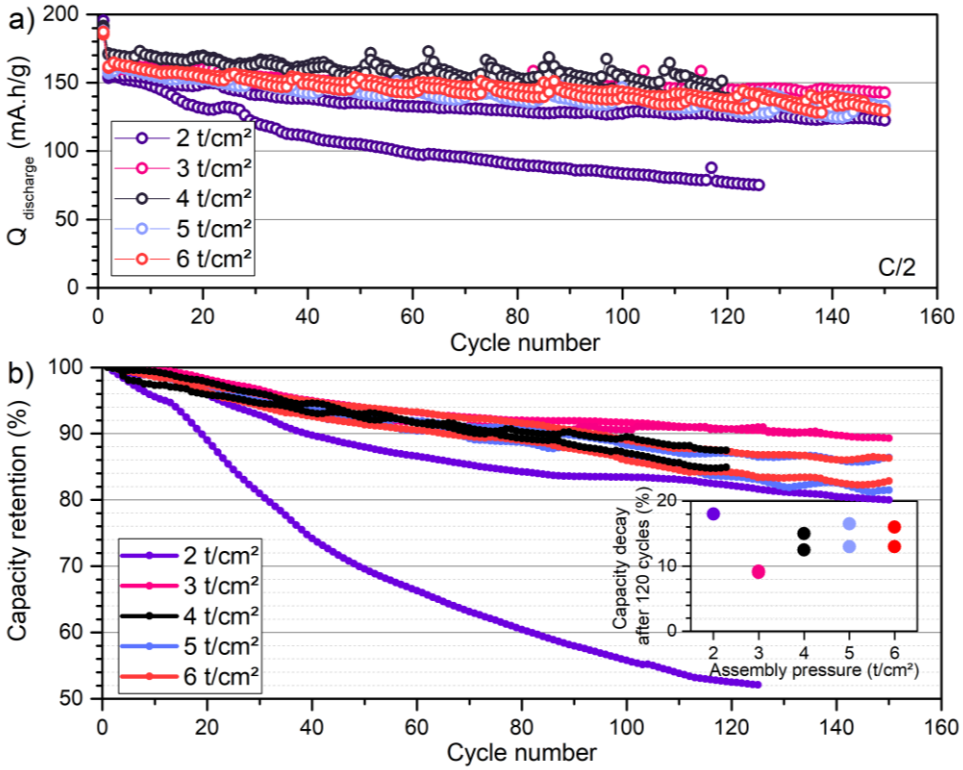

Figure 4.7: **(a)** Discharge capacity versus cycle number as function of assembly pressure. The assembly pressure is defined between 2 t/cm² and 6 t/cm², and applied for 10 minutes on the battery stack. The first cycle is made at C/10, in the [2.1- 3.9 V vs. Li-In/In] potential window. **(b)** Capacity retention of the discharge capacity moving

average curve (%). The moving average is done by selecting 8 data points for each average. Inset shows the values of capacity decay after 120 cycles, for each assembly pressure. Two cells per system are presented with at least 120 cycles for each.

4.3.2 Cathode loading influence

A typical constraint in achieving high energy density in present-day ASSBs is the low active material loading of the composite, as indicated in previous studies[41,43,59]. Enhancing the composite loading is frequently accompanied by challenges related to limited ionic and electronic percolations. Thus, we examined the influence of the loading on both the initial cycle capacity at C/10 and the capacity retention and results are depicted in **Figure 4.8**, using distinct ranges of loading, specifically 8–10, 12–14, 16–18, 20–22, 24-26 mg of composite per cm^2. Each loading range is represented by two individual cells. The lowest loading (8-10 mg/cm^2) and the highest loading (24-28 mg/cm^2) show slightly higher polarization than the rest of the loadings. The behaviour upon cycling is presented in **Figure 4.9**, revealing a consistent capacity decay trend across all loading conditions (with an average capacity loss of in 12.2 % 100 cycles, with a standard deviation of 1.7 %), thereby implying the negligible impact of this parameter on the overall stability of the system. Interestingly, the capacity at C/2 is similar between 12 and 26 mg/cm^2 (150-160 mA.h/g), meaning that we can increase our cathode loading up to 26 mg/cm^2 without penalty on the capacity. Overall, no significant changes are observed with the loading, in the range studied.

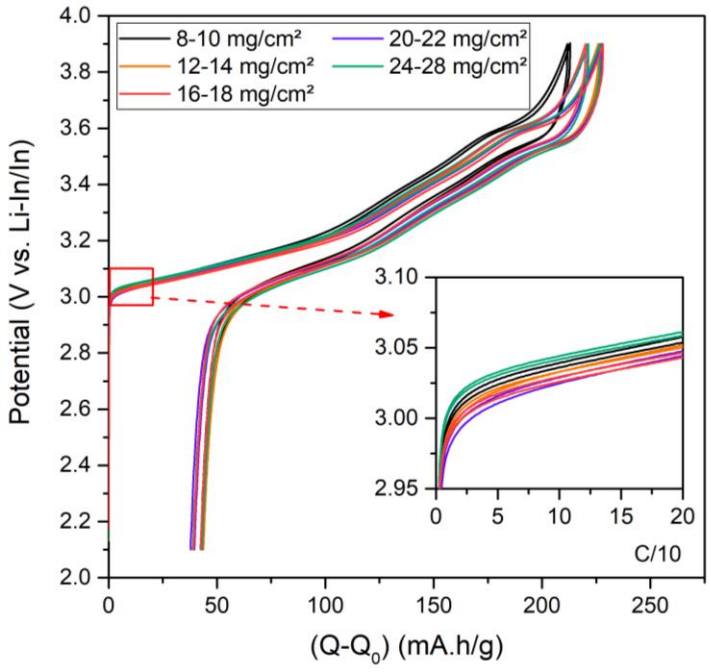

Figure 4.8: First cycle galvanostatic curve at C/10, using different loading of cathode composites: 8-10, 12-14, 16-18, 20-22 and 24-26 mg/cm². NMC 811 (MSE) + Li_6PS_5Cl (70/30 wt. %) composite is used, and an additional 1.5 wt. % VGCF is added. Cells are cycled in the 2.1 – 3.9 V vs. Li-In/In potential window. Two cells per system are shown. All cells were launched on the same week.

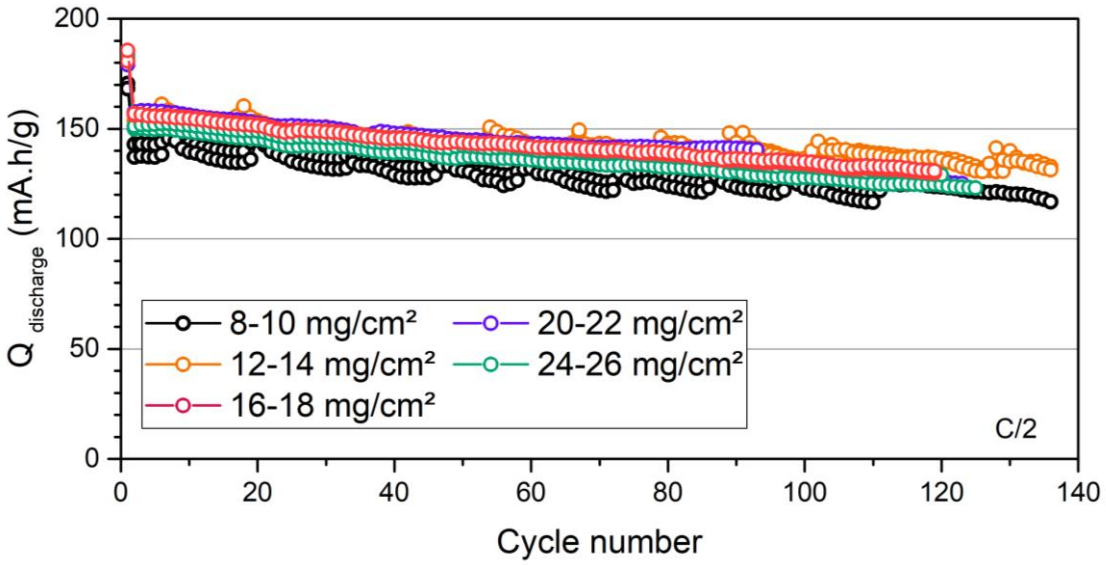

Figure 4.9: Capacity retention at C/2 after one cycle at C/10, using different loading of cathode composites: 8-10, 12-14, 16-18, 20-22 and 24-26 mg/cm². NMC 811 (MSE) + Li_6PS_5Cl (70/30 wt. %) composite is used, and an additional 1.5 wt. % VGCF is added. Cells are cycled in the 2.1 – 3.9 V vs. Li-In/In potential window. Two cells per system are shown with at least 90 cycles for each.

4.4 Coating benefits on high potential stability

4.4.1 Carbonates-coated NMC 811

Previously, NMC materials heat-treated in air environment have been used to improve the capacity stability of Li6PS5Cl-based solid-state composite batteries, through the deposition of carbonate species on the NMC surface[88,95]. This coating occurs by a reaction between CO_2 and the lithium residues on the NMC surface. In this study, we have exposed our NMC 811 material to heat treatment in air at temperatures ranging from 100°C to 800°C, using a heating rate of 5°C/min and for a duration of 8 hours. The resulting active materials were subsequently combined with argyrodite in a 70/30 wt. % ratio, followed by the addition of 1.5 wt. % VGCF. After an initial cycle at C/10, a galvanostatic cycle at C/2 was performed and the resulting curves are shown in **Figure 4.9**, with two cells per composite. Notably, all composites exhibited reduced capacity compared to the non-heated NMC 811-based composite, and the 800°C treated one presenting the worst capacity. This behaviour is linked to the increase in electronic resistance resulting from a thicker carbonate deposit, as demonstrated in **Figure 4.9.c**. Additionally, all the NMC 811-based composites display similar capacity decay. Thus, these cumulative findings indicate no advantage of the carbonate coating in this context.

However, we must bear in mind that this behaviour is significantly contingent on the specific surface of the active material used, as demonstrated in the **Appendix 4.4**. In this case, we used an NMC 622 from UMICORE, which had been stored outside an inert environment and whose capacity had initially deteriorated. The heat treatment under air was shown to largely improve both the initial capacity and stability in this specific case of a degraded NMC surface. As a result, the applicability of this methodology for active materials presenting a clean and fresh surface is questionable.

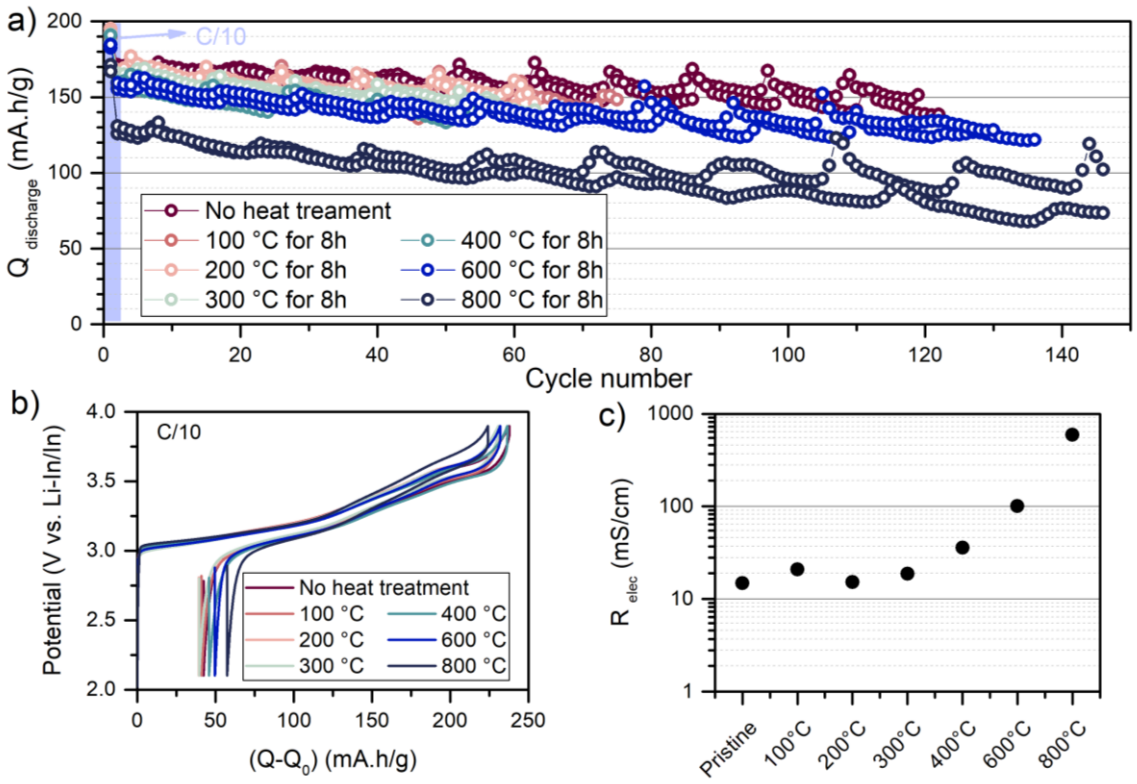

Figure 4.9 : Impact of heat treatment of NMC 811 (MSE) under air for 8h at different temperature (100°C, 200°C, 300°C, 400 °C, 600 °C and 800°C). 5°C/min heat rate is used. **(a)** The resulting NMC 811 composites are cycled in the [2.1-3.9 V vs. Li-In/In] potential window, at C/2 after one cycle at C/10. Two cells per composites are shown. The cells are cycled under ambient temperature. **(b)** First cycle at C/10. **(c)** Electronic conductivity of NMC 811 powders mixed with 1 wt. % PTFE, took with DC conductivity on pellet system. All cells were launched on the same week.

4.4.2 Carbonate-coated Li_6PS_5Cl

In light of the recent successful coating of carbonate on Li_6PS_5Cl, we propose to investigate this methodology[105]. Following the previously reported procedure, we subjected 300 mg of argyrodite to a CO_2 flow (30 mL/min) for various durations (ranging from 10 to 60 minutes), resulting in a powder that was subsequently incorporated into NMC 811 composites with 1.5 wt. % VGCF. For a photo of the experimental setup used, check **Appendix 4.5**. These composites underwent cycling at C/2 after an initial cycle at C/10, and the resulting capacity retention data are depicted in **Figure 4.10.a** over a duration of at least 120 cycles. It is evident that the CO_2 treatment significantly affects the capacity retention, leading to an enhanced

stability when utilizing carbonate-coated Li_6PS_5Cl. Especially, the 20 minutes CO_2 treated SE presents the highest stability, with only 5.4 % capacity loss in 100 cycles. In terms of discharge capacities, it was observed that longer treatment durations correlate well with lower extracted capacities, as evident from the first cycle at C/10 shown in **Figure 4.10.b**. This phenomenon could be attributed to kinetic limitations arising from the decrease in ionic conductivity of the solid electrolyte, given that Li_2CO_3 has been reported to exhibit an ionic conductivity of approximately ~10^{-6} S/cm. To investigate this hypothesis further, we conducted DC conductivity measurements and constructed Arrhenius plots using a two-electrode pellet measurement procedure, akin to the approach previously employed in **Figure 2.5**. This trend in ionic conductivity is shown in **Figure 4.10.c**, with triplicate measurements taken at ambient temperature together with Arrhenius plot in **Figure 4.10.d**. As expected, at room temperature the ionic conductivity decreases as the CO_2 treatment duration increases, with the conductivity values transitioning from 2 mS/cm to 0.2 mS/cm between the pristine and the 60-minute treated Li_6PS_5Cl. It should be noted that no significant change in activation energy was observed (Ea is comprised between 3.8 and 4.3 eV), indicating no discernible alterations in the core particles of argyrodite. Overall, the 20 minutes CO_2 treated SE seems like a good compromise for an enhanced stability (- 5.4 % capacity loss in 100 cycles) and an acceptable discharge capacity (140 mA.h/g at C/2). However, it's debatable whether this increased stability is due to the reduced capacity, or to more stable interfaces with our SE. A longer cycling is therefore necessary.

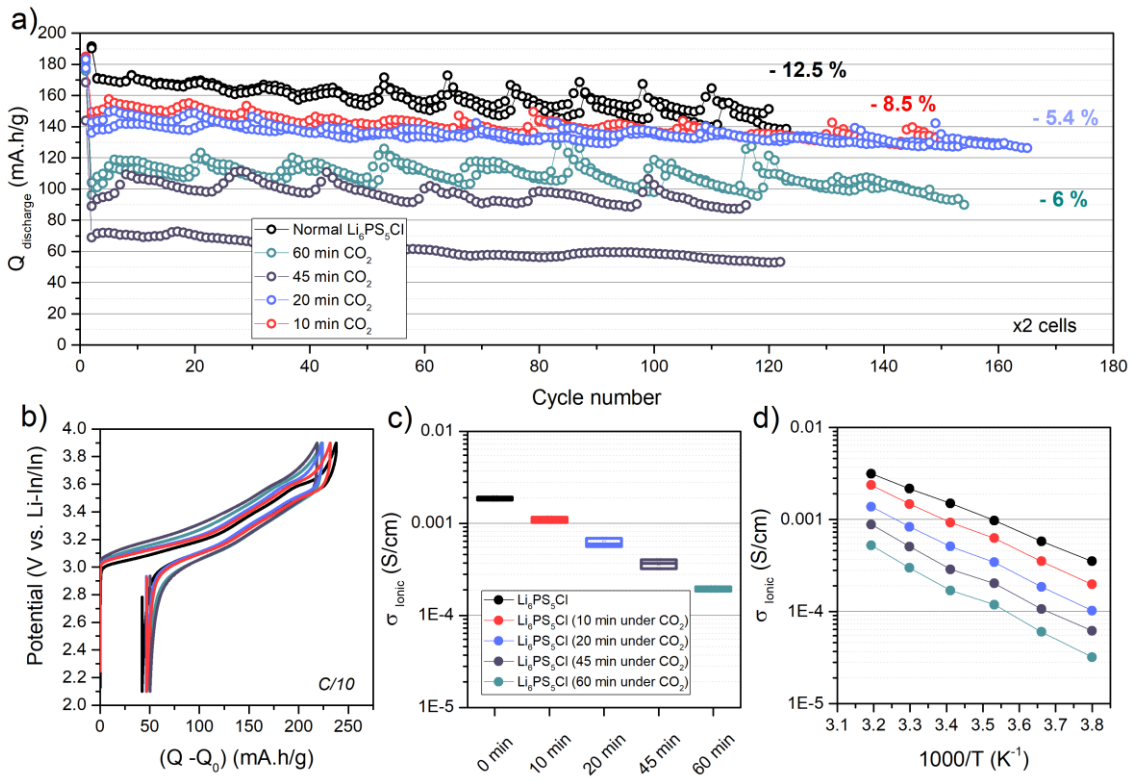

Figure 4.10: Impact of carbonate-coated Li_6PS_5Cl by CO_2 gas flow treatment. **(a)** Capacity retention of cells integrating normal argyrodite and argyrodite with 10 min, 20 min, 45 min and 60 min CO_2 treatment in their cathode composites. Cycling is done between 2.1 and 3.9 V vs. Li-In/In. One cycle is done at C/10 followed by C/2 cycling. Two cells are done per system with at least 100 cycles for each. **(b)** First cycle at C/10 of the aforementioned cells. **(c)** Ionic resistance of the distinct argyrodite. Three pellets are done per system. Average values are depicted, alongside the standard deviations. **(d)** Arrhenius plot of the distinct argyrodite, took between -10 to 40 °C.

4.5 Exploring formation cycles

We next conducted a comprehensive investigation into the effects of various formation cycle conditions, encompassing temperature, potential window, and the number of formation cycles. As reference composite, we still employed NMC 811 (MSE) + Li_6PS_5Cl (70/30 wt. %) + 1.5 wt. % VGCF.

4.5.1 Slow cycling and temperature effects

The formation stage of liquid Li-ion batteries encompasses multiple possible protocols involving high temperature, slow cycling, pulses... Of interest for this study, literature suggests the application of slow charge and discharge rates (ranging from 3 to 5 cycles at C/20), followed by cycles at elevated temperatures as a mean to stabilize the battery interfaces[163,164]. Despite the ongoing exploration of faster and more efficient protocols, this method is known to generate a robust solid electrolyte interphase, thereby enabling stable cycling performance. In this context, we have adopted a similar methodology to investigate the combined influence of temperature and slow cycling on the capacity retention of all-solid-state batteries.

First, the cells undergo two cycles at C/20 at temperatures ranging from 0°C to 55°C. Subsequently, we assessed the following C/2 cycling at ambient temperature. **Figures 4.11.a-c** illustrate the results obtained from the two formation cycles conducted at C/20 under 0°C, 40°C and 55°C, respectively. Observations indicate that the cell's first-charge capacity at 55°C surpasses the theoretical capacity of NMC 811, (which is approximately 275 mA.h/g) by an additional 16 mA.h/g, indicating the onset of a parasitic reaction strongly determined by kinetics (**Figure 4.11.a**). Such results mirror the results obtained in **Chapter II**. Furthermore, if we consider the C/2 cycling at room temperature (**Figure 4.11.c**), the results reveal that the high-temperature formation cycles are detrimental for both capacity and stability, as the 55 °C cells exhibit almost no capacity afterward, and the 40 °C solely display 120 mA.h/g. Switching to low temperature (0°C), the capacity at C/2 is around 165 mA.h/g, but an enhanced capacity decay is found, reaching 25 % loss in 100 cycles. Overall, there was no improvement in performance in either high- or low-temperature formation cycles.

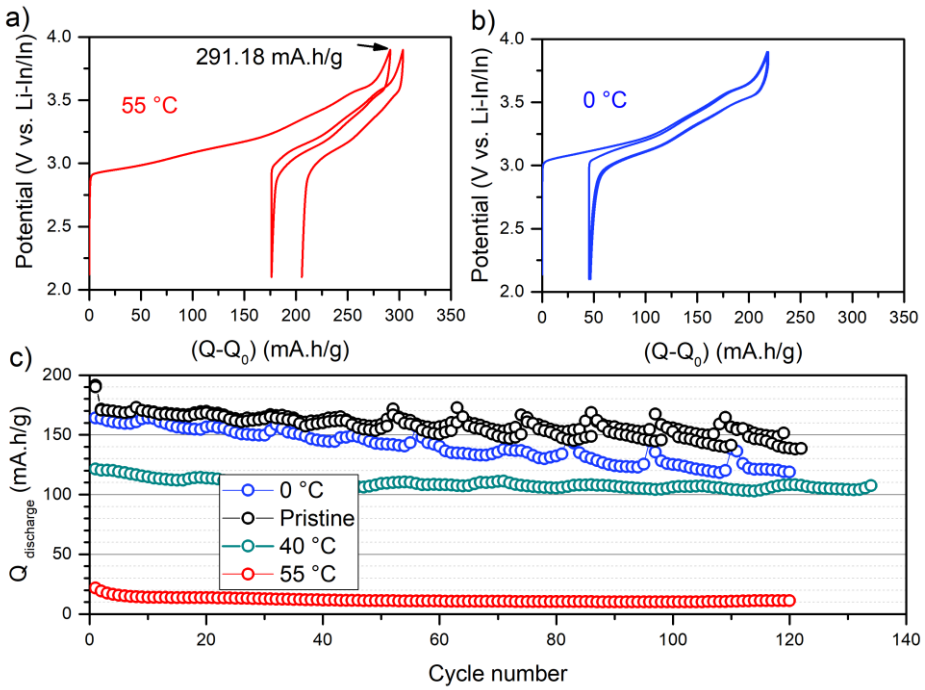

Figure 4.11: **(a)** Two first cycles between 2.1 and 3.9 V at C/20 and at 55°C. **(b)** Two first cycles between 2.1 and 3.9 V at C/20 and at 0°C. **(c)** Discharge capacity evolution after formation cycles and at ambient temperature.

We then studied the impact of the number of slow cycles on capacity retention. To do so, we compared cells with 0, 1, 2, 5 and 10 formation cycles at C/20 prior switching to C/2 cycles. The resulting capacity and capacity retention are depicted in **Figure 4.12**, with the capacity retention computed on the moving average discharge capacity curve for more clarity. All original curves are available in **Appendix 4.6**. Notably, the absence of C/20 formation cycles (0 cycles) corresponds to a capacity decay of - 12%, whereas a progression to 5 cycles presents a more substantial -14.5 % capacity decline. Intriguingly, further escalation to 10 cycles at the C/20 rate engenders enhanced stability, alongside a possibly slightly diminished capacity during the C/2 cycling (in the range of 140 mA.h/g). This strategy of 10 formation cycles considerably improves stability, with approximately ~ 5.5 % loss over the course of 100 cycles. This experiment raises a legitimate question about a plausible similar passivation phenomenon in cells subjected to prolonged cycling at a rate of C/2, for the same time. To test this hypothesis, an alternative way of plotting the data was used wherein the ten formation cycles conducted at C/20, were transposed in time to the 0 cycle and 1 cycle curves, as outlined in the accompanying **Appendix 4.7**. As the trend of the curves are found similar, it

inclines us to think that the process of stabilization achieved through ten formation cycles might be reproduced with prolonged cycling at C/2. Further studies are necessary to fully unravel this behaviour.

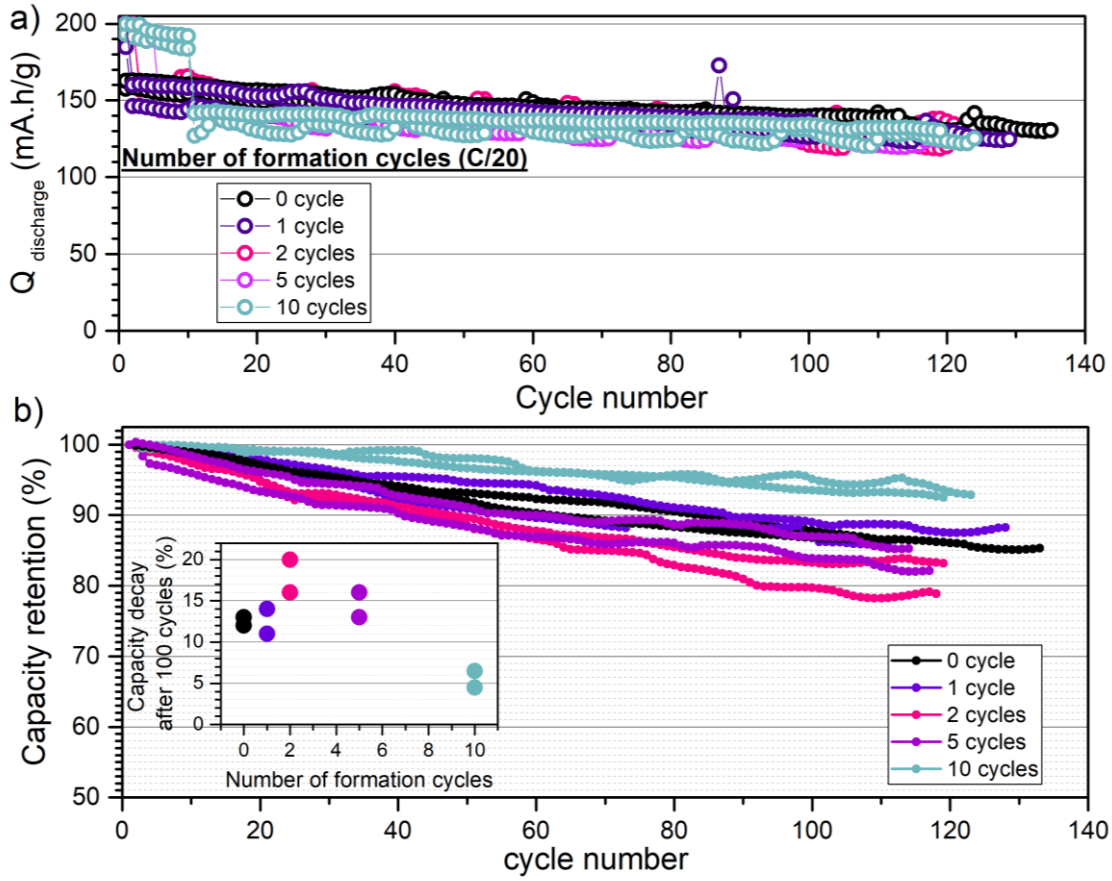

Figure 4.12: Impact of formation cycle number on NMC811 C-containing composite, using 1, 2, 5, 10 or no formation cycle. A formation cycle is made at C/20, in the potential window of [2.1-3.9 V vs. Li-In/In]. **(a)** Discharge capacity versus cycle number and **(b)** capacity retention (%) versus cycle number, starting after the formation protocol. The capacity retention is computed on the moving average discharge capacity curve for more clarity. The moving average is done by selecting 8 data points for each average. Two cells are depicted per system with at least 100 cycles for each. All cells were launched on the same week.

4.5.2 Potential window influence

We initially start by following the methodology outlined in **Figure 4.13.a**, to tackle the impact of upper cut-off potential. This involves applying two formation cycles at C/20, utilizing distinct cut-off potentials (3.4 V, 3.6 V, and 3.9 V). Subsequently, normal cycling was

performed at C/2 within the potential window of [2.1 – 3.9 V vs. Li/In/In]. The resulting moving average discharge capacity and corresponding capacity retention evolutions are presented in **Figure 4.13.b** and **Figure 4.13.c**, respectively, while the original curves are depicted in **Appendix 4.8**. Note that certain data points were lost due to a software issue on the related computer. Overall, our findings demonstrate that high potential formation cycling has a detrimental impact on capacity retention. Cells subjected to 3.6 V and 3.9 V cut-off potentials exhibit high capacity decays with capacity losses reaching 15.5 % and 18.5 % in 120 cycles, respectively. In contrast, two formation cycles up to 3.4 V vs. Li-In/In demonstrate similar stability as our reference cycles, with 12.5 % capacity losses in 120 cycles. However, the origin of such stability with low cut-off potential during formation cycle is questionable. Indeed, we might just observe the detrimental impact of longer time at high potential, as mirrored by our previous experiments in **Figure 4.12**. Thus, further studies are necessary to comprehend this phenomenon.

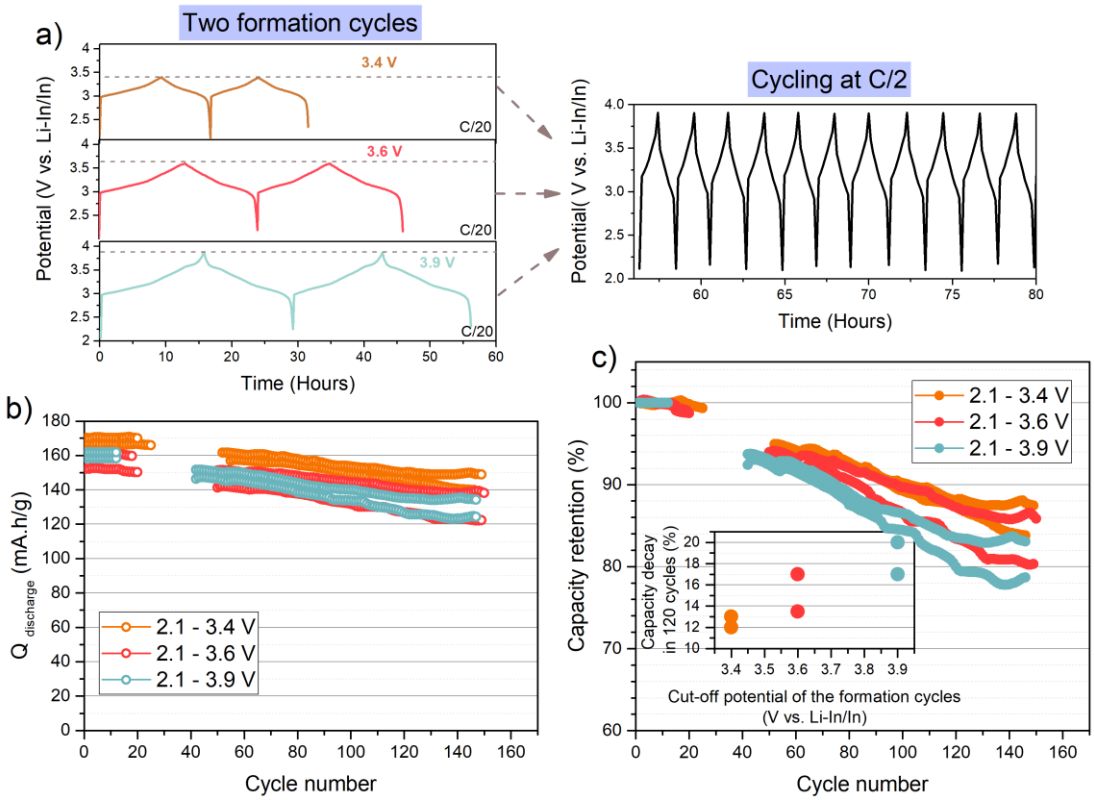

Figure 4.13: **(a)** Schematic of the cycling protocol for formation cycles: 2 cycles are done at C/20 with distinct cut-off potential, namely 3.4, 3.6 and 3.9 V vs. Li-In/In. The lower cut-off potential is defined at 2.1 V vs. Li-In/In. The following cycles are done at C/2 in the potential window of [2.1 – 3.9 V vs. Li-In/In]. **(b)** The resulting discharge capacities are plotted as moving average and as function of cycle number. Two cells are plotted per system with

at least 100 cycles for each. **(c)** Capacity retention of the moving average of the discharge capacity of the aforementioned cells. The moving average is done by selecting 8 data points for each average. All cells were launched on the same two days.

Figure 4.14 illustrates the impact of formation cycle low cut off potential on capacity retention. Following the methodology described in **Figure 4.14.a**, we conducted two formation cycles at C/20 using distinct low cut-off potentials (1.3 V, 1.5 V, 1.8 V, 2.1 V, and 2.5 V vs. Li-In/In). Subsequently, normal cycling was performed at C/2 within the potential window of [2.1 – 3.9 V vs. Li/In/In]. The resulting discharge capacity and capacity retention evolutions are presented as moving average in **Figure 4.14.b** and **Figure 4.14.c**, respectively. The original curves are depicted in **Appendix 4.9**. Interestingly, the use of a 2.5 V low cut-off potential in the formation cycles led to disastrous capacity decay during C/2 cycling, with capacity losses reaching up to 17.5% within 100 cycles. On the contrary, reducing the low cut-off potential to 1.5 V or 1.8 V vs. Li-In/In resulted in increased stability with capacity decay of 8 %. However, further decreasing the low cut-off potential to 1.3 V led to a decrease in capacity retention, reaching values of 9.5% capacity loss within 100 cycles. We can hypothesize that this positive impact of low cut-off potential might be linked to the reduction of the degradation products formed with Li_6PS_5Cl intrinsic decomposition. Indeed, S and P_2S_5 are reported to reduce below 1.8 V vs. Li-In/In[74]. All in all, the low and high cut-off potentials are very interesting parameters that strongly influence stability, while not having any effect on the capacity. The best performances should arise from cells that underwent formation cycles between 1.8 V and 3.4 V vs. Li-In/In.

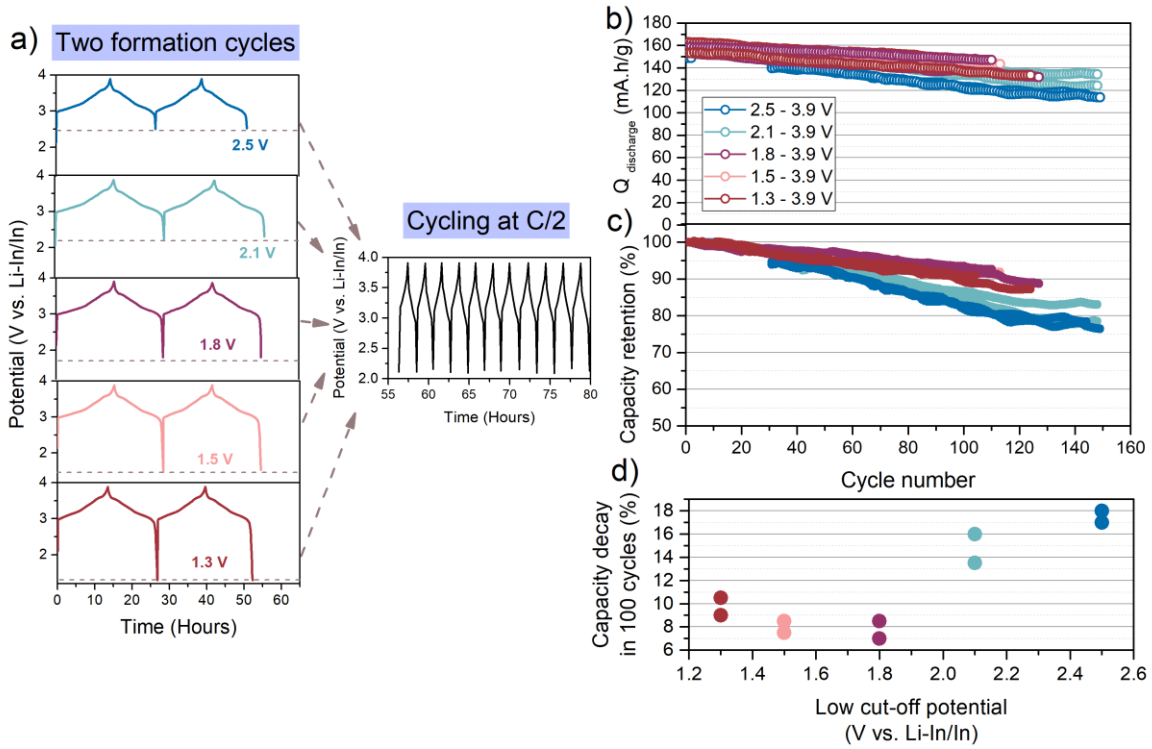

Figure 4.14: **(a)** Schematic of the cycling protocol for formation cycles: 2 cycles are done at C/20 with distinct low cut-off potential, namely 2.5, 2.1, 1.8, 1.5 and 1.3 V vs. Li-In/In. The upper cut-off potential is defined at 3.9 V vs. Li-In/In. The following cycles are done at C/2 in the potential window of [2.1 – 3.9 V vs. Li-In/In]. **(b)** The resulting discharge capacities are plotted as moving average and as function of cycle number. Two cells are plotted per system with at least 100 cycles for each. **(c)** Capacity retention of the discharge capacity moving average of the aforementioned cells. The moving average is done by selecting 8 data points for each average. All cells were launched on the same week.

4.6 Conclusion

This chapter is dedicated to the investigation of distinct approaches for mitigating the capacity degradation observed in Li_6PS_5Cl-NMC composites during cycling up to 3.9 V vs. Li-In/In. Because of the large number of parameters considered, we realized that we risked losing the reader. We therefore decided to summarize all the parameters studied with their advantages and disadvantages, in a consumer-style report table in **Table 4.2**.

	Range assessed	stability	capacity	Best parameters
Assembly pressure	2 t/cm² to 6 t/cm²	+	**none**	3 t/cm²
Loading	8 mg/cm² to 26 mg/cm²	**none**	**none**	none
Coated AM	0 to 800 ° C for 8 h	-	- -	none
Coated SE	0 to 60 min under CO_2	+ +	-	20 min CO_2
Temperature	0 to 55 °C	- -	- -	ambiant
Cycle number	0 to 10 cycles	**?**	**?**	Not sure
High cut-off potential of formation cycles	3.4 to 3.9 V vs. Li-In/In	+	**none**	3.4 V vs. Li-In/In
Low cut-off potential of formation cycles	1.3 to 2.5 V vs. Li-In/In	++	**none**	1.8 V vs Li-In/In

Table 4.2: Summary of the impact of each parameter on the stability of the cycling and the capacity.

By combining the best parameters, our study resulted in a capacity loss of approximately 23-24 % after 300 cycles in cells undergoing 2 formation cycles and to 18-22 % after 200 cycles in cells undergoing 10 formation cycles, as demonstrated in **Figure 4.15**. Such results are somewhat disappointing, and there is no synergetic beneficial effects of the distinct optimized parameters. On the contrary, these results suggest that there is a detrimental interaction between at least two parameters.

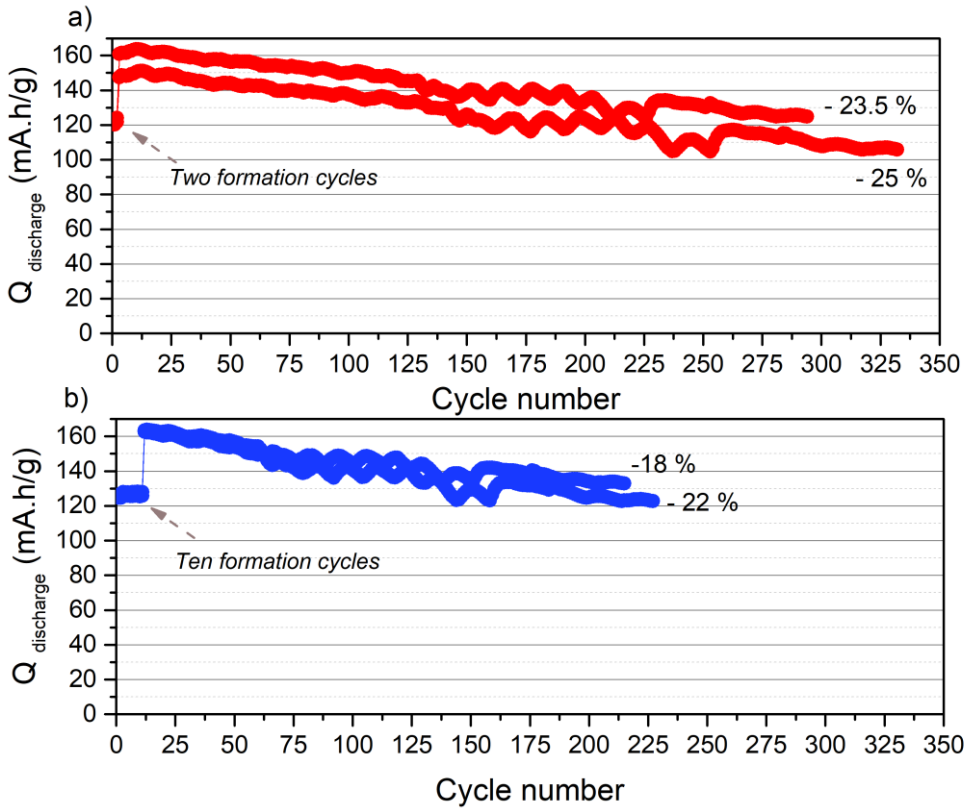

Figure 4.15: Capacity retention at C/2 between 2.1 and 3.9 V vs. Li-In/In, after **(a)** two cycles at C/20 in the 1.8-3.4 V vs. Li-In/In potential window or **(b)** 10 cycles at C/20. We use a NMC 811 (MSE) + Li_6PS_5Cl (20 min under CO_2) in a 70/30 wt. % ratio, with the addition of 1.5 wt. % VGCF. The assembly pressure is set at 3 t/cm². All cells were launched on the same day.

Overall, although these results are very interesting from a methodological point of view, they do not solve the problem of the stability of Li_6PS_5Cl-based cathode composites. This highlights the need to explore other ways of stabilizing ASSB cathode interfaces. As a first step, we present the performances of coated NMC 622 and halide-based composites in **Appendix 4.10**. Despite the preliminary nature of our results, they manifest considerable promise in terms of both stability and capacity. Especially, by replacing Li_6PS5Cl by Li_3InCl_6, we can increase the stability retention up to 91 % after 100 cycles, with an initial capacity of 160 mA.h/g. Additionally, the usage of $LiNbO_3$-coated NMC 622 yields to considerable stability improvement with 97.2 % capacity retention after 100 cycles. Thus, a transition towards halide solid electrolytes and a meticulous design of active materials may represent a promising direction in the context of ASSB cathode composites.

General conclusions and perspectives

This thesis elucidated the fundamental parameters and criteria governing the performance of Li_6PS_5Cl/NMC cathode composites in the context of All-Solid-State Batteries. We have conducted a comprehensive assessment of the pivotal role played by interfacial evolutions in solid electrolytes and have introduced novel tools and methodologies for their characterization.

Through this approach, we have conducted an in-depth exploration of the degradation phenomena occurring within NMC 622 + Li_6PS_5Cl composites, yielding fresh insights into the dynamics governing this system. By employing techniques such as global resistance monitoring, Potentiostatic Electrochemical Impedance Spectroscopy in three-electrode cells, and classical galvanostatic charge-discharge cycling, we have identified two critical parameters: the quantity of carbon additive and the cut-off potential.

To start with the **carbon additive**, our investigation revealed a dual negative impact of its presence on the composite's performance. Firstly, we demonstrated that the presence of more than 2 wt. % of VGCF adversely affects the ionic conductivity of the composite, a phenomenon substantiated by DC and PEIS measurements conducted prior cycling. Secondly, we established that the presence of VGCF exacerbates capacity losses during cycling in the voltage range of 2.1 to 3.6 V vs. Li-In/In. This effect arises from the high intrinsic reactivity of Li_6PS_5Cl, which undergoes oxidation throughout the entire potential window. This behaviour is closely associated with a decline in the ionic conductivity of the composites during cycling due to the formation of highly insulating by-products, such as elementary sulphur.

Adding the impact of **potential on cycling stability**, we have elucidated the distinct behaviours that depend on the chosen cut-off potential and the presence of VGCF. To this end we designed and successfully used a transmission line model for Potentiostatic Electrochemical Impedance Spectroscopy measurements during cycling in a three-electrode cell configuration. When subjected to cycling up to **3.6 V vs. Li-In/In**, we have identified that the primary source of capacity degradation stems from the interfaces between the solid electrolyte and VGCF, resulting in a 10% reduction in capacity over 100 cycles when utilizing 5 wt. % VGCF and a C-rate of C/10. This deterioration significantly affects the ionic resistance of

the composite. After a further increase in potential to **3.9 V against Li-In/In**, we observed a shift in the primary source of degradation towards the interfaces between the active material and solid electrolyte, manifested by an increase in charge transfer resistance. This transition leads to the formation of a passivating, highly resistive interface surrounding the AM particles, resulting in a substantial capacity loss of 20-25% in 25 cycles for our specific protocol. Intriguingly, we noted that similar decreases in capacity are observed, regardless of the presence or absence of VGCF in this potential window. This observation underlines the need for further research to better understand the underlying mechanisms.

It should be noted that these interactions between carbon and cut-off potential were subsequently reaffirmed by the evaluation of another analogous NMC 622 and a NMC 811 active material, as detailed in **Chapter IV**. This corroboration strengthens the belief that we have here a general mechanism with high Ni-content NMC and Li_6PS_5Cl here.

In light of the uncertainty surrounding the utility of VGCF incorporation, we directed our attention towards investigating the **evolution of electronic conductivity** in carbon-free composites. To address this inquiry, we developed an innovative apparatus designed to monitor the in-situ electronic conductivity dynamics of ASSB composites. Our initial efforts involved assessing the reliability and advantages of this experimental setup by examining composites based on LCO, known to exhibit a distinctive metal-insulator transition during the early delithiation stages. Following the successful validation of our method, we proceeded to investigate the influence of primary and secondary particle sizes in the context of zero strain anode material LTO, shedding light on how particle size and morphology impact electronic percolation—a question of paramount importance. Subsequently, we transitioned we focused on NMC-based composites and carried-out a comparison between LNO, NC 9010, NMC 111, 811, and 622. This examination allowed us to qualitatively assess the influence of Li-induced chemical-mechanical effects on the electronic conductivity of the composites, particularly when operating at high states of charge.

The accumulation of these new and original results strongly indicates that, if aspects reactivity are judiciously controlled, a minimal quantity of carbon additive could bring substantial benefits in such systems.

For this reason, we have embarked on a systematic exploration aimed at solving the problem of the **stability within Li_6PS_5Cl-based composites** containing a minimum carbon content (1.5 wt. %). Our research was designed to improve the stability of composites composed of NMC 811, Li_6PS_5Cl, and 1.5 wt. % VGCF, when cycled over a voltage range spanning from 2.1 to 3.9 V vs. Li-In/In. In this comprehensive experimental design, we examined eight key parameters of interest, encompassing assembly parameters (assembly pressure and loading), coating strategies (including the application of carbonate coatings on both the solid electrolyte and the active material), as well as specific formation cycles attributes (such as temperature, number of formation cycles, and high and low cut-off potentials). By careful optimizing each parameters, we were able to achieve optimized stability with a capacity at C/2 of 140-160 mA.h/g and a capacity retention of 92 % after 100 cycles.

Collectively, the ideas presented in this manuscript contribute to a better understanding of the interfaces and critical parameters that influence the performance of Li_6PS_5Cl-based cathode composites. In addition, this research introduces a novel experimental setup, expanding the methodological toolbox for the study of All-Solid-State Batteries. We expect these results to enrich the experimental landscape of ASSB research, offering new methodological approaches and avenues for further experimentation.

Ultimately, our investigations have led to improvements in the stability of systems with significant capacity for ASSBs. Nevertheless, it is essential to recognize that while these while these improvements are notable, they fall short in addressing the challenge of capacity retention over long cycling. Thus, given the complex and multifaceted nature of the interfacial reactions inherent to Li_6PS_5Cl, these results underscore the imperative need for a transition toward more stable solid electrolytes. More specifically, halide-type solid electrolytes appear to be promising alternatives, offering the possibility of enhanced stability.

Advices for ASSB research

This section presents a list of pragmatic guidelines pertaining to the construction of ASSBs. It is important to note that the majority of these recommendations are founded upon my personal experimental insights and intuitive understanding cultivated throughout the course of my doctoral research, rather than being substantiated by empirical evidences.

Glovebox and degradation over time:

An essential preliminary measure in conducting research on ASSB entails the establishment of a **dedicated glovebox** exclusively designated for ASSB experimentation, and free of any solvents (with the exception of DMC (Dimethyl Carbonate) for washing purposes in our case), as this aligns with the inherent reactivity of sulphur-based SE. Note that, using such glovebox for our experiments we did not see an increase of stability upon cycling comparing inside and outside cycling of our cells, thus assessing the airtightness capability of our cycling cell.

In the context of **composites storage**, the Li-In composites displayed excellent resistance to degradation over time, sustaining their integrity for at least six months in the glovebox while maintaining favourable cycling performance in two-electrode cells. Conversely, numerous cathode composites experienced significant capacity loss after 4 to 5 months. Thus, it is crucial to assess their time degradation in your own glovebox when initiating ASSB research. In our case, we prepared limited quantities of composites (approximately 300 mg per batch) for 1 to 2 months of use.

Composites hand grinding:

During the preparation of **Li-In composites through hand grinding**, it is imperative to diligently mix the components until a state of homogeneity is achieved. In my case, this process typically demands approximately 10 minutes. Failure to attain homogeneity may result in inadequate adhesion of the composite to the piston after pressing, attributed to incomplete mixing of certain segments of lithium or indium foils with Li_6PS_5Cl. To address this concern, we also recommend the addition of an aluminum foil layer onto the Li-In composite

prior to the application of assembly pressure (note that the addition of Al foil does not affect potential nor capacity retention, despite minim alloying of Al and Li might occur). This precautionary measure ensures the subsequent removal of pistons, if necessary during the continuation of the assembly process, as well as a facilitate recovery of clean pistons for future utilization.

The investigation pertaining to **cathode composites grinding procedure** highlights the paramount importance of hand-grinding duration and applied force. Notably, an extended grinding period (for my case > 12 minutes) was found to render the composite brittle and resulting in diminished performances. Additionally, excessive force during grinding led to the fracturing of the active material. Consequently, we propose employing a delicate hand-grinding approach, applying minimal force, for a duration ranging from 6 to 10 minutes. Importantly, our experimental results demonstrate no disparity between the 6 and 10-minute intervals, though shorter durations were not explored.

Cell assembly:

Multiple practical considerations arise during cell assembly to optimize performance. Firstly, caution must be exercised regarding the **speed of piston insertion**, as excessively rapid insertion can lead to composite powder deposition on the cell's side walls. Moreover, to ensure adequate coverage of the cell surface, the operator should rotate the piston in contact with the added powder before pressing.

During assembly pressure, meticulous **alignment of the pistons** is of paramount importance to maximize the contact surface between the cathode composites and the pistons. Failure to achieve proper alignment has been shown to result in significant performance discrepancies of C-free cathode composites, with deviations of approximately 50 mA.h./g observed when alignment is not executed. Another potential remedy for this issue involves incorporating carbon paper on the cathode composite side following assembly pressure.

Lastly, when **tightening the screws** to apply pressure during cycling, a strategic approach should be used. Employing the "triangles" method with the six screws and incrementally increasing pressure steps (consecutively 0.5, 0.75, 1, 1.5, 2, and 2.3 N.m torque on screws in our case) enables a well-distributed pressure throughout the cell. Such

meticulous attention to assembly details can contribute to optimizing cell performance and most importantly, to the repeatability.

AM surface & synthesis:

An exceedingly critical aspect in the investigation of interfaces and composite performances lies in acknowledging the significance of active material synthesis and state of the material's surface. Even when employing NMC 622 active materials with comparable particle sizes, pronounced discrepancies in behaviours can manifest. These disparities may originate from distinct synthesis conditions (leading to varying quantities of transition metals in lithium sites for example), or may be influenced by the storage environment of the material. Consequently, it becomes impractical to generalize interfacial behaviour without considering the specificities of the AM synthesis and surface state. To lend greater credibility to your interpretations, conducting multiple experiments utilizing diverse AM or, ideally, incorporating AM synthesis studies into the research approach would be advised. This more rigorous approach will ensure a comprehensive understanding interface behaviour and composite performance, however being time-consuming and/or unpractical with most laboratory facilities.

Repeatability:

In the fast-paced and dynamic world of battery research, there is a prevailing temptation to conduct numerous experiments in haste to swiftly arrive at conclusions, often deferring repeatability measurements for later consideration. However, such a rush to conclusions without ensuring repeatability is highly dangerous, particularly in the context of ASSBs where the assembly process plays a critical role. The consequences of premature conclusions can be severe, as researchers may find themselves confronted with contradictions and dilemmas after months of study, necessitating the choice between disregarding certain data or embarking on an extensive redo of the entire study. Ethically, the intelligent course of action would be to embark on a comprehensive redo, but this entails a substantial loss of time and effort. **Thus, the most important counsel I can offer is as follows:**

- **Firstly**, prioritize understanding the repeatability of your reference system by launching 5 to 10 cells and meticulously assessing their consistency in terms of

capacity and capacity retention. In cases where repeatability is not achieved, it indicates discrepancies in the assembly procedure that warrant immediate attention and rectification.

- **Secondly**, when initiating any new experiment, diligently undertake two cells for the given investigation concurrently, rather than deferring the second one for a later time. This approach ensures a more robust experimental dataset and minimizes the risks associated with uncertainties in data interpretation.

By adhering to these prudent guidelines, researchers can navigate the ASSB research with greater confidence and methodological rigor, ultimately enhancing the reliability and validity of their findings.

Appendix

Appendix for chapter 2

2.1: Protocol to assemble ASSB cell

Li-In/In composite having the 2/1 atomic ratio was prepared via a two steps route. Firstly, the proper amount of Lithium foil was enveloped in an Indium foil. Secondly, the foil was laminated and folded several times with a glass tube until the Li-In alloy became darker and brittle. Finally, Li_6PS_5Cl powder is added in a mortar and hand-ground for 10 minutes to ensure optimum homogeneity to form the $Li_{0.5}In$/SE composite (60:40 wt. % ratio). The composite anode has a constant potential of 0.62 V vs. Li^+/Li. Lithium metal was not used since interfacial and dendrite issues prevent its usage. Besides, it cannot withstand a 1 t/cm² upon cycling without short-circuiting the cells.

Cathode composites are prepared by weighting the desired amount of active material and Li_6PS_5Cl solid electrolyte in the glovebox, to reach a ratio of 70/30 wt. % and hand-ground for 10 minutes to make composites. Occasionally a defined amount of vapor-grown carbon fibers (VGCF) was added to the mixture, after weighting the 70/30 wt. % AM/SE.

Two-electrode cells assembly is made via a three steps process using a hardware developed in house that consists of a PEI body and two stainless steel pistons of 0.5 cm² surface (8 mm diameter) (a scheme of the cell is shown in **Figure S2.1**). Herein, if not otherwise specified, 30 mg of Li_6PS_5Cl as ionic separator are first pressed at 0.5 t/cm².Subsequently, 25 mg of anode ($Li_{0.5}In$/Li_6PS_5Cl 60:40 wt. %) and 8 - 9 mg of cathode composites (loading of 16 mg/cm²) are placed on both sides and the stack is then pressed at 4 t/cm². Finally, a pressure of 1 t/cm² is imposed during cycling by the mean of six screws.

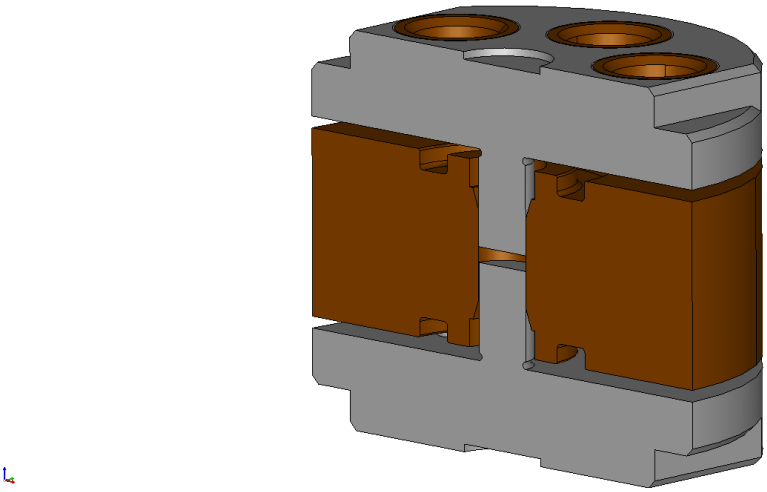

Figure S2.1: Two-electrode cell setup

2.2: XRD of Li_6PS_5Cl decomposed products:

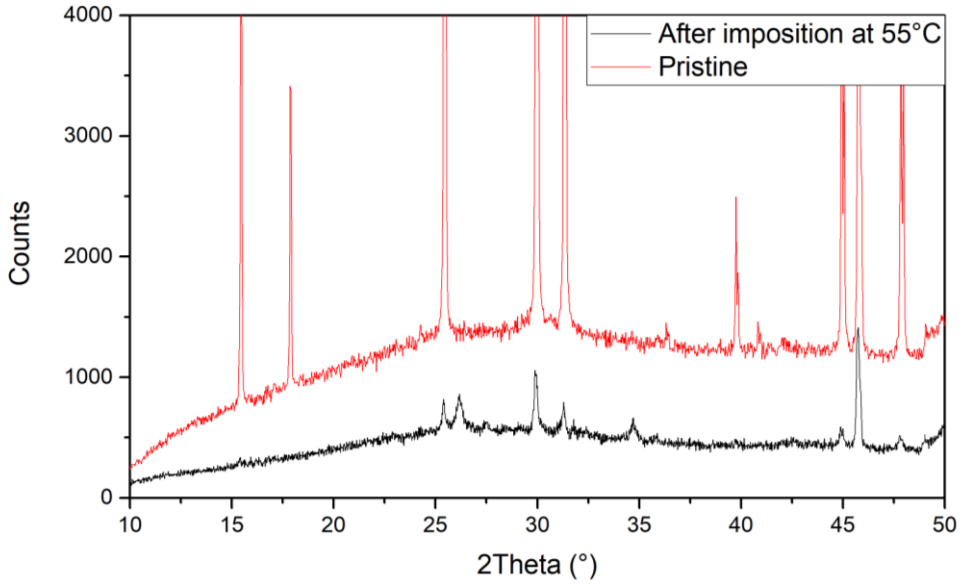

Figure S2.2: XRD of pristine solid-state Argyrodite. XRD of VGCF/Li_6PS_5Cl composite (5/95 wt. %) after 3.6 V vs. Li-In/In imposition for 3 weeks at 55°C.

2.3: Protocol to assemble three-electrode cell setup:

Three-electrode cells are built following the protocol described in Dugas et al. article, using hardware developed in house (a scheme of the cell is shown in **Figure S2.3**)[9]. The cell integrates a 50 mg layer of $Li_{0.5}In/Li_6PS_5Cl$ (60/40 wt. %) (same as the anode composite) that serves as reference layer, an aluminum ring is used as current collector for this reference layer and approximately 50 mg of SE is used on both side of the reference layer, and the same amounts of cathode and anode composite used in the two-electrode cells is used here.

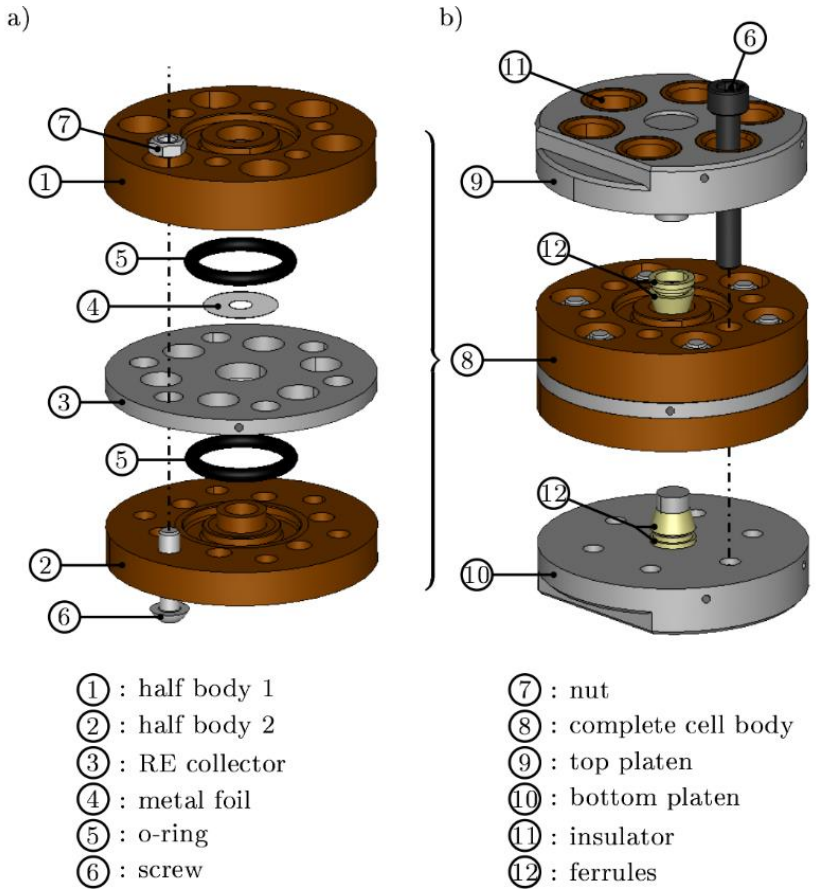

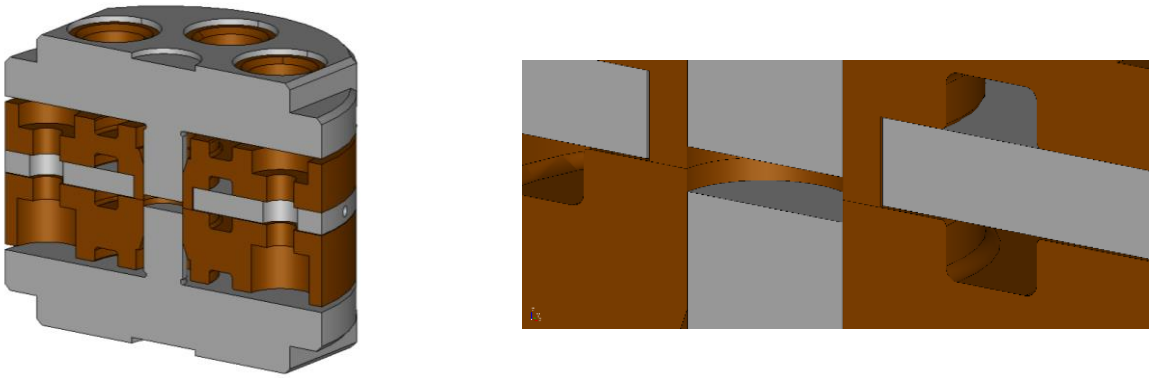

Figure S2.3: Three-electrode cell setup with a) detailed assembly of the cell body and b) detailed assembly of the complete cell.

2.4: First cycle irreversibility using distinct solid electrolyte

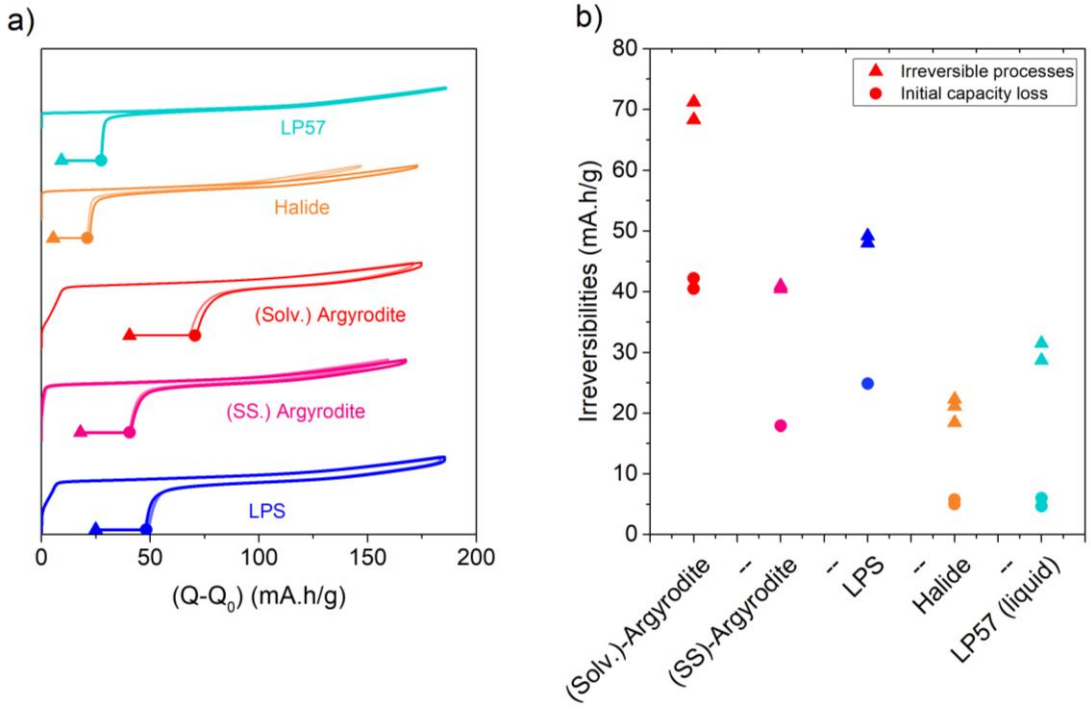

Figure S2.4: First cycle of NMC 622 + 30 wt. % solid electrolyte + 5 wt. % VGCF at C/20, with 3.6 V vs. Li-In/In cut-off potential. A constant potential of 2.1 V vs. Li-In/In is applied for 20 hours at the end of discharge. Two cells are done for each system. a) Galvanostatic cycling b) Extracted points of initial and final irreversibility.

2.5: Comparison of final and apparent irreversibility at 55°C or 25 °C:

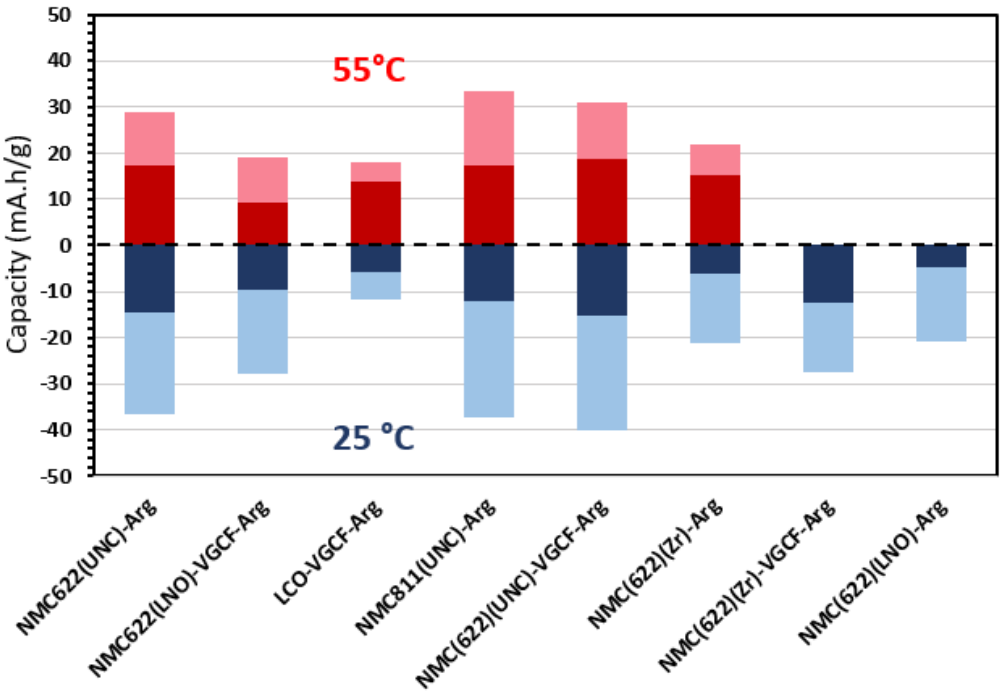

Figure S2.5: True and apparent irreversibility at 25 °C or 55°C in various system using 70/30 wt. % ratio of AM/SE and with or without 5 wt. % additional VGCF: NMC 622 (UMICORE), NMC 622 ($LiNbO_3$ coated, UMICORE) with or without VGCF, $LiCoO_2$ (UMICORE), NMC 811 (UMICORE) and NMC 622 (Zr-based coated, UMICORE) with or without VGCF. The "true" irreversibility is obtained after one cycle, by clamping the potential at 2.1 V vs. Li-In/In at the end of discharge for 30 hours, ensuring an ending current below C/500. Galvanostatic cycling is made between [3.6 V-2.1 V vs. Li-In/In] at C/10.

2.6: C rate tests with and without 5 wt. % VGCF:

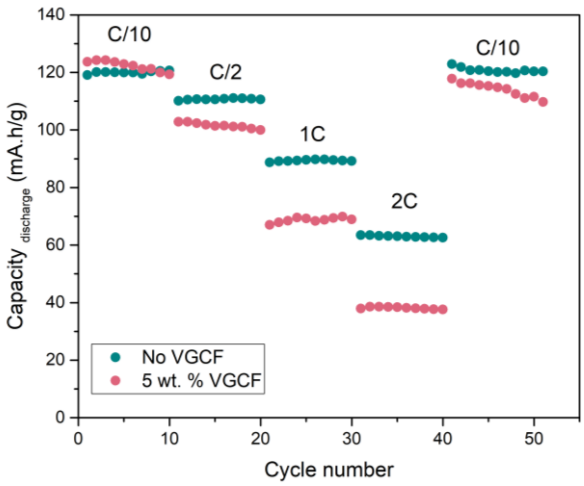

Figure S2.6: C rate tests using NMC 622 + Li_6PS_5Cl (70/30 wt. % ratio) as cathode composites with 5 wt. % or without VGCF. The cut-off potential is 3.6 V vs. Li-In/In.

2.7: Detailed explanations regarding impedance fitting and model:

Transmission line models are generally used when the impedance response of a system is distributed in multiple directions regarding the electronic current, such as in porous electrode. The base model consists of an upper and a bottom line, representing ionic and electronic currents. In this configuration, the system's response to the alternative excitation imposed while taking EIS is not uniform and both ionic and electronic contribution are dependent on x, y and z positions. Therefore, a discretized and position dependent model is theoretically needed to represent each specific active material/electrolyte/carbon additives distinct interfaces sites. However, as such approach makes it difficult or impossible to obtain an analytical solution, a convenient way to model data is to consider that the values of the cathode elementary components does not depend on position. This macroscopically uniform scenario enables to obtain the model transfer function of the system via an infinite number of infinitesimal component elements. The solution are solved analytically with a differential equation problem, and this approach has been widely used and has proved its efficiency to model complexed systems.

Theoretical base model:

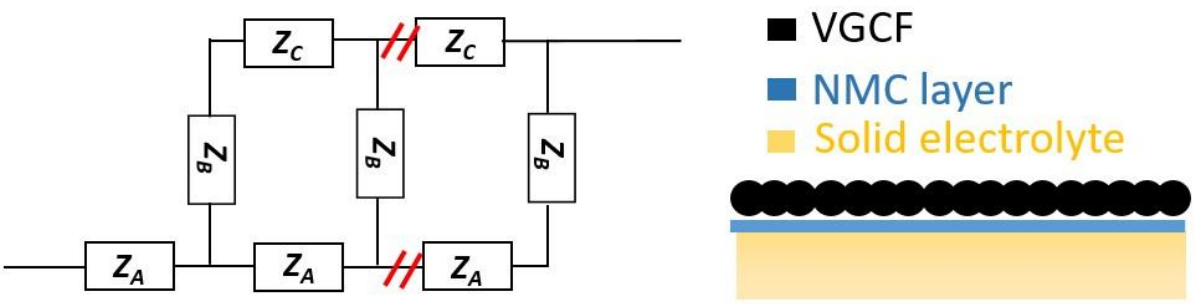

Figure S2.6: Presentation of a base TLM model for solid-state composite.

$$Z_{open-open} = \frac{Z_A Z_C}{Z_A + Z_C}.L + \frac{\sqrt{Z_B}}{(Z_A + Z_C)^{\frac{3}{2}}}.\frac{(Z_A^2 + Z_C^2)cosh(\beta) + 2.Z_A Z_C}{sinh(\beta)} \quad (1)$$

$$\beta = \sqrt{\frac{Z_A + Z_C}{Z_B}} * L \quad (2)$$

L = electrode thickness

The theoretical model depicted in **Figure S2.6** in open-open conditions (no boundary effects) is extracted from Siroma et Al.[16] article presenting the mathematical solutions of a wide variety of TLM models.

In the cases considered, Z_A and Z_C are replaced by the ionic and electronic resistivity of the cathode composite respectively (R_{ion} and R_{elec}) and Z_B will firstly be represented by the charge transfer CPE in parallel with charge transfer resistance as depicted in **Figure S2.6**. A CPE is used to account for active surface inhomogeneities obviously present in such unideal system.

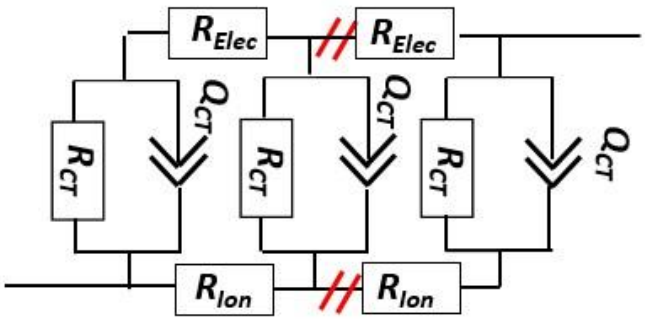

$$Z_A = R_{ion}$$

$$Z_C = R_{elec}$$

$$Z_B = \frac{R_{CT}}{1 + R_{CT} * (jw)^{\alpha_{CT}} * C_{CT}} \quad (3)$$

Figure S2.7: TLM model Z (R_{ion}, R_{elec}) scheme

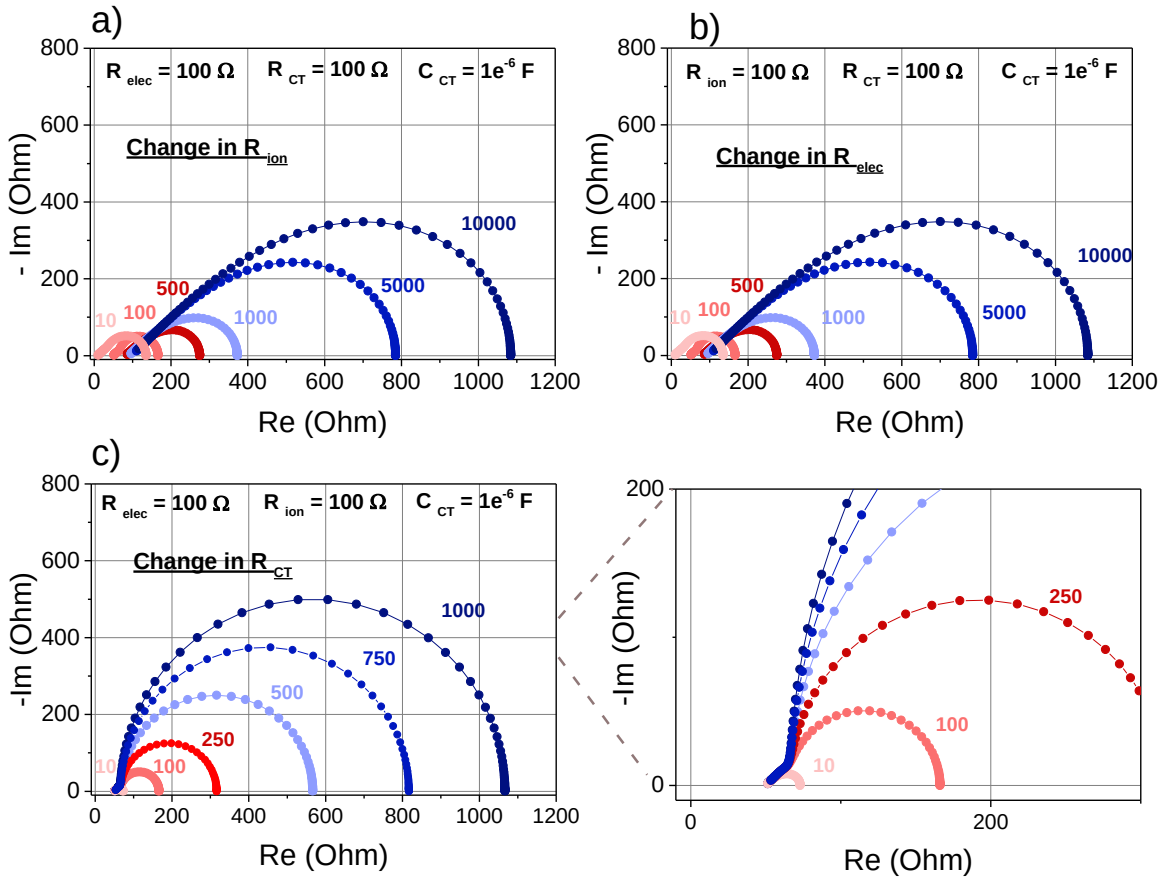

Figure S2.8: Theoretical spectra evolution with **(a)** changing R_{ion} **(b)** changing R_{elec} and **(c)** changing R_{CT}.

Looking at **Figure S2.8**, a qualitative comparison of the transport resistances compared to the charge transfer one can be visually obtained by looking at the presence of an inflexion point from the 45° slope in high frequencies, and the charge transfer "semi-circle". Note that compared to liquid systems often represented by a series of R/Q, the low frequency value here is not equal to the sum of the resistances, but follow the equation below:

$$\lim_{\omega \to 0} Z = \frac{R_{elec} * R_{ion}}{R_{elec} + R_{ion}} + \frac{\sqrt{R_{CT}}}{(R_{elec} + R_{ion})^{\frac{3}{2}}} * \frac{(R_{elec}^2 + R_{ion}^2) * \cosh\left(\sqrt{\frac{R_{elec} + R_{ion}}{R_{CT}}}\right) + 2 * R_{elec} * R_{ion}}{\sinh\left(\sqrt{\frac{R_{elec} + R_{ion}}{R_{CT}}}\right)} \quad (4)$$

As seen in this model previously shown (**Figure S2.7**), R_{Ion} and R_{elec} have a similar position in the TLM equivalent circuit. As they shared same unit and have a mirror behaviour in the system, plural couple of resistances can be used while obtaining the same impedance response. Using such model, it is not possible to deconvolute them, as seen on **Figure S2.8.a** and **8.b** presenting the same responses.

Model with R $_{global}$:

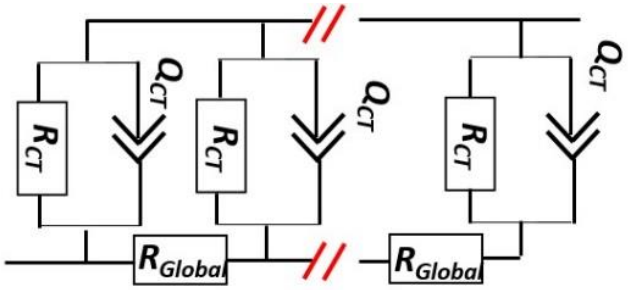

Figure S2.9: TLM model Z (R_{global}) scheme

$$Z_{open-open,Zc=0} = \frac{\sqrt{R_{Global} * Z_B}\cosh\left(\sqrt{\frac{R_{Global}}{Z_B}} * L\right)}{\sinh\left(\sqrt{\frac{R_{Global}}{Z_B}} * L\right)} \quad (5)$$

Instead of fitting spectra with R_{elec} and R_{ion} values that does not make sense, we choose to consider an R_{elec} value equal to zero, and replace R_{ion} by an R_{global} (**Figure S2.9**). Equalizing the two transfer functions (when $Z_C = 0$ or when $Z_C = R_{elec}$) and knowing that the charge transfer related values (R_{CT}, Q_{CT} and α_{CT}) will be equal in both TLM representations, we found the following relationship between the three resistances:

$$\sqrt{R_{Global} * Z_B} * \coth\left(\sqrt{\frac{R_{Global}}{Z_B}} * L\right) = \frac{R_{Ion} * R_{Elec}}{R_{Ion} + R_{Elec}} + \frac{\sqrt{Z_B}}{(R_{Ion} + R_{Elec})^{\frac{3}{2}}} * \frac{\left(R_{Ion}^2 + R_{Elec}^2\right) * \cosh\beta + 2R_{Ion} * R_{Elec}}{\sinh\beta} \quad (6)$$

In **Figure S2.9**, the 45° slope originating from the TLM is having the same tendency as in the previous case, as it grows with the increase of R_{global}. It is not surprising, as this scenario is similar to one of a cathode composite containing enough carbon additive so that the electronic conductivity becomes negligible (and therefore R_{global} would equalize R_{Ion}).

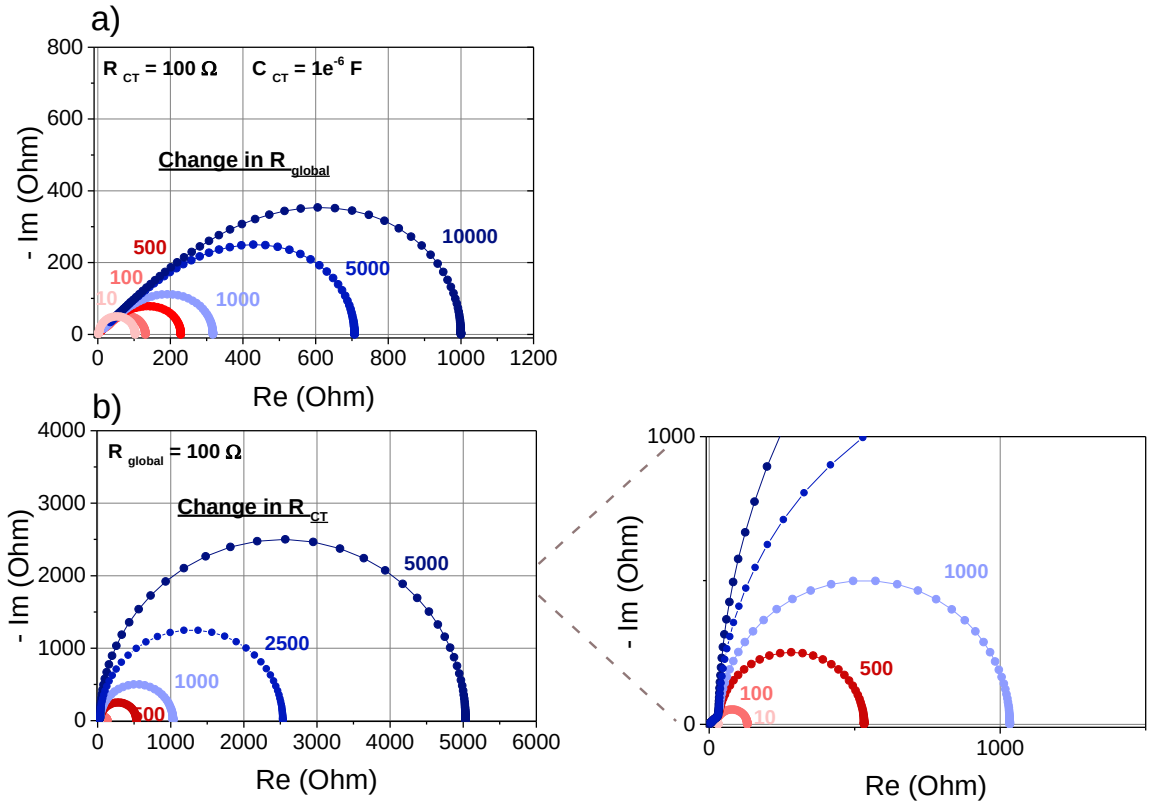

Figure S2.10: Theoretical spectra evolution with **(a)** changing R_{global} and **(b)** changing R_{CT}.

Modelisation:

Overall, plural phenomena needs to be represented in the equivalent circuit of the cathode composites under study in this article:

- The ionic and electronic transport phenomena, which are represented by the two railways of the TLM, already shown before.
- The charge transfer phenomena, which is represented by a CPE in parallel with a charge transfer resistance.
- The solid-state diffusion occurring inside our active material particles (here NMC 622).

Fitting experimental data solely with a TLM just having charge transfer in between the two railways does not able to fit well the low frequency part of the spectra, as seen in **Figure S2.11.a**. Indeed this one is attributed to the solid-state diffusion due to the 45° slope observed, characteristic of transport diffusion phenomena. However, implementing solid-state diffusion

(which is actually another transmission line model) in parallel with R_{CT} enables to mimic the low frequencies, but one additional feature is missing **Figure S2.11.b**.

To account for such difference we added another R//CPE in series with (R_{CT} + W)//CPE_{CT}, which could represent an additional layer arising from side reactions around NMC particles. This new feature will be called R_{int}//CPE_{int}. We therefore succeed to model efficiently our cathode composite spectra **Figure S2.11.c**.

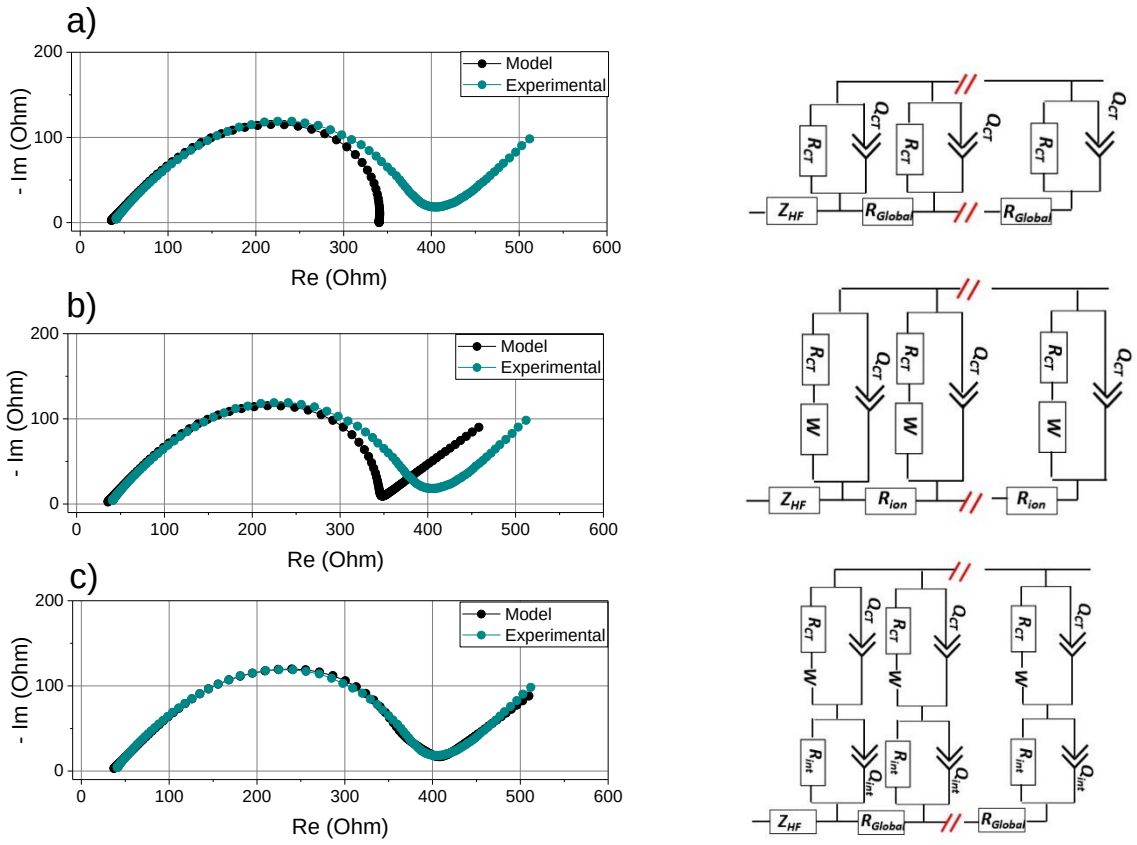

Figure S2.11: Step implementation of our TLM model used for the fitting procedure in this paper **(a)** Charge transfer **(b)** Charge transfer + solid-state diffusion represented by a Warburg element **(c)** Charge transfer + Solid-state diffusion + Additional R/CPE.

Case without carbon additive:

In system without VGCF, an additional feature is seen at high frequency and does not evolve upon cycling. For the fitting procedure, this feature is model by an R//Q prior to cycling, and the values are held constant for the following fits. This particularity has already been

described but the origin remains unclear, as it has been hypothetically assumed to arise from the grain boundaries of either the ion path, or the electron path[120]. We demonstrate that the addition of the carbon additive enables to make this feature disappear, therefore pushing the belief of an origin lying in the electron path (possibly NMC interparticle contact) (see **Figure S2.12**)

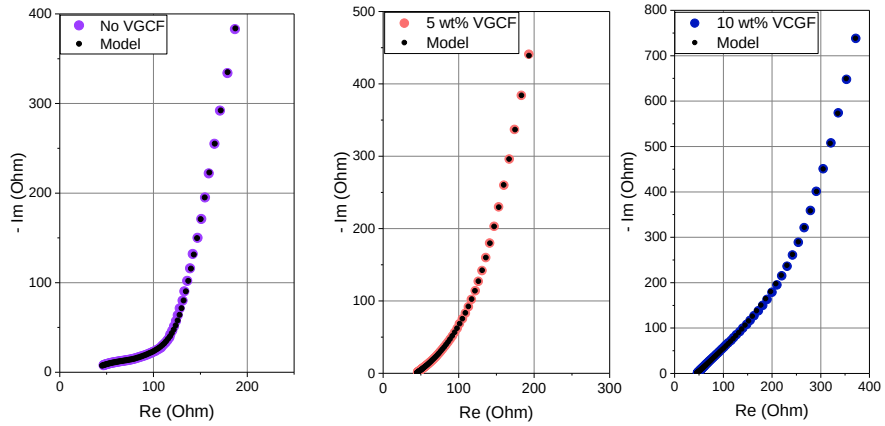

Figure S2.12: Comparison of uncycled NMC/Li_6PS_5Cl composites with 5, 10 or 0 wt. % VGCF. PEIS spectra are took in three-electrode setup.

Despite this particularity, C-free systems also present the same response as the C-containing ones as seen in **Figure S2.13**, where the enhancement of cathode composite thickness enables to clearly observe the 45° slope and a similar response as in C-containing systems.

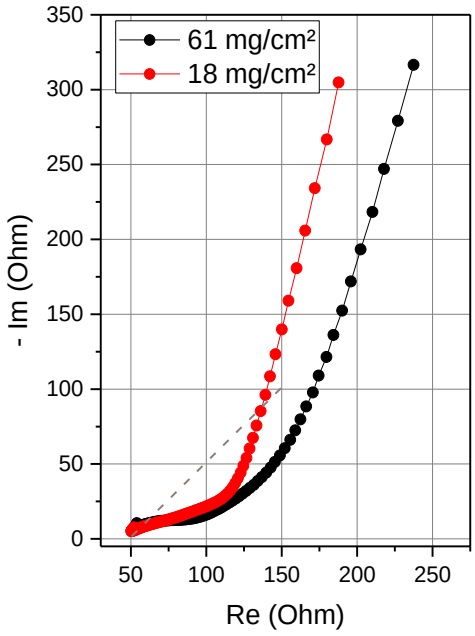

Figure S2.13: Comparison of two uncoated-NMC + Li_6PS_5Cl (70/30 wt. %) PEIS spectra after building in three-electrode setup, with two different loadings: 18 or 61 mg/cm².

MATLAB programming:

The optimization program created for the fitting procedure is based on a Broyden-Fletcher-Goldfarb-Shanno code to diminish our experimental-model distance. The choice of this method has been done after comparing three other optimization methods namely, quasi-Newton method (David-Fletcher-Powell, DFP), Conjugated gradient method and a trust-region method. Both DFP and BGFS methods were presenting smaller distances, with a little advantage for BGFS.

The experimental-model distance (d) is calculated via the following formula:

$$d(f_i) = 0.5 * \sqrt{\left(Im_{exp} - Im_{mod}\right)^2 + \left(Re_{exp} - Re_{mod}\right)^2} \quad (7)$$

$$D = \sum_{N}^{1} d(f_i) \quad (8)$$

2.8: Detailed explanations on R_{Ion} and R_{Elec} decorrelation from R_{Global} :

To enable a decoupling of R_{elec} and R_{ion} contribution to R_{global}, we proceeded to resolve a system of nonlinear equations, playing on R_{ion} characteristic dependence with temperature. The electronic conductivity of the cathode composites is assumed constant versus temperature. This system uses two types of equation that will be described in the following sections. To fasten computation, we only fit the high/mi-frequencies part of the spectra, not taking the solid-state diffusion and the extra interfacial semi-circle features.

Four temperatures are took per spectra: 0 °C, 10 °C, 25 °C and 30 °C.

Equalizing transfer function models:

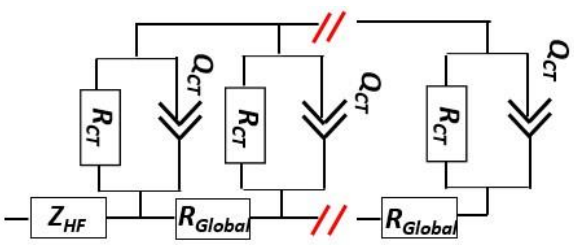

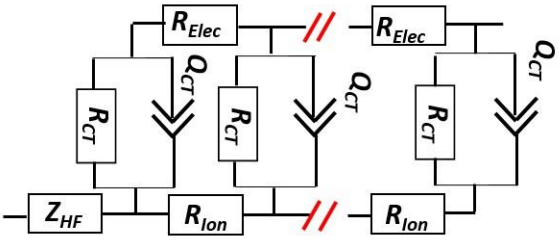

Figure S2.14: Model with R_{Global} **Figure S2.15**: Model with R_{Ion} and R_{Elec}

With the four spectra (4 temperatures), we obtain four equations by using **eq.6,** with R_{global}, R_{CT} and Q_{CT} known (computed from fitting process with model on **Figure S2.14**. Assuming temperature change has negligible impact on R_{elec}, we have 4 equations for 5 unknowns (R_{elec}, $R_{ion,0°C}$, $R_{ion,\ 10\ °C}$, $R_{ion,\ 25\ °C}$ and $R_{ion,\ 30\ °C}$). There is a need for more equations to solve this system.

Arrhenius evolution of the ionic conductivity:

Further equalities can be obtained from the dependence of R_{ion} with temperature. We assume the ionic resistance of the composite to follow an Arrhenius behaviour:

$$R_{ion}(T) = \frac{l}{\sigma_0 e^{-\frac{E_a}{kT}} * S} (9)$$

$$R_{ion}(T) = \frac{1}{C e^{-\frac{E_a}{kT}}} (10)$$

Four equations and two additional unknowns (E_a and σ_0) are obtained. Overall, we have 7 unknowns [R_{ion} (0°C) | R_{ion} (10 °C) | R_{ion} (25 °C) | R_{ion} (30 °C)| R_{elec} | C | E_a] and 8 nonlinear equations.

Using a similar optimization program as the one presented previously, we can solve this problem. The values obtained for the cycle 10 of the 4 cells presented in **Figure 2.11** are shown in **Table S1**.

	$R_{ion,0°C}$	$R_{ion,10°C}$	$R_{ion,25°C}$	$R_{ion,30°C}$	R_{elec}	Prefactor (C)	E_a
3.6 V VGCF	9638,6	5052,5	2079,8	1577,7	1,0	9088,6	0,43
3.9 V VGCF	712,6	432,3	217,5	175,6	2,6	1969,5	0,33
3.9 V No VGCF	429,2	272,1	145,4	119,7	50,1	938,3	0,30
3.6 V No VGCF	201,2	120,7	59,6	47,9	52,8	9871,0	0,34

Table S1: Results of the optimization program to decorrelate R_{ion} and R_{elec} from R_{global}.

Note that the prefactor takes into account the usual σ_0 of the Arrhenius law, but also the cathode composite thickness. With the small amount of cathode composite (~ 16 mg/cm²), we can expect a variation of thickness with cell repetition, surface roughness, flatness of the current collector… We can assume a similar thickness in between cells. However, the different values of R_{ion} and R_{elec} cannot be compared in between cells if they are close to each other.

To evaluate the optimization efficiency, we plotted the evolution of R_{ion} (T) in logarithm plot and the difference of Z (R_{Global}) and Z (R_{elec}, R_{ion})) compared with Z (R_{global}) in Bode plots. The optimization shows remarkable results as the temperature evolution of the fitted R_{ion} fits perfectly with an Arrhenius law (**Figure S2.17**) and the residues are low enough (**Figure S2.16**).

On cells without VGCF, the residues are in the same order as Z (R_{global}) at high frequencies, certainly linked with the additional feature observed at high frequencies in those systems. This does not bring concern on the optimization results validity, as the residues become more than 10 times lower than Z (R_{global}) starting from 3 kHz, below which frequency the spectra features of interest are largely observed.

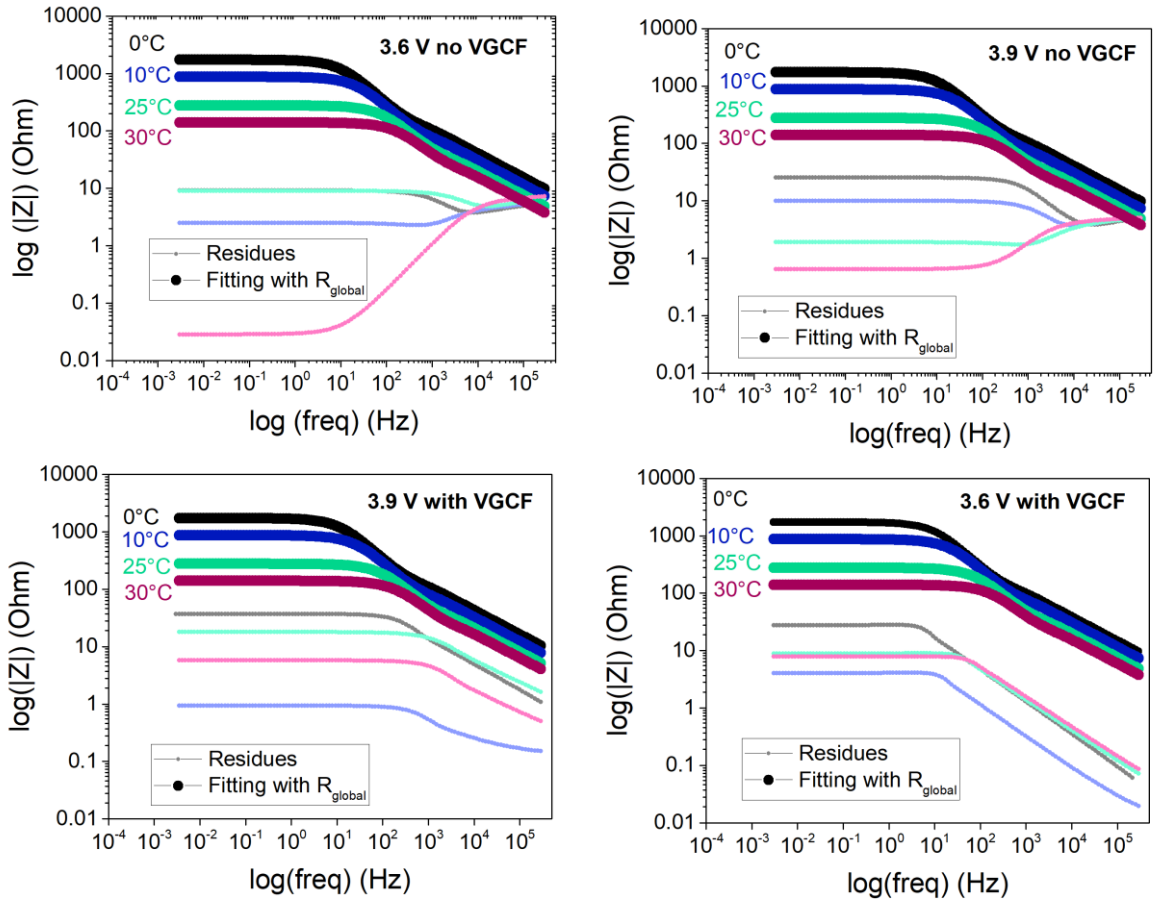

Figure S2.16: Bode plots of Z (R_{global}) – Z (R_{ion}, R_{elec}) module and Z (R_{global}) module for each frequency between 300 kHz and 3 mHz.

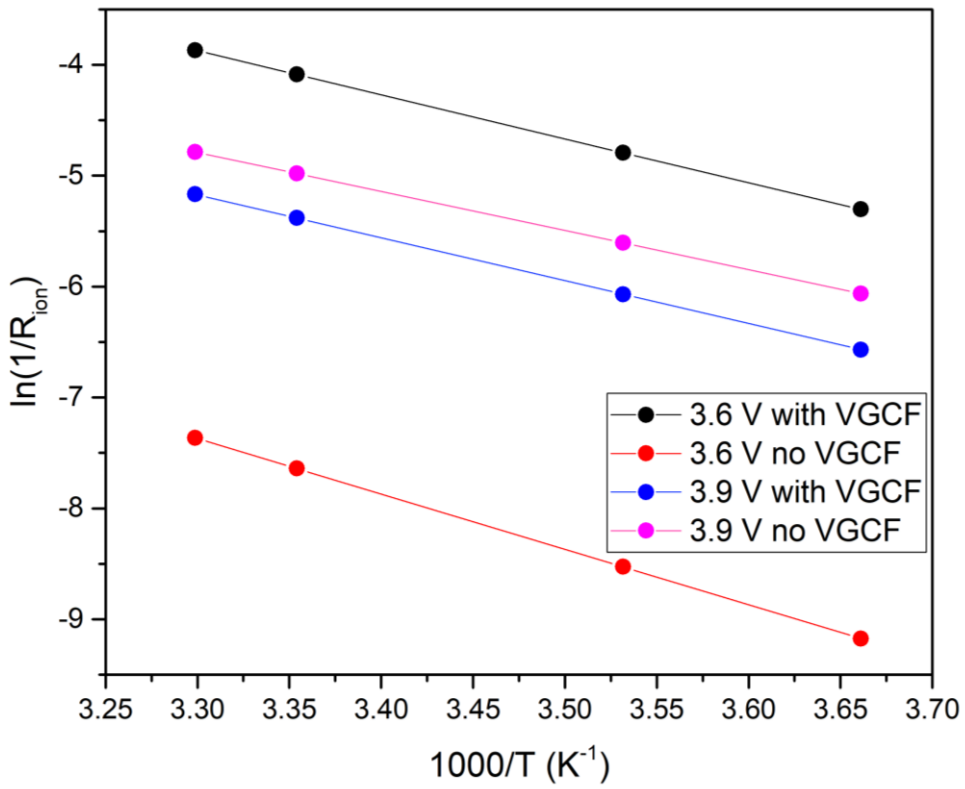

Figure S2.17: Arrhenius plot of the R_{ion} (T) optimized values

Appendix for chapter 3

3.1: Protocol for LCO DC conductivity measurement using LCO delithiated in liquid cells

$LiCoO_2$ delithiated in liquid cells (*ex situ* points of conductivity) are done by electrochemically delithiating 100 mg of LCO from UMICORE company using no carbon additive, lithium metal as counter electrode and LP30 as electrolyte, in a Swagelok setup. The powder is further washed with DMC and dried, prior mixing it with argyrodite in a 70/30 wt. % ratio. A pellet is made and placed in the routine two-electrode solid-state cell, to take DC conductivity measurements.

3.2: Active materials used

TMLO materials, enlisting $LiCoO_2$ (LCO), $LiNi_{0.6}Mn_{0.2}Co_{0.2}O_2$ (NMC622 uncoated, monolithic, d_{10} = 3.21 µm; d_{50} = 5.28 µm and d_{90} = 8.47 µm, BET = 0.5 m^2/g), $LiNi_{0.33}Mn_{0.33}Co_{0.33}O_2$ (NMC111, uncoated, monolithic), $LiNi_{0.8}Mn_{0.1}Co_{0.1}O_2$ (NMC811, uncoated, monolithic) and $LiNi_{0.9}Co_{0.1}O_2$ (NC9010) were kindly provided by UMICORE. $LiNiO_2$ was purchased from BASF.

3.3: Potential vs. capacity curves of TLMO-based composites using in situ conductivity cell

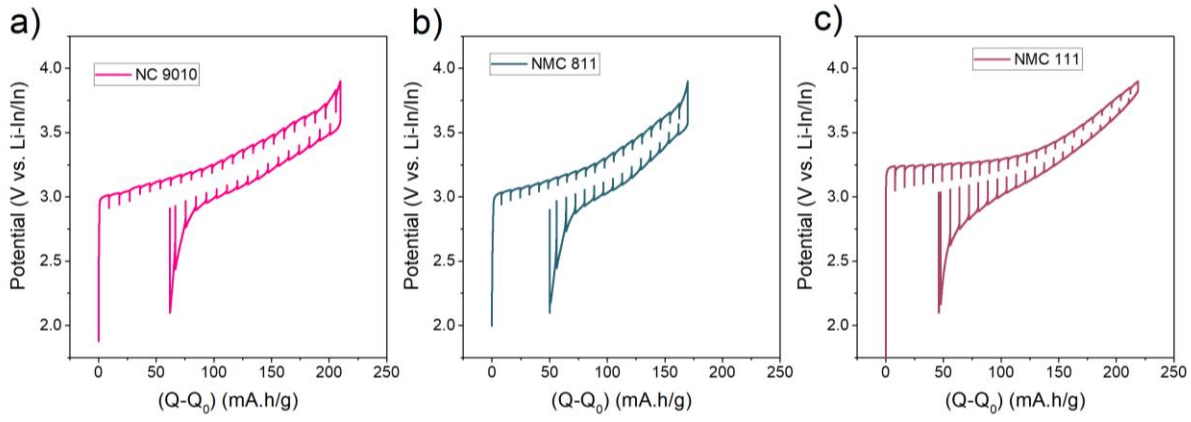

Figure S3.1: Exemplary curve of galvanostatic first cycle done with aluminium mesh and in-situ electronic conductivity measurements points. Cycling is done at C/50.

3.4: First cycle σ_{elec} evolution: polylithic vs. monolithic NMC 622

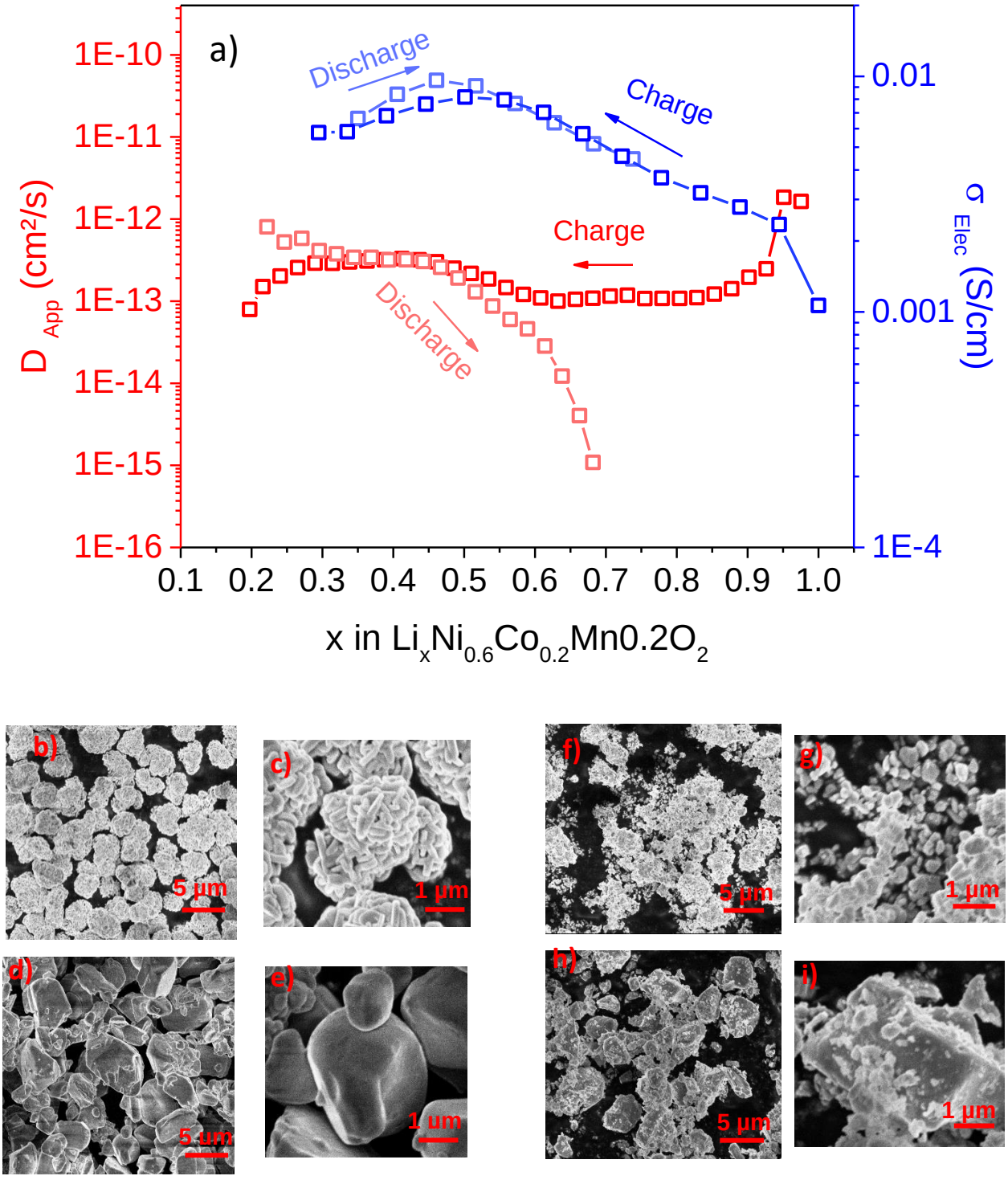

Figure S3.2: (a) Electronic conductivity and diffusion coefficient upon first cycle in polylithic NMC 622. SEM pictures of NMC 622 monolithic and polylithic **(b)-(e)** prior hand grinding **(f)-(i)** after smooth hand grinding for 8 minutes.

3.5: GITT of NMC 111 and NMC 811 composites

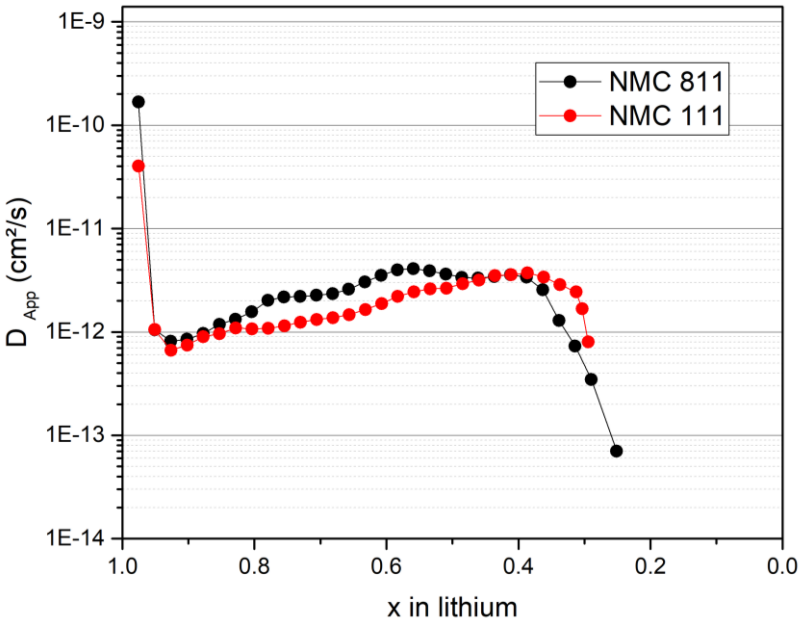

Figure S3.3: Apparent diffusion coefficient upon first cycle in NMC 111 and NMC 811 took in two-electrode cell setup.

3.6: Protocol for in situ and ex situ measurements of NMC 811

NMC 811 *in situ* electronic conductivity in liquid cell was done in a convenient three-electrode cell setup (EL-CELL PAT). An aluminum mesh is placed at the reference connection level, and a NMC 811/PTFE film (98/2 wt. % NMC 811/PTFE, 50 mg) is placed between the Al mesh and the working electrode current collector. Lithium metal and LP30 are respectively used as counter electrode and electrolyte. The cell is closed by the mean of one screw tightened manually, and is cycled inside the glovebox. Cycling is done at C/30, and electronic conductivity measurements are done every 45 min, after 30 min relaxation.

NMC 811 delithiated in liquid cells (*ex situ* points of conductivity) are done by electrochemically delithiating 100 mg of NMC 811 from UMICORE company using no carbon additive, lithium metal as counter electrode and LP30 as electrolyte, in a Swagelok setup. The powder is further washed and dried with DMC, prior mixing it with argyrodite in a 70/30 wt. % ratio. A pellet is made and placed in the routine two-electrode solid-state cell, to take DC conductivity measurements.

3.7: Rietveld refinements of the four solution-combustion synthesized LTO

Laboratory powder XRD measurements were performed with a Bruker D8 Advance diffractometer operating in the Bragg-Brentano geometry at with Cu Kα radiation ($\lambda(K\alpha_1)$ = 1.54056 Å, $\lambda(K\alpha_2)$ = 1.54439 Å) and a Lynxeye XE detector. Rietveld refinements were performed using the FullProf program.

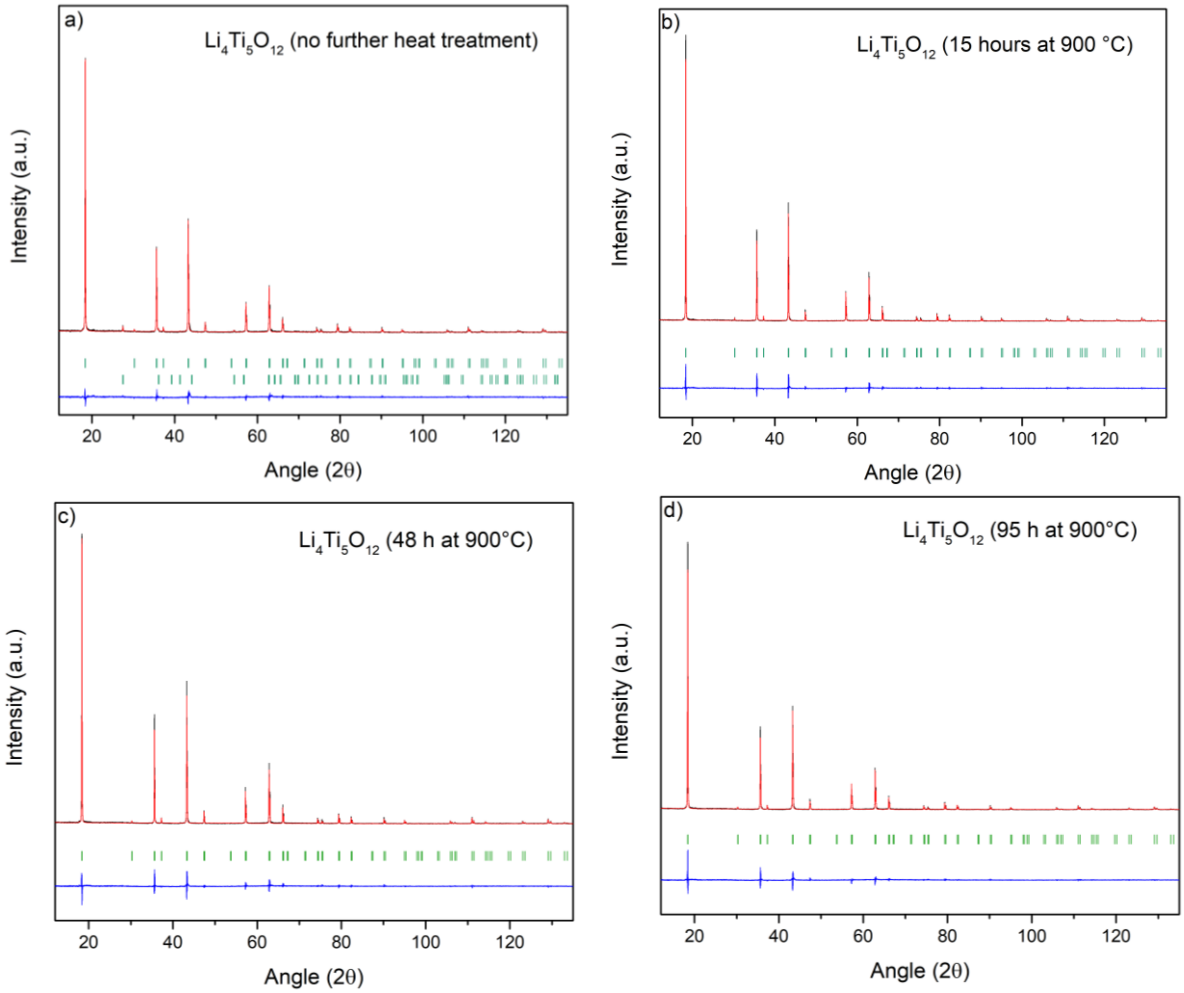

Figure S3.4: Rietveld refinement of X-ray diffraction patterns of the four LTO under study (λ_{Cu}). The black continuous line, red continuous line, and bottom blue line represent the observed, calculated, and difference patterns, respectively. Vertical green tick bars are the Bragg positions. **(a)** LTO without further heat-treatment **(b)** LTO (15 h at 900°C) **(c)** LTO (48 h at 900°C) **(d)** LTO (95 h at 900°C).

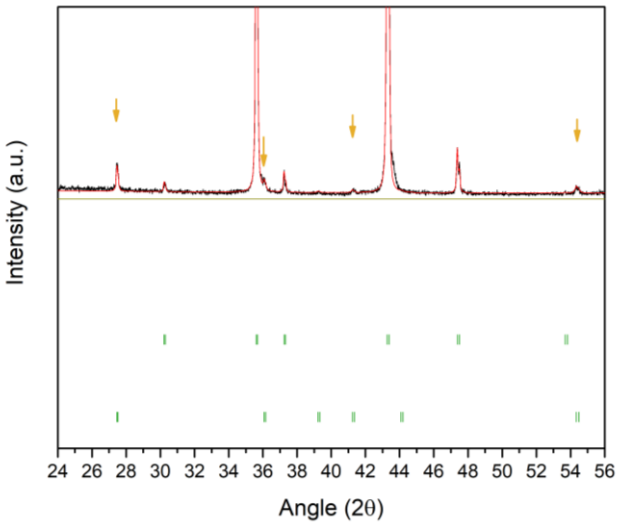

Figure S3.5: Zoomed Rietveld refinement of X-ray diffraction pattern of the 0 h LTO (λ_{Cu}). The black continuous line, red continuous line, represent the observed and calculated patterns, respectively. Vertical green tick bars are the Bragg positions. Orange arrows highlight TiO_2 rutile peaks.

3.8: Williamson-Hall plots of the four solution-combustion synthesized LTO

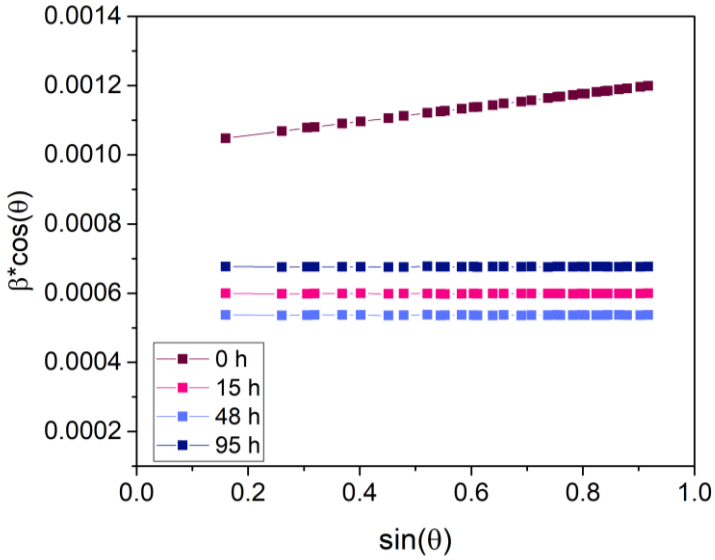

	0 h	15 h	48 h	95 h
cristallite size (nm)	96(6)	164(12)	183(12)	145(13)
microstrain $\varepsilon = \frac{\Delta d}{d}$ (x10^{-4})	0.7784(6)	none	none	none

Figure S3.6: Williamson-Hall plots deduced from the Rietveld refinements of the LTO samples made from solution-combustion synthesis.

3.9: Accusizer optical sizing protocol

Particle size distribution of LTO materials is made with an Accusizer using single-particle optical sizing to count one particle at a time. The device range is 0.5 - 500 µm in term of particle diameter. LTO powders are diluted in MilliQ water and at least 100 000 particles are measured for one experiment. Each measurement is repeated twice.

3.10: AM/SE ratio influence on LTO (NEI and solid-state synthesized LTO composites performances

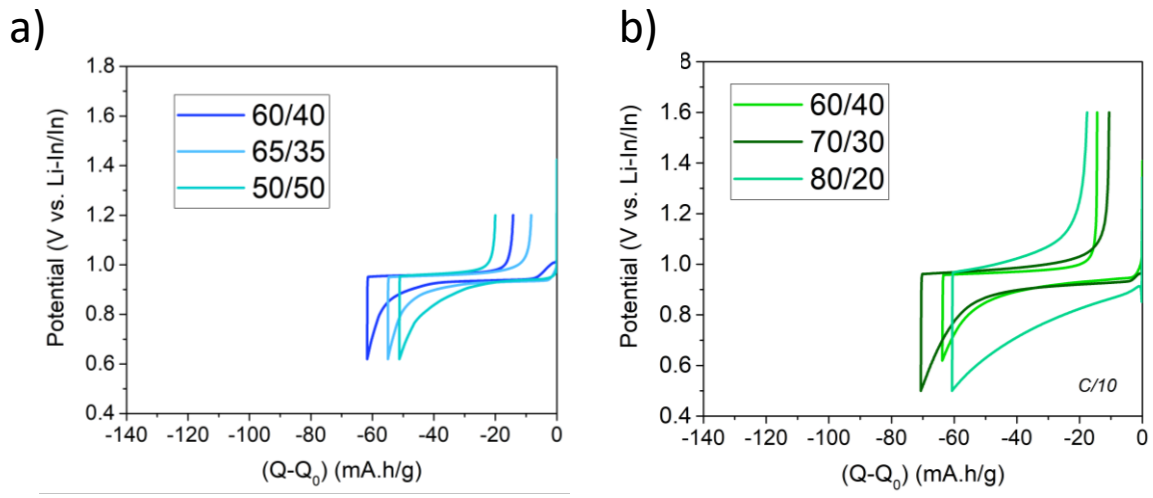

Figure S3.7: Optimization of the AM/SE wt. ratio in **(a)** LTO from NEI and **(b)** LTO from solid-state synthesis.

3.11: First cycle at C/10 of the four solution-combustion synthesized LTO

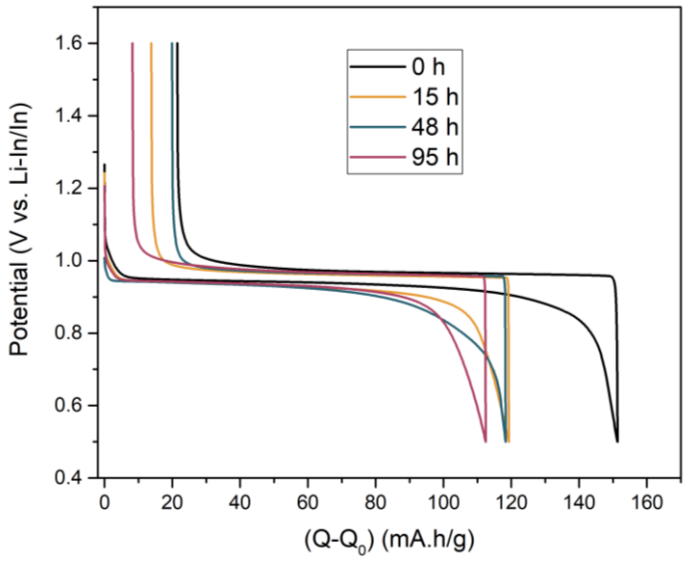

Figure S3.8: First galvanostatic cycle of the four solution-combustion LTO (0 h, 15 h, 48 h, 95 h at 900°C). Cycling is done at C/10 in two-electrode setup, using $Li_{0.8}In$ + Li_6PS_5Cl (60/40 wt. %) as counter electrode.

3.12: Repeatability and accuracy of LTO-based composites using LTO (48 h) as example

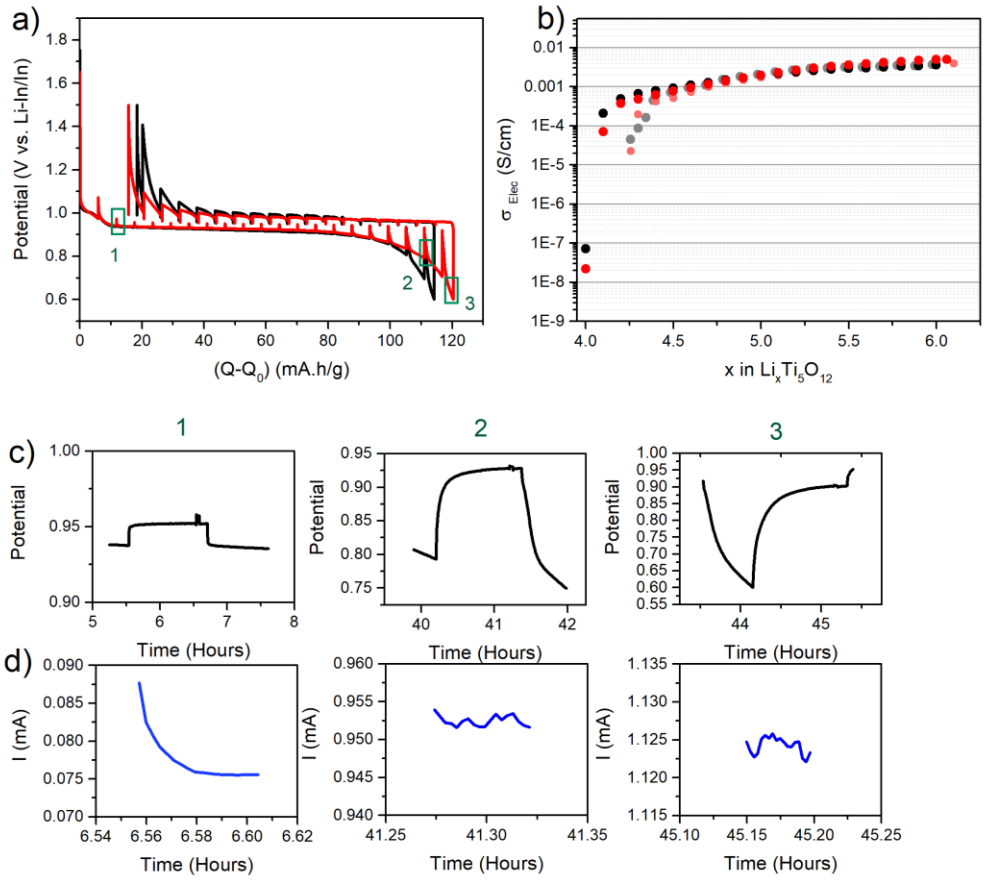

Figure S3.9: Exemplary data of in situ electronic conductivity of LTO (48 h) composite. **(a)** GITT-like C/30 cycling curve obtained from channel 1 from two composites **(b)** Electronic conductivity vs. x curve of two composites **(c)** Relaxation step of three specific points in lithiation **(d)** Corresponding DC polarization step. It is worth noting that fluctuations can be found in point 2 and 3 restricted to a range of merely 0.003 mA, which would only result in an insignificant deviation below 1 % (especially 0.3 % for point 2 and 3).

3.13: C rate influence on electronic conductivity evolution using LTO (0 h) based composites

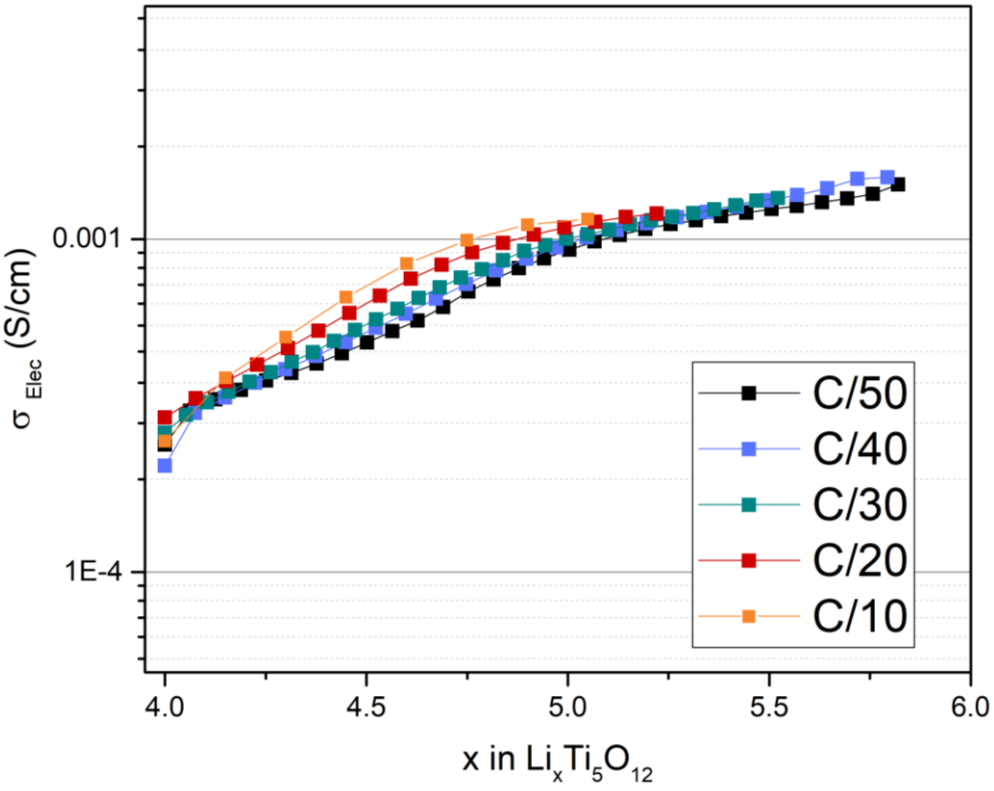

Figure S3.10: Charge of Cycle 2 to Cycle 6, made at different C-rate in LTO (48 h). The curves are pushed to x = 4 starting point for the sake of comparison. Discharge is made at C/50, without any electronic conductivity measure made.

Appendix Chapter 4

4.1: Cycling behaviour of NMC 622 + Li_6PS_5Cl (70/30 wt. %) composites, with or without 1.5 wt.% VGCF.

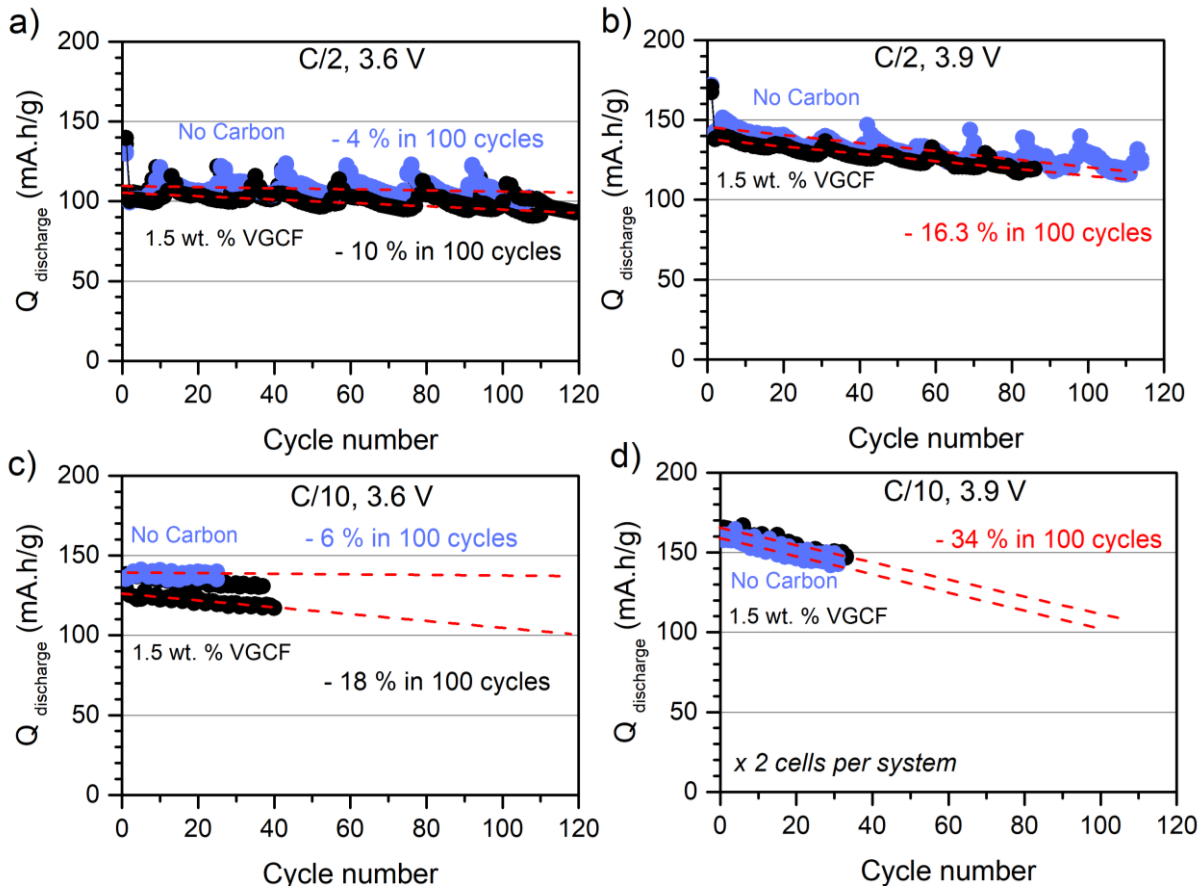

Figure S4.1: Cycling behaviour of NMC 622 + Li_6PS_5Cl composites (70/30 wt. %). 1.5 wt. % additional VGCF can be used. **(a)** Cycling in C-free and C-containing system, at C/2 and up to 3.6 V vs. Li-In/In. **(b)** Cycling in C-free and C-containing system, at C/2 and up to 3.9 V vs. Li-In/In. **(c)** Cycling in C-free and C-containing system, at C/10 and up to 3.6 V vs. Li-In/In. **(d)** Cycling in C-free and C-containing system, at C/10 and up to 3.9 V vs. Li-In/In. Two cells are shown per system.

4.2: Cycling behaviour of NMC 811 + Li_6PS_5Cl (70/30 wt. %) composites, with or without 1.5 wt. % VGCF

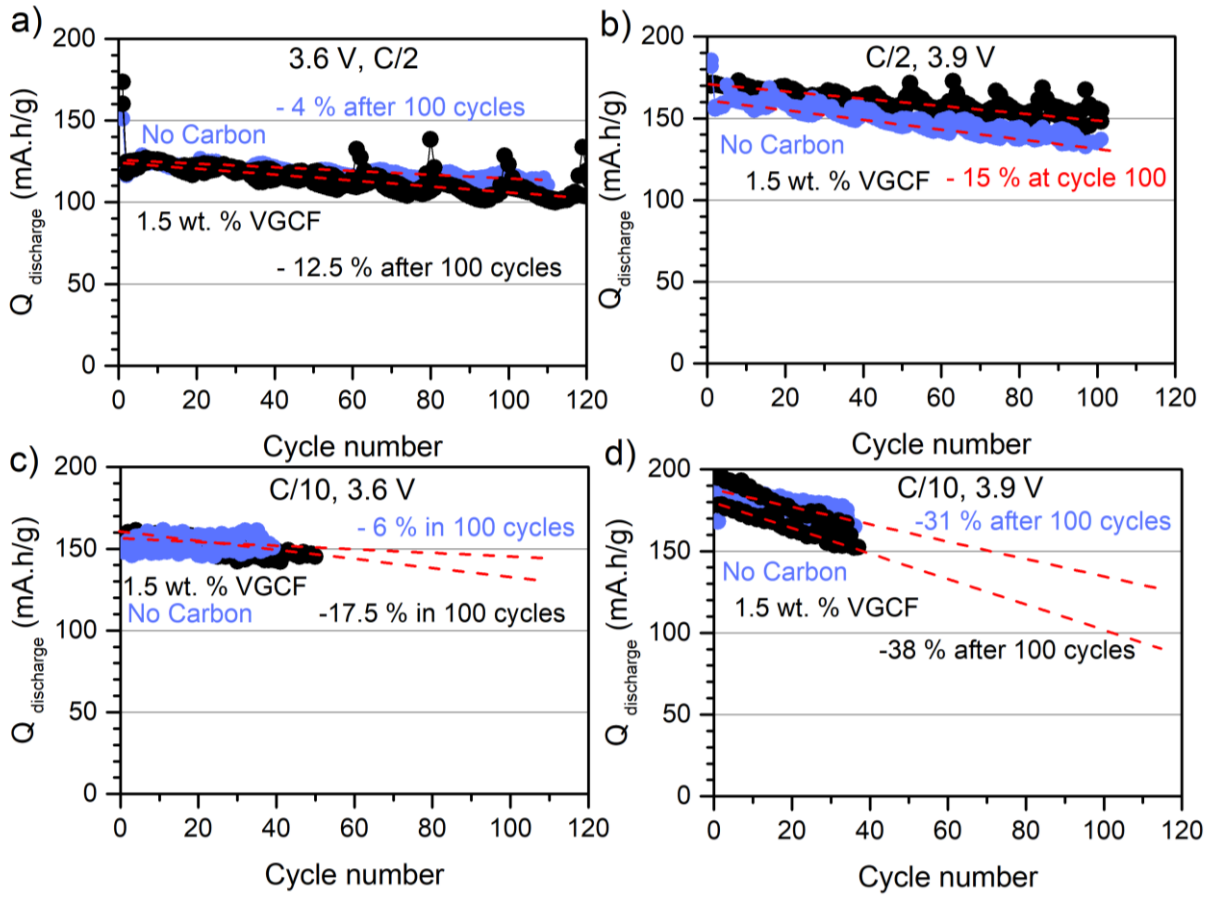

Figure S4.2: Cycling behaviour of NMC 811 + Li_6PS_5Cl composites (70/30 wt. %). 1.5 wt. % additional VGCF can be used. **(a)** Cycling in C-free and C-containing system, at C/2 and up to 3.6 V vs. Li-In/In. **(b)** Cycling in C-free and C-containing system, at C/2 and up to 3.9 V vs. Li-In/In. **(c)** Cycling in C-free and C-containing system, at C/10 and up to 3.6 V vs. Li-In/In. **(d)** Cycling in C-free and C-containing system, at C/10 and up to 3.9 V vs. Li-In/In. Two cells are shown per system.

4.3: Original capacity retention curves as function of assembly pressure

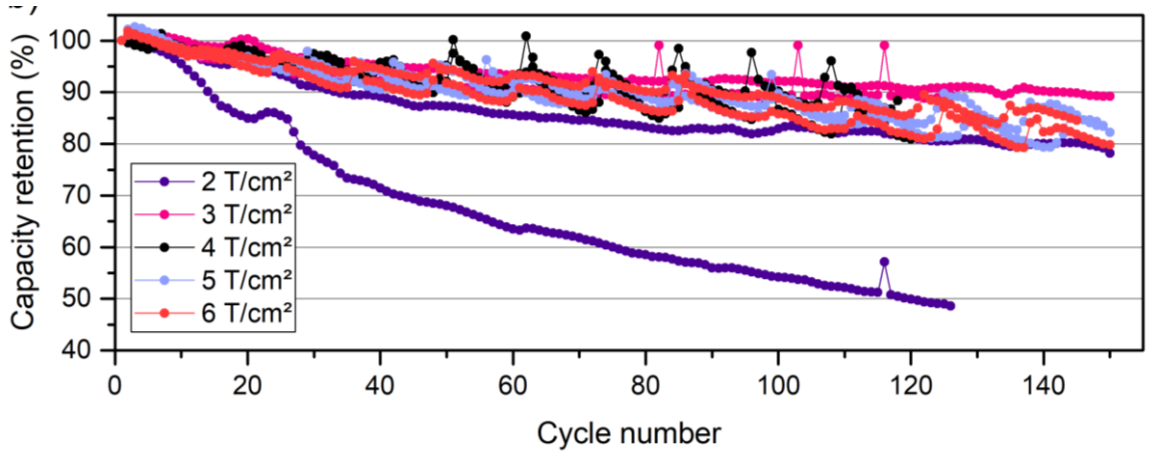

Figure S4.3: Capacity retention versus cycle number as function of assembly pressure. The assembly pressure is defined between 2 T/cm² and 6 T/cm², and applied for 10 minutes on the battery stack. The first cycle is made at C/10, in the [2.1- 3.9 V vs. Li-In/In] potential window. Two cells per system are presented with at least 100 cycles for each.

4.4: Effect of carbonates coating on high potential cycling of NMC 622 (UMICORE, stored outside for a year prior it was sent to us)

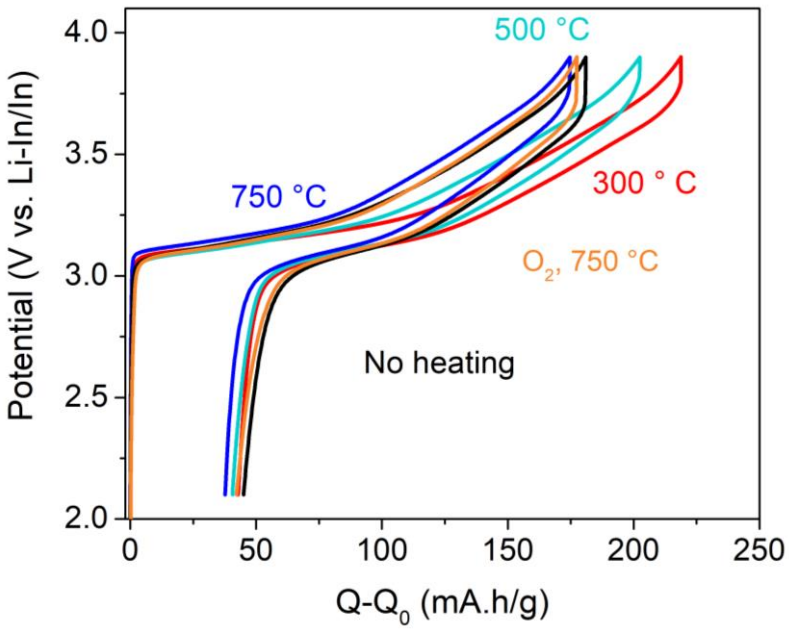

Figure S4.4: First cycle curves of C-free carbonate-coated NMC 622 (UMICORE, stored) composites. Galvanostatic cycling is done at C/10, in the [2.1-3.9 V vs. Li-In/In] potential window.

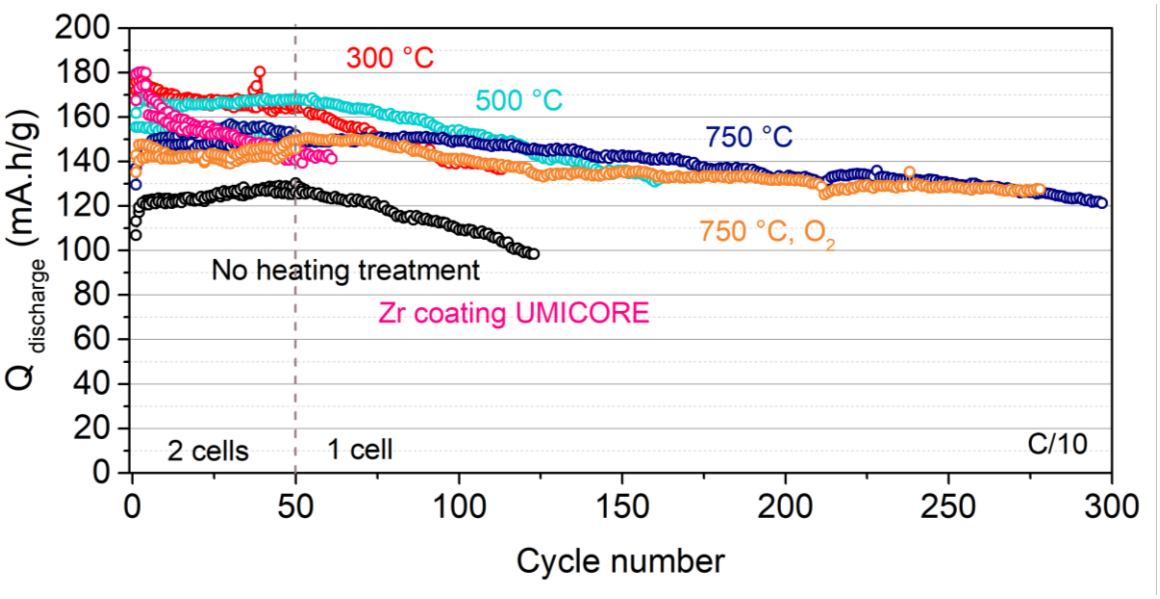

Figure S4.5: Galvanostatic cycling of C-free carbonate-coated NMC 622 (UMICORE, stored) composites, at C/10 in the [2.1-3.9 V vs. Li-In/In] potential window.

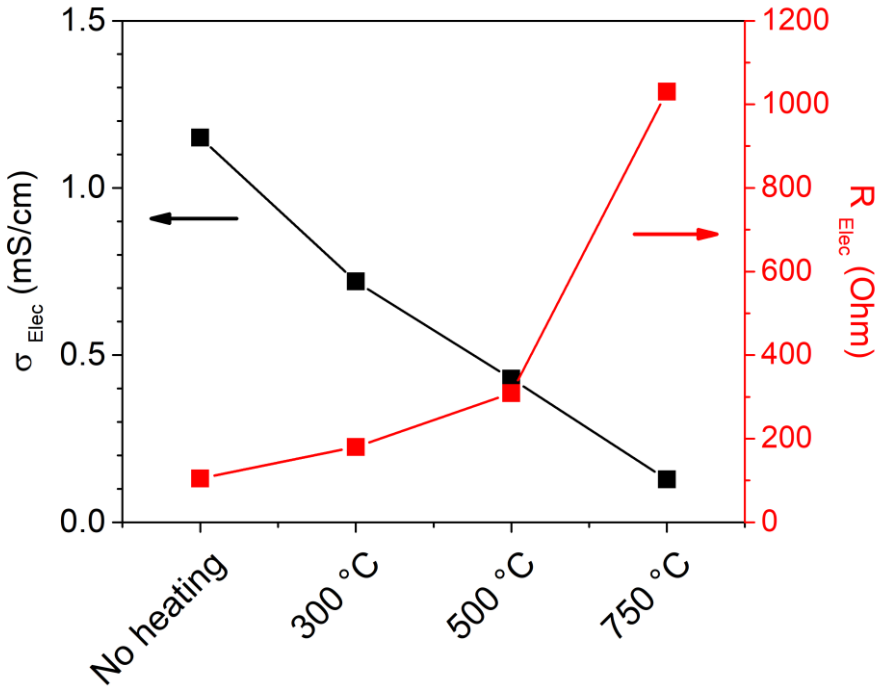

Figure S4.6: Electronic conductivity with one pellet done for each air treated NMC 622-based composites

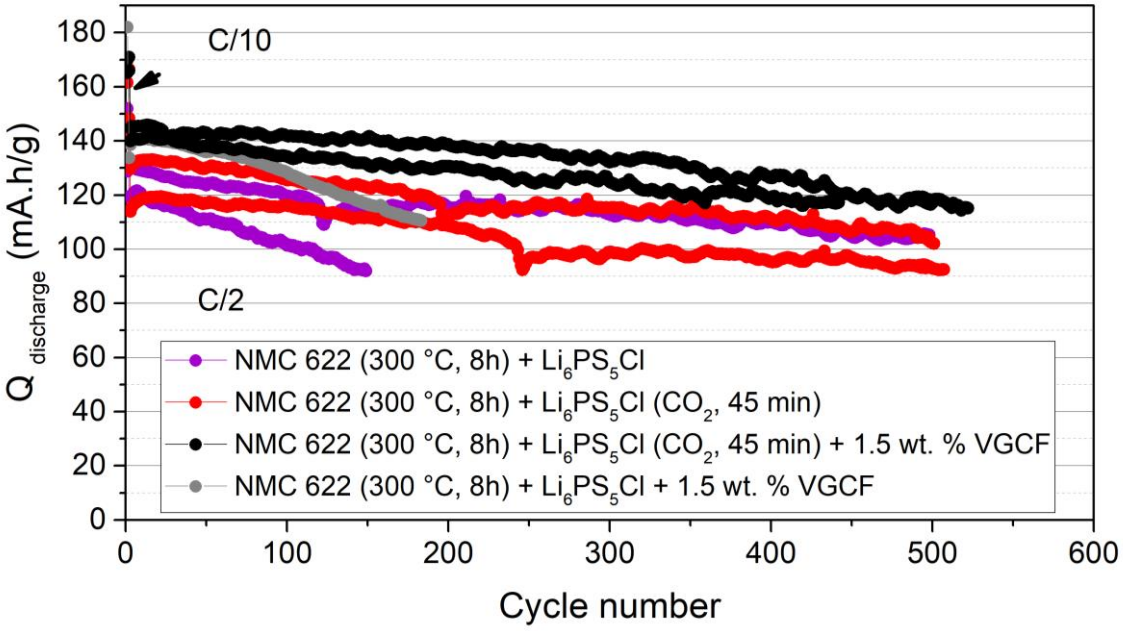

Figure S4.7: Impact of carbonate-coated Li_6PS_5Cl on the high potential stability of NMC 622 (stored) composites.

4.5: Picture of the setup used for CO_2 flow on Li_6PS_5Cl powder

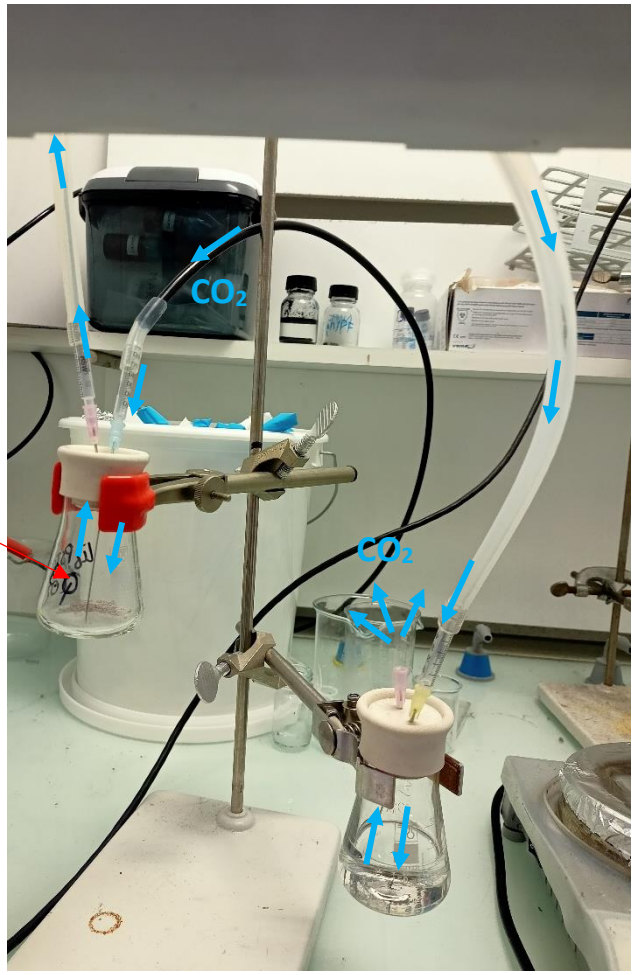

Figure S4.8: Picture of the setup used to coat argyrodite with carbonates.

4.6: Original capacity retention curves as function of formation cycle number

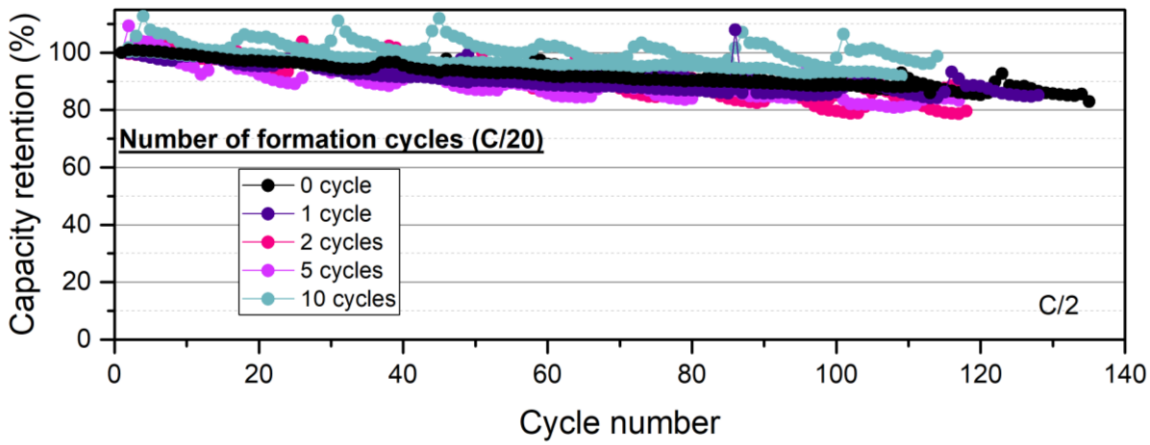

Figure S4.9: Impact of formation cycle number on NMC811 C-containing composite, using 1, 2, 5, 10 or no formation cycle. A formation cycle is made at C/20, in the potential window of [2.1-3.9 V vs. Li-In/In]. Capacity retention (%) versus cycle number, starting after the formation protocol. Two cells are depicted per system with at least 100 cycles for each.

4.7: Shifting the 10 cycles curves

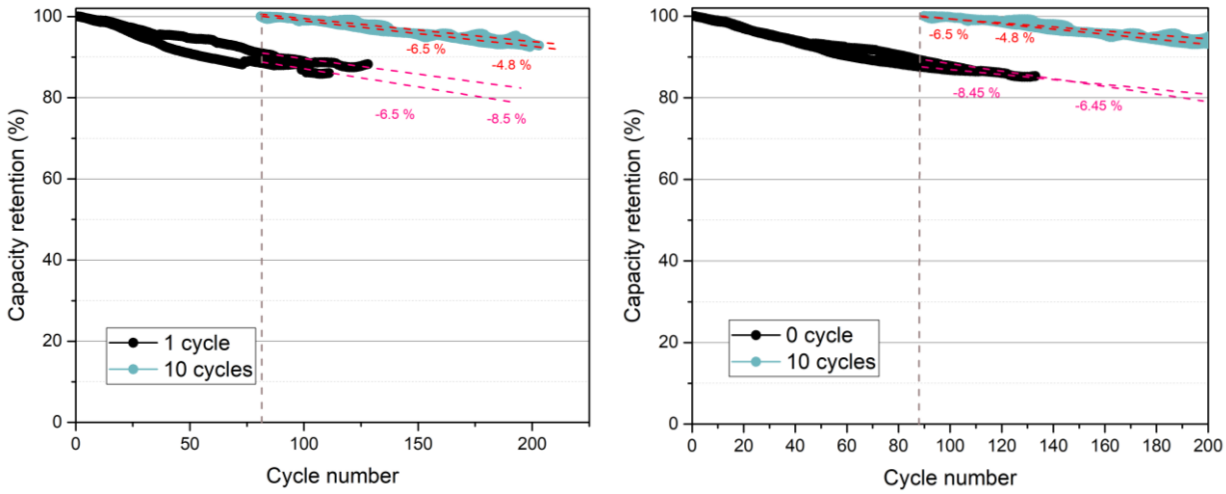

Figure S4.10: The 10 cycles curves are shifted on the cycle number axis, to reach a same "starting time" as the 0 or 1 cycles curves. On the left, 1 cycle is compared with 10 formation cycles. On the right, 0 cycle is compared with 10 formation cycles.

4.8: Original discharge capacity and capacity retention curves as function of high cut-off potential of formation cycle

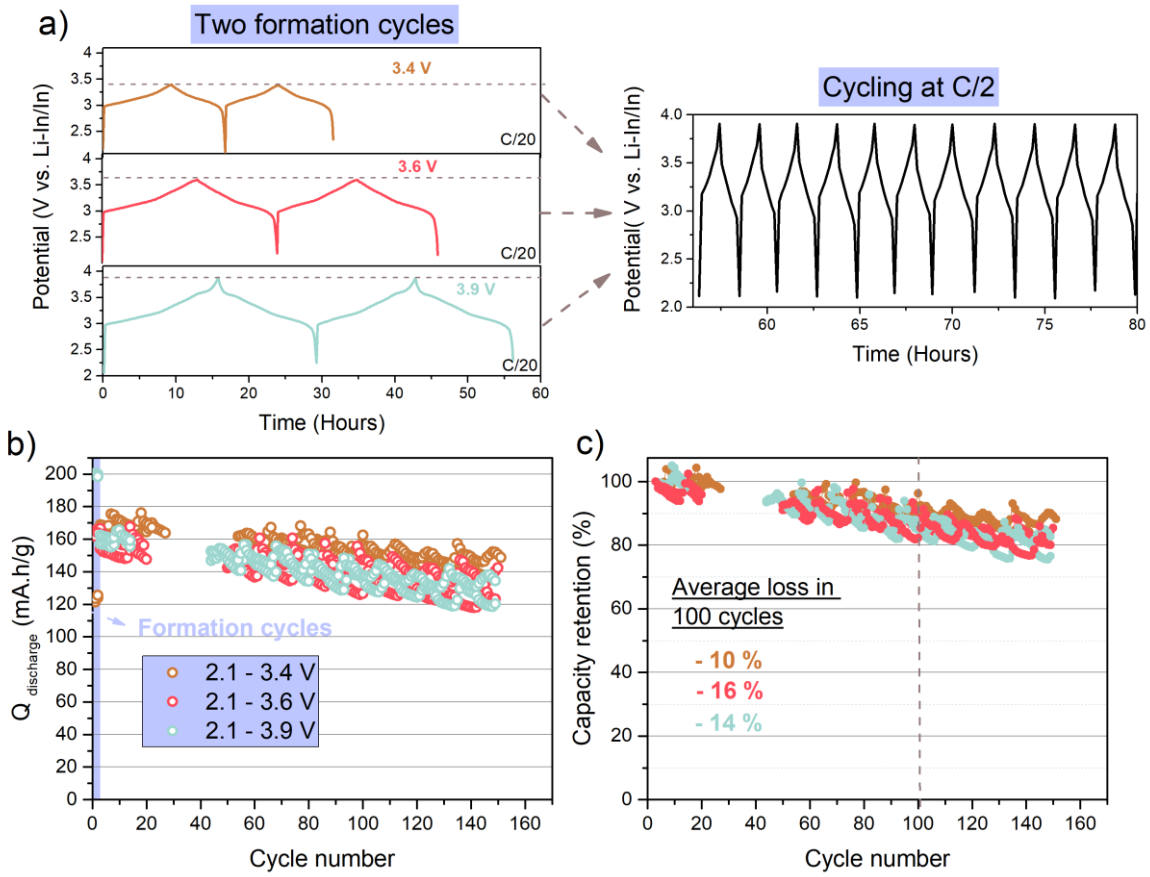

Figure S4.11: (a) Schematic of the cycling protocol for formation cycles: 2 cycles are done at C/20 with distinct cut-off potential, namely 3.4, 3.6 and 3.9 V vs. Li-In/In. The lower cut-off potential is defined at 2.1 V vs. Li-In/In. The following cycles are done at C/2 in the potential window of [2.1 – 3.9 V vs. Li-In/In]. **(b)** The resulting discharge capacities are plotted as function of cycle number, and compared with the pristine curves. Two cells are plotted per system with at least 100 cycles for each. **(c)** Capacity retention of the aforementioned cells.

4.9: Original discharge capacity and capacity retention curves as function of low cut-off potential of formation cycle

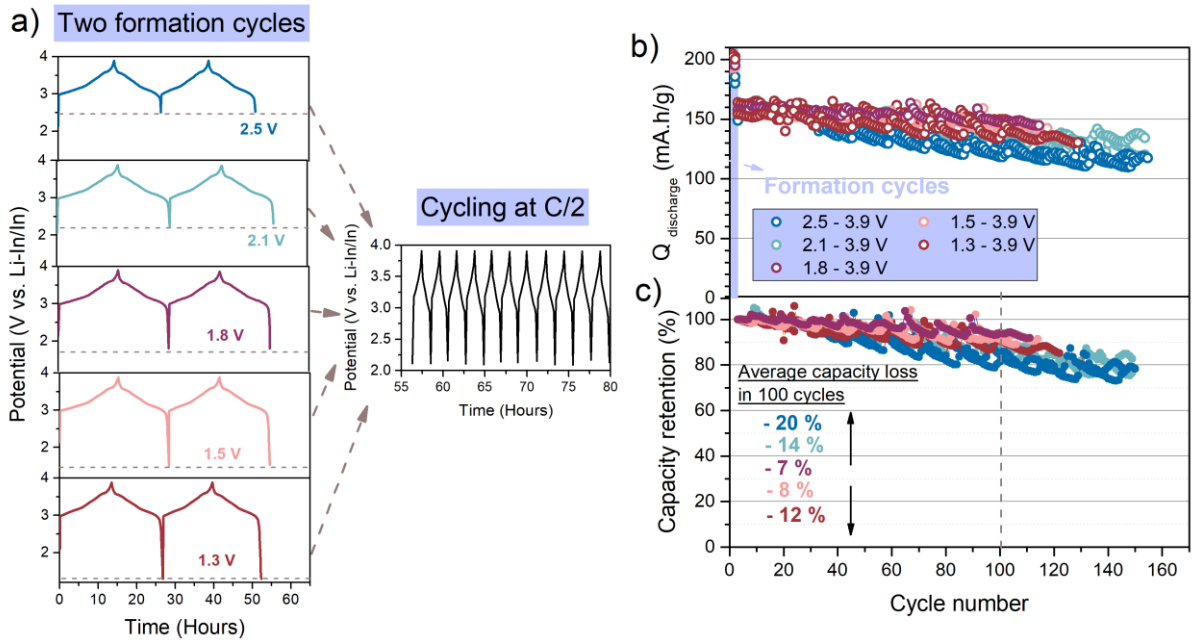

Figure S4.12: **(a)** Schematic of the cycling protocol for formation cycles: 2 cycles are done at C/20 with distinct low cut-off potential, namely 2.5, 2.1, 1.8, 1.5 and 1.3 V vs. Li-In/In. The upper cut-off potential is defined at 3.9 V vs. Li-In/In. The following cycles are done at C/2 in the potential window of [2.1 – 3.9 V vs. Li-In/In]. **(b)** The resulting discharge capacities are plotted as function of cycle number, and compared with the pristine curves. Two cells are plotted per system with at least 100 cycles for each. **(c)** Capacity retention of the aforementioned cells.

4.10: Exploring new paths to enhance the stability of ASSB composites

We decided to explore the impact of two coatings made by industrials and of halide solid electrolytes on the stability of ASSB cells.

Starting with coatings, we used a $LiNbO_3$ coated NMC 622 (1.5 wt. %) from MSE company and a Zr-based coating from UMICORE company (~7 nm coating). Both AM present a monolithic morphology and a similar particle size around 4 µm (see **Figure S4.13** insets for further details). The capacity retention is depicted in **Figure S4.13**. The materials reach, after 380 cycles and at C/2, 120 and 135 mA.h/g and 9.8 % and 29 % capacity loss for the $LiNbO_3$ and Zr-based coated AM, respectively.

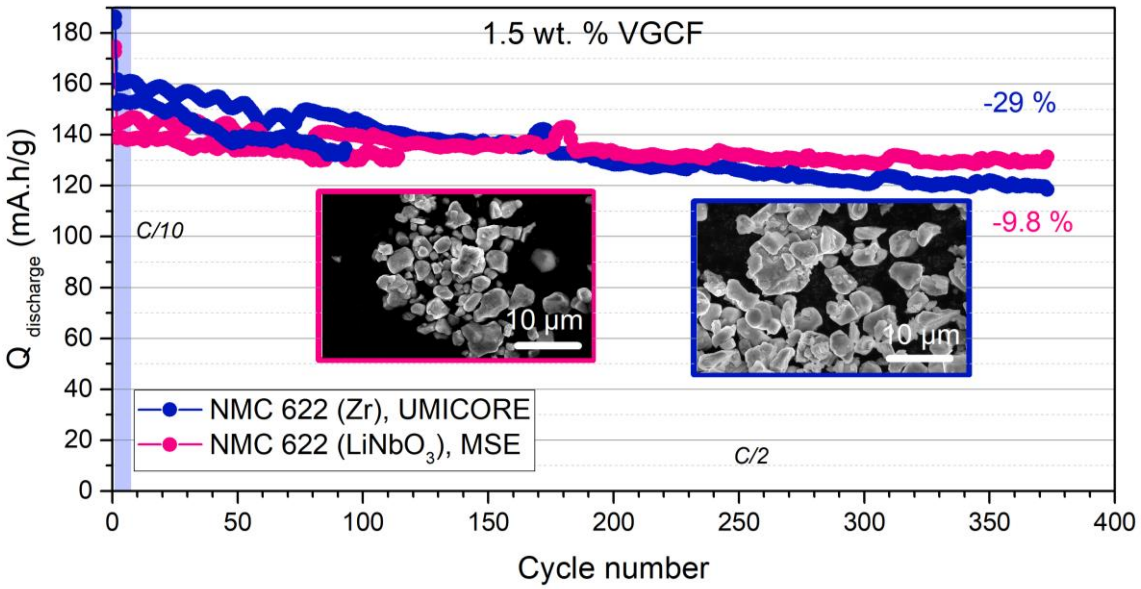

Figure S4.13: Capacity retention at C/2 between 2.1 and 3.9 V vs. Li-In/In, after one cycle at C/10 in the 2.1-3.9 V vs. Li-In/In potential window. We use a NMC 622 (UMICORE, Zr-based coating) or a NMC 622 (MSE, $LiNbO_3$ coated) + Li_6PS_5Cl in a 70/30 wt. % ratio, with the addition of 1.5 wt. % VGCF. Two cells per system are shown.

We conducted tests on **Halide SEs**, namely $Li_3YBr_2Cl_4$ (LYBC pristine or sieved < 5 µm) provided by Saint Gobain and Li_3InCl_6 (LIC) obtained from homemade synthesis, to evaluate their capacity retention at a C/2 rate (see **Figure S4.14**). Please refer to the following **materials and method** section for details on these solid electrolytes and the cell assembly protocol. The first cycle at C/10 is depicted in **Figure S4.15**. LYBC (pristine or sieved < 5 µm) solid electrolytes

showed a higher capacity than Li_6PS_5Cl, with an additional 15 mA.h/g (resulting in a capacity of around 195 mA.h/g at C/10). However, despite the capacity advantage, the capacity retention was found to be quite similar to Li_6PS_5Cl, with an average capacity loss of 13 % over 100 cycles. Note that decreasing the cut-off potential to 3.7 V vs. Li-In/In did not improve capacity retention for LYBC, but made it worse, with an average capacity loss of 25 % after 100 cycles, as shown in the **Figure S4.16**. Finally, Li_3InCl_6 exhibited a capacity of 160 mA.h/g at C/2 and an average capacity loss of 9 % over 100 cycles, which is slightly higher than our reference cells with Li_6PS_5Cl. We additionally tried Li_3YBr_6 (LYB) and Li_3YCl_6 (LYC) solid electrolytes provided by Saint Gobain, but they both display disastrous capacity, as depicted in **Figure S4.17**. In summary, the capacity retentions obtained in this chapter are shown in **Figure S4.18**. The optimized NMC 811-Li_6PS_5Cl cells (shown in **Figure 4.15**) and the NMC 622 ($LiNbO_3$)-Li_6PS_5Cl cells exhibited the best stability, with respectively 8 and 2.8 % capacity loss in 100 cycles. Moreover, they present a good C/2 capacity ranging from 140 to 160 mA.h/g.

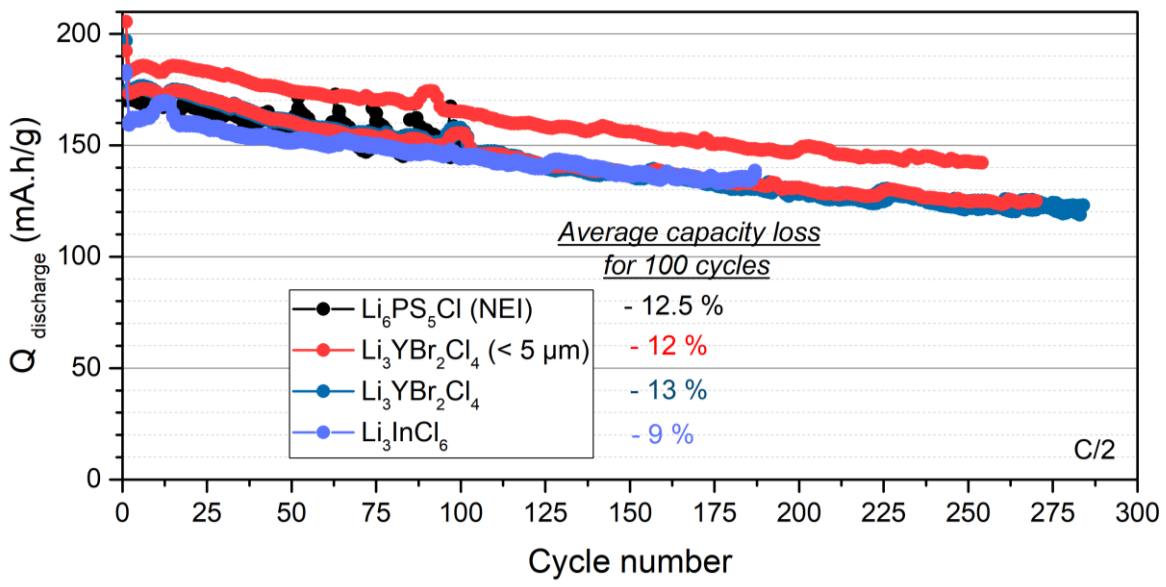

Figure S4.14: Capacity retention at C/2 between 2.1 and 3.9 V vs. Li-In/In, after one cycle at C/10 in the 2.1-3.9 V vs. Li-In/In potential window. We use NMC 811 (MSE) as active material, and distinct solid electrolyte in a 70/30 wt. % ratio, with the addition of 1.5 wt. % VGCF. The solid electrolyte used are: Li_6PS_5Cl (NEI), $Li_3YBr_2Cl_4$ (LYBC) sieved < 5 µm or not from Saint Gobain and Li_3InCl_6 (LIC) homemade synthesized. Two cells per system are shown. All cells were launched on the same week.

First cycle at C/10 of halide composites

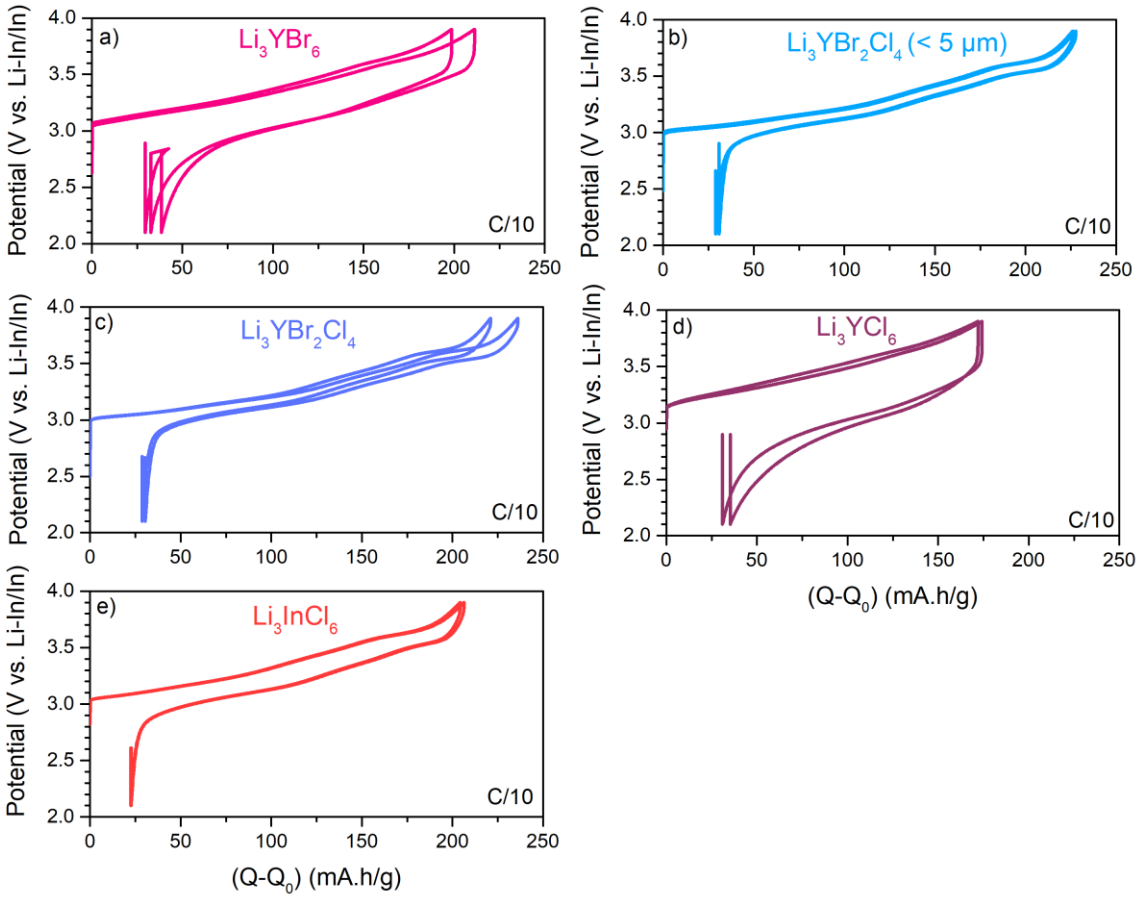

Figure S4.15: First cycle at C/10 and up to 3.9 V vs. Li-In/In of two NMC 811 (MSE) + SE cells per system assembled in a 70/30 wt. % ratio and with an additional 1.5 wt. % VGCF. **(a)** LYB **(b)** LYBC (< 5 µm) **(c)** LYBC **(d)** LYC and **(e)** LIC.

Capacity retention of LYBC composite up to 3.7 V vs. Li-In/In

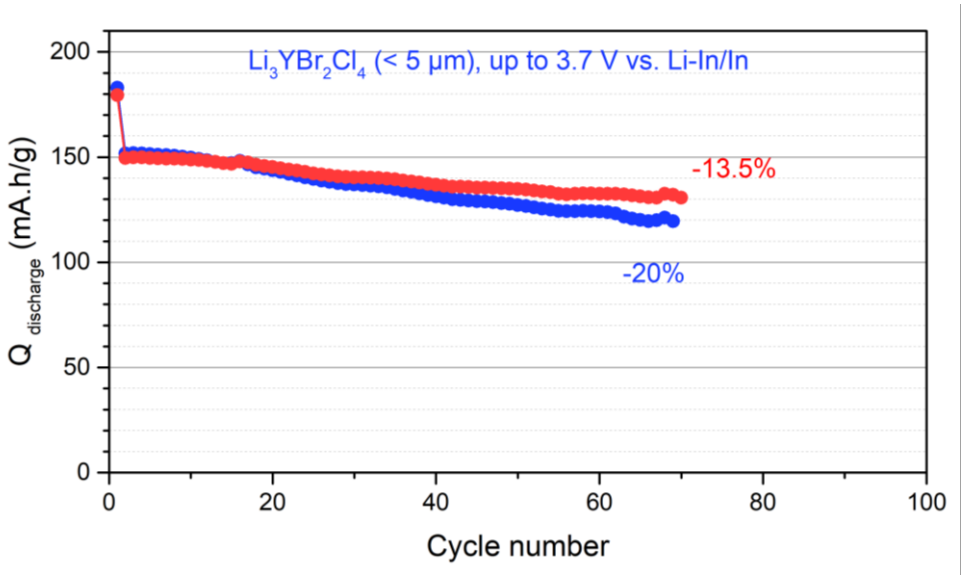

Figure S4.16: Capacity retention up to 3.7 V vs. Li-In/In of two NMC 811 (MSE) + LYBC (< 5 µm) in a 70/30 wt. % ratio with an additional 1.5 wt. % VGCF. First cycle is made at C/10 and is followed by C/2 cycling.

Capacity retention of LYB and LYC based composites

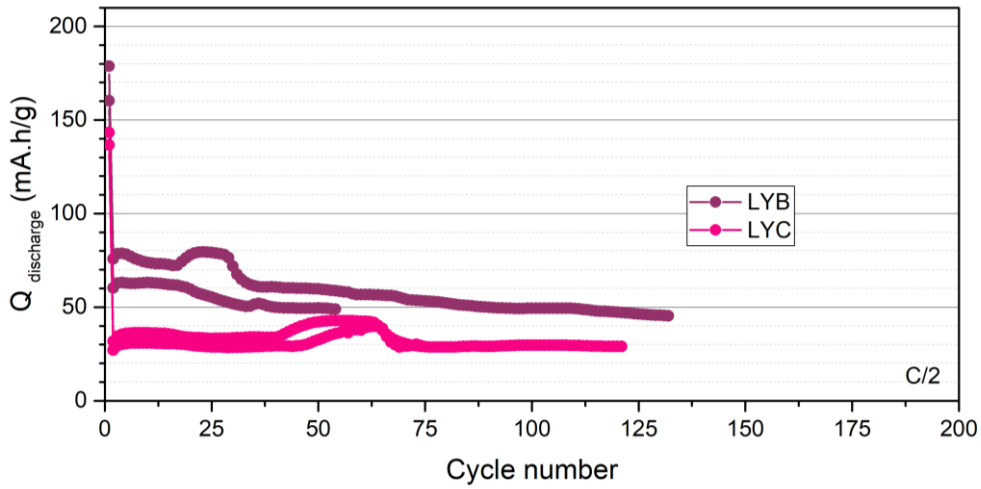

Figure S4.17: Capacity retention up to 3.9 V vs. Li-In/In of two NMC 811 (MSE) + LYB or LYC in a 70/30 wt. % ratio with an additional 1.5 wt. % VGCF. First cycle is made at C/10 and is followed by C/2 cycling.

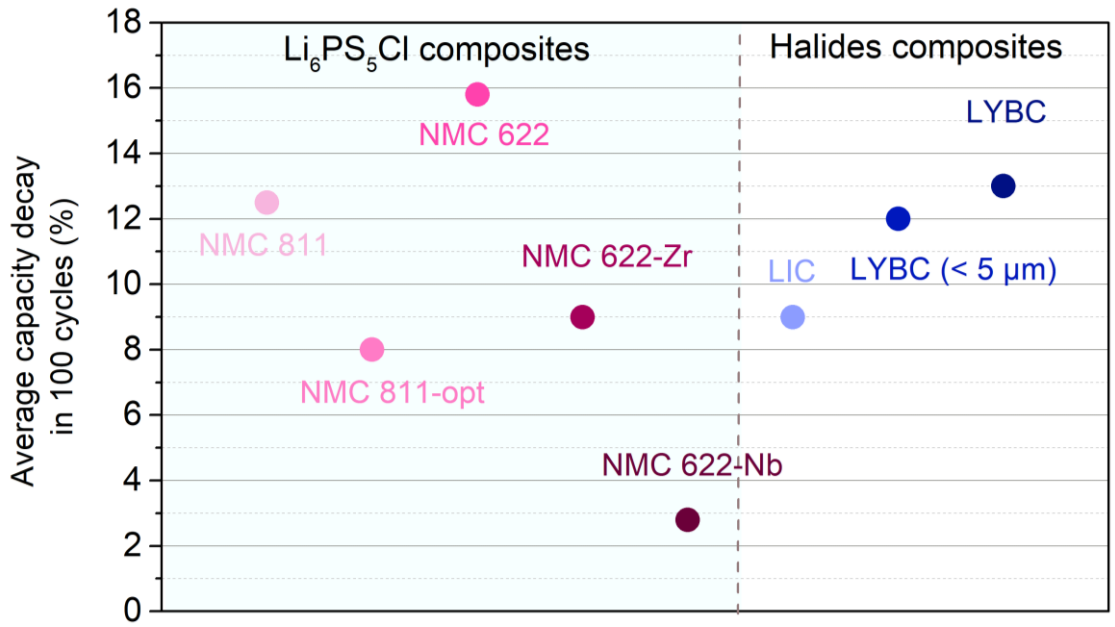

Figure S4.18: Summary of the capacity retention obtained in the systems having a first cycle at C/2 capacity above 135 mA.h/g.

To conclude, despite the preliminary nature of our results, we demonstrated that LYBC halide SE can bring additional capacity. However, the conventional belief that halide solid electrolytes exhibit superior stability compared to the conventional argyrodite is questionable, as similar or worse stability is found using halide. Instead, a more interesting approach to deal with cathode composite stability could be to introduce a well-design coating, as we demonstrated that it can significantly improve the stability. Such methodology necessitates the design of a conformal and thin coating with a repeatable process, something industrials are better equipped to do than academics.

Halide solid electrolytes materials and methods

Solid electrolytes:

LYBC,LYC and LYB were kindly provided by Saint Gobain.

The Li_3InCl_6 SE was synthesized by mechanochemical milling of a stoichiometric mixture of $InCl_3$ and LiCl using planetary ball-mill followed by annealing step, as previously reported[140]. The ball-

mill apparatus was used, with 6 milling process set at 510 rpm for 24 h, applying 15 min milling followed by 15 min of cooling step. After the ball-milling process, the obtained powder was pelletized and annealed at 260 °C (heating rate 5 °C/min) for 5 h in a quartz tube sealed under vacuum. After the annealing process, the sample was cooled naturally.

Cell assembly:

The protocol for the two-electrode cell assembly for halide-based composites follow our typical procedure, with the exception that both the solid electrolyte and anode layer is composed of LYBC. This choice is driven by the well-known reactivity of LIC and LYB at the anode side, opposite to LYBC stability (see **Hennequart B. et al**. *ACS Energy letter*, **2023**, *submitted*).

Lexicon

CC: Constant current

DC: Direct Current

NMC: Lithium Nickel Manganese Cobalt Oxide

LTO: Lithium Titanade Oxide

LCO: Lithium Cobalt Oxide

AM: Active Material

SE: Solid Electrolyte

CE: Counter Electrode

WE: Working Electrode

PEIS: Potentiostatic Electrochemical Impedance Spectroscopy

TLM: Transmission Line Model

TLMO: Transition Layered Metal Oxide

GIIT: Galvanostatic Intermittent Titration Technique

VGCF: Vapour Grown Carbon Fiber

EV: Electric Vehicle

XRD: X-ray diffraction

ASSB: All-Solid-State-Battery

SEM: Scanning Electron Microscopy

CV: Cyclic Voltammetry

LYB: Li_3YBr_6

LYC: Li_3YCl_6

LYBC: $Li_3YBr_2Cl_4$

LIC: Li_3InCl_6

References

(1) Lewis, S. L.; Maslin, M. A. Defining the Anthropocene. *Nature* **2015**, *519* (7542), 171–180. https://doi.org/10.1038/nature14258.

(2) Larcher, D.; Tarascon, J.-M. Towards Greener and More Sustainable Batteries for Electrical Energy Storage. *Nat. Chem.* **2015**, *7* (1), 19–29. https://doi.org/10.1038/nchem.2085.

(3) Goodenough, J. B.; Park, K.-S. The Li-Ion Rechargeable Battery: A Perspective. *J. Am. Chem. Soc.* **2013**, *135* (4), 1167–1176. https://doi.org/10.1021/ja3091438.

(4) Birol, D. F. World Energy Outlook 2022.

(5) Masias, A.; Marcicki, J.; Paxton, W. A. Opportunities and Challenges of Lithium Ion Batteries in Automotive Applications. *ACS Energy Lett.* **2021**, *6* (2), 621–630. https://doi.org/10.1021/acsenergylett.0c02584.

(6) Placke, T.; Kloepsch, R.; Dühnen, S.; Winter, M. Lithium Ion, Lithium Metal, and Alternative Rechargeable Battery Technologies: The Odyssey for High Energy Density. *J. Solid State Electrochem.* **2017**, *21* (7), 1939–1964. https://doi.org/10.1007/s10008-017-3610-7.

(7) Scrosati, B.; Garche, J. Lithium Batteries: Status, Prospects and Future. *J. Power Sources* **2010**, *195* (9), 2419–2430. https://doi.org/10.1016/j.jpowsour.2009.11.048.

(8) Abakumov, A. M.; Fedotov, S. S.; Antipov, E. V.; Tarascon, J.-M. Solid State Chemistry for Developing Better Metal-Ion Batteries. *Nat. Commun.* **2020**, *11* (1), 4976. https://doi.org/10.1038/s41467-020-18736-7.

(9) Whittingham, M. S. Electrical Energy Storage and Intercalation Chemistry. *Science*. 1976, pp 1126–1127.

(10) Whittingham, M. S. Chemistry of Intercalation Compounds: Metal Guests in Chalcogenide Hosts. *Prog.Solid State Chem*. 1978, pp 12, 41–99.

(11) Whittingham, M. S. Lithium Batteries and Cathode Materials. *Chem.Rev.104*. 2004, pp 4271–4302.

(12) Blomgren, G. E. The Development and Future of Lithium Ion Batteries. *J. Electrochem. Soc.* **2017**, *164* (1), A5019–A5025. https://doi.org/10.1149/2.0251701jes.

(13) Lazzari, M.; Scrosati, B. A Cyclable Lithium Organic Electrolyte Cell Based on Two Intercalation Electrodes. *J. Electrochem. Soc.* **1980**, *127* (3), 773–774. https://doi.org/10.1149/1.2129753.

(14) Yazami, R. A Reversible Graphite-Lithium Negative Electrode for Electrochemical Generators. *Journal of Power Sources, 9 (3)*. 1983, pp 365–371.

(15) Mizushima, K.; Jones, P. C.; Wiseman, P. J.; Goodenough, J. B. (Received April 3, 1980; Communicated by J. B. Goodenough). *15* (6).

(16) Ozawa, K. Lithium-Ion Rechargeable Batteries with LiCoO2 and Carbon Electrodes: The LiCoO2/C System. *Solid State Ion.* **1994**, *69* (3–4), 212–221. https://doi.org/10.1016/0167-2738(94)90411-1.

(17) Anesty International. This Is What We Die for: Human Rights Abuses in the Democratic Republic of Congo Power the Global Trade in Cobalt. *Index: AFR 62/3183/2016*. 2016. https://www.amnesty.org/en/documents/afr62/3183/2016/en/.

(18) Tarascon, J. M. The Li-Ion Battery: 25 Years of Exciting and Enriching Experiences. *Interface Mag.* **2016**, *25* (3), 79–83. https://doi.org/10.1149/2.F08163if.

(19) Padhi, A. K.; Nanjundaswamy, K. S.; Goodenough, J. B. Phospho-olivines as Positive-Electrode Materials for Rechargeable Lithium Batteries. *J. Electrochem. Soc.* **1997**, *144* (4), 1188–1194. https://doi.org/10.1149/1.1837571.

(20) Thackeray, M. M.; David, W. I. F.; Bruce, P. G.; Goodenough, J. B. Lithium Insertion into Manganese Spinels. *Mater. Res. Bull.* **1983**, *18* (4), 461–472. https://doi.org/10.1016/0025-5408(83)90138-1.

(21) Lee, S.; Manthiram, A. Can Cobalt Be Eliminated from Lithium-Ion Batteries? *ACS Energy Lett.* **2022**, *7* (9), 3058–3063. https://doi.org/10.1021/acsenergylett.2c01553.

(22) Rozier, P.; Tarascon, J. M. Review—Li-Rich Layered Oxide Cathodes for Next-Generation Li-Ion Batteries: Chances and Challenges. *J. Electrochem. Soc.* **2015**, *162* (14), A2490–A2499. https://doi.org/10.1149/2.0111514jes.

(23) Yoon, C. S.; Park, K.-J.; Kim, U.-H.; Kang, K. H.; Ryu, H.-H.; Sun, Y.-K. High-Energy Ni-Rich Li[Ni $_x$ Co $_y$ Mn $_{1-x-y}$]O $_2$ Cathodes via Compositional Partitioning for Next-Generation Electric Vehicles. *Chem. Mater.* **2017**, *29* (24), 10436–10445. https://doi.org/10.1021/acs.chemmater.7b04047.

(24) Noh, H.-J.; Youn, S.; Yoon, C. S.; Sun, Y.-K. Comparison of the Structural and Electrochemical Properties of Layered Li[NixCoyMnz]O2 (x = 1/3, 0.5, 0.6, 0.7, 0.8 and 0.85) Cathode Material for Lithium-Ion Batteries. *J. Power Sources* **2013**, *233*, 121–130. https://doi.org/10.1016/j.jpowsour.2013.01.063.

(25) Kamaya, N.; Homma, K.; Yamakawa, Y.; Hirayama, M.; Kanno, R.; Yonemura, M.; Kamiyama, T.; Kato, Y.; Hama, S.; Kawamoto, K.; Mitsui, A. A Lithium Superionic Conductor. *Nat. Mater.* **2011**, *10* (9), 682–686. https://doi.org/10.1038/nmat3066.

(26) Janek, J.; Zeier, W. G. A Solid Future for Battery Development. *Nat. Energy* **2016**, *1* (9), 16141. https://doi.org/10.1038/nenergy.2016.141.

(27) Bachman, J. C.; Muy, S.; Grimaud, A.; Chang, H.-H.; Pour, N.; Lux, S. F.; Paschos, O.; Maglia, F.; Lupart, S.; Lamp, P.; Giordano, L.; Shao-Horn, Y. Inorganic Solid-State Electrolytes for Lithium Batteries: Mechanisms and Properties Governing Ion Conduction. *Chem. Rev.* **2016**, *116* (1), 140–162. https://doi.org/10.1021/acs.chemrev.5b00563.

(28) Zhang, Z.; Shao, Y.; Lotsch, B.; Hu, Y.-S.; Li, H.; Janek, J.; Nazar, L. F.; Nan, C.-W.; Maier, J.; Armand, M.; Chen, L. New Horizons for Inorganic Solid State Ion Conductors. *Energy Environ. Sci.* **2018**, *11* (8), 1945–1976. https://doi.org/10.1039/C8EE01053F.

(29) Kasemchainan, J.; Zekoll, S.; Spencer Jolly, D.; Ning, Z.; Hartley, G. O.; Marrow, J.; Bruce, P. G. Critical Stripping Current Leads to Dendrite Formation on Plating in Lithium Anode Solid Electrolyte Cells. *Nat. Mater.* **2019**, *18* (10), 1105–1111. https://doi.org/10.1038/s41563-019-0438-9.

(30) Schnell, J.; Günther, T.; Knoche, T.; Vieider, C.; Köhler, L.; Just, A.; Keller, M.; Passerini, S.; Reinhart, G. All-Solid-State Lithium-Ion and Lithium Metal Batteries – Paving the Way to Large-Scale Production. *J. Power Sources* **2018**, *382*, 160–175. https://doi.org/10.1016/j.jpowsour.2018.02.062.

(31) Lee, Y.-G.; Fujiki, S.; Jung, C.; Suzuki, N.; Yashiro, N.; Omoda, R.; Ko, D.-S.; Shiratsuchi, T.; Sugimoto, T.; Ryu, S.; Ku, J. H.; Watanabe, T.; Park, Y.; Aihara, Y.; Im, D.; Han, I. T. High-Energy Long-Cycling All-Solid-State Lithium Metal Batteries Enabled by Silver–Carbon Composite Anodes. *Nat. Energy* **2020**, *5* (4), 299–308. https://doi.org/10.1038/s41560-020-0575-z.

(32) Albertus, P.; Babinec, S.; Litzelman, S.; Newman, A. Publisher Correction: Status and Challenges in Enabling the Lithium Metal Electrode for High-Energy and Low-Cost Rechargeable Batteries. *Nat. Energy* **2022**, *7* (9), 899–899. https://doi.org/10.1038/s41560-022-01077-8.

(33) Hlushkou, D.; Reising, A. E.; Kaiser, N.; Spannenberger, S.; Schlabach, S.; Kato, Y.; Roling, B.; Tallarek, U. The Influence of Void Space on Ion Transport in a Composite Cathode for All-Solid-State Batteries. *J. Power Sources* **2018**, *396*, 363–370. https://doi.org/10.1016/j.jpowsour.2018.06.041.

(34) Zhang, W.; Schröder, D.; Arlt, T.; Manke, I.; Koerver, R.; Pinedo, R.; Weber, D. A.; Sann, J.; Zeier, W. G.; Janek, J. (Electro)Chemical Expansion during Cycling: Monitoring the Pressure Changes in Operating Solid-State Lithium Batteries. *J. Mater. Chem. A* **2017**, *5* (20), 9929–9936. https://doi.org/10.1039/C7TA02730C.

(35) Zaman, W.; Hatzell, K. B. Processing and Manufacturing of next Generation Lithium-Based All Solid-State Batteries. *Curr. Opin. Solid State Mater. Sci.* **2022**, *26* (4), 101003. https://doi.org/10.1016/j.cossms.2022.101003.
(36) Kato, Y.; Shiotani, S.; Morita, K.; Suzuki, K.; Hirayama, M.; Kanno, R. All-Solid-State Batteries with Thick Electrode Configurations. *J. Phys. Chem. Lett.* **2018**, *9* (3), 607–613. https://doi.org/10.1021/acs.jpclett.7b02880.
(37) Schnell, J.; Tietz, F.; Singer, C.; Hofer, A.; Billot, N.; Reinhart, G. Prospects of Production Technologies and Manufacturing Costs of Oxide-Based All-Solid-State Lithium Batteries. *Energy Environ. Sci.* **2019**, *12* (6), 1818–1833. https://doi.org/10.1039/C8EE02692K.
(38) Mauler, L.; Duffner, F.; Zeier, W. G.; Leker, J. Battery Cost Forecasting: A Review of Methods and Results with an Outlook to 2050. *Energy Environ. Sci.* **2021**, *14* (9), 4712–4739. https://doi.org/10.1039/D1EE01530C.
(39) Horváth, D. V.; Tian, R.; Gabbett, C.; Nicolosi, V.; Coleman, J. N. Quantifying the Effect of Separator Thickness on Rate Performance in Lithium-Ion Batteries. *J. Electrochem. Soc.* **2022**, *169* (3), 030503. https://doi.org/10.1149/1945-7111/ac5654.
(40) Balaish, M.; Gonzalez-Rosillo, J. C.; Kim, K. J.; Zhu, Y.; Hood, Z. D.; Rupp, J. L. M. Processing Thin but Robust Electrolytes for Solid-State Batteries. *Nat. Energy* **2021**, *6* (3), 227–239. https://doi.org/10.1038/s41560-020-00759-5.
(41) Bielefeld, A.; Weber, D. A.; Janek, J. Microstructural Modeling of Composite Cathodes for All-Solid-State Batteries. *J. Phys. Chem. C* **2019**, *123* (3), 1626–1634. https://doi.org/10.1021/acs.jpcc.8b11043.
(42) Bielefeld, A.; Weber, D. A.; Janek, J. Modeling Effective Ionic Conductivity and Binder Influence in Composite Cathodes for All-Solid-State Batteries. *ACS Appl. Mater. Interfaces* **2020**, *12* (11), 12821–12833. https://doi.org/10.1021/acsami.9b22788.
(43) Minnmann, P.; Strauss, F.; Bielefeld, A.; Ruess, R.; Adelhem, P.; Burkhard, S.; Trevisanello, E.; Brezesinski, T.; Janek, J. Designing Cathodes and Cathode Active Materials for Solid-State Batteries. *Advanced Energy Materials*. 2022. https://doi.org/10.1002/aenm.202201425.
(44) Raju, M. M.; Altayran, F.; Johnson, M.; Wang, D.; Zhang, Q. Crystal Structure and Preparation of Li7La3Zr2O12 (LLZO) Solid-State Electrolyte and Doping Impacts on the Conductivity: An Overview. *Electrochem* **2021**, *2* (3), 390–414. https://doi.org/10.3390/electrochem2030026.
(45) Tsai, C.-L.; Ma, Q.; Dellen, C.; Lobe, S.; Vondahlen, F.; Windmüller, A.; Grüner, D.; Zheng, H.; Uhlenbruck, S.; Finsterbusch, M.; Tietz, F.; Fattakhova-Rohlfing, D.; Buchkremer, H. P.; Guillon, O. A Garnet Structure-Based All-Solid-State Li Battery without Interface Modification: Resolving Incompatibility Issues on Positive Electrodes. *Sustain. Energy Fuels* **2019**, *3* (1), 280–291. https://doi.org/10.1039/C8SE00436F.
(46) Behnood, A.; Modiri Gharehveran, M. Morphology, Rheology, and Physical Properties of Polymer-Modified Asphalt Binders. *Eur. Polym. J.* **2019**, *112*, 766–791. https://doi.org/10.1016/j.eurpolymj.2018.10.049.
(47) Rubio, M. C.; Martínez, G.; Baena, L.; Moreno, F. Warm Mix Asphalt: An Overview. *J. Clean. Prod.* **2012**, *24*, 76–84. https://doi.org/10.1016/j.jclepro.2011.11.053.
(48) Ferraris, C. F. Concrete Mixing Methods and Concrete Mixers: State of the Art. *J. Res. Natl. Inst. Stand. Technol.* **2001**, *106* (2), 391. https://doi.org/10.6028/jres.106.016.
(49) Kerman, K.; Luntz, A.; Viswanathan, V.; Chiang, Y.-M.; Chen, Z. Review—Practical Challenges Hindering the Development of Solid State Li Ion Batteries. *J. Electrochem. Soc.* **2017**, *164* (7), A1731–A1744. https://doi.org/10.1149/2.1571707jes.
(50) Park, K. H.; Bai, Q.; Kim, D. H.; Oh, D. Y.; Zhu, Y.; Mo, Y.; Jung, Y. S. Design Strategies, Practical Considerations, and New Solution Processes of Sulfide Solid Electrolytes for All-Solid-State Batteries. *Adv. Energy Mater.* **2018**, *8* (18), 1800035. https://doi.org/10.1002/aenm.201800035.
(51) Kim, J.; Kim, M. J.; Kim, J.; Lee, J. W.; Park, J.; Wang, S. E.; Lee, S.; Kang, Y. C.; Paik, U.; Jung, D. S.; Song, T. High-Performance All-Solid-State Batteries Enabled by Intimate Interfacial Contact

Between the Cathode and Sulfide-Based Solid Electrolytes. *Adv. Funct. Mater.* **2023**, *33* (12), 2211355. https://doi.org/10.1002/adfm.202211355.

(52) Cronau, M.; Duchardt, M.; Szabo, M.; Roling, B. Ionic Conductivity versus Particle Size of Ball-Milled Sulfide-Based Solid Electrolytes: Strategy Towards Optimized Composite Cathode Performance in All-Solid-State Batteries. *Batter. Supercaps* **2022**, *5* (6). https://doi.org/10.1002/batt.202200041.

(53) Inada, T. Fabrications and Properties of Composite Solid-State Electrolytes. *Solid State Ion.* **2003**, *158* (3–4), 275–280. https://doi.org/10.1016/S0167-2738(02)00889-5.

(54) Nam, Y. J.; Cho, S.-J.; Oh, D. Y.; Lim, J.-M.; Kim, S. Y.; Song, J. H.; Lee, Y.-G.; Lee, S.-Y.; Jung, Y. S. Bendable and Thin Sulfide Solid Electrolyte Film: A New Electrolyte Opportunity for Free-Standing and Stackable High-Energy All-Solid-State Lithium-Ion Batteries. *Nano Lett.* **2015**, *15* (5), 3317–3323. https://doi.org/10.1021/acs.nanolett.5b00538.

(55) Laue, V.; Wolff, N.; Roder, F.; Krewer, U. Modeling the Influence of Mixing Strategies onMicrostructural Properties of All-Solid-State Electrodes Vincent Laue, Nicolas Wolff, Fridolin Röder, and Ulrike Krewe. *Energy Technology*. 2020. https://doi.org/10.1002/ente.201801049.

(56) Nam, Y. J.; Oh, D. Y.; Jung, S. H.; Jung, Y. S. Toward Practical All-Solid-State Lithium-Ion Batteries with High Energy Density and Safety: Comparative Study for Electrodes Fabricated by Dry- and Slurry-Mixing Processes. *J. Power Sources* **2018**, *375*, 93–101. https://doi.org/10.1016/j.jpowsour.2017.11.031.

(57) Zhang, F.; Guo, Y.; Zhang, L.; Jia, P.; Liu, X.; Qiu, P.; Zhang, H.; Huang, J. A Review of the Effect of External Pressure on All-Solid-State Batteries. *eTransportation* **2023**, *15*, 100220. https://doi.org/10.1016/j.etran.2022.100220.

(58) Doux, J.-M.; Nguyen, H.; Tan, D. H. S.; Banerjee, A.; Wang, X.; Wu, E. A.; Jo, C.; Yang, H.; Meng, Y. S. Stack Pressure Considerations for Room-Temperature All-Solid-State Lithium Metal Batteries. *Adv. Energy Mater.* **2020**, *10* (1), 1903253. https://doi.org/10.1002/aenm.201903253.

(59) Shi, T.; Tu, Q.; Tian, Y.; Xiao, Y.; Miara, L. J.; Kononova, O.; Ceder, G. High Active Material Loading in All-Solid-State Battery Electrode via Particle Size Optimization. *Adv. Energy Mater.* **2020**, *10* (1), 1902881. https://doi.org/10.1002/aenm.201902881.

(60) Zhang, W.; Leichtweiß, T.; Culver, S. P.; Koerver, R.; Das, D.; Weber, D. A.; Zeier, W. G.; Janek, J. The Detrimental Effects of Carbon Additives in $Li_{10}GeP_2S_{12}$ -Based Solid-State Batteries. *ACS Appl. Mater. Interfaces* **2017**, *9* (41), 35888–35896. https://doi.org/10.1021/acsami.7b11530.

(61) Froboese, L.; Sichel, J. F. V. D.; Loellhoeffel, T.; Helmers, L.; Kwade, A. Effect of Microstructure on the Ionic Conductivity of an All Solid-State Battery Electrode. *J. Electrochem. Soc.* **2019**, *166* (2), A318–A328. https://doi.org/10.1149/2.0601902jes.

(62) Strauss, F.; Bartsch, T.; de Biasi, L.; Kim, A.-Y.; Janek, J.; Hartmann, P.; Brezesinski, T. Impact of Cathode Material Particle Size on the Capacity of Bulk-Type All-Solid-State Batteries. *ACS Energy Lett.* **2018**, *3* (4), 992–996. https://doi.org/10.1021/acsenergylett.8b00275.

(63) Ren, Y.; Chen, K.; Chen, R.; Liu, T.; Zhang, Y.; Nan, C.-W. Oxide Electrolytes for Lithium Batteries. *J. Am. Ceram. Soc.* **2015**, *98* (12), 3603–3623. https://doi.org/10.1111/jace.13844.

(64) Wang, C.; Liang, J.; Kim, J. T.; Sun, X. Prospects of Halide-Based All-Solid-State Batteries: From Material Design to Practical Application. *Sci. Adv.* **2022**, *8* (36), eadc9516. https://doi.org/10.1126/sciadv.adc9516.

(65) Nikodimos, Y.; Huang, C.-J.; Taklu, B. W.; Su, W.-N.; Hwang, B. J. Chemical Stability of Sulfide Solid-State Electrolytes: Stability toward Humid Air and Compatibility with Solvents and Binders. *Energy Environ. Sci.* **2022**, *15* (3), 991–1033. https://doi.org/10.1039/D1EE03032A.

(66) Zhu, Y.; He, X.; Mo, Y. Origin of Outstanding Stability in the Lithium Solid Electrolyte Materials: Insights from Thermodynamic Analyses Based on First-Principles Calculations. *ACS Appl. Mater. Interfaces* **2015**, *7* (42), 23685–23693. https://doi.org/10.1021/acsami.5b07517.

(67) Dewald, G. F.; Ohno, S.; Kraft, M. A.; Koerver, R.; Till, P.; Vargas-Barbosa, N. M.; Janek, J.; Zeier, W. G. Experimental Assessment of the Practical Oxidative Stability of Lithium Thiophosphate Solid Electrolytes. *Chem. Mater.* **2019**, *31* (20), 8328–8337. https://doi.org/10.1021/acs.chemmater.9b01550.

(68) Han, F.; Zhu, Y.; He, X.; Mo, Y.; Wang, C. Electrochemical Stability of $Li_{10}GeP_2S_{12}$ and $Li_7La_3Zr_2O_{12}$ Solid Electrolytes. *Adv. Energy Mater.* **2016**, *6* (8), 1501590. https://doi.org/10.1002/aenm.201501590.

(69) Koç, T.; Hallot, M.; Quemin, E.; Hennequart, B.; Dugas, R.; Abakumov, A. M.; Lethien, C.; Tarascon, J.-M. Toward Optimization of the Chemical/Electrochemical Compatibility of Halide Solid Electrolytes in All-Solid-State Batteries. *ACS Energy Lett.* **2022**, *7* (9), 2979–2987. https://doi.org/10.1021/acsenergylett.2c01668.

(70) Zuo, T.-T.; Rueß, R.; Pan, R.; Walther, F.; Rohnke, M.; Hori, S.; Kanno, R.; Schröder, D.; Janek, J. A Mechanistic Investigation of the Li10GeP2S12|LiNi1-x-yCoxMnyO2 Interface Stability in All-Solid-State Lithium Batteries. *Nat. Commun.* **2021**, *12* (1), 6669. https://doi.org/10.1038/s41467-021-26895-4.

(71) Koerver, R.; Aygün, I.; Leichtweiß, T.; Dietrich, C.; Zhang, W.; Binder, J. O.; Hartmann, P.; Zeier, W. G.; Janek, J. Capacity Fade in Solid-State Batteries: Interphase Formation and Chemomechanical Processes in Nickel-Rich Layered Oxide Cathodes and Lithium Thiophosphate Solid Electrolytes. *Chem. Mater.* **2017**, *29* (13), 5574–5582. https://doi.org/10.1021/acs.chemmater.7b00931.

(72) Walther, F.; Randau, S.; Schneider, Y.; Sann, J.; Rohnke, M.; Richter, F. H.; Zeier, W. G.; Janek, J. Influence of Carbon Additives on the Decomposition Pathways in Cathodes of Lithium Thiophosphate-Based All-Solid-State Batteries. *Chem. Mater.* **2020**, *32* (14), 6123–6136. https://doi.org/10.1021/acs.chemmater.0c01825.

(73) Auvergniot, J.; Cassel, A.; Foix, D.; Viallet, V.; Seznec, V.; Dedryvère, R. Redox Activity of Argyrodite Li6PS5Cl Electrolyte in All-Solid-State Li-Ion Battery: An XPS Study. *Solid State Ion.* **2017**, *300*, 78–85. https://doi.org/10.1016/j.ssi.2016.11.029.

(74) Tan, D. H. S.; Wu, E. A.; Nguyen, H.; Chen, Z.; Marple, M. A. T.; Doux, J.-M.; Wang, X.; Yang, H.; Banerjee, A.; Meng, Y. S. Elucidating Reversible Electrochemical Redox of Li_6PS_5Cl Solid Electrolyte. *ACS Energy Lett.* **2019**, *4* (10), 2418–2427. https://doi.org/10.1021/acsenergylett.9b01693.

(75) Strauss, F.; Stepien, D.; Maibach, J.; Pfaffmann, L.; Indris, S.; Hartmann, P.; Brezesinski, T. Influence of Electronically Conductive Additives on the Cycling Performance of Argyrodite-Based All-Solid-State Batteries. *RSC Adv.* **2020**, *10* (2), 1114–1119. https://doi.org/10.1039/C9RA10253A.

(76) Tan, D. H. S.; Banerjee, A.; Chen, Z.; Meng, Y. S. From Nanoscale Interface Characterization to Sustainable Energy Storage Using All-Solid-State Batteries. *Nat. Nanotechnol.* **2020**, *15* (3), 170–180. https://doi.org/10.1038/s41565-020-0657-x.

(77) Manthiram, A.; Fu, Y.; Su, Y.-S. Challenges and Prospects of Lithium–Sulfur Batteries. *Acc. Chem. Res.* **2013**, *46* (5), 1125–1134. https://doi.org/10.1021/ar300179v.

(78) Pan, H.; Cheng, Z.; He, P.; Zhou, H. A Review of Solid-State Lithium–Sulfur Battery: Ion Transport and Polysulfide Chemistry. *Energy Fuels* **2020**, *34* (10), 11942–11961. https://doi.org/10.1021/acs.energyfuels.0c02647.

(79) Roitzheim, C.; Sohn, Y. J.; Kuo, L.-Y.; Häuschen, G.; Mann, M.; Sebold, D.; Finsterbusch, M.; Kaghazchi, P.; Guillon, O.; Fattakhova-Rohlfing, D. All-Solid-State Li Batteries with NCM–Garnet-Based Composite Cathodes: The Impact of NCM Composition on Material Compatibility. *ACS Appl. Energy Mater.* **2022**, *5* (6), 6913–6926. https://doi.org/10.1021/acsaem.2c00533.

(80) Finsterbusch, M.; Danner, T.; Tsai, C.-L.; Uhlenbruck, S.; Latz, A.; Guillon, O. High Capacity Garnet-Based All-Solid-State Lithium Batteries: Fabrication and 3D-Microstructure Resolved

Modeling. *ACS Appl. Mater. Interfaces* **2018**, *10* (26), 22329–22339. https://doi.org/10.1021/acsami.8b06705.

(81) Kochetkov, I.; Zuo, T.-T.; Ruess, R.; Singh, B.; Zhou, L.; Kaup, K.; Janek, J.; Nazar, L. Different Interfacial Reactivity of Lithium Metal Chloride Electrolytes with High Voltage Cathodes Determines Solid-State Battery Performance. *Energy Environ. Sci.* **2022**, *15* (9), 3933–3944. https://doi.org/10.1039/D2EE00803C.

(82) Zhou, L.; Zuo, T.-T.; Kwok, C. Y.; Kim, S. Y.; Assoud, A.; Zhang, Q.; Janek, J.; Nazar, L. F. High Areal Capacity, Long Cycle Life 4 V Ceramic All-Solid-State Li-Ion Batteries Enabled by Chloride Solid Electrolytes. *Nat. Energy* **2022**, *7* (1), 83–93. https://doi.org/10.1038/s41560-021-00952-0.

(83) Auvergniot, J.; Cassel, A.; Ledeuil, J.-B.; Viallet, V.; Seznec, V.; Dedryvère, R. Interface Stability of Argyrodite Li_6PS_5Cl toward $LiCoO_2$, $LiNi_{1/3}Co_{1/3}Mn_{1/3}O_2$, and $LiMn_2O_4$ in Bulk All-Solid-State Batteries. *Chem. Mater.* **2017**, *29* (9), 3883–3890. https://doi.org/10.1021/acs.chemmater.6b04990.

(84) Kuo, L.-Y.; Guillon, O.; Kaghazchi, P. Origin of Structural Phase Transitions in Ni-Rich $Li_xNi_{0.8}Co_{0.1}Mn_{0.1}O_2$ with Lithiation/Delithiation: A First-Principles Study. *ACS Sustain. Chem. Eng.* **2021**, *9* (22), 7437–7446. https://doi.org/10.1021/acssuschemeng.0c07675.

(85) Kong, D.; Zhang, M.; Xiao, Y.; Hu, J.; Zhao, W.; Han, L.; Pan, F. Insights into the Structural Evolution and Li/O Loss in High-Ni Layered Oxide Cathodes. *Nano Energy* **2019**, *59*, 327–335. https://doi.org/10.1016/j.nanoen.2019.02.059.

(86) Ruan, Y.; Song, X.; Fu, Y.; Song, C.; Battaglia, V. Structural Evolution and Capacity Degradation Mechanism of LiNi0.6Mn0.2Co0.2O2 Cathode Materials. *J. Power Sources* **2018**, *400*, 539–548. https://doi.org/10.1016/j.jpowsour.2018.08.056.

(87) Xu, C.; Reeves, P. J.; Jacquet, Q.; Grey, C. P. Phase Behavior during Electrochemical Cycling of Ni-Rich Cathode Materials for Li-Ion Batteries. *Adv. Energy Mater.* **2021**, *11* (7), 2003404. https://doi.org/10.1002/aenm.202003404.

(88) Walther, F.; Strauss, F.; Wu, X.; Mogwitz, B.; Hertle, J.; Sann, J.; Rohnke, M.; Brezesinski, T.; Janek, J. The Working Principle of a Li_2CO_3/$LiNbO_3$ Coating on NCM for Thiophosphate-Based All-Solid-State Batteries. *Chem. Mater.* **2021**, *33* (6), 2110–2125. https://doi.org/10.1021/acs.chemmater.0c04660.

(89) Kim, A.-Y.; Strauss, F.; Bartsch, T.; Teo, J. H.; Hatsukade, T.; Mazilkin, A.; Janek, J.; Hartmann, P.; Brezesinski, T. Stabilizing Effect of a Hybrid Surface Coating on a Ni-Rich NCM Cathode Material in All-Solid-State Batteries. *Chem. Mater.* **2019**, *31* (23), 9664–9672. https://doi.org/10.1021/acs.chemmater.9b02947.

(90) Walther, F.; Koerver, R.; Fuchs, T.; Ohno, S.; Sann, J.; Rohnke, M.; Zeier, W. G.; Janek, J. Visualization of the Interfacial Decomposition of Composite Cathodes in Argyrodite-Based All-Solid-State Batteries Using Time-of-Flight Secondary-Ion Mass Spectrometry. *Chem. Mater.* **2019**, *31* (10), 3745–3755. https://doi.org/10.1021/acs.chemmater.9b00770.

(91) Zhang, R.; Strauss, F.; Jiang, L.; Casalena, L.; Li, L.; Janek, J.; Kondrakov, A.; Brezesinski, T. Transition-Metal Interdiffusion and Solid Electrolyte Poisoning in All-Solid-State Batteries Revealed by Cryo-TEM. *Chem. Commun.* **2023**, *59* (31), 4600–4603. https://doi.org/10.1039/D3CC00516J.

(92) Wang, Z.; Wang, Z.; Xue, D.; Zhao, J.; Zhang, X.; Geng, L.; Li, Y.; Du, C.; Yao, J.; Liu, X.; Rong, Z.; Guo, B.; Fang, R.; Su, Y.; Delmas, C.; Harris, S. J.; Wagemaker, M.; Zhang, L.; Tang, Y.; Zhang, S.; Zhu, L.; Huang, J. Reviving the Rock-Salt Phases in Ni-Rich Layered Cathodes by Mechano-Electrochemistry in All-Solid-State Batteries. *Nano Energy* **2023**, *105*, 108016. https://doi.org/10.1016/j.nanoen.2022.108016.

(93) McGrogan, F. P.; Swamy, T.; Bishop, S. R.; Eggleton, E.; Porz, L.; Chen, X.; Chiang, Y.-M.; Van Vliet, K. J. Compliant Yet Brittle Mechanical Behavior of Li2S-P2S5 Lithium-Ion Conducting Solid Electrolyte. *Advanced Energy Materials*. 2017, p 7(12), 1602011.

(94) Culver, S. P.; Koerver, R.; Zeier, W. G.; Janek, J. On the Functionality of Coatings for Cathode Active Materials in Thiophosphate-Based All-Solid-State Batteries. *Adv. Energy Mater.* **2019**, *9* (24), 1900626. https://doi.org/10.1002/aenm.201900626.

(95) Strauss, F.; Teo, J. H.; Maibach, J.; Kim, A.-Y.; Mazilkin, A.; Janek, J.; Brezesinski, T. Li_2ZrO_3 -Coated NCM622 for Application in Inorganic Solid-State Batteries: Role of Surface Carbonates in the Cycling Performance. *ACS Appl. Mater. Interfaces* **2020**, *12* (51), 57146–57154. https://doi.org/10.1021/acsami.0c18590.

(96) Haruyama, J.; Sodeyama, K.; Han, L.; Takada, K.; Tateyama, Y. Space–Charge Layer Effect at Interface between Oxide Cathode and Sulfide Electrolyte in All-Solid-State Lithium-Ion Battery. *Chem. Mater.* **2014**, *26* (14), 4248–4255. https://doi.org/10.1021/cm5016959.

(97) de Klerk, N. J. J.; Wagemaker, M. Space-Charge Layers in All-Solid-State Batteries; Important or Negligible? *ACS Appl. Energy Mater.* **2018**, acsaem.8b01141. https://doi.org/10.1021/acsaem.8b01141.

(98) He, W.; Zhang, C.; Wang, M.; Wei, B.; Zhu, Y.; Wu, J.; Liang, C.; Chen, L.; Wang, P.; Wei, W. Countering Voltage Decay, Redox Sluggishness, and Calendering Incompatibility by Near-Zero-Strain Interphase in Lithium-Rich, Manganese-Based Layered Oxide Electrodes. *Adv. Funct. Mater.* **2022**, *32* (29), 2200322. https://doi.org/10.1002/adfm.202200322.

(99) Liang, J.; Zhu, Y.; Li, X.; Luo, J.; Deng, S.; Zhao, Y.; Sun, Y.; Wu, D.; Hu, Y.; Li, W.; Sham, T.-K.; Li, R.; Gu, M.; Sun, X. A Gradient Oxy-Thiophosphate-Coated Ni-Rich Layered Oxide Cathode for Stable All-Solid-State Li-Ion Batteries. *Nat. Commun.* **2023**, *14* (1), 146. https://doi.org/10.1038/s41467-022-35667-7.

(100) Sakuda, A.; Hayashi, A.; Tatsumisago, M. Interfacial Observation between $LiCoO_2$ Electrode and Li_2S−P_2S_5 Solid Electrolytes of All-Solid-State Lithium Secondary Batteries Using Transmission Electron Microscopy. *Chem. Mater.* **2010**, *22* (3), 949–956. https://doi.org/10.1021/cm901819c.

(101) Zou, C.; Zang, Z.; Tao, X.; Yi, L.; Chen, X.; Zhang, X.; Yang, L.; Liu, X.; Wang, X. Stabilized Cathode/Sulfide Electrolyte Interface through Conformally Interfacial Nanocoating for All-Solid-State Batteries. *ACS Appl. Energy Mater.* **2023**, *6* (6), 3599–3607. https://doi.org/10.1021/acsaem.3c00255.

(102) Conforto, G.; Ruess, R.; Schröder, D.; Trevisanello, E.; Fantin, R.; Richter, F. H.; Janek, J. Editors' Choice—Quantification of the Impact of Chemo-Mechanical Degradation on the Performance and Cycling Stability of NCM-Based Cathodes in Solid-State Li-Ion Batteries. *J. Electrochem. Soc.* **2021**, *168* (7), 070546. https://doi.org/10.1149/1945-7111/ac13d2.

(103) Bae Song, Y.; Kwak, H.; Cho, W.; Kim, K. S.; Seok Jung, Y.; Park, K.-H. Electrochemo-Mechanical Effects as a Critical Design Factor for All-Solid-State Batteries. *Curr. Opin. Solid State Mater. Sci.* **2022**, *26* (1), 100977. https://doi.org/10.1016/j.cossms.2021.100977.

(104) Liu, X.; Zheng, B.; Zhao, J.; Zhao, W.; Liang, Z.; Su, Y.; Xie, C.; Zhou, K.; Xiang, Y.; Zhu, J.; Wang, H.; Zhong, G.; Gong, Z.; Huang, J.; Yang, Y. Electrochemo-Mechanical Effects on Structural Integrity of Ni-Rich Cathodes with Different Microstructures in All Solid-State Batteries. Advanced Energy Materials. 2021. https://doi.org/10.1002/aenm.202003583.

(105) Zhang, X.; Li, X.; Weng, S.; Wu, S.; Liu, Q.; Cao, M.; Li, Y.; Wang, Z.; Zhu, L.; Xiao, R.; Su, D.; Yu, X.; Li, H.; Chen, L.; Wang, Z.; Wang, X. Spontaneous Gas–Solid Reaction on Sulfide Electrolytes for High-Performance All-Solid-State Batteries. *Energy Environ. Sci.* **2023**, *16* (3), 1091–1099. https://doi.org/10.1039/D2EE03358E.

(106) Hood, Z. D.; Mane, A. U.; Sundar, A.; Tepavcevic, S.; Zapol, P.; Eze, U. D.; Adhikari, S. P.; Lee, E.; Sterbinsky, G. E.; Elam, J. W.; Connell, J. G. Multifunctional Coatings on Sulfide-Based Solid Electrolyte Powders with Enhanced Processability, Stability, and Performance for Solid-State Batteries. *Adv. Mater.* **2023**, 2300673. https://doi.org/10.1002/adma.202300673.

(107) Feng, Z.; Zhang, S.; Rajagopalan, R.; Huang, X.; Ren, Y.; Sun, D.; Wang, H.; Tang, Y. Dual-Element-Modified Single-Crystal $LiNi_{0.6}Co_{0.2}Mn_{0.2}O_2$ as a Highly Stable Cathode for Lithium-

Ion Batteries. *ACS Appl. Mater. Interfaces* **2021**, *13* (36), 43039–43050. https://doi.org/10.1021/acsami.1c10799.

(108) Ou, X.; Liu, T.; Zhong, W.; Fan, X.; Guo, X.; Huang, X.; Cao, L.; Hu, J.; Zhang, B.; Chu, Y. S.; Hu, G.; Lin, Z.; Dahbi, M.; Alami, J.; Amine, K.; Yang, C.; Lu, J. Enabling High Energy Lithium Metal Batteries via Single-Crystal Ni-Rich Cathode Material Co-Doping Strategy. *Nat. Commun.* **2022**, *13* (1), 2319. https://doi.org/10.1038/s41467-022-30020-4.

(109) Sun, Y.; Huang, W.; Zhao, G.; Liu, Q.; Duan, L.; Wang, S.; An, Q.; Wang, H.; Yang, Y.; Zhang, C.; Guo, H. LiNi $_{0.9}$ Co $_{0.09}$ Mo $_{0.01}$ O $_{2}$ Cathode with Li $_{3}$ PO $_{4}$ Coating and Ti Doping for Next-Generation Lithium-Ion Batteries. *ACS Energy Lett.* **2023**, *8* (3), 1629–1638. https://doi.org/10.1021/acsenergylett.2c02412.

(110) Sun, H. H.; Kim, U.-H.; Park, J.-H.; Park, S.-W.; Seo, D.-H.; Heller, A.; Mullins, C. B.; Yoon, C. S.; Sun, Y.-K. Transition Metal-Doped Ni-Rich Layered Cathode Materials for Durable Li-Ion Batteries. *Nat. Commun.* **2021**, *12* (1), 6552. https://doi.org/10.1038/s41467-021-26815-6.

(111) Tan, D. H. S.; Chen, Y.-T.; Yang, H.; Bao, W.; Sreenarayanan, B.; Doux, J.-M.; Li, W.; Lu, B.; Ham, S.-Y.; Sayahpour, B.; Scharf, J.; Wu, E. A.; Deysher, G.; Han, H. E.; Hah, H. J.; Jeong, H.; Lee, J. B.; Chen, Z.; Meng, Y. S. Carbon-Free High-Loading Silicon Anodes Enabled by Sulfide Solid Electrolytes. *Science* **2021**, *373* (6562), 1494–1499. https://doi.org/10.1126/science.abg7217.

(112) Kim, S. Y.; Cha, H.; Kostecki, R.; Chen, G. Composite Cathode Design for High-Energy All-Solid-State Lithium Batteries with Long Cycle Life. *ACS Energy Lett.* **2023**, *8* (1), 521–528. https://doi.org/10.1021/acsenergylett.2c02414.

(113) Peng, L.; Yu, C.; Zhang, Z.; Ren, H.; Zhang, J.; He, Z.; Yu, M.; Zhang, L.; Cheng, S.; Xie, J. Chlorine-Rich Lithium Argyrodite Enabling Solid-State Batteries with Capabilities of High Voltage, High Rate, Low-Temperature and Ultralong Cyclability. *Chem. Eng. J.* **2022**, *430*, 132896. https://doi.org/10.1016/j.cej.2021.132896.

(114) Yoonjae, H.; Sung Hoo, J.; Hiram, K.; Seunggoo, J.; Hunho H., K.; Jong Hoon, L.; Seung-Tae, H.; Yoon Seok, J. Single- or Poly-Crystalline Ni-Rich Layered Cathode, Sulfide or Halide Solid Electrolyte: Which Will Be the Winners for All-Solid-State Batteries? Advance Energy Materials. 2021. https://doi.org/10.1002/aenm.202100126.

(115) Kasnatscheew, J.; Evertz, M.; Streipert, B.; Wagner, R.; Klöpsch, R.; Vortmann, B.; Hahn, H.; Nowak, S.; Amereller, M.; Gentschev, A.-C.; Lamp, P.; Winter, M. The Truth about the 1st Cycle Coulombic Efficiency of LiNi $_{1/3}$ Co $_{1/3}$ Mn $_{1/3}$ O $_{2}$ (NCM) Cathodes. *Phys. Chem. Chem. Phys.* **2016**, *18* (5), 3956–3965. https://doi.org/10.1039/C5CP07718D.

(116) Grenier, A.; Reeves, P. J.; Liu, H.; Seymour, I. D.; Märker, K.; Wiaderek, K. M.; Chupas, P. J.; Grey, C. P.; Chapman, K. W. Intrinsic Kinetic Limitations in Substituted Lithium-Layered Transition-Metal Oxide Electrodes. *J. Am. Chem. Soc.* **2020**, *142* (15), 7001–7011. https://doi.org/10.1021/jacs.9b13551.

(117) Strauss, F.; Stepien, D.; Maibach, J.; Pfaffmann, L.; Indris, S.; Hartmann, P.; Brezesinski, T. Influence of Electronically Conductive Additives on the Cycling Performance of Argyrodite-Based All-Solid-State Batteries. *RSC Adv.* **2020**, *10* (2), 1114–1119. https://doi.org/10.1039/C9RA10253A.

(118) Randau, S.; Walther, F.; Neumann, A.; Schneider, Y.; Negi, R. S.; Mogwitz, B.; Sann, J.; Becker-Steinberger, K.; Danner, T.; Hein, S.; Latz, A.; Richter, F. H.; Janek, J. On the Additive Microstructure in Composite Cathodes and Alumina-Coated Carbon Microwires for Improved All-Solid-State Batteries. *Chem. Mater.* **2021**, *33* (4), 1380–1393. https://doi.org/10.1021/acs.chemmater.0c04454.

(119) Dugas, R.; Dupraz, Y.; Quemin, E.; Koç, T.; Tarascon, J.-M. Engineered Three-Electrode Cells for Improving Solid State Batteries. *J. Electrochem. Soc.* **2021**, *168* (9), 090508. https://doi.org/10.1149/1945-7111/ac208d.

(120) Siroma, Z.; Sato, T.; Takeuchi, T.; Nagai, R.; Ota, A.; Ioroi, T. AC Impedance Analysis of Ionic and Electronic Conductivities in Electrode Mixture Layers for an All-Solid-State Lithium-Ion

Battery. *J. Power Sources* **2016**, *316*, 215–223. https://doi.org/10.1016/j.jpowsour.2016.03.059.
(121) Cericola, D.; Spahr, M. E. Impedance Spectroscopic Studies of the Porous Structure of Electrodes Containing Graphite Materials with Different Particle Size and Shape. *Electrochimica Acta* **2016**, *191*, 558–566. https://doi.org/10.1016/j.electacta.2016.01.121.
(122) Moškon, J.; Žuntar, J.; Drvarič Talian, S.; Dominko, R.; Gaberšček, M. A Powerful Transmission Line Model for Analysis of Impedance of Insertion Battery Cells: A Case Study on the NMC-Li System. *J. Electrochem. Soc.* **2020**, *167* (14), 140539. https://doi.org/10.1149/1945-7111/abc769.
(123) Braun, P.; Uhlmann, C.; Weiss, M.; Weber, A.; Ivers-Tiffée, E. Assessment of All-Solid-State Lithium-Ion Batteries. *J. Power Sources* **2018**, *393*, 119–127. https://doi.org/10.1016/j.jpowsour.2018.04.111.
(124) Kaiser, N.; Spannenberger, S.; Schmitt, M.; Cronau, M.; Kato, Y.; Roling, B. Ion Transport Limitations in All-Solid-State Lithium Battery Electrodes Containing a Sulfide-Based Electrolyte. *J. Power Sources* **2018**, *396*, 175–181. https://doi.org/10.1016/j.jpowsour.2018.05.095.
(125) Landesfeind, J.; Pritzl, D.; Gasteiger, H. A. An Analysis Protocol for Three-Electrode Li-Ion Battery Impedance Spectra: Part I. Analysis of a High-Voltage Positive Electrode. *J. Electrochem. Soc.* **2017**, *164* (7), A1773–A1783. https://doi.org/10.1149/2.0131709jes.
(126) Siroma, Z.; Fujiwara, N.; Yamazaki, S.; Asahi, M.; Nagai, T.; Ioroi, T. Mathematical Solutions of Comprehensive Variations of a Transmission-Line Model of the Theoretical Impedance of Porous Electrodes. *Electrochimica Acta* **2015**, *160*, 313–322. https://doi.org/10.1016/j.electacta.2015.02.065.
(127) Alexander, C. L.; Tribollet, B.; Orazem, M. E. Contribution of Surface Distributions to Constant-Phase-Element (CPE) Behavior: 1. Influence of Roughness. *Electrochimica Acta* **2015**, *173*, 416–424. https://doi.org/10.1016/j.electacta.2015.05.010.
(128) Alexander, C. L.; Tribollet, B.; Orazem, M. E. Contribution of Surface Distributions to Constant-Phase-Element (CPE) Behavior: 2. Capacitance. *Electrochimica Acta* **2016**, *188*, 566–573. https://doi.org/10.1016/j.electacta.2015.11.135.
(129) Liang, L.; Zhang, W.; Zhao, F.; Denis, D. K.; Zaman, F. uz; Hou, L.; Yuan, C. Surface/Interface Structure Degradation of Ni-Rich Layered Oxide Cathodes toward Lithium-Ion Batteries: Fundamental Mechanisms and Remedying Strategies. *Adv. Mater. Interfaces* **2020**, *7* (3), 1901749. https://doi.org/10.1002/admi.201901749.
(130) Amin, R.; Chiang, Y.-M. Characterization of Electronic and Ionic Transport in $Li_{1-x}Ni_{0.33}Mn_{0.33}Co_{0.33}O_2$ (NMC_{333}) and $Li_{1-x}Ni_{0.50}Mn_{0.20}Co_{0.30}O_2$ (NMC_{523}) as a Function of Li Content. *J. Electrochem. Soc.* **2016**, *163* (8), A1512–A1517. https://doi.org/10.1149/2.0131608jes.
(131) Besnard, N.; Etiemble, A.; Douillard, T.; Dubrunfaut, O.; Tran-Van, P.; Gautier, L.; Franger, S.; Badot, J.-C.; Maire, E.; Lestriez, B. Multiscale Morphological and Electrical Characterization of Charge Transport Limitations to the Power Performance of Positive Electrode Blends for Lithium-Ion Batteries. *Adv. Energy Mater.* **2017**, *7* (8), 1602239. https://doi.org/10.1002/aenm.201602239.
(132) Seid, K. A.; Badot, J. C.; Dubrunfaut, O.; Caldes, M. T.; Stephant, N.; Gautier, L.; Guyomard, D.; Lestriez, B. Multiscale Electronic Transport in Li1+xNi1/3−uCo1/3−vMn1/3−wO2: A Broadband Dielectric Study from 40 Hz to 10 GHz. *Phys. Chem. Chem. Phys.* **2013**, *15* (45), 19790. https://doi.org/10.1039/c3cp52384e.
(133) Seid, K.-A.; Badot, J.-C.; Perca, C.; Dubrunfaut, O.; Soudan, P.; Guyomard, D.; Lestriez, B. An In Situ Multiscale Study of Ion and Electron Motion in a Lithium-Ion Battery Composite Electrode. *Adv. Energy Mater.* **2015**, *5* (2), 1400903. https://doi.org/10.1002/aenm.201400903.
(134) Badot, J.-C.; Ligneel, É.; Dubrunfaut, O.; Guyomard, D.; Lestriez, B. A Multiscale Description of the Electronic Transport within the Hierarchical Architecture of a Composite Electrode for

Lithium Batteries. *Adv. Funct. Mater.* **2009**, *19* (17), 2749–2758. https://doi.org/10.1002/adfm.200900379.

(135) Ménétrier, M.; Saadoune, I.; Levasseur, S.; Delmas, C. The Insulator-Metal Transition upon Lithium Deintercalation from LiCoO2: Electronic Properties and 7Li NMR Study. *J. Mater. Chem.* **1999**, *9* (5), 1135–1140. https://doi.org/10.1039/a900016j.

(136) Marianetti, C. A.; Kotliar, G.; Ceder, G. A First-Order Mott Transition in LixCoO2. *Nat. Mater.* **2004**, *3* (9), 627–631. https://doi.org/10.1038/nmat1178.

(137) Reimers, J. N.; Dahn, J. R. Electrochemical and In Situ X-Ray Diffraction Studies of Lithium Intercalation in Li x CoO2. *J. Electrochem. Soc.* **1992**, *139* (8), 2091–2097. https://doi.org/10.1149/1.2221184.

(138) Zhu, Y.; Wang, C. Galvanostatic Intermittent Titration Technique for Phase-Transformation Electrodes. *J. Phys. Chem. C* **2010**, *114* (6), 2830–2841. https://doi.org/10.1021/jp9113333.

(139) Oyama, G.; Yamada, Y.; Natsui, R.; Nishimura, S.; Yamada, A. Kinetics of Nucleation and Growth in Two-Phase Electrochemical Reaction of Li_xFePO_4. *J. Phys. Chem. C* **2012**, *116* (13), 7306–7311. https://doi.org/10.1021/jp300085n.

(140) Koç, T.; Marchini, F.; Rousse, G.; Dugas, R.; Tarascon, J.-M. In Search of the Best Solid Electrolyte-Layered Oxide Pairing for Assembling Practical All-Solid-State Batteries. *ACS Appl. Energy Mater.* **2021**, *4* (12), 13575–13585. https://doi.org/10.1021/acsaem.1c02187.

(141) Lee, J. M.; Park, Y. S.; Moon, J.-W.; Hwang, H. Ionic and Electronic Conductivities of Lithium Argyrodite Li6PS5Cl Electrolytes Prepared via Wet Milling and Post-Annealing. *Front. Chem.* **2021**, *9*, 778057. https://doi.org/10.3389/fchem.2021.778057.

(142) Sun, H.; Zhao, K. Electronic Structure and Comparative Properties of $LiNi_xMn_yCo_zO_2$ Cathode Materials. *J. Phys. Chem. C* **2017**, *121* (11), 6002–6010. https://doi.org/10.1021/acs.jpcc.7b00810.

(143) Jetybayeva, A.; Schön, N.; Oh, J.; Kim, J.; Kim, H.; Park, G.; Lee, Y.-G.; Eichel, R.-A.; Kleiner, K.; Hausen, F.; Hong, S. Unraveling the State of Charge-Dependent Electronic and Ionic Structure–Property Relationships in NCM622 Cells by Multiscale Characterization. *ACS Appl. Energy Mater.* **2022**, *5* (2), 1731–1742. https://doi.org/10.1021/acsaem.1c03173.

(144) Wang, C.; Wang, X.; Zhang, R.; Lei, T.; Kisslinger, K.; Xin, H. L. Resolving Complex Intralayer Transition Motifs in High-Ni-Content Layered Cathode Materials for Lithium-Ion Batteries. *Nat. Mater.* **2023**, *22* (2), 235–241. https://doi.org/10.1038/s41563-022-01461-5.

(145) Mu, L.; Lin, R.; Xu, R.; Han, L.; Xia, S.; Sokaras, D.; Steiner, J. D.; Weng, T.-C.; Nordlund, D.; Doeff, M. M.; Liu, Y.; Zhao, K.; Xin, H. L.; Lin, F. Oxygen Release Induced Chemomechanical Breakdown of Layered Cathode Materials. *Nano Lett.* **2018**, *18* (5), 3241–3249. https://doi.org/10.1021/acs.nanolett.8b01036.

(146) Dahbi, M.; Saadoune, I.; Amarilla, J. M. LixNi0.7Co0.3O2 Electrode Material: Structural, Physical and Electrochemical Investigations. *Electrochimica Acta* **2008**, *53* (16), 5266–5271. https://doi.org/10.1016/j.electacta.2008.02.072.

(147) Li, W.; Reimers, J. N.; Dahn, J. R. In Situ X-Ray Diffraction and Electrochemical Studies of Lil _xNiO2.

(148) Kondrakov, A. O.; Schmidt, A.; Xu, J.; Geßwein, H.; Mönig, R.; Hartmann, P.; Sommer, H.; Brezesinski, T.; Janek, J. Anisotropic Lattice Strain and Mechanical Degradation of High- and Low-Nickel NCM Cathode Materials for Li-Ion Batteries. *J. Phys. Chem. C* **2017**, *121* (6), 3286–3294. https://doi.org/10.1021/acs.jpcc.6b12885.

(149) Prakash, A. S.; Manikandan, P.; Ramesha, K.; Sathiya, M.; Tarascon, J.-M.; Shukla, A. K. Solution-Combustion Synthesized Nanocrystalline $Li_4Ti_5O_{12}$ As High-Rate Performance Li-Ion Battery Anode. *Chem. Mater.* **2010**, *22* (9), 2857–2863. https://doi.org/10.1021/cm100071z.

(150) Scharner, S.; Weppner, W.; Schmid-Beurmann, P. Evidence of Two-Phase Formation upon Lithium Insertion into the Li1.33Ti1.67 O 4 Spinel. *J. Electrochem. Soc.* **1999**, *146* (3), 857–861. https://doi.org/10.1149/1.1391692.

(151) Borghols, W. J. H.; Wagemaker, M.; Lafont, U.; Kelder, E. M.; Mulder, F. M. Size Effects in the $Li_{4+x}Ti_5O_{12}$ Spinel. *J. Am. Chem. Soc.* **2009**, *131* (49), 17786–17792. https://doi.org/10.1021/ja902423e.

(152) Pang, W. K.; Peterson, V. K.; Sharma, N.; Shiu, J.-J.; Wu, S. Lithium Migration in $Li_4Ti_5O_{12}$ Studied Using in Situ Neutron Powder Diffraction. *Chem. Mater.* **2014**, *26* (7), 2318–2326. https://doi.org/10.1021/cm5002779.

(153) Tanaka, Y.; Ikeda, M.; Sumita, M.; Ohno, T.; Takada, K. First-Principles Analysis on Role of Spinel (111) Phase Boundaries in $Li_{4+3x}Ti_5O_{12}$ Li-Ion Battery Anodes. *Phys. Chem. Chem. Phys.* **2016**, *18* (33), 23383–23388. https://doi.org/10.1039/C6CP04131K.

(154) Wagemaker, M.; Mulder, F. M.; Van der Ven, A. The Role of Surface and Interface Energy on Phase Stability of Nanosized Insertion Compounds. *Adv. Mater.* **2009**, *21* (25–26), 2703–2709. https://doi.org/10.1002/adma.200803038.

(155) Wen, Y.; Chen, X.; Lu, X.; Gu, L. Interface Charges Boosted Ultrafast Lithiation in Li4Ti5O12 Revealed by In-Situ Electron Holography. *J. Energy Chem.* **2018**, *27* (5), 1397–1401. https://doi.org/10.1016/j.jechem.2018.02.019.

(156) Verde, M. G.; Baggetto, L.; Balke, N.; Veith, G. M.; Seo, J. K.; Wang, Z.; Meng, Y. S. Elucidating the Phase Transformation of $Li_4Ti_5O_{12}$ Lithiation at the Nanoscale. *ACS Nano* **2016**, *10* (4), 4312–4321. https://doi.org/10.1021/acsnano.5b07875.

(157) Park, Y. S.; Kim, K.; Lee, J.; Moon, J.; Park, H.; Hwang, H. Effect of Cell Pressure on the Electrochemical Performance of All-solid-state Lithium Batteries with Zero-excess Li Metal Anode. *J. Am. Ceram. Soc.* **2023**, jace.19322. https://doi.org/10.1111/jace.19322.

(158) Cronau, M.; Szabo, M.; König, C.; Wassermann, T. B.; Roling, B. How to Measure a Reliable Ionic Conductivity? The Stack Pressure Dilemma of Microcrystalline Sulfide-Based Solid Electrolytes. *ACS Energy Lett.* **2021**, *6* (9), 3072–3077. https://doi.org/10.1021/acsenergylett.1c01299.

(159) Doux, J.-M.; Yang, Y.; Tan, D. H. S.; Nguyen, H.; Wu, E. A.; Wang, X.; Banerjee, A.; Meng, Y. S. Pressure Effects on Sulfide Electrolytes for All Solid-State Batteries. *J. Mater. Chem. A* **2020**, *8* (10), 5049–5055. https://doi.org/10.1039/C9TA12889A.

(160) Hänsel, C.; Kundu, D. The Stack Pressure Dilemma in Sulfide Electrolyte Based Li Metal Solid-State Batteries: A Case Study with Li_6PS_5Cl Solid Electrolyte. *Adv. Mater. Interfaces* **2021**, *8* (10), 2100206. https://doi.org/10.1002/admi.202100206.

(161) Sang, J.; Tang, B.; Qiu, Y.; Fang, Y.; Pan, K.; Zhou, Z. How Does Stacking Pressure Affect the Performance of Solid Electrolytes and All-Solid-State Lithium Metal Batteries? *ENERGY Environ. Mater.* **2023**, e12670. https://doi.org/10.1002/eem2.12670.

(162) Singh, A.; Finegan, D. P.; Hamilton, D.; Zhu, J.; Li, W.; Martin, T. R. Controls Stack Pressure Induced Fracture Using Microstructural Modulation in Solid-State Batteries. *ECS Meet. Abstr.* **2023**, *MA2023-01* (6), 1075–1075. https://doi.org/10.1149/MA2023-0161075mtgabs.

(163) An, S. J.; Li, J.; Du, Z.; Daniel, C.; Wood, D. L. Fast Formation Cycling for Lithium Ion Batteries. *J. Power Sources* **2017**, *342*, 846–852. https://doi.org/10.1016/j.jpowsour.2017.01.011.

(164) An, S. J.; Li, J.; Daniel, C.; Mohanty, D.; Nagpure, S.; Wood, D. L. The State of Understanding of the Lithium-Ion-Battery Graphite Solid Electrolyte Interphase (SEI) and Its Relationship to Formation Cycling. *Carbon* **2016**, *105*, 52–76. https://doi.org/10.1016/j.carbon.2016.04.008.

Résumé

Les technologies de stockage énergétiques jouent un rôle crucial en accommodant le caractère intermittent des énergies renouvelable. Actuellement, les batteries lithium-ion prédominent le marché des appareils portables. Cependant, pour les véhicules électriques, des avancées sont nécessaires en termes de sécurité et de densité énergétique, conduisant à l'exploration de nouvelles technologies de batterie, notamment les batteries tout-solide. Cette thèse se concentre sur les obstacles entravant l'application pratique de ces batteries tout-solide, en mettant particulièrement en lumière le rôle des composites cathodes. L'attention s'est portée sur un composite couramment utilisé, composé de Li_6PS_5Cl comme électrolyte solide (SE) associé à un matériau actif de type NMC. Les mécanismes de dégradation se révèlent être influencés par deux interfaces : SE/additif carbone et SE/AM (matériau actif). Le cyclage en dessous de 3,6 V par rapport au Li-In/In montrent que la dégradation prédominante provient de l'interface SE/additif carbone, tandis qu'à 3,9 V, l'interface SE/AM devient le principal foyer de dégradation. A partir de là, l'effet des additifs de carbone dans le composite a été minutieusement étudié. Ainsi, une concentration de plus de 2 % en poids de VGCF a un impact négatif sur la conduction ionique des composites. De plus, une analyse in situ de la conductivité électronique des composites sans carbone révèle des changements induits par l'insertion/désinsertion du lithium dans le transport électronique, avec une réduction de la conductivité électronique à états de charge élevés, en particulier dans les NMC riches en nickel. Globalement, les résultats indiquent qu'une faible quantité d'additif carbone peut avoir des avantages significatifs, à condition que les réactions chimiques soient maitrisées. Ainsi, des stratégies minimisant les pertes de capacité à long terme ont été explorées, en examinant des paramètres tels que la pression d'assemblage, le loading, les cycles de formation, la température et les coating carbonate. En fusionnant les conditions optimales, un composite de cathode optimisé est présenté, ouvrant la voie à des avancées prometteuses dans la technologie des batteries tout-solide.

Mots-clés: Tout-solide, Interfaces, Spectroscopie d'impédance, Argyrodite, Conductivité électronique

Abstract

While Lithium-ion batteries dominate portable devices, growing safety and energy density demands in electric vehicle batteries have led to the exploration of "beyond Li-ion" technology. All-Solid-State Batteries (ASSBs) have emerged as a promising alternative to Li-ion batteries. Thus, this doctoral research focuses on overcoming challenges hindering the practical implementation of ASSBs, with a specific emphasis on cathode composites. The investigation revolves around a common composite comprising Li_6PS_5Cl solid electrolyte (SE) and NMC active material (AM). The research unveils the degradation mechanisms within ASSBs, governed by SE/Carbon additive and SE/AM interfaces. It is observed that capacity deterioration, occurring below 3.6 V vs. Li-In/In, is primarily attributed to SE/Carbon interfaces. Conversely, elevating the voltage to 3.9 V shifts the primary degradation source to SE/AM interfaces. Then, the adverse effects of carbon additives on the ionic conduction of composites are demonstrated, particularly when exceeding 2 wt. % VGCF. Moreover, the study delves into the electronic conductivity of carbon-free composites using innovative in situ monitoring. This reveals Li-induced alterations hindering electronic conductivity, especially at high charge levels, notably in high Ni-content NMC. Furthermore, the influence of particle size and morphology on electronic percolation is extensively examined, advocating for minimal VGCF to enhance kinetics and stability. Strategies for effectively incorporating carbon additives while mitigating long-term capacity loss are explored, encompassing assembly pressure, loading, formation cycles, temperature, and carbonate coating. By mixing these optimal conditions, an enhanced cathode composite is introduced, holding promising potential for the progression of All-Solid-State Battery technology.

Keywords: Solid-state, Interfaces, Impedance spectroscopy, Argyrodite, Electronic conductivity